Fluorine-18 labelling of novel voltage-gated sodium channel ligands for applications in positron emission tomography (PET) imaging and oncology

A thesis submitted for the degree of

Doctor of Philosophy

By

Antonia Louisa Desmond

Department of Pharmacology

UCL School of Pharmacy

University College London

I, Antonia Louisa Desmond confirm that the work presented in this thesis is my own. Where information has been derived from other sources, I confirm that this has been indicated in the thesis.

Antonia Louisa Desmond MSci (Hons)

Abstract

Voltage-gated sodium channels (VGSCs) are essential for the initiation and propagation of neuronal impulses. Specifically, these channels initiate the rising phase of action potentials in electrically excitable cells, allowing the conduction of electrical information. There are 9 different sub-types of VGSCs, each found in different tissues, with a minimum 50% identical genetic code.[1] Recently, it has been reported that some VGSC sub-types are over-expressed in highly metastatic tumours.[2] Their presence allows the up-regulation of some key biochemical processes. In fact, the metastatic potential of the tumours has a positive correlation with the expression of sodium channels.[2-6] This thesis focussed on developing a novel positron emission tomography (PET) tracer to target VGSCs. We hypothesised that a PET scan using a VGSC ligand may be able to highlight tumours with high metastatic potential, and assist in the selection of the most appropriate clinical treatment. At present, there is no known clinical PET tracer for imaging VGSCs.

Our project involved the adaptation of the 3-(4-substituted-phenoxyphenyl) pyrazoles,[7] a known group of VGSC modulators, into novel fluorine-18 labelled PET imaging agents. These were chosen due to their strong affinity for VGSCs and their structural characteristics, which allowed multiple approches to introduce a fluorine-18 label. Several compounds of interest were successfully synthesised. Optimal radiolabelling strategies were identified and methodologies developed, to produce PET agents in good synthesis time, yield and purity. The fluorine-19 standards for these compounds underwent a full VGSC isoform selectivity screen to identify the most potent and selective compounds. The fluorine-18 PET agents were also put through a series of *in vitro* and *in vivo* studies including automated and manual electrophysiology, biodistribution, metabolism and autoradiography. Ultimately, we aimed to target specific VGSC sub-types that were highly expressed by specific aggressive tumour types.

Following this study, an interesting VGSC PET agent was revealed that warrants further investigation.

Acknowledgments

Over the last three years my studies have allowed me to work across a variety of disciplines and importantly encounter a range of colleagues. Working with you all, has been a great pleasure.

My thanks must firstly go to my academic supervisor Andrew Constanti for allowing me the opportunity, to undertake this project. I am hugely grateful for the faith you have shown in me and of course for the encouragement, guidance and advice you have given me along the way. The thanks for guidance must be extended to my industrial supervisors, Edward Robins, Helen Betts, Alexander Jackson and Sajinder Luthra. You have all mentored me during different periods of this project, and all have been instrumental in keeping this project moving forward, offering invaluable expertise and guidance. I hope this thesis does justice to my excellent supervision.

I have worked in various labs during my PhD both academic and industrial. Briefly, I would like to show my appreciation to:

Hammersmith Imanet for an enjoyable 18 months spent working alongside the R and D team. I will never forget Monday morning progress meetings.

The Aboagye group, Imperial College, the three months in your lab allowed me to remain effective in my studies, at an uncertain time.

The Hilton group, UCL School of Pharmacy, the 12 months working part-time in your lab, was invaluable to producing much of the synthetic chemistry described.

The Grove Centre, GE Healthcare, for allowing continuation of radiochemistry studies and for assisting *in vivo* and *in vitro* biology. Too many to name, but a huge thank you to the chemistry, radiochemistry and biology team.

This project would not have been possible without funding from the EPSRC and GE Healthcare – thank you.

I would like to express my gratitude to my parents. For all the confidence and encouragement you have given in me over the last three years, and always, my heartfelt thank you to you both.

My friends, you have all been instrumental in keeping my spirits up over the last three years. Thanks for all the support, distractions and words of wisdom. Your generosity knows no bounds.

To Tom, words cannot do justice to your sustained encouragement and support over the last three years. I will forever be grateful to the number of times you helped me move labs, dropped me off at The Grove Centre at 7 am, and finally reading third and fourth chapter drafts. I think you have more than returned the favour from your PhD days.

Finally, the work described herein has been a discovery into a new area of imaging, the help, support and guidance I have encountered, has made this thesis possible. I dedicate this work to you all.

Table of Contents

List of Figures

List of Tables

List of Schemes

Abbreviations

Abbreviation	Meaning
AD	Alzheimer's disease
AHP	After-hyperpolarisation
AP	Action potentials
BBB	Blood brain barrier
Boc	Di-tert-butyl dicarbonate
B Ca	Breast cancer
BTX	Batrachotoxin
CA1	Cornus Ammonis
CC	Column chromatography
C Ca	Cervical cancer
CNS	Central nervous system
CELEX	Cellular excitability
C_m	Cell lipid Bilayer
COSY	Correlation spectroscopy
CSM	Cell surface membrane
CT	Computed tomography
D	Domain
DMF	Dimethylformamide
DMSO	Dimethylsulfoxide
DRG	Dorsal root ganglion
EGF	Epidermal growth factor
EI	Electrospray ionisation
EOS	End of synthesis
[^{18}F]-FDG	[^{18}F]-Fluorodeoxyglucose
GCMS	Gas chromatography mass spectrometry
GNa	Non-linear conductance
HPLC	High performance liquid chromatography
HPV	Human papillomavirus
$T_{1/2}$	Half-Life
[^{11}C]*m*HED	[^{11}C]-*meta*-Hydroxyephedrine
HEK	Human embryonic kidney

HH	Hodgkin and Huxley
Kryptofix	4,7,13,16,21,2-Hexaoxa-1,10-diazabicyclo[8.8.8]hexacosane
HRMS	High resolution mass spectroscopy
IHC	Immunohistochemistry
IR	Infrared
LA	Local anaesthetics
LCMS	Liquid chromatography mass spectroscopy
LOR	Line of response
LQT3	Long QT syndrome type 3
MCB	Metastatic cell behaviours
MIBG	[^{123}I]-*meta*-Iodobenzylguanidine
MMP-9	Matrix metallopeptidase 9
MRI	Magnetic resonance imaging
MS	Mass spectrometry
***m*-CPBA**	*meta*-Chloro per-benzoic acid
NCA	Non-carrier added
NDC	Non-decay corrected
NET	Norepinephrine transporter
NGF	Nerve growth factor
NHE 1	Na^+/H^+ exchanger type 1
NMDAR	*N*-Methyl-D-aspartate receptor
NMP	*N*-Methyl-2-pyrrolidone
NMR	Nuclear magnetic resonance
NOESY	Nuclear overhauser effect spectroscopy
QSAR	Quantitative structural analysis relationship
PABA	*Para*-amino benzoic acid
P Ca	Prostate Cancer
PBS	Phosphate buffer solution
PET	Positron emission tomography
PKA	Protein kinase A
PNS	Peripheral nervous system
P Ca	Prostate cancer
PCP	Phencyclidine
PPC	Population patch clamp

PSA	Prostate-specific antigen
QMA	Quaternary methyl ammonium Sep-pak™
QSAR	Quantitative structure analysis relationship
RCY	Radiochemical yield
RPMI	Roswell park memorial institute
RT	Room temperature
RT-PCR	Real time-polymerase chain reaction
SB	Specific binding
SPECT	Single photon emission computed tomography
STX	Saxitoxin
TA	Test article
TEMPO	2,2,6,6-Tetramethyl-1-piperidinyloxy
TFA	Trifluoroacetic acid
TLC	Thin layer chromatography
TMS	Transmembrane segment
TTX	Tetrodotoxin
UV	Ultra-violet
VGSC	Voltage-gated sodium channel
V_m	Membrane potential
WRT	With respect to

1. Introduction

An overview of voltage-gated sodium channels and medical imaging for applications in oncology

1.0 Voltage-gated sodium channel overview

VGSCs are integral membrane proteins that allow sodium ions to permeate through the cell membrane in excitable cells such as neurones, myocytes and certain types of glia. Sodium influx is responsible for the rising phase of action potentials. VGSCs consist of an α-subunit of approximately 260 kDa, associated with one or more accessory β subunits of lower molecular mass. The α-subunit forms a Na^+-selective pore spanning the plasma membrane. The arrangement is such that six α-helical transmembrane segments (TMS) are repeated on the sequence four times, creating four different domains (DI-IV), connected by a cytoplasmic linker. Within these four domains, there is a relatively short and non-helical segment between TMS five and TMS six, forming the pore (Figure 1.1). The fourth transmembrane helix in each domain, has a positively charged residue at every third position allowing for voltage sensing.[1] A sliding helix model has been proposed to describe how the polar helix "unscrews" within the cell membrane, causing conformational changes to occur in the loop region between D III and IV, thus activating the channel.[1] The β subunits typically have a large N-terminal domain that is extracellular and immunoglobulin-like, plus a relatively short C-terminal segment which has an intracellular single transmembrane region.[1]

VGSCs exist in three conformational states: closed, open and inactivated. VGSCs in the closed state are blocked both intracellularly and extracellularly by the *h* gate and *m* gate respectively. This not only stops the influx of Na^+ ions into the channel pore, but also inhibits Na^+ ions in the channel gaining access to the cell. Activation of the channel by membrane depolarisation opens the *m* gate (extracellular) allowing further depolarsation of the cell during the rising phase of an action potential. The ability of the channel to inactivate (closure of the intracellular *h* gate) is due to a tethered 'plug' formed between domains III and IV of the α subunit making the *h* gate, and stopping Na^+ ions entering the channel on the intracellular side thus stopping the depolarisation phase.

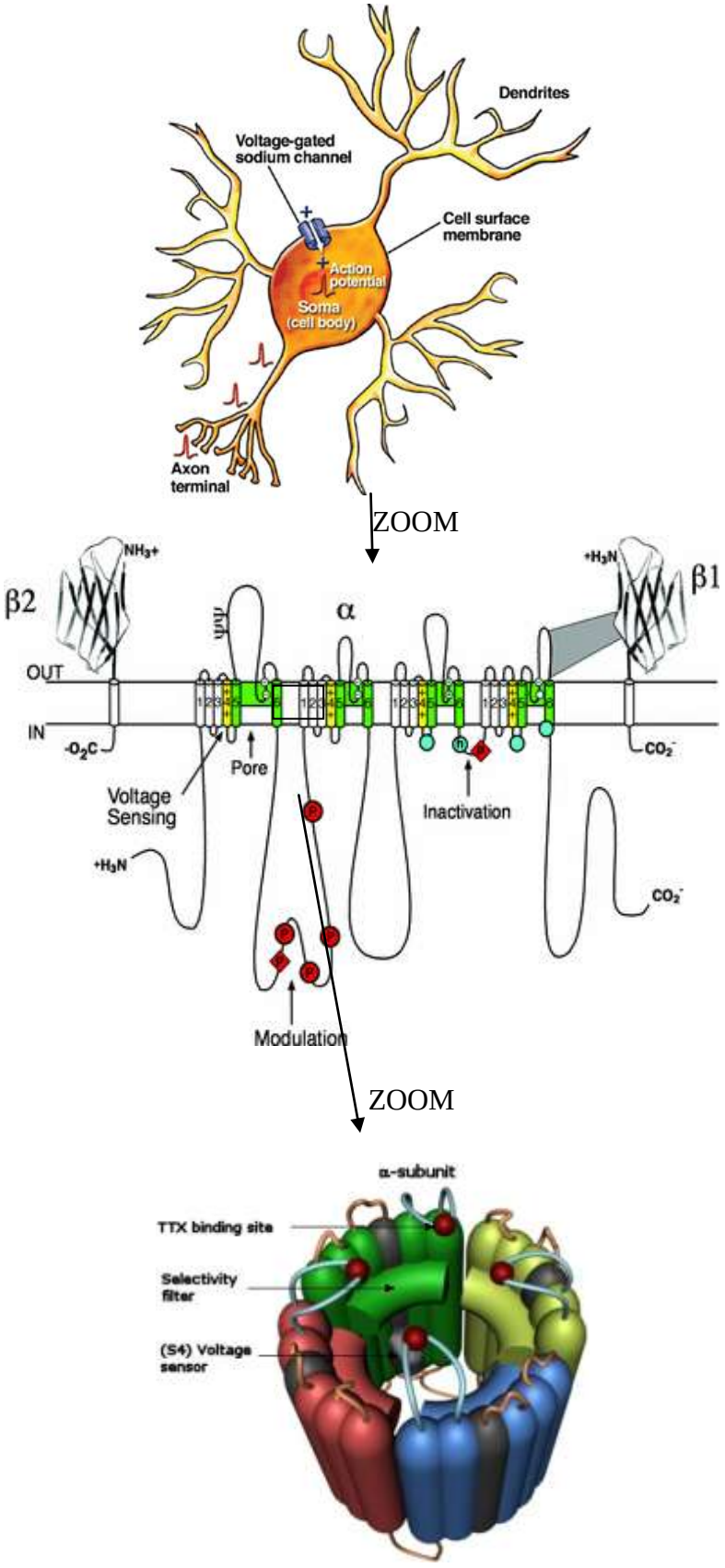

Figure 1.1: Proposed structure and topology of the voltage-gated sodium channel [1]

1.0.0 Anatomy of neurotransmission

Neurotransmission is the process which allows the release of neurotransmitters by the presynaptic neurone; subsequently they bind to and activate receptors of the postsynaptic neurone. Neurotransmission usually takes place at a synapse and occurs when an action potential (AP) (Section 1.0.1) is initiated in the presynaptic neurone.[8]

Neurones can vary with respect to the number, length and branching on the cell body (soma). Each neurone has four major characteristic features namely; the soma, dendrites, axon and presynaptic terminals (Figure 1.2). The soma contains the nucleus and acts as the cells energy centre. The main activities of the soma include metabolism and the synthesis of macromolecules that support the execution of cellular functions and structural maintenance. The dendrites which extend from the soma are responsible for receiving synaptic input messages from other neurones. These messages can be either excitatory or inhibitory. Most neurones in the central nervous system (CNS) have a high degree of dendritic branching, resulting in multiple messages being received from a number of juxtaposed neurones at any one time. A cellular response is due to a summation of these input signals. The axon (protruding from the soma) supports the rapid transfer of messages received from the dendrites to the axon terminals. If the input message is sufficient to produce a response, the voltage difference between the inside and outside of the neuronal membrane at rest, is transiently modified. If the change in voltage reaches the threshold potential an action potential is fired and propagates along the axon to the presynaptic terminal. Nerve cells are not directly connected, but have a gap ~100 Å wide, known as the synapse, which prevents the direct propagation of an action potential from one nerve cell to another. The electrical signal generated from an action potential is translated into a chemical message in the form of a neurotransmitter, stored and concentrated within vesicles in the presynaptic terminal.[9-10]

Neurotransmitter release occurs *via* a calcium-dependent excitation-secretion coupling which allows synaptic vesicles to dissociate from the network of filaments in the presynaptic terminal. Neurotransmitter vesicles are then free to fuse with the plasma membrane and participate in exocytosis. Once released into the synaptic cleft, the neurotransmitter can diffuse across the synapse and transmit a stimulatory or inhibitory message to the target cell.[9-10]

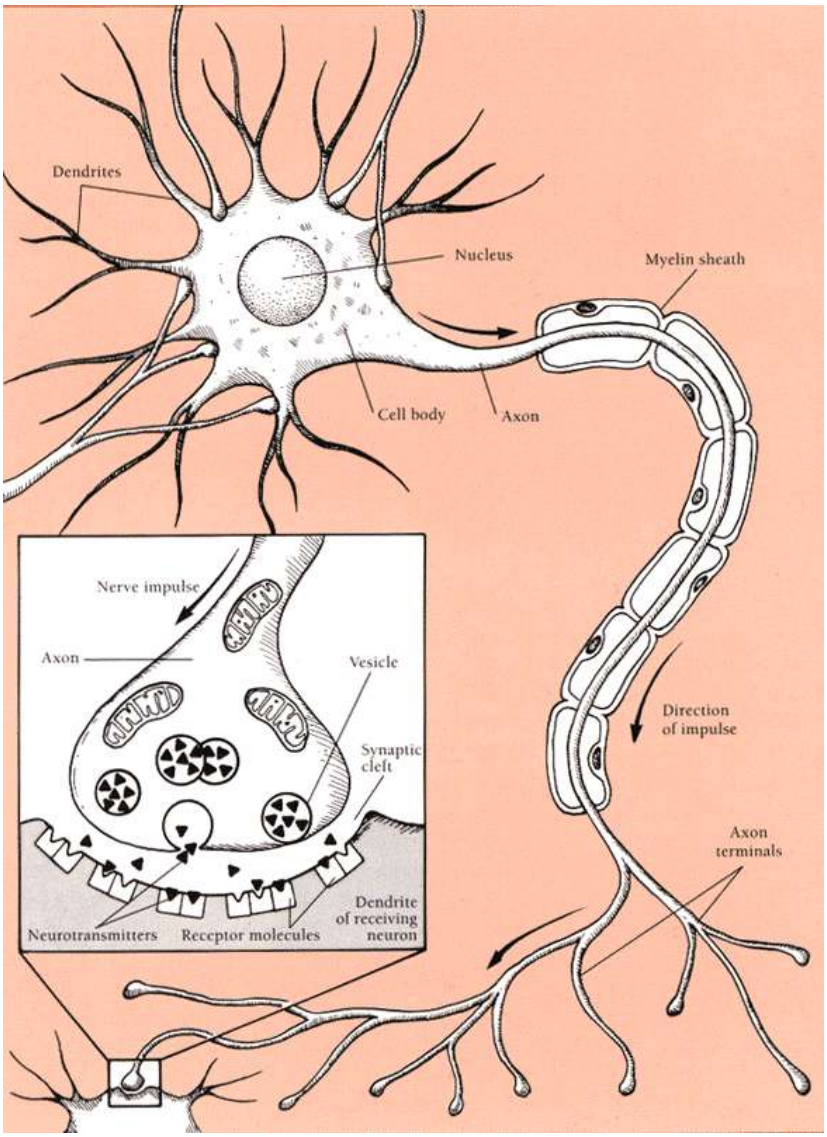

Figure 1.2: Model of neurotransmission [11]

Normally, a nerve cell releases only one type of neurotransmitter for example, glutamate, dopamine, serotonin *etc.* Neurotransmitters communicate with the postsynaptic cell by interacting with a specific receptor embedded in the cell membrane. The interaction between the neurotransmitter and the binding domain of the receptor is temporary with the neurotransmitter leaving unaffected, once the message has been passed on to the postsynaptic cell.

Neurotransmitters need to be quickly removed from the synapse so that their actions can be short-lived and the postsynaptic membrane made available for further stimulation. This is achieved by a number of mechanisms with different kinds of neurotransmitters having preferred routes. Simple diffusion away from the synaptic cleft does occur but it

is too slow to be the principal mechanism. Free neurotransmitter can be catabolised by enzymes in the synaptic cleft (*e.g.* acetylcholinesterase) or re-uptaken by the presynaptic terminal, glial cells or postsynaptic processes. The synapse is responsible for the unidirectional flow of information, the delay and the control of message transfer from one nerve to another. Communication and integration of responses is essential for the normal working of the human body.[9-10]

1.0.1 The action potential

An AP is an all-or-nothing event in which the electrical membrane potential of a cell rapidly rises and falls (Figure 1.3). In neurones, they play a central role in cell-to-cell communication. In other cell types, their main function is to activate intracellular processes. In muscle cells for example, an action potential is the first step in the chain of events leading to contraction.[12]

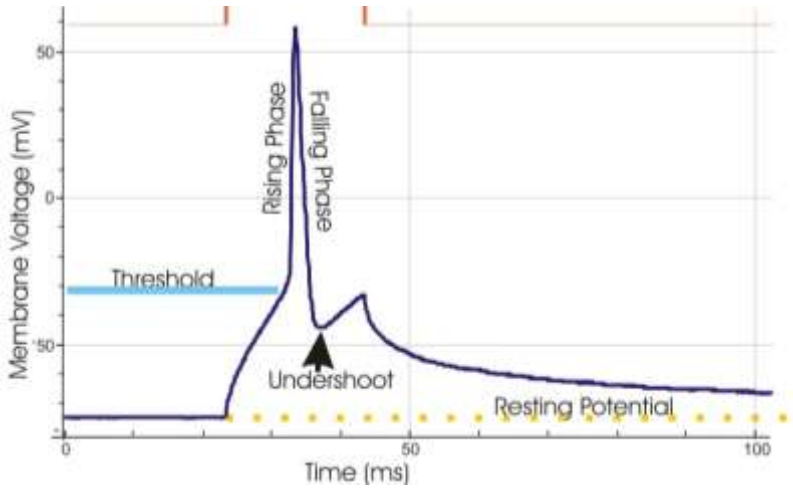

Figure 1.3: Schematic of an action potential [13]

Action potentials are initiated by VGSCs.[13] At rest, the cell membrane potential is approximately -60 to -80 mV and the majority of VGSCs are closed. The channels rapidly open when the membrane potential becomes less negative, due to a positive stimulus. When the membrane potential reaches threshold (around -55 mV), the *m* gate opens, causing a net inward flow of Na^+ ions, the membrane potential decreases towards the reversal potential for sodium (E_{Na}), where E_{Na} = +60 mV. The net inward flow of Na^+ ions is known as depolarisation. The depolarisation causes adjacent channels to

open through charge conductance, producing a greater electric current. The rapid influx of Na^+ ions causes the polarity of the plasma membrane to transiently reverse, and the channel then rapidly inactivates (closing of the *h* gate). As the Na^+ channel inactivates, Na^+ ions can no longer enter the neurone (and after many action potentials have been fired), the Na^+/K^+ ion pump actively transports them out of the plasma membrane. K^+ channels are then activated to allow a net outward flow of K^+ ions (repolarisation), returning the electrochemical gradient to the resting state. Whilst K^+ ions are leaving the cell, the *m* gate closes on the Na^+ channel, stopping any Na^+ ions entering the channel. However, the concentration of K^+ ions leaving the cell overshoots (hyperpolarisation). These channels close more slowly than VGSCs, thus causing a larger K^+ conductance across the membrane and therefore temporarily placing the membrane at a higher stimulating threshold. Thus, a greater stimulus would be required to fire an action potential. This period is known as the relative refractory period and is the mechanism that causes an action potential to travel unidirectionally. The action potential usually lasts for less than one millisecond.[13]

The temporal behaviour of VGSCs can be modelled by the Hodgkin-Huxley-type formalism.[14] The Na^+ and K^+ channels are treated as a population that are affected by three independent gating variables, *m*, *h* for Na^+ and *n* for K^+. Each of these variables can attain a value between 0 (fully impermeable) and 1 (fully permeable to ions). The summation of these variables yields the percentage of conducting channels.

1.0.2 Overview of the Hodgkin and Huxley gating model

The Hodgkin and Huxley (HH) model, based on their work on the giant squid axon, is a mathematical model addressing how an AP in neurones is intiated (Figure 1.4).[14] The HH model is a set of non-linear mathematical equations developed empirically on their voltage-clamp data, that approximates electrical activity in excitable cells. The cell lipid bilayer acts as a capacitor (C_m) and the VGSC acts as a non-linear conductor (G_{Na}), where the conductance has time and voltage-dependent components.

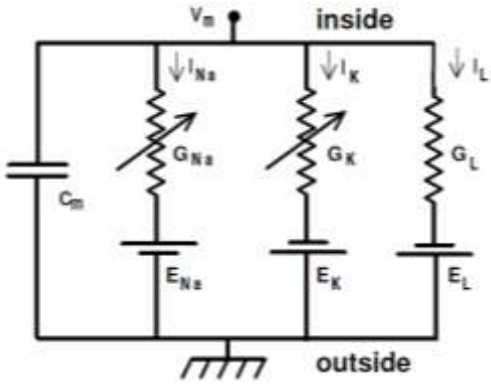

Figure 1.4: Schematic of the Hodgkin and Huxley model circuit [14]

The conductance is mediated by the probability that the channel will be open, which in turn is voltage-dependent. G_L represents 'leak' channels (linear conductances). The electrochemical gradients which drive the ion flow, are represented by batteries ($E_{Na/K/L}$). The ionic flows ($I_{Na/K/L}$) are represented by current sources. The time derivative of the potential (V_m) across the membrane is proportional to the sum of the currents in the circuit.

$$dV_m / dt = - 1/C_m (\Sigma I_i)$$

where I_i represents the individual ionic currents of the model. Hodgkin and Huxley determined that each VGSC state could be defined by one or more gates responding to an electrical field. For a channel to be open all the gates must be open, but for the channel to be closed, only one gate needs to be closed. The rate at which channels open for any given voltage step, is dependent upon the proportion of channels already opened multiplied by the closing rate constant.[15]

The model is slightly inaccurate as it over simplifies some dependencies, for example, the inactivation gate should not be able to close unless the activation gate is open and the inactivation gate, once closed, is located inside the cell membrane where it cannot be directly affected by the transmembrane potential. However, it is useful for gaining insight into activation and inactivation of VGSCs.[14-15]

1.0.3 Voltage-clamp recordings of sodium currents

The voltage-clamp technique is a method of recording the current flowing through the cell membrane while the membrane potential remains constant. This does not mimic processes found in nature, but is an important technique. When studying voltage-gated

channels, this technique allows the control of the voltage which determines the opening and closing of channels. By clamping the membrane potential, the experimenter ensures the current flowing through the membrane is linearly proportional to the conductance (G), being measured.

Transmembrane voltage is recorded through a "voltage-electrode" relative to ground and a "current-electrode" passing current into the cell. In order to maintain the membrane potential at -80 mV, a holding voltage is set and the voltage clamp uses negative feedback to maintain the cell at this voltage. The electrodes are connected to an amplifier which measures the potential and feeds the signal into the feedback amplifier. The amplifier also receives a signal determining the command potential and it subtracts the membrane potential from this value, magnifies any differences and sends an output signal to the current electrode. If the cell deviates from -80 mV (holding voltage), the amplifier generates a signal that is the difference between the two. The feedback circuit passes the current into the cell to reduce this signal back to zero. Therefore, the clamp circuit produces a current equal and opposite to the ionic current. Figure 1.5 shows whole-cell voltage clamp recordings of sodium currents evoked from positive voltage steps of -70 to 0 mV.

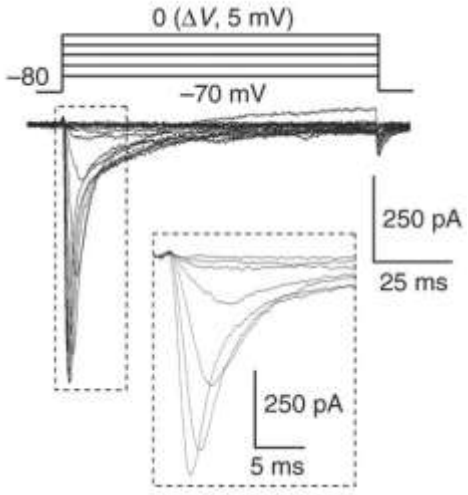

Figure 1.5: Whole-cell voltage clamp recording of sodium currents of mouse myenteric neurones by patch-clamp. Sodium currents evoked by voltage-steps from -70 to 0 mV in 5 mV increments from a holding potential of -80 mV. Inset shows traces between -45 and -15 mV.16

Voltage steps of +5 mV were applied to depolarise the cell (where current is sent *via* the amplifier). On the rising phase of the step this current is equal to the capacitive current necessary to charge the membrane capacitance to its new value (plus leak channels). Since a depolarising step opens Na^+ channels, an inward current flows through the open

channel after a small delay. Normally, this flowing inward current should depolarise the membrane but in voltage clamp experiments it does not. A current constantly equal to but of opposite direction is continuously sent in the circuit to compensate the sodium current and to clamp the membrane. Figure 1.5 illustrates those sodium currents due to step-wise changes in the membrane potential.

1.0.4 Resolution of VGSCs into respective sub-types

During numerous studies to understand the structure and physiology of these complex channels, VGSCs have now been resolved into their respective sub-types or isoforms. All sub-types are in the Na_v 1 family *e.g.* Na_v 1.1. This comprises channels that have 50% identical sequence homology to each other; the subscript $_v$ denotes voltage and the number following the decimal place, the specific sub-type. This classifies a single family based on their evolutionary relationships. In total, there are nine mammalian sub-types Na_v 1.1 - Na_v 1.9 (Table 1.1), which were numbered according to the order in which the gene was identified. VGSCs that have less than 50% sequence homology to each other were classed separately. The Na_v x or Na_v 1.10 channels were proposed to stem from late branch Na_v 1.7, but lacked the amino acid needed for proper voltage gating.[17]

Na_v 1	**Tissue Expressed**
Na_v 1.1	Central Nervous System, Dorsal Root Ganglion, Motor Neurones
Na_v 1.2	Predominantly Central Nervous System
Na_v 1.3	Embryonic, Adult Central Nervous System, Injured Dorsal Root Ganglions
Na_v 1.4	Skeletal Muscle
Na_v 1.5	Heart, Embryonic Dorsal Root Ganglions
Na_v 1.6	Dorsal Root Ganglions, Motor Neurones, Central Nervous System
Na_v 1.7	Thyroid, Dorsal Root Ganglion (nerve terminals)
Na_v 1.8	Dorsal Root Ganglion
Na_v 1.9	Dorsal Root Ganglion, Central Nervous System
Na_v x	Heart, Hypothalamus, Glial Cells, Large Dorsal Root Ganglion

Table 1.1: The Nav 1 VGSC sub-types

1.0.5 Function of VGSC isoforms

1.0.5.0 VGSCs expressed in the central nervous system

The Na_v 1.1, 1.2, 1.3 and 1.6 channel subtypes, encoded by the SCN1A, SCN2A, SCN3A and SCN8A genes respectively, are the primary VGSCs in the central nervous system (CNS).[18-19] The SCN1A acronym stands for voltage-gated sodium channel, type I, alpha subunit. Na_v 1.1 and 1.3 channels are primarily localised in cell bodies.[20-21] Na_v 1.2 channels are located in unmyelinated or pre-myelinated axons and dendrites, whilst Na_v 1.6 channels are found in myelinated axons and dendrites.[22] These channels participate in generation of both somatodendritic and axonal APs.[23] Resurgent sodium currents are commonly found in Na_v 1.6; these are brief surges of current during repolarisation at voltages of -50 to -60 mV where normally VGSCs are closed and recovering from inactivation. The reason for resurgence is attributed to the presence of an endogenous open channel blocker that hastens recovery from inactivation.[23] Resurgent currents may be an adaptive mechanism for high frequency firing of APs in specific brain regions, such as cerebellum and subthalamic nucleus.

In rodents, Na_v 1.3 channels are highly expressed in the brain during embryonic life and their expression declines after birth as Na_v 1.1 and 1.2 channels become more abundant.[24] Na_v 1.1 expression is the first detected VGSC isoform, measurable from postnatal day seven. Knockout of any of the three VGSC α subunit genes expressed primarily in adult brain (SCN1A, SCN2A and SCN8A) is lethal, demonstrating that each channel performs some essential function.[22]

1.0.5.1 VGSCs expressed in skeletal muscle

Na_v 1.4 is encoded by the SCN4A gene. This channel is not well understood, however it is known that this channel is related to a number of channelopathies, including hyper- and hypokalemic periodic paralysis (episodes of extreme muscle weakness, usually beginning in infancy or early childhood) and paramytonia congenita (bouts of sustained muscle tensing that prevent muscles from relaxing normally).[25]

1.0.5.2 VGSCs expressed in cardiac cells

Na_v 1.5 is encoded by the SCN5A gene. This VGSC isoform is found primarily in cardiac muscle and is responsible for the initial upstroke of the action potential in an electrocardiogram. Mutations in the gene are associated with long Q-wave T-wave syndrome type 3 (LQT3), Brugada syndrome, primary cardiac conduction disease and idiopathic ventricular fibrillation. This channel is one of the few VGSCs found to be resistant to tetrodotoxin (TTX), a known VGSC toxin found in the Japanese puffer fish *fugu*. The ability of Na_v 1.5 to generate physiologically effective APs is determined by its cellular localisation as well as its channel properties. Na_v 1.5 is concentrated at intercalated discs (specialised sites of contact between cardiomyocytes) and are enriched in gap junctions. Proximity of Na_v 1.5 to gap junctions, which provide rapid ion exchange between adjacent cells, allows efficient propagation of APs. In addition, Na_v 1.5 is localised in cardiomyocyte T-tubules adjacent to voltage-gated Ca^{2+} channels, thus is well positioned to initiate the calcium-induced calcium release that triggers contraction of the heart muscle.[26-28]

1.0.5.3 VGSCs expressed by the peripheral nervous system

Na_v 1.7, 1.8 and 1.9 are expressed in the peripheral nervous system (PNS). Na_v 1.7 is encoded by the SCN9A gene and plays a critical role in the generation and conduction of AP's. Na_v 1.7 is expressed at nociceptors (pain-sensing nerves), close to the region where the impulse is initiated. Stimulation of the nociceptor nerve endings produces 'generator potentials'; these are small changes in the potential difference across the neuronal membranes. Na_v 1.7 amplifies these membrane depolarisations, and when the membrane potential difference reaches threshold, the neurone fires an AP. Na_v 1.7 is defined by a slow transition into the inactivation state, leaving the channel active for longer.

Evidence that Na_v 1.7 is involved in pain transduction, originates from the observation that dorsal root ganglion (DRG) neurones in animal models of inflammatory pain show increased response to this isoform. Knockout mice also showed reduced response to inflammatory pain, however, response to neuropathic pain remained intact.[29-30]

The Na_v 1.8 channel encoded by the SCN10A gene, has a more depolarised activation threshold, producing most of the transmembrane current responsible for the depolarising

phase of action potentials. From studies with mice deficient in Na_v 1.8, reduced sensing of inflammatory and visceral but not neuropathic pain was seen.[29-30] Mice that lacked both Na_v 1.7 and 1.8 had twice the pain threshold of knockout mice lacking either isoform, suggesting a clear functional link between these two isoforms.[29-30]

Na_v 1.9 is encoded by the SCN11A gene; it is preferentialy expressed in nociceptive neurones within the DRG. Na_v 1.9 is a TTX-resistant isoform; it's unique properties indicate that Na_v 1.9 has a significant effect on the electroresponsive properties of primary nocieption.

Strickland *et. al.*, investigated the changes in expression of Na_v 1.7, 1.8 and 1.9 in a rat model. They showed that the DRG innervating the knee joint had increased expression of all three subtypes up to 28 days after the initial insult, showing a clear link between neuronal injury and ion channel expression.[31] Thus these channels are an attractive target in the search for more effective treatments in pain.

1.1 Voltage-gated sodium channels and cancer

From oncology research, it has now become evident that VGSCs play a crucial role in tumour invasiveness. It has been reported that VGSCs are up-regulated in certain metastatic diseases, for example prostate, breast and small-cell lung carcinoma (Table 1.2). VGSC activity appears to potentiate some metastatic cell behaviours. During the change from a normal epithelial cell towards cancer, a series of genetic alterations occur, which may also affect the expression of ion channels or cause a change in ion channel activity. This abnormal activity supports proliferation of the tumour cells. For example, expression of amiloride-sensitive VGSCs were detected in malignant glioma cells and non-selective cation channels have also been associated with proliferation and cancer.[32] However, the mechanism of regulating functional VGSCs is not fully understood.[2, 33-35] It has been shown through tissue culture experiments that it is the neo-natal isoforms of VGSCs which are expressed in tumours.[6] This is another example of oncofoetal gene expression in cancer.[36-37]

Interestingly, Djamgoz *et. al.*, showed in domain I, TMS 3 & 4, there are seven amino acid differences between neo-natal and adult VGSCs. [38] The most significant difference was the charge-reversing aspartate (adult) to lysine (neo-natal) substitution at amino acid position 211. Switching the lysine back to aspartate showed an overall functional

shift back towards the adult isoform characteristics. In fact, it is thought that the significant lysine residue in the neo-natal channel could alter the local electric field sensed by the TMS 4 voltage segment by introducing extra positive electrostatic potential, thereby moderately resisting the outward movement of the positively charged TMS 4 segment.[39-41] This is in contrast to the adult channel, where the negatively charged aspartate is likely to potentiate outward TMS 4 movement by attracting positively charged TMS 4 residues.[38]

Tumour Type	**VGSC isoform expression**
Prostate	Na_v 1.7
Breast	Neonatal - Na_v 1.5 (82%)
	Adult - Na_v 1.7 (18%)
Colon	Na_v 1.5
Leukaemia	Na_v 1.5, 1.6, 1.7 &1.9
Non-small cell Lung	Na_v 1.7 & 1.6
Ovarian	Na_v 1.6
Cervical	Na_v 1.6
Mesothelioma	Na_v 1.2, 1.6 and 1.7

Table 1.2: Examples of VGSC sub-type expression in specific tumours

1.1.0 Na_v1.5 in breast cancer

Breast cancer (B Ca) is the most common cancer of women and the second leading cause of female cancer mortality, accounting for about 10% of all cancer deaths in the western world.[42-43] VGSC activity has been reported to contribute to much cellular behaviour integral to metastasis.[44-49] In cell culture work, Gao *et. al.* functionally expressed Na_v 1.5 in the strongly metastatic MDA-MB-231 B Ca, and normal smooth muscle cell lines.[50] It was found that the type of VGSCs expressed in the normal cells, were genetically different to the type of VGSCs expressed in the MDA-MB-231 cell lines. This led them to propose that the type of VGSCs expressed in B Ca may be of the neo-natal and not adult form, which was independently supported by Djamgoz *et. al*.[51] They hypothesised that in the cells of mature organs the neo-natal form is silenced and re-expressed in cancer cells. They followed on this work by studying the immunofluorescence of weakly metastatic MCF-7 and MDA-MB-231 cell lines. They

found that VGSCs were distributed on the cell membrane of MDA-MB-231 and located in the cytoplasm of MCF-7. It was thought that the aggressive nature of MDA-MB-231 was due to the location of the VGSCs in the cell membrane.[50]

In contrast to adult Na_v 1.5, VGSC β1 subunit functions as a cell adhesion molecule in B Ca cells. Thus, VGSC α and β sub-units appear to play dynamic roles in regulating cell adhesion, migration and invasion.

From previous studies on tumour invasiveness, MMP-9 (matrix metallopeptidase 9) secretion was shown to be strongly associated with invasive potential.[52-53] MMP-9 is a zinc protease which degrades the extracellular matrix (first step in cancer metastasis). Through RT-PCR (real time-polymerase chain reaction), it was shown that expression levels of MMP-9 decreased by 44% when MDA-MB-231 was pre-incubated with tetrodotoxin (TTX) a known potent VGSC blocker for 24 hrs. It was inferred that Na_v 1.5 might control the secretion of this zinc protease and thus have an effect on invasive potential.[50]

More recently however, Roger *et. al.* confirmed that it is the neo-natal isoform of Na_v 1.5 that is expressed in the metastatic cell line MDA-MB-231 (Figure 1.6).[54-55] 1000-Fold higher mRNA expression of neo-natal Na_v 1.5 was seen compared to adult Na_v 1.5 expression.[6]

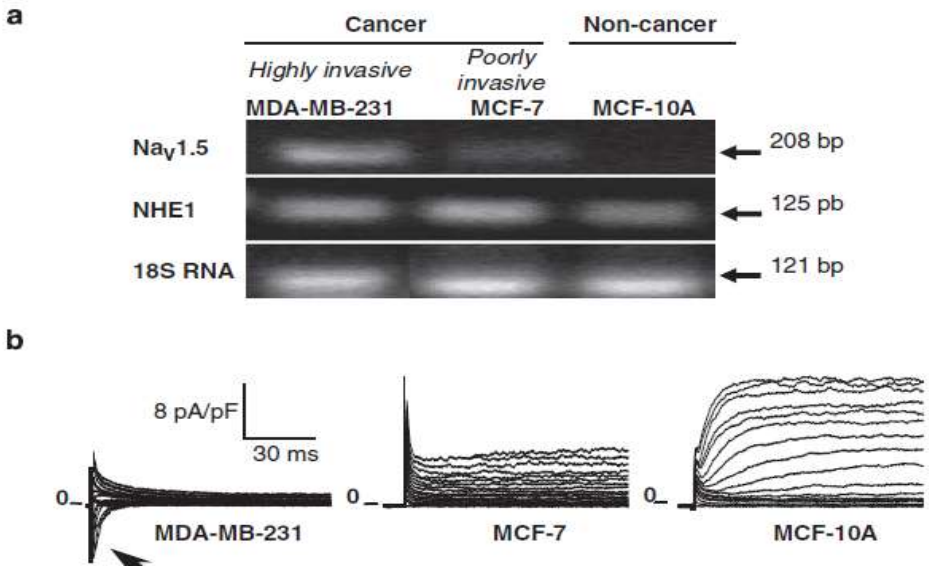

Figure 1.6: (a) RT-PCR expression of Na_v 1.5, NHE 1 and 18S RNA in the cell lines, MDA-MB-231, MCF-7 and MCF-10A. (b) Sodium currents expressed in three cell lines to show the difference in excitation between strongly (MDA-MB-231) and weakly metastatic models (MCF-7)[54-55]

Some Na_v 1.5 expression was reported in weakly metastatic models (MCF-7), however studies by Yang *et. al.,* showed that no sodium currents could be recorded from these cells[56] and no expression in healthy breast tissue. Interestingly, Chioni *et al,* showed that there is a higher expression level of β1 in MCF-7 cells.[57]

Recently, the difference between the neo-natal and adult Na_v 1.5 isoform has been identified. A key type of alternative splicing of VGSCα genes involves the presence of two mutually exclusive alternative exons, namely, exon 6: 5'genomic and 3'genomic encoding part of DI: TMS3, most of DI:TMS4, and DI:TMS3-S4. These two exon 6 alternatives are notable by the presence (3' genomic; adult) or absence (5' genomic; neo-natal) of an aspartate residue at position seven in DI:TMS3-S4. DI:TMS3 splicing was thought to be developmentally regulated, as the 5' variant is abundant at birth and quickly replaced by the 3' variant within a few days. Hence, channels deemed 5' are known as the neo-natal channel and 3' adult. [58]

The neo-natal Na_v 1.5 has a number of key characteristics which makes it an ideal target for breast cancer treatment and even diagnosis. The change in the exon variant as previously discussed, results in a seven amino acid change, through genomic analysis this amino acid sequence was revealed to be unique to the rest of the human genome. The most important of these amino acid changes occurring in the DI:S3 region which changes a negatively charged aspartate, to a positively charged lysine, causing a charge reversal. Neo-natal Na_v1.5 also has a characteristic electrophysiological (study of neuronal activity) profile. This isoform activates at more depolarised voltages with slower activation and inactivation kinetics, potentially allowing a larger influx of Na^+ ions. Importantly, mutation of the lysine back to the aspartate abolished these characteristics. Curiously, Onkal *et. al.,* highlighted that neo-natal Na_v 1.5 is present in the CNS of healthy adults which correlates with findings by Chioni *et. al.,* in mice. [38, 57]

Further work on the involvement of this channel in metastatic progression, showed the importance of Na_v 1.5 was coupled to increased cysteine cathepsin activity.[54-55] Cysteine cathepsins are proteolytic enzymes with many roles in cancer metastasis.[33] This work was independently supported by Gillet *et. al.* who published their findings on the role of VGSCs in cancer.[59] It was shown that Na_v 1.5 activity enhances extracellular matrix invasion by increasing the activity of acidic cysteine cathepsins B and S through acidification of the pericellular microenvironments. Na^+/H^+ exchanger type 1 (NHE 1) is the central regulator of intracellular pH and its activity is enhanced by the function of

Na_v 1.5.[54-55] Among all pH regulators, the ubiquitous NHE 1 allows cancer cells to adapt to their high metabolic H^+ production environment.[6, 54]

To determine all the pH regulators involved, Gillet *et. al.,* analysed the effects of various inhibitors.[59] Their results indicated H^+ efflux was dependent upon Na^+ not Cl^- ions. Silencing NHE 1 led to a 60% reduction of H^+ efflux compared with the control. Na_v 1.5 could promote H^+ efflux through NHE 1. TTX had no effect on regulating H^+ efflux from MCF-7 cell lines devoid of Na^+ ions.[54] It was proposed that cellular invasiveness is regulated by Na_v 1.5 and thus allows a persistent Na^+ ion entry. Inhibition of NHE 1 or Na_v 1.5 produced 35% reduction in cell invasiveness. Co-inhibition had no greater effect. This was the first study to show that Na_v 1.5 and NHE 1 channels interact to enhance H^+ efflux, therefore, allowing acidic- dependent invasion of the extracellular matrix,[54] which correlates with previous reports on MMP-9 and zinc protease.[50]

To understand how Na_v 1.5 and NHE 1 influences matrix degradation, Roger *et. al.* used DG-gelatin which released fluorescent activity after proteolytic cleavage by gelatinases in a 3D matrix of matrigel.[54] Gelatinolytic activity was shown to be mainly distributed at the pericellular zone of cancer cells. When cultured with TTX, the gelatinolysis of the pericellular matrix was reduced by 63%. Inhibiting both NHE 1 and Na_v 1.5 showed no additional reduction suggesting that both are involved in the same pH dependent pathway, furthermore, NHE 1 and Na_v 1.5 were found to co-localise in the plasma membrane of cancer cells grown on Matrigel.[54]

In summary, the on-going research has emphasised the key role that Na_v 1.5 plays in keeping an acidic environment around the extracellular membrane to up-regulate the activity of different proteases (the first step in metastasis).

1.1.1 Na_v1.7 in prostate cancer

The prostate is a compound tubular-alveolar exocrine gland, which is part of the male reproductive system in mammals. Prostate Cancer (P Ca), uncontrolled and abnormal growth of the prostate gland, continues to be a major cause of morbidity and mortality in ageing men worldwide.[60] Adjacent to the on-going research in B Ca, researchers are also seeking to understand the pathobiological link between P Ca and VGSCs.

The original work by Grimes *et. al.* on the Dunning rat model of P Ca, showed that the strongly metastatic Mat-LyLu cell line expressed neo-natal VGSCs, whilst the weakly metastatic AT-2 cells did not.[5, 61] Later, Bennett *et. al.* found that direct transfection of a VGSC α-subunit into the LNCaP P Ca model was "necessary and sufficient" to increase the *in vitro* invasiveness of the cells.[34] These findings also supported that VGSC expression is linked to more highly metastatic tumours.

From these studies the CELEX (cellular excitability) model was hypothesised. This proposes that metastatic cell membranes are 'excitable' and that this excitability determines the cells 'hyperactive' behaviour during metastasis.[35] VGSCs in the metastatic model are activated at moderately depolarised potentials and exhibit 'fast' inactivation kinetics. Following on from this work, Brackenbury *et. al.* investigated the possibility of activity-dependent auto-regulation of VGSC functional expression in the strongly metastatic model of rat P Ca. After pre-treatment of Mat-LyLu cells with TTX for 24-72 hrs, they showed suppression of peak VGSC current densities without affecting voltage-dependence. Their hypothesis being, that the VGSC auto-regulation occurred *via* a VGSC-mediated Na^+ influx and subsequent activation of protein kinase A (PKA). It was concluded that the VGSC activity in rat P Ca cells was up-regulated in steady-state, *via* a positive feedback mechanism involving PKA and this enhanced the cells' migratory potential.[2,35, 62,4]

At the molecular level, studies into semi-quantitative PCR analysis of rat Mat-LyLu and human PC-3 cell lines showed that the predominant VGSC present was Na_v 1.7, at an mRNA expression level >1000 fold higher than the corresponding weakly metastatic cells (as also seen in MDA-MB-231 breast cancer cell lines).[63] Some other minor VGSC sub-types were also present: Na_v 1.2, 1.4 and 1.6, but their functional role if any, is still unknown.[64-65]

Some VGSC blockers have been shown to inhibit P Ca cell proliferation,[66] specifically the VGSC-blocking anticonvulsants phenytoin and carbamazepine were found to directly inhibit secretion of prostate-specific antigen (PSA) and interleukin-6 in PC-3 cell lines.[66] Regulation of VGSC expression by a positive feedback mechanism appeared to potentiate the metastatic process.[67] Inhibiting this mechanism by suppressing VGSCs with long-term (48 h) TTX treatment eliminated the VGSC-dependent component of the cells' metastatic potential.

From early research on the expression of VGSCs in P Ca, it was shown by Brackenbury *et. al.*, that varying the levels of serum factors for example, nerve growth factor (NGF), had a significant effect on the VGSC current, showing that expression and activity were under stimulatory and inhibitory control by substances present in the serum. For Mat-LyLu cells, NGF application improved peak VGSC current density, following a time- and dose-dependent relationship.[68] High NGF levels shifted the peak voltage and the half-inactivation voltage to more positive potentials, and produced currents with faster kinetics. Through further investigations, it was shown that the effect of NGF appeared to be through a PKA-mediated pathway that did not affect the expression of Na_v 1.7 mRNA, but did up-regulate the total VGSC α-subunit protein level. A plausible hypothesis was proposed that NGF induces local synthesis of VGSCs by translating 'docked' mRNA.[68]

Another serum factor, epidermal growth factor (EGF) contained within the prostatic fluid, is known to be linked to P Ca progression, cellular invasiveness and androgen independence.[69,70] Exogenous EGF up-regulated both VGSC current density in Mat LyLu cells and Na_v 1.7 in rat and human P Ca cells *in vitro*.[71] Importantly, it has been shown that EGF also increased the migratory potential of both MatLyLu and PC-3 cells, in part due to enhanced VGSC activity.[72] It was proposed, that endogenous EGF has a key role in the up-regulation of Na_v 1.7 expression and activity and the two could characterise an 'in-built' positive feedback mechanism accelerating the progression of P Ca.[73]

1.1.2 Na_v 1.6 in Cervical Cancer

Cervical cancer (C Ca) is the third most common female cancer worldwide in 2008.[74] The main cause of C Ca is the carcinogenic human papillomavirus (HPV).[75] A study by Hernandez-Plata *et. al.*, reported that the relative expression of Na_v 1.6 and 1.7b (one of two genetic sequences for this sub-unit) specifically, were 40- and 22-fold higher in C Ca tissue, respectively, than in non-cancerous tissue samples.[76] In the C Ca tissue, the channels were widely distributed in the plasma membrane and cytosolic compartments, but in the non-cancerous tissue, the channels were limited to the cell membrane of the mid-zone and superficial zone of the cervical squamous epithelium. Blocking of the sodium current produced by Na_v 1.6 (accounting for one-third of the total current), was

achieved by using Cn2, a B-class scorpion toxin from *Centruroides noxius* species. On average 350 nM of Cn2 decreased the sodium current amplitude by 30.3 ± 5.0% (n = 8). The remaining current was totally blocked with 1 µM TTX.[76]

To explore the function of these channels in metastatic cell behaviour, *in vitro* assays in the presence and absence of TTX and Cn2 were performed. The proliferative potential of the C Ca primary culture cells was unchanged after exposure to TTX for 72 hrs. Migration was not significantly changed by the presence of the TTX or Cn2; in contrast, the relative invasiveness of these cells was sensitive to both toxins, showing a significant decrease (79.5 ± 7.6% and 78.3 ± 7.6% with TTX and Cn2 respectively) when compared to control conditions. Interestingly, the specific splice isoform of Na_v 1.6 and 1.7 does not correspond to any splice variant reported for humans.[76]

There is no unanimously accepted mechanism to explain the role of VGSC in the metastatic behaviour. Hernandez-Plata *et. al.*, considered two roles for the action of VGSCs in C Ca: the channel itself acting as an adhesion molecule and the sodium influx causing an electronic effect. Studies with TTX and veratridine (a VGSC agonist), had proved to diminish and enhance VGSC currents, however, the transient current may be negligible on the global sodium influx into these cells.[59, 76]

Alternatively, VGSCs could participate in metastasis through a non-conducting function *via* direct interaction with the β-subunits of VGSCs with other plasma membrane and/or intracellular proteins.[58, 77] For example, VGSC β-subunits could interact with tenascin C and R and participate in homophilic cell adhesion, allowing cellular aggregation and ankyrin recruitment.[3] This is supported through work by Chioni *et. al.*, who showed that stable expression of β1 in the breast cancer cell line MDA-MB-231 cells increased the VGSC activity and cell adhesion, but reduced cellular motility, suggesting that the cell adhesive effects might be independent of changes in cellular excitability.[57] Overall, the functional expression of Na_v 1.6 and to a lesser extent Na_v 1.7 in C Ca might represent the identification of a novel molecular marker for C Ca.

1.1.3 Summary of VGSCs and tumour invasiveness

The neo-natal form of the normal adult VGSC has been identified in multiple cancers. Since VGSC expression is strongly linked to tumour invasiveness, it could act as a useful diagnostic indicator in the detection and differentiation of metastatic and non-

metastatic tumours, thereby potentially influencing the choice of therapeutic intervention in cancer treatment. Thus, if the current hypothesis is correct, it could be said that patients not expressing VGSCs should be metastasis-free for longer than those expressing VGSCs. Therefore, these ion channels represent a useful biological target for development of new diagnostic and therapeutic agents. The main difficulty is targeting the specific VGSC sub-type and as the neo-natal form.

1.2 Medical Imaging

Biomedical imaging is a significant tool for cancer diagnosis, prognosis and therapy monitoring, but is also useful in diagnosing other diseases such as Parkinson's Disease (PD) and Alzheimer's Disease (AD).[78-84] It has many advantages including real-time monitoring, accessibility without tissue destruction, minimal or no invasiveness, whilst giving information on anatomical and pathological processes.

1.2.0 Types of Medical Imaging

An X-ray image can be useful for the diagnosis of metastases in the lung and bones (chest or individual bone radiography), but this technique is limited as there may be only a small contrast between the tumour and surrounding tissues.[85]

Computed Tomography (CT) scanning uses multiple X-ray projections from different angles to produce three-dimensional images. CT scans can be used to detect cancer in a range of tissue types (lung, bone, soft tissue, etc.). It is possible to conduct whole-body CT examinations, and CT images may also be enhanced with the administration of oral or intravenous contrast agents.[86,87]

Ultrasound uses information from reflected high-frequency sound waves to produce images of tissues. More recently, contrast agents have been developed for use with ultrasound that enhance images.[85,88]

Ultrasonography in oncology is commonly used in the detection of distant metastases and can be used to detect metastases in the liver and kidneys, but the technique relies upon the expertise of the operator.[85]

Bone scintigraphy uses radionuclides of technetium-99m-labelled disphosphonates for the identification of bone metastases.[85] The degree of uptake into bone mainly depends upon blood flow and rate of new bone formation. Sites of high radio-emission may represent the presence of a tumour.[85]

Magnetic resonance imaging (MRI) can visualise detailed internal structures.[85] MRI makes use of the property of nuclear magnetic resonance (NMR) to image nuclei of atoms inside the body. MRI can provide contrast between the different soft tissues of the body, which makes it especially useful in imaging brain, muscle, heart and cancers compared with other medical imaging techniques such as CT or X-rays (Table 1.3). MRI contrast agents are used to improve the visibility of anatomical structures; the most common are gadolinium-based agents, for example ™ProHance, ™MultiHance and ™Primovist.

The MRI scanner produces a powerful magnetic field, which causes nuclei within the body to become aligned with the magnetic field. A short radiofrequency pulse is applied causing a brief varying electromagnetic field, which has the right frequency (resonance frequency) to be absorbed and 'flip' some nuclei (including those of the agent), known as 'spinning'. Once the pulse is stopped, the nuclei then relax. During relaxation, a radio frequency signal is emitted which is detected by the scanner and converted into an image. These agents increase the relaxation time of nuclei within the body to improve image quality.

Positron emission tomography (PET) and, more recently, PET/CT produce quantitative 3D images of a radiotracer distributed within the body. PET tracers emit positrons that annihilate with electrons up to a few millimetres away, causing two gamma photons to be emitted in opposite directions. A PET scanner detects these emissions 'coincident' in time, highlighting localisation of radiation and, thus, higher resolution images. PET/CT has many applications in the detection of various diseases, for example, cancer and Alzheimer's disease. As these multimodal technologies provide different types of data (PET gives functional and CT anatomical data), their combination provides greater diagnostic information. [89,90]

Single photon emission computed tomography (SPECT), is an imaging technique using gamma rays. SPECT is similar to PET in its use of a radioactive tracer and detection of gamma rays. In contrast with PET, the tracer used in SPECT emits gamma radiation

that are measured directly giving images with a resolution of approximately 10 mm. SPECT scans, however, are significantly less expensive than PET scans, in part because they are able to use longer-lived more easily-obtained radioisotopes than PET. The longer half-life allows for centralised production and generally the tracers are less expensive to produce per-dose. In contrast, SPECT is two to three orders of magnitude less sensitive than PET; thus, it is unable to detect as many emitted events as PET. [91-92]

Modality	Spatial Resolution (mm)	Concentration of Imaging Agents (M)	Radiation Dose
CT	1	10^{-4}	Yes
MRI	<1	10^{-5}	No
PET	3-10	10^{-8} - 10^{-10}	Yes
SPECT	8-20	10^{-6}	Yes

Table 1.3: Comparison of the performance of various imaging modalities [93]

1.2.1 Positron Emission Tomography (PET)

Non-invasive molecular imaging of biochemical mechanisms *in vivo* is a promising interdisciplinary field of research. PET is a nuclear medicine imaging technique that produces a three-dimensional image or picture of functional processes in the body.[94] The system detects pairs of gamma rays emitted indirectly by a positron-emitting radionuclide (tracer), which is introduced into the body on a biologically active molecule. Three-dimensional images of tracer concentration within the body are then constructed by computer analysis. In modern scanners (Figure 1.7), imaging is often accomplished with the aid of a CT X-ray scan performed on the patient during the same session, in the same machine. This allows for attenuation correction and co-registration. PET is currently the most effective way to check for cancer recurrence and it offers significant advantages over other forms of imaging such as CT or MRI scans in detecting disease in many patients. In 2005, an estimated 1,129,900 clinical PET patient studies were performed across the UK.[95] Of the two common nuclear medicine imaging modalities, SPECT and PET, PET is by far the superior in both sensitivity and resolution by 2 or 3 orders of magnitude (Table 1.3).[93]

Figure 1.7: A human PET scanner

Despite the remarkable advances in PET technology, both CT and MRI still have superior spatial resolution. Conversely, CT and MRI have considerably lower sensitivity. This limits the choice of targeting agents that can be developed for imaging with these systems, as low sensitivity requires a higher concentration of the imaging agent, which may be toxic to the subject, and difficult to target biological processses. PET imaging offers the ability to non-invasively and quantitatively study drug targets in animal models and humans at low target concentrations.[96]

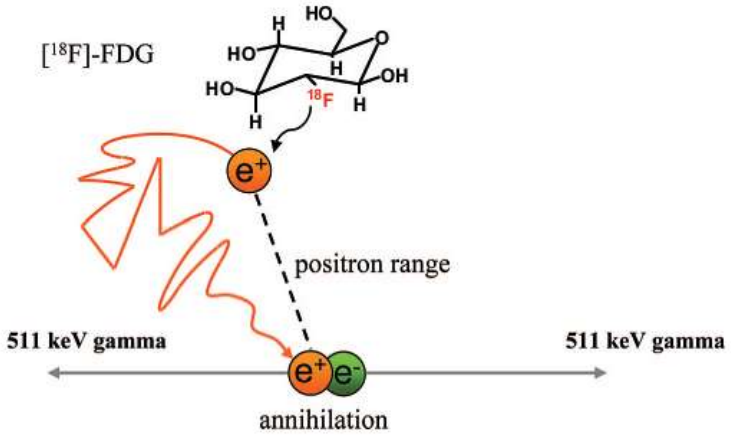

Figure 1.8: Pictorial schematic of the action of [^{18}F]FDG [97]

A PET ligand incorporates a radionuclide such as fluorine-18 used in the imaging ligand 2-deoxy-2-[^{18}F]fluoro-D-glucose ([^{18}F]FDG). As the radionuclide β^+-decays, a positron and neutrino are emitted (Figure 1.8) maximum positron range in water 0.02 cm.[97] A positron is the anti-matter equivalent of an electron. The energy of the positron emitted depends on the radionuclide used. The positron encounters and annihilates with an electron, producing two γ photons that are emitted at almost 180° to each other. The photons are detected in the scanner when they reach the scintillator material in the

scanning device, creating an emission of light. Photomultiplier tubes in the detector detect the photon energy. Only photons arriving in pairs are recorded and it is possible to localise the annihilation point to a specific part of the body or organ, along a straight line of incidence known formally as the line of response (LOR). As the timing resolution with new scanners improves, the signal to noise ratio (SNR) of the image will improve.

1.2.2 Types of radionuclides and their production

Radionuclides used in PET typically have a short half-life, such as ^{11}C (20 minutes), ^{18}F (110 minutes), ^{13}N (10 minutes) and ^{15}O (2 minutes) and are produced on demand using a cyclotron. While minimisation of radiation dose to the subject is an attractive feature of these short-lived radioisotopes (Table 1.4), they must be produced close to the PET imaging facility, and ideally on-site. Limitations to the widespread use of PET arise due to the high costs of running and maintaining a cyclotron. [84, 98]

Isotope	Half-life ($t_{1/2}$)	Preparation	Positron Energy (MeV)
^{7}Be	53 days	$^{7}Li(p,n)$	20
^{11}C	20 minutes	$^{14}N(p,\alpha)$	15
^{13}N	10 minutes	$^{16}O(p,\alpha)$	15
^{15}O	2 minutes	$^{14}N(d,n)$	10
^{18}F	110 minutes	$^{18}O(p,n)$	15
^{22}Na	2.6 years	$^{22}Ne(p,n)$	15
		$^{25}Mg(p,\alpha)$	20
^{28}Mg	21 hrs	$^{27}Al(\alpha,3p)$	45
^{34m}Cl	31.2 minutes	$^{34}S(p,n)$	20
^{48}V	16 days	$^{48}Ti(p,n)$	11

Table 1.4: Example of PET isotopes and their half-lives [84, 98]

One of the most attractive PET isotopes for clinical imaging is fluorine-18, with a half-life ($t_{1/2}$) long enough for centralised production. Fluorine-18 is a versatile isotope, which has been manipulated into a variety of PET ligands.[80-81, 83, 99] Its radiosynthesis from oxygen-18 through proton bombardment ($[^{18}O]H_2O$ (p,n) $[^{18}F]F$), can yield up to

370 GBq over a 2 hr bombardment time, in a current generation cyclotron production system.

1.3 Fluorine-18 PET imaging agents

2-Deoxy-2-[^{18}F]fluoro-D-glucose ([^{18}F]FDG) is the most frequently used fluorine-18 PET imaging agent.[99] [^{18}F]FDG is a glucose analogue taken up by cells such as the brain, kidney and cancer cells, which require high levels of glucose to function. It can be used for the assessment of glucose metabolism in heart, lungs and the brain but also has many applications within oncology.

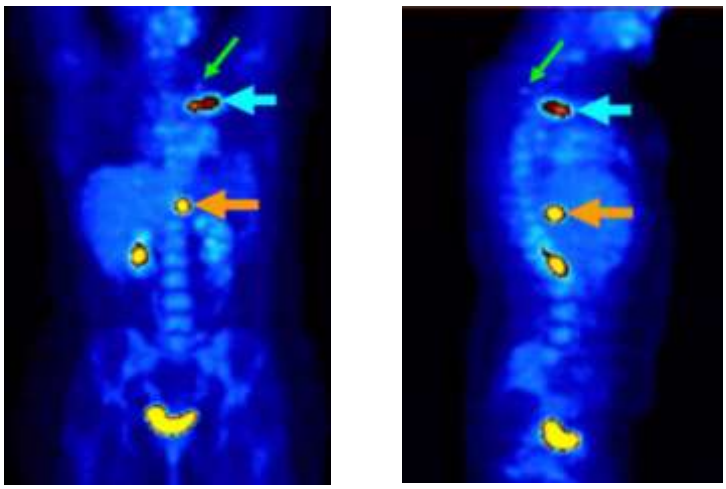

(A) **(B)**

Figure 1.9: (A) anterior image (B) lateral image PET [^{18}F]FDG scan showing masses associated with high uptake of [^{18}F]FDG [100]

As part of a study in 2004, Patient X was diagnosed with Hodgkin's disease following an [^{18}F]FDG-PET scan (Figure 1.9). The images show high activity in the prevascular mass (blue arrow) and in the left adrenal mass (orange arrow). Low-grade [^{18}F]FDG activity is shown at the posterior left lung apex, likely to represent nonspecific inflammation or a resolving infection (green arrow). Activity present in the liver represents metabolised [^{18}F]FDG excreted into the right kidney and passing through to the bladder.[100]

The main problems associated with [^{18}F]FDG as a PET radiotracer are due to the difficulties in differentiating between a tumour, inflammation and infection. However,

this ligand is still used clinically, not only in oncology but also in neurology due to its wide availability. For example, in (AD) which exhibits greatly decreased brain metabolism of both glucose and oxygen in tandem, a standard [^{18}F]FDG scan of the brain can measure regional glucose use and successfully differentiate late stage (AD) from other dementia's.[101-105]

(AD) is a common neurodegenerative disorder characterised by memory dysfunction and pathologically as deposition of amyloid-β, neurofibrillary tangles and neuronal loss. There is now an emerging market of PET tracers for imaging amyloid plaques. ([^{18}F]AV-45) (Figure 1.10) studied by Lin and colleagues has shown excellent binding affinity (K_d=3.72 ± 0.30 nM) and good initial brain uptake in biodistribution studies.[106]

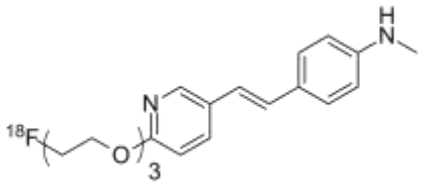

Figure 1.10: Structure of ([^{18}F]AV-45)[106]

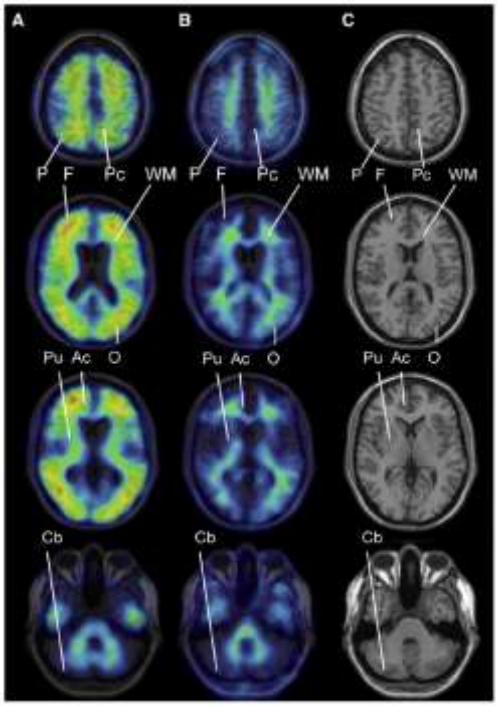

Figure 1.11: ([^{18}F]AV-45) PET images from a patient with Alzheimer's disease (A) and a healthy control (B) taken at 45-55 minutes after tracer injection. All images are superimposed with sample MRI study in Montreal Neurologic Institute space (C) and the intensities were normalized to each cerebellar cortex for comparison. [106]

Ac = anterior cingulum, F = frontal cortex, P = parietal cortex, Pc = precuneus, Pu = putamen, O = occipital cortex, Cb = cerebellar cortex, WM = subcortical white matter.

During PET imaging (Figure 1.11), this ligand displayed high brain uptake and fast washout in primate brain. The results of the study indicated ([^{18}F]AV-45) is a safe PET tracer for the study of amyloid beta protein distribution in the brain.[106] Subsequently, this PET tracer received FDA approval in April 2012.[107]

Over the last two decades, there has also been a concerted effort to develop PET tracers for imaging of *N*-methyl-D-aspartate-type glutamate receptors (NMDARs), ligand-gated heteromeric ion channels that regulate fast neurotransmission by allowing prolonged influx of Ca^{2+}, Na^{+} and K^{+} ions into the synapse. It is one of several types of ionotropic glutamate receptor that is thought to be responsible for excitatory transmission in the CNS. A number of analogues have been radiolabelled previously, based on the use-dependent NMDA receptor/ion channel antagonist phencyclidine (PCP); however, imaging studies with these tracers have given inconclusive results. These results were attributed to high non-specific binding, poor metabolic stability or insufficient affinity.

Ametamey and co-workers produced ([^{18}F]AFA) (Figure 1.12) an NMDA antagonist also binding to the PCP binding site.[108]

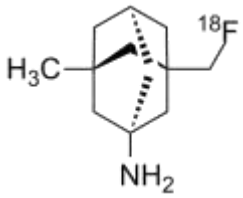

Figure 1.12: Structure of [^{18}F]AFA [108]

From biodistribution studies in mice, [^{18}F]AFA showed high brain uptake consistent with good blood brain barrier (BBB) penetration. In a regional dissection study, elevated radioactivity concentrations were observed in the cerebellum, frontal cortex and in the hippocampus, regions known to contain high densities of the NMDA receptor.[108] Binding of ([^{18}F]AFA) to the PCP binding site was examined through non-human primate PET imaging.

Robins and co-workers reported the synthesis and *in vitro* evaluation of S-[^{18}F]alkyl diarylguanidines (Figure 1.13), NMDA antagonists binding to the PCP binding site.[109] These compounds showed high affinity and selectivity *in vitro* as well as suitable lipophilicity (log $D_{7.4}$ 2.49 ± 0.1), indicating this class of compounds should be capable of crossing the BBB with good metabolic stability and low non-specific binding. Imaging of ion channels as targets (as opposed to neurotransmitter receptors) is a

relatively novel and challenging field and to date, there is still not a clinical PET agent available for this target, due to the difficulties surrounding specific binding, metabolic stability *in vivo* and affinity for the target.[109]

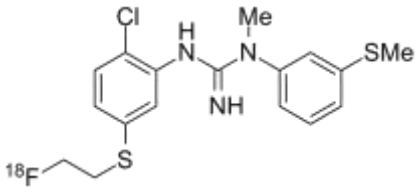

Figure 1.13: The structure of S-[^{18}F]alkyl diarylguanidines [109]

More recently, Labas *et. al.* developed several fluorinated ligands selective for the NR2B subunit containing NMDA receptors. Their antagonistic effects were measured by an *in vitro* assay. Two compounds showed high affinity and selectivity. After analysis of [^{18}F]1a and [^{18}F]2a in rats (Figure 1.14), micro PET scans showed low brain uptake and high bone uptake. The accumulation of radioactivity in bones, skull and articulations were assumed to be due to an *in vivo* defluorination on the 4-(4-(^{18}F)fluorobenzyl)piperidine moiety independently of the piperidinyl substituent. The poor brain penetration and defluorination of [^{18}F]1a and [^{18}F]2a slowed the evaluation of these radiotracers as NR2B NMDA receptor PET ligands.[110]

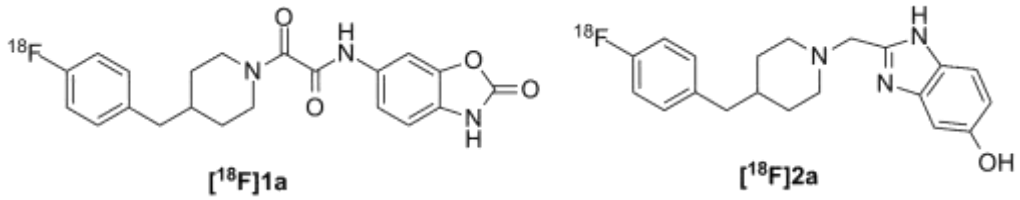

Figure 1.14: Structure of the NR2B NMDA receptor PET ligands

1.4 Voltage-gated sodium channel ligands

VGSC ligands modulate the function of the Na^+ channel, thereby impairing the conduction of Na^+ ions. These ligands can bind either intracellularly or extracellularly, depending on their mechanism of action. Some ligands act as total conductance blockers leading to paralysis, such as TTX; others inhibit the inactivation of the channel leading to over-excitation and seizures *e.g.* conotoxins. There are a variety of sodium channel ligands targeting pain pathways, epilepsy, cardiac arrhythmias and more recently, cancer.

1.4.0 Local Anaesthetics

Local anaesthetics (LAs) are a group of chemical compounds which transiently interrupt the electrical process of excitation-conduction in peripheral nerve fibres and thus, possess the ability to reversibly block the sensation of pain with no residual effects on nerve fibres.

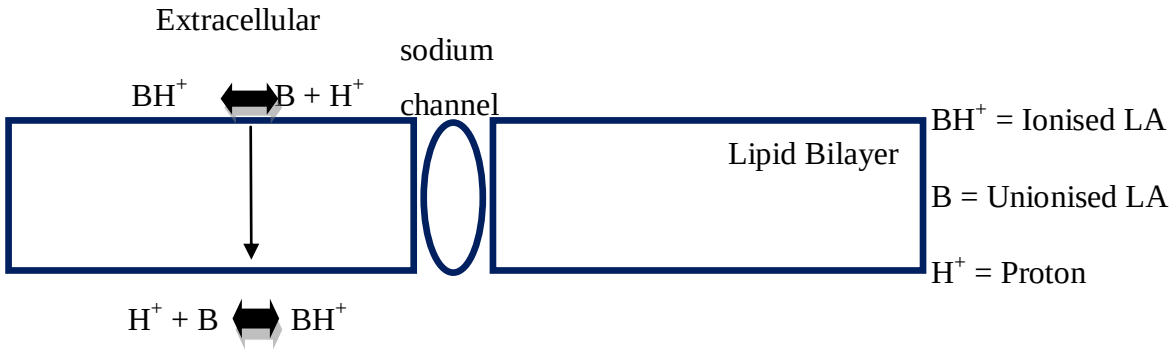

Figure 1.15: The Hille model for local anaesthetic action pathway [111]

According to the classical model proposed by Hille (Figure 1.15), tertiary amine-type LAs are believed to diffuse through the lipophilic nerve membrane in their unioinised neutral form.[111] At physiological pH (~7.4), LAs exist as tertiary amines predominantly in a protonated state (as a quaternary ammonium salt). It is however, the uncharged form that diffuses across the cell surface membrane (CSM). At the lower intracellular pH (~ 6.8 - 7.0), the ionised form is generated, which enters the intracellular portion of the Na^+ channel in its open state and binds reversibly with the TMS IV - VI part of the α-subunit to block the Na^+ influx. The interaction not only physically blocks the Na^+ conductance and therefore pulse conduction, but also directly stabilises the fast inactivated state of the Na^+ channel.

The resting membrane and threshold potential of the nerve fibres are unaffected by LA binding. This slows the rate of depolarisation and therefore reduces the rate-of-rise of action potentials, which culminates in slow axonal conduction near the LA injection site. In addition, the unionised basic form of the LA can also partition into the lipid/lipoprotein matrix surrounding the Na^+ channel, causing membrane expansion and therefore disrupting the channel function indirectly. It could also access the LA receptor within the channel *via* lateral movement in the membrane lipid phase. Some LAs exhibit use-dependent inhibition, meaning that the depth of conduction block depends on the action potential frequency, as LAs gain access to the channel more readily when the channel is open. LAs also have higher affinity for inactivated rather than resting

channels. Use-dependence is mainly of importance in relation to anti-arrhythmic and anticonvulsant effects of LAs. Voltage-dependence of block will also occur, as a greater proportion of VGSCs will be in the inactive state at depolarised potentials than at more negative potentials.[111-112]

The first known LA agent was the naturally occuring alkaloid cocaine (Figure 1.16), isolated from the leaves of the bush *Erythroxylum coca* which grows in South America. There are accounts dating back to the 1500's referring to Peruvian Indians chewing on the leaves for its CNS stimulating effects. Its mechanism of action was not fully understood until 1884, when Carl Koller, a Viennese opthalmologist demonstrated its usefulness as a topical anaesthetic for the eyes; it was at that time widely regarded as the "holy grail" of LAs.[113]

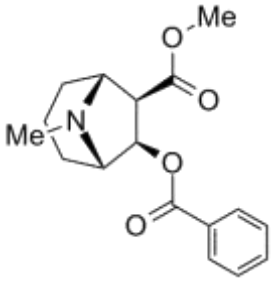

Figure 1.16: The structure of cocaine

Due to its effects on the mesolimbic reward pathway to prevent the reuptake of dopamine, cocaine is addictive. During metabolism, cocaine's ester linkage is hydrolysed by plasma pseudochlolinesterase into toxic metabolites, which may cause an allergic reaction.[112, 114] This observation led to efforts to discover a novel class of LA which did not contain an ester linkage. In 1943, Nils Lofgren synthesised lidocaine (lignocaine), a new amide LA which had far fewer allergic responses, no addictive CNS effects, and a faster onset of action. This work introduced a new class of agents which led on to development other agents *e.g.* mepivacaine, prilocaine, bupivacaine, amethocaine and tetracaine.

Lidocaine is a common LA and anti-arrhythmic drug (Figure 1.17). It is characterised by a rapid onset of action and intermediate efficacy, making lidocaine suitable for topical and infiltration anaesthesia. Lidocaine is also the most important class 1B antiarrhythmic drug; it is used intravenously for the treatment of ventricular arrhythmias for acute myocardial infarction, digitalis poisoning, cardioversion or cardiac catheterisation. Relative insensitivity to lidocaine is genetic. [115-116]

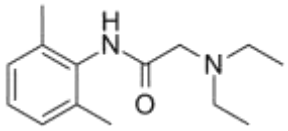

Figure 1.17: Structure of lidocaine

1.4.1 Tetrodotoxin

TTX is a well-known non-selective VGSC blocker from the Japanese puffer fish *Fugu* (Figure 1.18), working by binding to site 1 of the fast VGSC. TTX belongs to the hydrophilic heterocyclic guanidine toxins. Site 1 is located at the extracellular pore opening of the ion channel formed by the external loop linking TMS 5 and 6 in domains I-IV. The guanidine group of the TTX binds with very high affinity to the entrance of the channel that normally interacts with the hydrated Na^+ ion. Whereas the hydrated Na^+ ion binds reversibly for nanoseconds, the TTX molecule is bound for tens of seconds. The binding of any molecules to this site will temporarily disable the function of the ion channel. Saxitoxin and several of the snail conotoxins also bind to the same site. TTX causes total paralysis due to its inability to distinguish one VGSC sub-type from any other and blocks them all extracellularly, except Na_v 1.5 which is selectively TTX resistant. In μM concentrations, it can kill a mammal within minutes. The pharmacology of this drug is well understood and some research groups are currently trying to modify the structure of TTX to utilise the drug as a chemotherapeutic agent.[117]

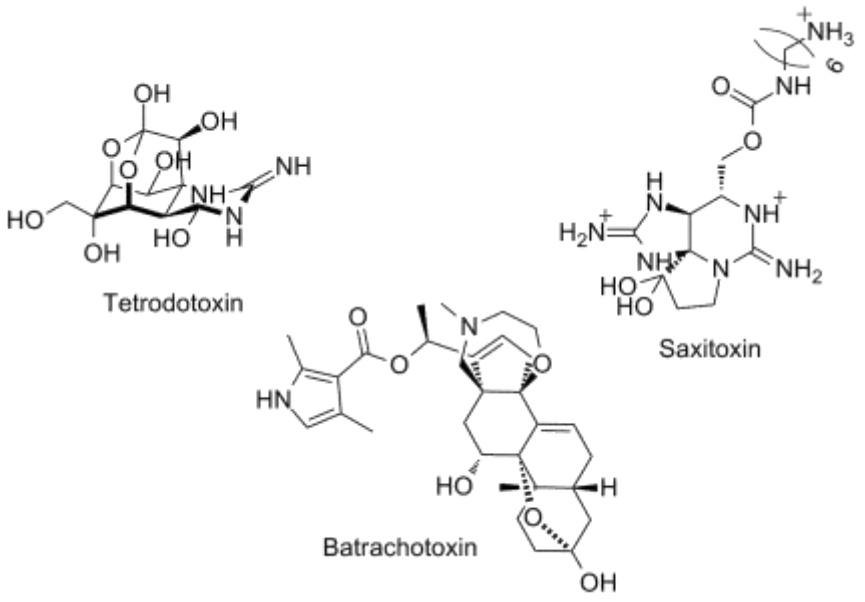

Figure 1.18: Structures of Tetrodotoxin, Saxitoxin and Batrachotoxin

Sodium channels can be classified according to their sensitivity to TTX, and use of this toxin as a biochemical probe has elucidated two distinct types of VGSCs present in humans; the TTX-sensitive and the TTX-resistant VGSCs. TTX binds to sensitive VGSCs with a binding affinity of 5-15 nM, while the resistant VGSCs bind TTX with low μM affinity. Nerve cells containing resistant Na^+ channels are located primarily in the cardiac tissue (Na_v 1.5), while nerve cells containing sensitive VGSCs dominate the rest of the body. TTX blocks the fast Na^+ current in human myocytes (the contractile cells of the muscles), thereby inhibiting their contraction leading to a myocardial infarction. By contrast, the VGSCs in pacemaker cells of the heart are of the slow variety, so action potentials in the cardiac nodes are not inhibited by TTX. The myocytes in the atrium, which surround the main cardiac pacemaker, do express this fast Na^+ current and therefore the electrical activity is blocked and the heart fails to beat.[118-119]

Through binding studies, it was shown that TTX does not bind to the channel at the LA site, but blocks at its own site (Site 1). With this information, research was undertaken to discover how many different binding sites on the channel exist. It is now known that there are at least eight different binding sites on the sodium channel (Table 1.5), each binding with its own class of ligand, therefore all VGSC ligands are classified according to where they bind.[120-123]

Receptor Site	Ligands
Site 1	Tetrodotoxin (TTX), Saxitoxin (STX)
Site 2	Batrachotoxin (BTX)
Site 3	α-Scorpion toxins
Site 4	β-Scorpion toxins
Site 5	Brevetoxin/Ciguatoxins
Site 6	Conotoxins
Site 7	DDT / Pyrethroid insecticides
Site 8	Local Anaesthetics

Table 1.5: Ligands and their binding sites on VGSCs [120-123]

These toxins and drugs bind to their respective sites on the channel, producing various effects, which all culminate in abnormal VGSC activity, whether it be over stimulation or total inhibition of activity.

1.4.2. Novel VGSC ligands

Over the years, several groups have published the synthesis of a range of novel Na^+ channel ligands, with the aim of producing subtype-selective compounds for possible therapeutic and/or research tool purposes. WIN 17317-3 (Figure 1.19) is one such small molecule initially developed for inhibiting K^+ channels but through *in vitro* and *in vivo* studies, was found to be a potent inhibitor of VGSCs, and is specifically selective for Na_v 1.2 (IC_{50} = 3.14 nM).[124-125] It exhibits selectivity for neuronal and skeletal muscle sodium channels over cardiac channel isoforms. Through *in vitro* studies, a ten-fold decrease in potency was seen as an inhibitor of adult Na_v 1.5.

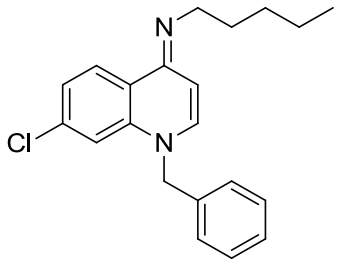

Figure 1.19: Structure of WIN 17317-3 [125]

Reported data indicated that WIN 17317-3 is a novel high-affinity probe for VGSCs, with the ability to differentiate between different sub-types, and this study concluded, that WIN 17317-3 would serve well as a template for a new generation of Na^+ channel inhibitors.[125]

Although this compound is a promising VGSC ligand which could be developed into a PET radiotracer, we were aware of another research group working on the development of the compound and therefore, we chose not to develop WIN 17317-3 within this project.

Chowdhry *et. al.*, have recently published findings on their VGSC ligand, R-(-)-2,4-diamino-6-fluoromethyl-5-(2,3,5-trichlorophenyl)-pyrimidines (Figure 1.20). This compound was derived from lamotrigine, a clinical antiepileptic agent. BW202W92 was shown to bind to a novel stereoselective drug-binding site, in the rat forebrain synaptosomes. It was further shown that the binding affinity for the ligand was greatly enhanced by doping in low concentrations of TTX. Unfortunately, the S-enantiomer exhibited up to 30-fold less potency and high sensitivity to increased K^+ concentration, causing an inhibitory effect.[126]

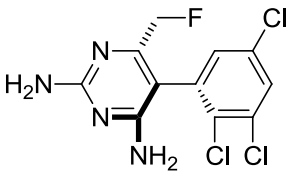

Figure 1.20: Structure of BW202W92 [126]

This study revealed that there is a significant difference in H-bonding to the target for the R- and S-enantiomer. These structural differences are likely to reflect the different pharmacological behaviours *in vivo.*[126]

Phenoxyphenyl pyrazoles are a class of compounds identified to be state-dependent blockers of VGSCs and exhibit anticonvulsant properties. These compounds have negligible effects at other neuroeffector sites, making them very promising for biological development.[7]

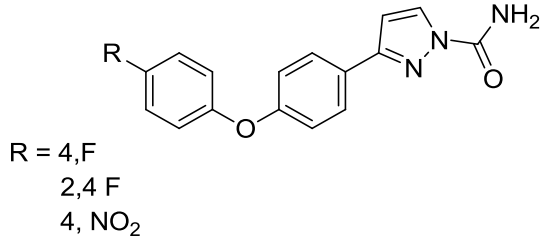

Figure 1.21: Structure of 3-(4-substituted-phenoxy)phenyl pyrazole-1-carboxamides

3-(4-R-phenoxy)phenyl pyrazoles (Figure 1.21) were derived from 4-(4-fluorophenoxy)-benzaldehyde semicarbazone (V102862) (Scheme 1.1), a potent blocker of neuronal VGSCs that interacts selectively with inactivated states, as opposed to resting states of the channel. However, *in vivo* metabolism experiments showed that the semicarbazone functional group was easily metabolised to the corresponding carboxylic acid, a reactive species *in vivo.*[7, 127-128] A quantitative structure analysis relationship (QSAR) study was used to afford a biologically stable alternative to the semi-carbazone moiety, which maintained and protected the carbon nitrogen double bond without losing biological activity. A pyrazole ring functionality was chosen to prevent this metabolism.

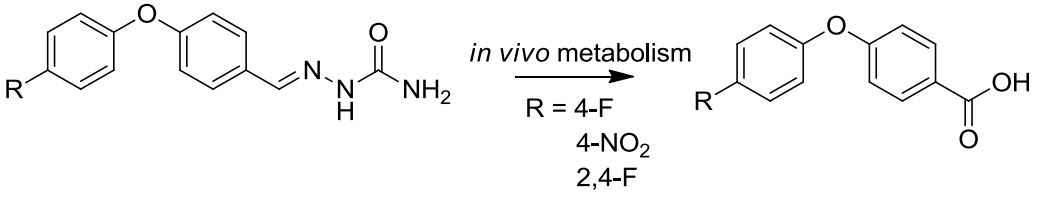

Scheme 1.1: In vivo metabolism of 4-(4-substituted-phenoxy)benzaldehyde semicarbazone (V102862) [81]

This five-membered ring allowed the same spatial arrangement between the carboxamide and the phenoxyphenyl moiety, while a higher affinity for VGSCs was seen for the pyrazole derivative (K_i = 0.031 μM ± 0.007), compared with 4-(4-fluorophenoxy)benzaldehyde semicarbazone (V102862) (K_i = 0.18 μM ± 0.03).

In view of their high affinity and promising characteristics, the 3-(4-R-phenoxy)phenyl pyrazole-1-carboxamides were chosen to develop into novel PET ligands. Their structure allowed much scope for potential direct and in-direct radiolabelling strategies to optimise [^{18}F]fluoride incorporation, and to hopefully provide a PET ligand that proves selective towards a particular VGSC isoform. Moreover, these compounds have been shown to be potent and issues surrounding *in vivo* stability have been resolved.

1.5 Required features of radiotracer design

The ability to image a molecular target or in this instance VGSCs is afforded by delivery of the radiotracer, retention at the specific binding site and washout of any non-specifically bound radiotracer. The chemical and pharmacological properties of the radiotracer exert a variety of effects on the ability to bind to the receptor. For example, high lipophilicity leads to greater nonspecific binding, reducing the signal-to-noise ratio, and therefore the ability to detect a specific signal.[129]

When developing a small molecule into a radiotracer, the affinity of the radiotracer for the binding site needs to be ascertained. The affinity of the radiotracer (normally measured as the dissociation constant, K_d) relative to the concentration of available binding site (B_{max}) is the most important characteristic of site-specific radiotracers.[130] There are additional factors that can lead to reduced specific signal, however, if radiotracers demonstrate poor affinity or the concentration of binding sites is too low, the radiotracer cannot be developed into an ideal PET agent. [129]

The process to develop a radiotracer follows a logical order:

(1) Determine the concentration of receptor (B_{max}) in the target tissue
(2) Estimate the minimum required affinity (e.g. K_d) to afford *in vivo* localisation and calculate the signal-to-noise ratio and binding potential
(3) Determine the log P and substrate characteristics
(4) Develop radiotracers for *in vitro* characterisation of affinity and binding site specificity using autoradiography or tissue homogenate studies.
(5) Demonstrate specific *in vivo* retention in target tissue

When developing a novel PET agent, the following process should be considered and adhered to.

Importantly, for a radiotracer to behave as a 'tracer', it must be injected at masses that do not significantly populate the receptor. The radiotracer should not produce any pharmacologic response. It is suggested that to remain at tracer occupancy, specific binding should be less than 5%.[129]

In order to ascertain the B_{max}, K_d and also bound (B) and free (F) concentration, a Scatchard plot (Figure 1.22) is used to combine data afforded from a radioligand binding assay .

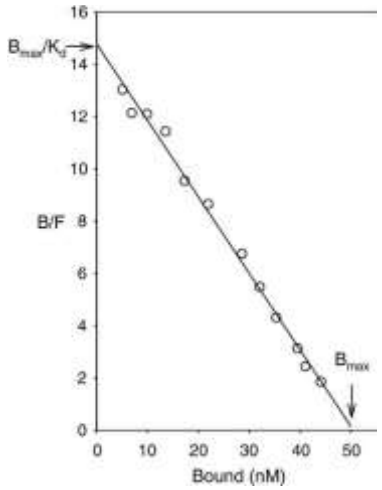

Figure 1.22: Example of in vitro radiotracer binding data, using a Scatchard plot to measure the B_{max} and K_d. As the specifically bound radiotracer approaches zero, the maximum B/F approaches B_{max}/K_d[129]

When specific binding reaches zero, the bound (B) to free ratio (F) (B/F) approaches the maximum value defined by (B_{max}/K_d). The ratio of B_{max}/K_d provides an estimate of the maximum bound to free ratio or so called binding potential, but can also be used as an approximation of the maximum specific to non-specific binding signal in a tissue. If B_{max} were to equal 10 nM for example and the K_d was 1 nM, then the binding potential would be 10. There is currently no optimal binding potential for radiotracers, however, it has been agreed using experimental data from currently developed PET tracers, that a $B_{max}/K_d \geq 10$ should be good enough to afford a reasonable signal-to-noise ratio. [129]

1.6 Aims

PET is a widely utilised technique to diagnose a variety of diseases such as cancer and (AD). Currently, many new PET agents are being developed to target specific receptors expressed in different diseases to produce less ambiguous images, allowing for quicker and more accurate diagnosis.

This project set out to design and synthesise novel fluorine-18 labelled PET agents to target VGSCs. It was hypothesised that VGSC activity in tumours could indicate metastatic potential, as the expression of neo-natal VGSC's positively correlating with strongly metastatic cancers. At present, there is no known clinical PET agent for targeting VGSC's or imaging metastatic potential in cancer; we hoped to utilise our novel PET agent to indicate malignant potential.

The 3-(4-R-phenoxy)phenyl pyrazole as reported by Yang *et. al.*, and the closely related 3-(4-((4-R-phenyl)thio)phenyl)-pyrazoles as described by Dimmock and co-workers, [131] were chosen to develop into PET agents due to their strong affinity for VGSC's and their structural characteristics, which allowed multiple approaches to introduce a fluorine-18 label. Our aim was to identify and develop optimal radiolabelling strategies and methodologies to produce PET agents in good synthesis time, yield and purity. The fluorine-19 standards for these compounds were also synthesised and subjected to electrophysiological testing before under-going a full VGSC isoform selectively screen to identify the most potent compounds. The compounds which exhibited good potency were then chosen for further study. The fluorine-18 PET agents were put through näive biodistribution studies to assess *in vivo* characteristics and finally, the most promising PET tracer was assessed in tumour studies both *in vitro* and i*n vivo*, to identify specific binding and give an indication of whether PET imaging of VGSCs in metastatic cancer was possible with our tracer.

2. Materials and Methods

2.0 General

All reagents including anhydrous solvents were sourced from VWR, Fisher Scientific or Sigma Aldrich. ^{1}H and ^{13}C NMR spectra were recorded on a Bruker AMX at 400 MHz and 100.6 MHz respectively, using tetramethylsilane as the internal standard. All spectra were recorded in $CDCl_3$ unless otherwise stated. Mass Spectra were recorded using a HPLC-MS apparatus combining an Agilent Technologies 1200 and Bruker Daltonics Esquire 3000 plus ESI-MS. Low resolution mass spectrometry was carried out on an Agilent Technologies 6890 GC coupled to an Agilent Technologies 5973 mass spectrometer in electron ionisation mode (EI). The system was controlled by MSD productivity Chemstation software. Infrared Spectra were recorded using a Perkin Elmer spectrum BX FT-IR system. Thin layer chromatography (tlc) was run on Fluka silica gel aluminium plates with fluorescent indicator 254 nm. Column chromatography (CC) was run using high purity grade silica gel, pore size 60 Å, 230-400 mesh particle size. Analytical radio HPLC was carried out using a Gilson instrument equipped with a γ detector (Bioscan Flow-count) and a UV detector (Gilson UV/VIS-156) set to 254 nm with Chromeleon software (Dionex). A Phenomenex Luna C18(2) column (50 x 4.6 mm, 3 µm, 100 Å; flow rate 1 mL/min) was used for analytical HPLC. Semi-preparative radio HPLC was also carried out using a Gilson instrument equipped with a γ detector (Bioscan Flow-count) and a UV detector (Gilson UV/VIS-156) set to 254 nm using Chromeleon software. A Phenomenex Luna C18 column, (250 x 10 mm, 5 µm, 100 Å; flow rate 3 mL/min) was used for semi-preparative HPLC. Non-radioactive compounds were purified on a preparative Agilent 1200 HPLC using a Phenomenex Luna C18(2) column, (75 x 30 mm, 5 µm, 100 Å; flow rate 12 mL/min). [Mobile phases used are expressed in Table 2.1]. To separate samples for log P calculations, a MSE Micro Centaur centrifuge apparatus was used. [^{18}F]Fluoride was produced by a cyclotron (PET Trace, GE Medical Systems) using the $^{18}O(p,n)^{18}F$ nuclear reaction with 16.4 MeV proton irradiation of an enriched [^{18}O]H_2O target. Automated radiochemistry was performed on either a GE Healthcare Tracerlab FX-N™ module or a GE Healthcare FASTlab™ module.

	Method
A	MeCN/H_2O; 5-95% B over 15 minutes, 1 mL/min
B	MeCN/H_2O; 10-95% B over 15 minutes, 1 mL/min
C	MeCN/H_2O; 60-80% B over 25 minutes, 3 mL/min
D	MeCN/H_2O; 40-80% B over 15 minutes, 3 mL/min
E	MeCN/H_2O; 50–95% B over 30 minutes, 3 mL/min
F	MeCN/H_2O; 50–95% B over 15 minutes, 1 mL/min
G	MeCN/H_2O; 10-95% B over 15 minutes, 3 mL/min
H	MeCN/H_2O; 5–80% B over 15 minutes, 1 mL/min
I	MeOH/NH_4OAc; 50–80% B over 25 minutes, 3 mL/min
J	MeCN/H_2O; 55–80% B over 25 minutes, 3 mL/min
K	MeCN/H_2O; 20-95% B over 25 minutes, 3 mL/min

Table 2.1: General methods and mobile phases used for reverse-phase HPLC purification

2.1 Chemistry

Synthesis of 4-(4-fluorophenoxy)acetophenone[7]

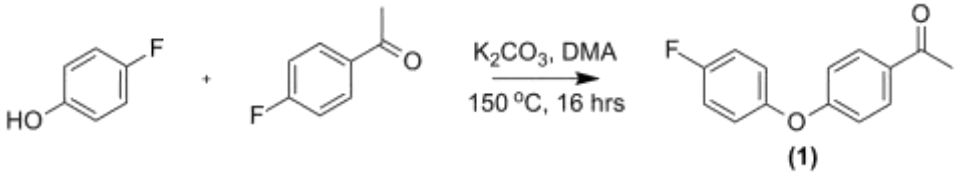

(1)

To a stirred mixture of 4-fluorophenol (6.78 g, 40.1 mmol) in DMA (20 mL) was added potassium carbonate (5.55 g, 40.1 mmol) followed by 4-fluoroacetophenone (5.00 g, 44.6 mmol). The resultant solution was heated to 150 °C for 16 hours and monitored by tlc until reaction complete. The mixture was then cooled to RT, diluted with $CHCl_3$ (10 mL) and washed with 2 M NaOH solution (2 x 25 mL). The organic layer was dried over $MgSO_4$, filtered and evaporated under reduced pressure. The crude product was further dried under high vacuum at 60 °C for 6 hours giving (**1**) as a dark brown oil. A small sample was purified for analysis by CC (hexane/EtOAc; 2:1) and the bulk product was used in the following step without further purification. ^{1}H NMR δ 7.98 (m, 2H, PhH), 6.98 (m, 2H, PhH), 6.79 (m, 2H, PhH), 6.77 (m, 2H, PhH), 2.49 (s, 3H, CH_3); ^{13}C NMR δ 197.49, 162.38, 158.38, 151.10, 131.73, 130.70, 121.89, 121.81, 116.85, 116.27, 116.00, 26.47; *m/z* $[M]^+$ = 230, calcd. for $C_{14}H_{11}FO_2$: 230.

Synthesis of 4-(4-nitrophenoxy)acetophenone[7]

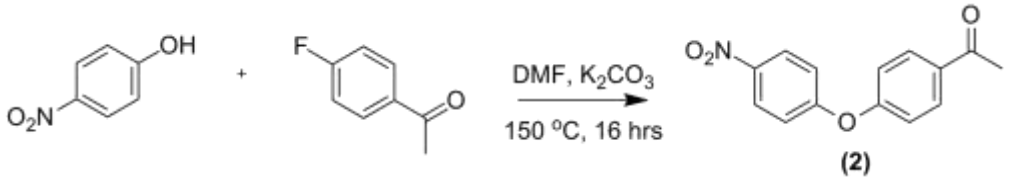

To a stirred mixture of 4-nitrophenol (6.83 g, 44.6 mmol) in DMA (20 mL) was added potassium carbonate (5.55 g, 40.1 mmol), followed by 4-fluoroacetophenone (5.00 g, 44.6 mmol). The resultant solution was heated to 150 °C for 16 hours and monitored by tlc until the reaction was complete. The mixture was then cooled to RT, diluted with $CHCl_3$ (10 mL) and washed with 2 M NaOH solution (2 x 25 mL). The organic layer was dried over $MgSO_4$, filtered and evaporated under reduced pressure. The product was further dried under high vacuum at 60 °C for 6 hours giving (**2**) as a dark brown oil. A small sample was purified for analysis, by CC (hexane/EtOAc; 2:1) and the bulk product was used in the following step without further purification. ^{1}H NMR δ 8.20 (d, (J=9 Hz), 2H, PhH), 7.92 (d, (J=9 Hz), 2H, PhH), 7.01-6.93 (m, 4H, PhH), 2.53 (s, 3H, CH_3); ^{13}C NMR δ 196.58, 162.77, 159.12, 143.5, 133.68, 130.81, 126.09, 119.52, 118.43, 26.59; *m/z* $[M]^+$ = 257, calcd. for $C_{14}H_{11}NO_4$: 257.

Synthesis of 4-(2,4-difluorophenoxy)acetophenone[7]

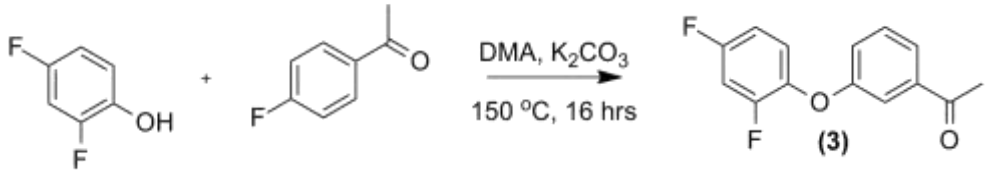

To a stirred mixture of 2,4-difluorophenol (5.80 g, 44.6 mmol) in DMA (20 mL) was added potassium carbonate (5.55 g, 40.1 mmol) followed by 4-fluoroacetophenone (5.00 g, 44.6 mmol). The resultant solution was heated to 150 °C for 16 hours. The mixture was then cooled to RT, diluted with $CHCl_3$ (10 mL) and washed with 2 M NaOH solution (2 x 25 mL). The organic layer was dried over $MgSO_4$, filtered and evaporated under reduced pressure. The product was further dried under high vacuum at 60 °C for 6 hours giving (**3**) as a dark brown oil. A small sample was purified for analysis, by CC (hexane/EtOAc; 2:1) and the bulk product was used in the following step without further purification. ^{1}H NMR δ 7.81 (m, 2H, PhH), 7.05 (m, 1H, PhH), 6.90-6.80 (m, 4H, PhH) 2.48 (s, 3H, CH_3); ^{13}C NMR δ 195.356, 160.69, 158.66, 154.83, 152.32, 137.38, 130.77, 129.50, 122.92, 114.66, 104.86, 25.41; *m/z* $[M]^+$ = 248, calcd. for $C_{14}H_{10}F_2O_2$: 248.

Synthesis of 3-[4-(4-fluorophenoxy)phenyl]-pyrazole[7]

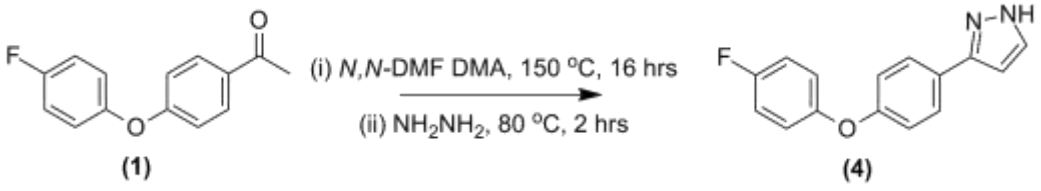

(1) (4)

To a stirred solution of **(1)** (8.90 g, 39.0 mmol) in DMF (20 mL) was added *N,N*-dimethylformamide dimethylacetal (5.00 g, 43.0 mmol). The reaction was heated to 150 °C for 16 hours. The solution was cooled to RT and distilled H_2O (30 mL) was added over 20 minutes until a yellow precipitate formed. This solid was collected by suction filtration and washed with distilled H_2O (20 mL). The product was further dried by high vacuum at 25 °C for 4 hours. The solid was dissolved in ethanol (20 mL) and 35% aq. hydrazine (1.50 mL, 43.0 mmol) added dropwise. The mixture was heated to 80 °C for 90 minutes after which the solvent was removed by rotary evaporation. The crude product was then re-dissolved in EtOAc (20 mL) and washed with distilled H_2O (3 x 20 mL) and brine (20 mL). The organic layer was dried over $MgSO_4$ and concentrated *in vacuo*. The crude product was purified by CC (hexane/EtOAc; 1/1) giving **(4)** as a yellow solid (6.73 g, 68.0%). ^{1}H NMR δ 7.83 (m, 2H, PhH), 7.73 (d, (J=12 Hz), 1H, **CH**=CH-NH), 6.97 (m, 4H, PhH), 6.88 (m, 2H, PhH), 5.62 (d, (J=12 Hz), 1H, **CH**-NH); ^{13}C NMR δ 163.21, 154.52, 142.80, 131.88, 130.06, 127.69, 127.50, 125.98, 120.78, 117.23, 102.71; *m/z* $[M+MeOH]^+$ = 286.2, calcd. for $C_{16}H_{15}FN_2O_2$: 286.1; mp 120.5-126.0 °C.

Synthesis of 3-[4-(4-nitrophenoxy)phenyl]-pyrazole[7]

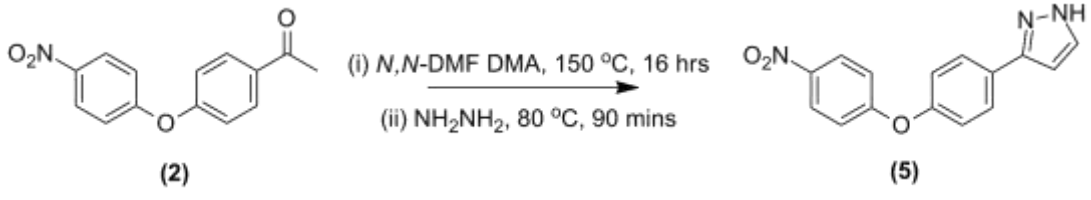

(2) (5)

To a stirred solution of (**2**) (3.30 g, 14.0 mmol) in DMF (10 mL) was added *N,N*-dimethylformamide dimethylacetal (2.10 mL, 16.0 mmol) the reaction was heated to 150 °C for 16 hours. The solution was cooled to RT and distilled H_2O (20 mL) was added over 20 minutes until a yellow precipitate formed. This solid was collected by suction filtration and washed with distilled H_2O (20 mL). The product was further dried by high vacuum at 25 °C for 4 hours. The solid was dissolved in EtOH (20 mL) and 35% aq. hydrazine (0.50 mL, 16.0 mmol) added dropwise. The mixture was heated to 80 °C for 90 minutes after which, the solvent was removed

by rotary evaporation. The crude product was re-dissolved in EtOAc (20 mL) and washed with distilled H_2O (3 x 20 mL) and brine (20 mL). The organic layer was dried over $MgSO_4$ and the solvent removed *in vacuo*. The crude product was purified by CC (hexane/EtOAc; 1:1) giving **(5)** as a yellow solid (982 mg, 25.0%). ^{1}H NMR δ 8.16-8.12 (tt, (J=3 Hz), 2H, PhH), 7.79-7.76 (tt, (J=2 Hz), 2H, PhH), 7.58 (d, (J=3 Hz), 1H, **CH**=CH-NH), 7.08-7.05 (tt, (J=2 Hz), 2H, PhH), 7.00-6.96 (tt, (J=2 Hz), 2H, PhH), 6.56 (d, (J=3 Hz), 1H, **CH**-NH); ^{13}C NMR δ 163.21, 154.52, 142.80, 131.88, 130.06, 127.69, 127.50, 125.98, 120.78, 117.23, 102.71; *m/z* $[M]^+$ = 281, calcd. for $C_{15}H_{11}N_3O_3$: 281; mp = 160.0-163.2 °C.

Synthesis of 3-[4-(2,4-difluorophenoxy)phenyl]-pyrazole[7]

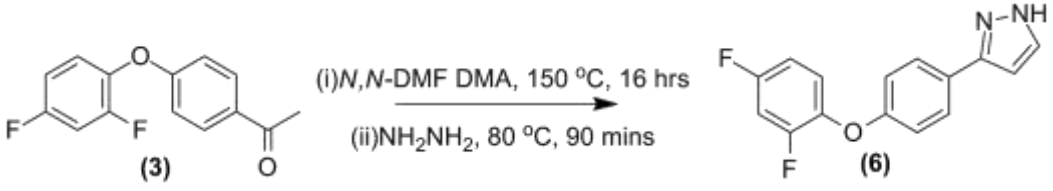

To a stirred solution of (**3**) (7.50 g, 30.0 mmol) in DMF (20 mL) was added *N,N*-dimethylformamide dimethylacetal (4.40 ml, 33.0 mmol) the reaction was heated to 150 °C for 16 hours. The solution was cooled to RT and distilled H_2O (20 mL) was added over 20 minutes until a yellow precipitate formed. The solid was collected by suction filtration and washed with distilled H_2O (20 mL). The product was further dried by high vacuum at 25 °C for 4 hours. The solid was dissolved in EtOH (20 mL) and 35% aq. hydrazine (1.10 mL, 33.0 mmol) added dropwise. The mixture was heated to 80 °C for 1.5 hours and the solvent removed by rotary evaporation. The crude product was then re-dissolved in EtOAc (20 mL) and washed with distilled H_2O (3 x 20 mL) and brine (20 mL). The organic layer was dried over $MgSO_4$ and the solvent was evaporated *in vacuo*. The crude product was purified by CC (hexane/EtOAc; 1:1) giving (**6**) as a yellow solid (6.36 g, 78.0%). ^{1}H NMR δ 7.64-7.61 (m, 2H, PhH), 7.52 (d, (J=2 Hz), 1H, **CH**=CH-NH), 7.05-6.99 (m, 2H, PhH), 6.92-6.86 (m, 3H, PhH), 6.82-6.76 (m, 1H, **CH**-NH); ^{13}C NMR δ 157.74, 157.64, 157.52, 153.19, 153.06, 139.77, 139.72, 139.65, 139.61, 127.27, 117.01, 105.54, 102.44; *m/z* $[M]^+$ = 272, calcd. for $C_{15}H_{10}F_2N_2O$: 272; mp = 99.0 -102.2 °C.

Synthesis of 3-[4-(4-fluorophenoxy)phenyl]-pyrazole-1-carboxamide[7]

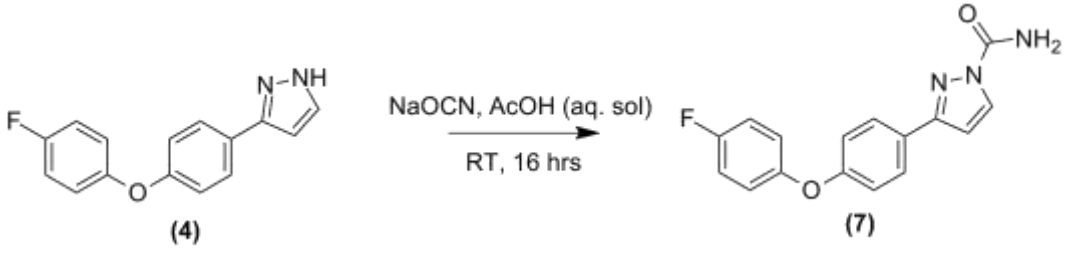

To a stirred solution of **(4)** (3.50 g, 14.0 mmol) in 90% aq. AcOH (15 mL) was added sodium cyanate (1.10 g, 16.0 mmol) as an aq. suspension. The reaction mixture was stirred for 16 hours at RT. Distilled H_2O (20 mL) was added until a precipitate formed and the product collected by suction filtration. The crude product was purified by CC, (EtOAc/hexane; 1:1) giving **(7)** as a cream solid (1.45 g, 35.0%). ^{1}H NMR δ 8.21 (d, (J=3 Hz), 1H, **CH**-N-C=O), 7.74 (m, 2H, PhH), 6.98-6.92 (m, 6H, PhH), 6.66 (d, (J=3 Hz), 1H, **CH**=CH-NH); ^{13}C NMR δ 162.3, 158.6, 157.9, 153.9, 152.4, 150.8, 130.1, 127.8, 126.9, 120.9, 120.8, 120.7, 118.5, 116.5, 116.3, 106.3; *m/z*: $[M+H]^+$ = 298.52, calcd. for $C_{16}H_{13}FN_3O_2$: 298.75; HRMS $[M+Na]^+$ = 320.0818, calcd. 320.2840; HPLC (method A), t_R = 11.7 minutes, >95% purity; mp = 132.5-136.8 °C; lit. mp 141.0-143.0 °C.[7]

Synthesis of 3-[4-(4-nitrophenoxy)phenyl]-pyrazole-1-carboxamide[7]

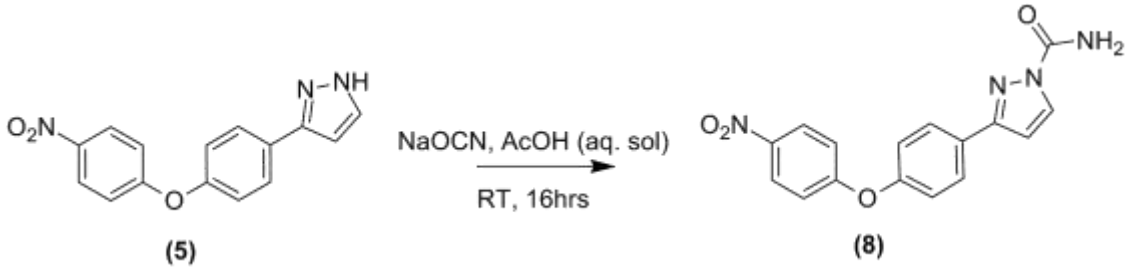

To a stirred solution of **(5)** (514 mg, 2.00 mmol) in 90% aq. AcOH (6.50 mL) was added sodium cyanate (156 mg, 2.40 mmol) as an aq. suspension. The reaction mixture was stirred for 16 hours at RT. Distilled H_2O (20 mL) was added until a precipitate formed and the product collected by suction filtration. The crude product was purified by CC, (EtOAc/hexane; 1:1) giving **(8)** as a cream solid (157 mg, 24.2%). ^{1}H NMR δ 8.21 (d, (J=3 Hz), 1H, **CH**-N-C=O), 8.16-8.14 (m, 2H, PhH), 7.85-7.83 (m, 2H, PhH), 7.10-7.07 (m, 2H, PhH), 7.02-6.98 (m, 2H, PhH), 6.66 (d, (J=3 Hz), 1H, **CH**=CH-N); ^{13}C NMR δ 162.9, 155.3, 153.3, 150.6, 143.1, 130.3, 129.2, 128.1, 126.0, 120.8, 117.3, 106.3; *m/z* $[M]^+$ = 324.29, calcd. for $C_{16}H_{12}N_4O_4$: 324.09, HRMS 324.0809, calcd.

324.2960; HPLC (method A), t_R = 8.1 minutes, >95% purity; mp = 132.0-137.0 °C; lit. mp 145.0-147.0 °C.[7]

Synthesis of 3-[4-(2,4-difluorophenoxy)phenyl]-pyrazole-1-carboxamide[7]

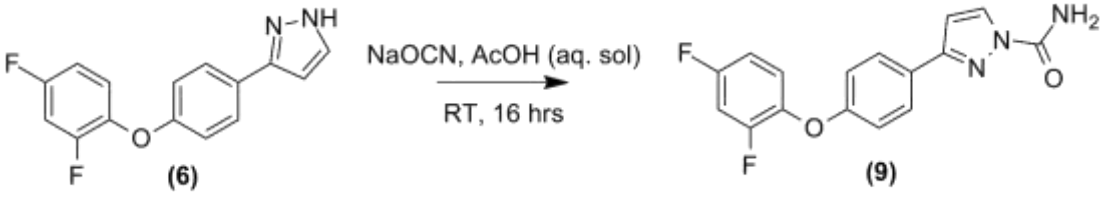

To a stirred solution of (**6**) (2.40 g, 8.70 mmol) in 90% aq. AcOH (30 mL) was added sodium cyanate (703 mg, 10.4 mmol) as an aq. suspension. The reaction mixture was stirred for 16 hours at RT. Distilled H_2O (20 mL) was added until a precipitate formed and the solid collected by suction filtration. The crude product was purified by CC (EtOAc/hexane; 1:1) giving (**9**) as a pure cream solid (2.15 g, 78.0%). ^{1}H NMR δ 8.17 (d, (J=3 Hz), 1H, **CH**-N-C=O), 7.72 (m, 2H, PhH), 7.08-7.02 (m, 2H, PhH), 6.92 (m, 3H, PhH), 6.81 (d, (J=3 Hz), 1H, **CH**=CH-NH), 5.23 (s, 1H, NH); ^{13}C NMR δ 189.97, 158.39, 153.80, 150.52, 130.07, 127.76, 126.95, 123.15, 116.83, 111.61, 111.38, 106.29, 105.62, 99.48; *m/z* $[M+H]^+$ = 316.54, calcd. for: $C_{16}H_{12}F_2N_3O_2$: 316.08, HRMS 316.0898, calcd. 316.2881; CHN C 61.10% H 3.39% N 12.98%, calcd. C 60.95% H 3.52% N 13.33%; HPLC (method A), t_R = 11.6 minutes, >90% purity; mp = 138.6-140.2 °C; lit. mp = 132.0-134.0 °C.[7]

Synthesis of tert-butyl (3-(4-(4-fluorophenoxy)phenyl)-pyrazole-1-carbonyl) carbamate[7]

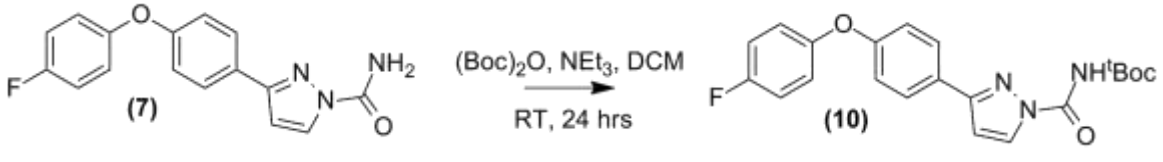

A stirred solution of (**7**) (150 mg, 510 µmol) in DCM (10 mL) and triethylamine (70.0 µL, 510 µmol) was stirred for 30 minutes. Di-*tert*-butyl dicarbonate (120 µL, 510 µmol) was added dropwise over 2 minutes and the resultant mixture stirred for 24 hours at RT. The reaction was washed with distilled H_2O (10 mL) and extracted with DCM (3 x 10 mL). The crude product was purified by CC (EtOAc/hexane; 1:4) giving (**10**) as an colourless solid (21.0 mg, 10.0%) . ^{1}H NMR δ 8.16 (d, (J=3 Hz), 1H, **CH**-NH), 7.73 (m, 2H, PhH), 6.91-6.99 (m, 6H, PhH), 6.60 (d, (J=3 Hz), 1H, **CH**=CH-NH), 5.47 (bs, 1H, NH), 1.38 (s, 9H, 3 x CH_3); ^{13}C NMR δ 160.27, 158.56, 157.87, 153.86, 152.41, 150.69, 130.06, 127.78, 126.89, 120.82, 118.27, 116.55, 106.27,

82.42, 23.24; *m/z* $[M]^+$ = 397.14 calcd. for $C_{16}H_{10}FN_2O_2$: 397.14, HPLC (method A), t_R = 13.7 minutes, >90% purity.

Synthesis of (4-fluorophenyl)(4-(trifluoromethyl)phenyl)methanone [132]

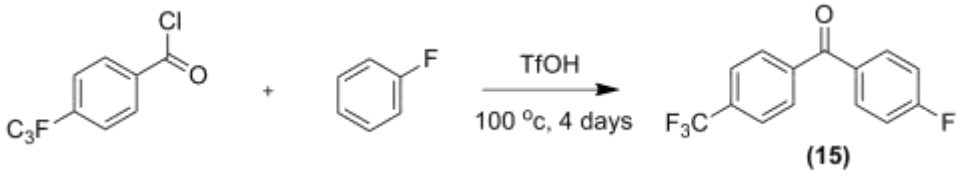

To a stirred solution of 4-trifluoromethyl benzoyl chloride (3.40 mL, 36.0 mmol) in fluorobenzene (440 µL, 3.00 mmol) under N_2 was added triflic acid (130 µL, 1.50 mmol) and heated to 100 °C for 4 days. The reaction was cooled to RT and a small amount of ice was added to decompose the mixture. The product was extracted into $CHCl_3$ (20 mL), washed with brine (2 x 20 mL), dried with $MgSO_4$, and the solvent removed *in vacuo*. The precipitate was then recrystallised from hot EtOH giving **(15)** as small off-white crystals (404 mg, 50.0%). ^{1}H NMR δ 7.95-7.80 (m, 6H, PhH), 7.02-7.18 (m, 2H, PhH); ^{13}C NMR δ 194.03, 167.04, 140.65, 134.31, 133.99, 132.82, 129.96, 125.50, 115.90, 115.68; *m/z* $[M+H]^+$ = 268.04, calcd. for $C_{14}H_9F_4O$: 268.05, HRMS $[M+Na]^+$ = 291.0406, calcd. 291.2003; HPLC (method A), t_R = 13.7 minutes, >90% purity; mp 101.0-101.3 °C; lit. mp 100.0-100.5 °C [132].

Synthesis of (4-(dimethylamino)phenyl)(4-(trifluoromethyl)phenyl)-methanone [133]

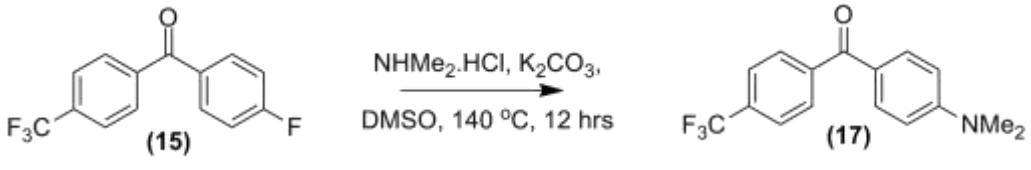

To a mixture of **(15)** (339 mg, 1.16 mmol) in DMSO (20 mL) and distilled H_2O (10 mL) was added dimethylamine hydrochloride (122 mg, 1.50 mmol) and potassium carbonate (417 mg, 3.02 mmol). The resultant mixture was heated to 140 °C under N_2 for 12 hours. After cooling to RT, the reaction was diluted with distilled H_2O (20 mL) and extracted into Et_2O (3 x 20 mL). The organic layer was extracted, dried over $MgSO_4$ and the solvent removed *in vacuo*. The crude off-white solid was purified *via* CC (Et_2O/hexane; 1:1) giving **(15)** as an off-white solid (293 mg, 86.2%). ^{1}H NMR (d_6-DMSO) δ 7.85-7.65 (m, 6H, PhH), 7.61-7.58 (m, 2H, PhH) 3.02 (s, 6H, 2 x CH_3); ^{13}C NMR (d_6-DMSO) δ 192.78, 152.63, 141.64, 131.90, 131.79, 131.37, 129.62, 128.89, 124.19, 109.64, 39.02; *m/z* $[M+H]^+$ = 294.1121, calcd. for $C_{16}H_{15}F_3NO$: 294.1106.

Synthesis of trimethyl-4-(4-(trifluoromethyl)benzoyl)-benzenaminium trifluoromethane sulphonate[133]

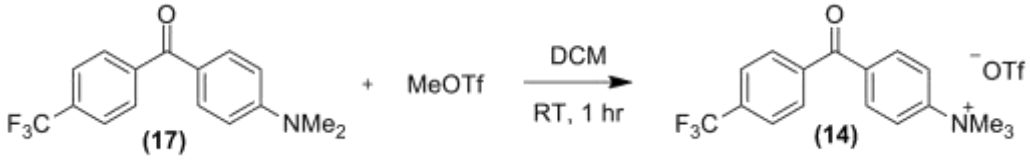

A solution of **(17)** (281 mg, 0.884 mmol) in DCM (10 mL) was added methyl triflate (100 µL, 0.890 mmol) under N_2. The solution was stirred for 1 hour at RT, before it was cooled to 0 °C and hexane (10 mL) added. A colourless precipitate formed and was collected by suction filtration. The solid was washed with Et_2O (20 mL) and dried under reduced pressure yielding **(13)** as a colourless solid (44.0 mg, 11.0%). ^{1}H NMR (d_6-DMSO) δ 8.20-8.15 (m, 2H, PhH), 8.04-7.92 (m, 6H, PhH), 3.67 (s, 9H, 3 x CH_3); ^{13}C NMR (d_6-DMSO) δ 197. 84, 142.89, 139.22, 134.73, 132.68, 131.25, 130.44, 121.25, 121.04, 119.00, 56.40; *m/z* $[M+H]^+$ = 308.13, calcd. for $C_{18}H_{17}F_6NO_4S$: 308.12; HPLC (method A), t_R = solvent front, >90% purity; mp 162.4-165.5 °C; lit. mp 167.0 °C [133].

Synthesis of 1-bromo-4-iodobenzene diacetate [134-135]

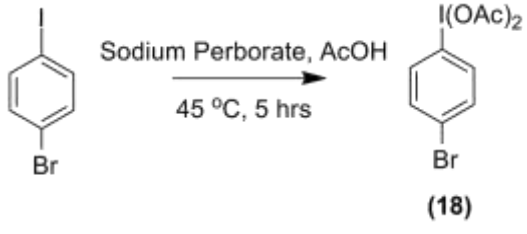

A stirred solution of 1-bromo-4-iodobenzene (2.83 g, 10.0 mmol) in AcOH (100 mL) was warmed to 45 °C for 50 minutes resulting in a yellow solution. The reaction mixture was allowed to cool to RT and sodium per-borate (15.3 g, 100 mmol) was added portion-wise over 20 minutes. The yellow solution turned a cloudy off-white colour and was heated to 45 °C for 5 hours. After cooling to RT, distilled H_2O (150 mL) was added to dilute the reaction and extracted into DCM (3 x 50 mL). The organic layer was washed with brine (3 x 50 mL) and dried with $MgSO_4$. DCM was removed *in vacuo* leaving an off-white solid. The crude product was purified by recrystallisation (hexane/Ac_2O; 1:1) giving **(18)** as an off-white solid (720 mg, 18.0%). ^{1}H NMR δ 7.96 (dd, (J=2 Hz, 9 Hz), 2H, PhH), 7.63 (dd, (J=2 Hz, 9 Hz), 2H, PhH), 2.02 (s, 6H, 2 x CH_3); ^{13}C NMR δ 176.48, 136.45, 134.21, 126.85, 119.70, 20.24; *m/z* $[M+H]^+$ = 401.88, calcd. for $C_{10}H_{11}BrIO_4$: 401.99.

Synthesis of bis(4-bromophenyl)iodonium triflate [134-135]

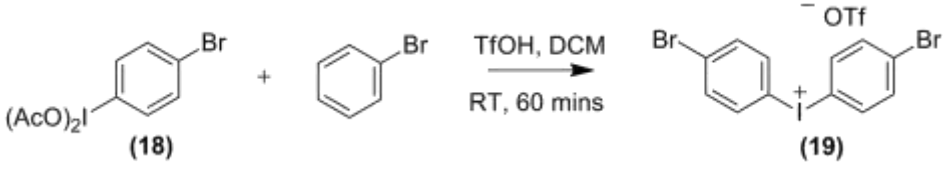

To a solution of **(17)** (710 mg, 1.80 mmol) in anhy. DCM (15 mL) under N_2 was added triflic acid (540 mg, 3.60 mmol) at -40 °C and stirred for 60 minutes at the same temperature. The solution was then warmed to RT for 60 minutes where a yellow solution formed. The solution was re-cooled to -30 °C and bromobenzene (292 mg, 1.90 mmol) was added dropwise. The mixture was allowed to stir for a further 60 minutes at this temperature, after which, the mixture was allowed to warm to RT. The reaction was concentrated *in vacuo* to a third of the volume and (ether/hexane; 1/1) added until a white precipitation formed. The solid was collected by suction filtration and washed with hexane (20 mL). The product was recrystallised from (hexane/Ac_2O; 1:1) giving **(18)** as large colourless crystals (497 mg, 47.0%). ^{1}H NMR (d_6-DMSO) δ 8.18 (dd, (J=2 Hz, 9 Hz), 4H, PhH), 7.77 (dd, (J=2 Hz, 9 Hz), 4H, PhH); ^{13}C NMR (d_6-DMSO) δ 136.97, 134.73, 126.35, 115.32; *m/z* $[M]^+$ = 587.75, calcd. for $C_{13}H_8Br_2F_3IO_3S$: 587.75; HPLC (method A), t_R = solvent front, >90% purity; mp = 205.3 °C (dec.), lit. mp 210.0 °C (dec.) [134-135].

Synthesis of 2-(4-fluorophenoxy)naphthalene [136]

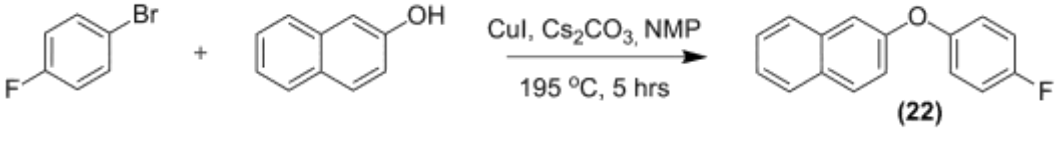

To a solution of 1-fluoro-4-bromobenzene (87.0 mg, 500 µmol) in *N*-methyl-2-pyrrolidone (700 µL) was added copper iodide (9.50 mg, 50.0 µmol), 1-naphthol (144 mg, 1.00 mmol) and caesium carbonate (325 mg, 1.00 mmol) under N_2. The sealed vial was heated to 195 °C for 5 hours. The reaction mixture was first purified on a silica cartridge eluting the crude product with Et_2O (10 mL), further purification by CC (hexane) gave **(22)** as an off-white solid (55.0 mg, 46.0%). ^{1}H NMR δ 7.78-7.73 (dd, (J=7, 7 Hz), 2H, PhH), 7.62 (d, (J=8 Hz), 1H, PhH), 7.41-7.31 (m, 2H, PhH) 7.19-7.15 (m, 2H, PhH), 7.03-6.95 (m, 4H, PhH); ^{13}C NMR δ 130.06, 129.97, 129.01, 127.75, 127.08, 126.62, 125.09, 124.73, 124.45, 120.86, 120.77, 119.52, 117.84, 116.53, 116.30, 113.25; *m/z* $[M]^+$ = 238.08, calcd. for $C_{16}H_{11}FO$: 238.06; HPLC (method A), t_R = 6.56 minutes, >90% purity.

Synthesis of 4-(4-fluorothiophenoxy)acetophenone

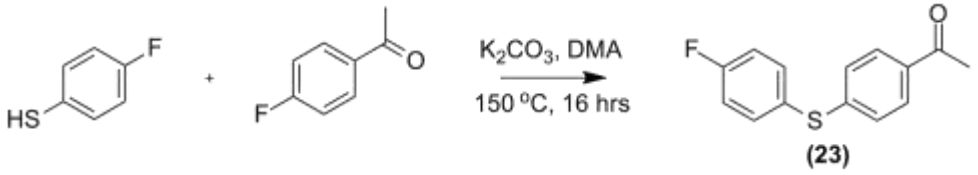

(23)

To a stirred mixture of 4-fluorothiophenol (5.10 g, 39.8 mmol) in DMF (20 mL) was added potassium carbonate (4.50 g, 32.6 mmol) followed by 4-fluoroacetophenone (5.00 g, 36.2 mmol). The resultant solution heated to 150 ^{o}C for 16 hours and monitored by tlc until reaction complete. The mixture was then cooled to RT, diluted with $CHCl_3$ (30 mL) and washed with 2 M NaOH solution (2 x 25 mL). The organic layer was dried over $MgSO_4$, filtered and evaporated under reduced pressure. The product was not isolated and **(23)** was used as a crude product in the following step.

Synthesis of 4-(4-nitrothiophenoxy)acetophenone

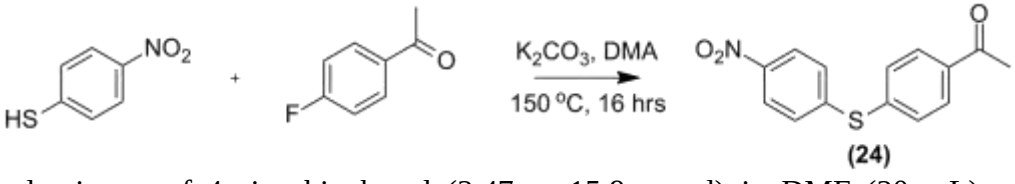

(24)

To a stirred mixture of 4-nitrothiophenol (2.47 g, 15.9 mmol) in DMF (20 mL) was added potassium carbonate (1.80 g, 13.0 mmol) followed by 4-fluoroacetophenone (2.00 g, 14.5 mmol). The resultant solution heated to 150 ^{o}C for 16 hours and monitored by tlc until reaction complete. The mixture was then cooled to RT, diluted with $CHCl_3$ (20 mL) and washed with 2 M NaOH solution (2 x 25 mL). The organic layer was dried over $MgSO_4$, filtered and evaporated under reduced pressure. The product was not isolated and **(24)** was used as a crude product in the following step.

Synthesis of 4-(2,4-difluorothiophenoxy)acetophenone

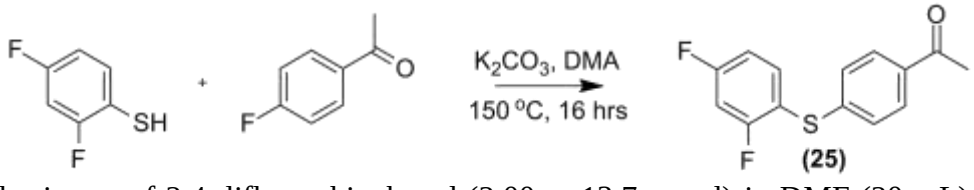

(25)

To a stirred mixture of 2,4-difluorothiophenol (2.00 g, 13.7 mmol) in DMF (20 mL) was added potassium carbonate (1.54 g, 11.1 mmol) followed by 4-fluoroacetophenone (1.71 g, 12.4 mmol). The resultant solution heated to 150 ^{o}C for 16 hours and monitored by tlc until reaction complete. The mixture was then cooled to RT, diluted with $CHCl_3$ (20 mL) and washed with 2 M NaOH

solution (2 x 25 mL). The organic layer was dried over $MgSO_4$, filtered and evaporated under reduced pressure. The product was not isolated and **(24)** was used as a crude product in the following step.

Synthesis of 3-[4-(4-fluorothiophenoxy)phenyl]-pyrazole

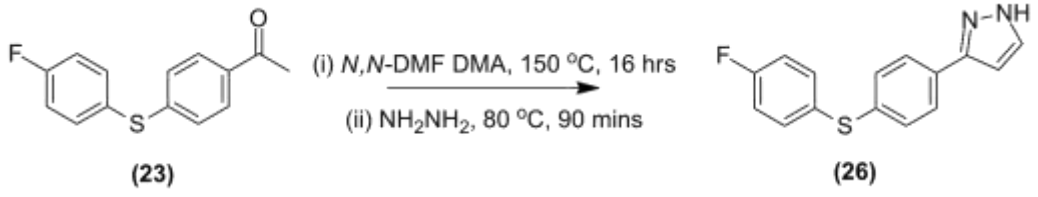

(23) **(26)**

To a stirred solution of (**23**) (8.65 g, 37.6 mmol) in DMF (20 mL) was added *N,N*-dimethylformamide dimethylacetal (4.93 g, 41.3 mmol) and the reaction was heated to 150 °C for 16 hours. The solution was cooled to RT and distilled H_2O (20 mL) was added over 20 minutes until a yellow precipitate formed. This solid was collected by suction filtration and washed with distilled H_2O (20 mL). The product was further dried by high vacuum at 25 °C for 4 hours. The solid was then dissolved in EtOH (20 mL) and 35% aq. hydrazine (1.32 g, 41.3 mmol) added dropwise. The mixture was heated to 80 °C for 90 minutes after which the solvent was removed by rotary evaporation. The crude product was then re-dissolved in EtOAc (20 mL), washed with distilled H_2O (3 x 20 mL) and brine (20 mL). The organic layer was dried over $MgSO_4$ and the solvent removed *in vacuo*. The crude product was purified by CC (hexane/EtOAc; 1:2) giving **(26)** as a yellow solid (7.83 g, 82.0%). ^{1}H NMR δ 7.67 (d, (J=8.1 Hz), 2H, PhH), 7.61-7.57 (m, 1H, **CH**=CH-NH), 7.40 (ddd, (J=8.6, 4.6, 1.7 Hz), 2H, PhH), 7.30-7.24 (m, 2H, PhH), 7.07-7.00 (m, 2H, PhH), 6.58 (d, (J=2.3 Hz), 1H, **CH**-NH); ^{13}C NMR δ 163.70, 161.23, 134.52, 134.18, 134.10, 131.57, 131.38, 130.18, 130.01, 126.57, 126.48, 116.66, 116.59, 116.37, 102.70; *m/z* $[M+H]^+$ = 271.1, calcd. for $C_{15}H_{12}FN_2S$: 271.1, HRMS 271. 0696, calcd. 271.3336; HPLC (method A), t_R = 12.0 minutes, >95% purity.

Synthesis of 3-[4-(4-nitrothiophenoxy)phenyl]-pyrazole

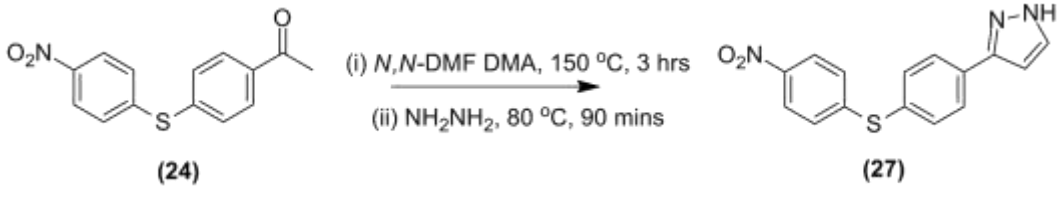

(24) **(27)**

To a stirred solution of (**24**) (3.96 g, 14.5 mmol) in DMF (10 mL) was added *N,N*-dimethylformamide dimethylacetal (1.90 g, 15.9 mmol) the reaction was heated to 150 °C for 3 hours. The solution was cooled to RT and distilled H_2O (20 mL) was added over 20 minutes until

a yellow precipitate formed. This solid was collected by suction filtration and washed with distilled H_2O (20 mL). The product was further dried by high vacuum at 25 °C for 4 hours. The precipitate was then dissolved in EtOH (20 mL) and 35% aq. hydrazine (510 mg, 15.9 mmol) added dropwise. The mixture was heated to 80 °C for 90 minutes after which the solvent was removed by rotary evaporation. The crude product was then re-dissolved in EtOAc (20 mL) and washed with distilled H_2O (3 x 20 mL) and brine (20 mL). The organic layer was dried over $MgSO_4$ and the solvent removed *in vacuo*. The crude product was purified by CC (hexane/EtOAc; 1:2) giving **(27)** as a yellow solid (1.12 mg, 25.9%). ^{1}H NMR δ 8.11-8.06 (m, 2H, PhH), 7.89 (dd, (J = 6.6, 1.7 Hz), 2H, PhH), 7.68 (d, (J = 2.3 Hz), 1H, **CH**=CH-NH), 7.61-7.56 (m, 2H, PhH), 7.27-7.19 (m, 2H, PhH), 6.71 (d, (J = 2.4 Hz), 1H, **CH**-NH); ^{13}C NMR δ 169.95, 147.13, 144.21, 134.04, 128.75, 126.42, 126.09, 125.70, 122.97, 114.48, 101.99; *m/z* $[M]^+$ = 297.2, calcd. for: $C_{15}H_{11}N_3O_2S$: 297.1, HRMS 297.0483, calcd. 297.3323; HPLC (method A), t_R = 11.9 minutes, >95% purity.

Synthesis of 3-[4-(2,4-difluorothiophenoxy)phenyl]-pyrazole

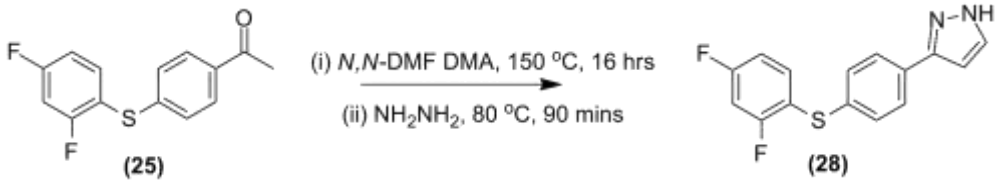

To a stirred solution of (**25**) (1.18 g, 4.45 mmol) in DMF (10 mL) was added *N,N*-dimethylformamide dimethylacetal (583 mg, 4.89 mmol) the reaction was heated to 150 °C for 16 hours. The solution was cooled to RT and distilled H_2O (20 mL) was added over 20 minutes until a yellow precipitate formed. This solid was collected by suction filtration and washed with distilled H_2O (20 mL). The product was further dried by high vacuum at 25 °C for 4 hours. The precipitate was then dissolved in EtOH (20 mL) and 35% aq. hydrazine (157 mg, 4.89 mmol) added dropwise. The mixture was heated to 80 °C for 90 minutes after which the solvent was removed by rotary evaporation. The crude product was then re-dissolved in EtOAc (20 mL) and washed with distilled H_2O (3 x 20 mL) and brine (20 mL). The organic layer was dried over $MgSO_4$ and the solvent removed *in vacuo*. The crude product was purified by CC (hexane/EtOAc; 1:2) giving **(28)** as a yellow solid (770 mg, 60.0%). ^{1}H NMR δ 7.72-7.67 (m, 2H, PhH), 7.59 (d, (J=2.1 Hz), 1H, **CH**=CH-NH), 7.34 (dd, (J=8.4, 2.2 Hz), 2H, PhH), 6.95-6.90 (m, 3H, PhH), 6.59

(d, (J=2.2 Hz), 1H, **CH**-NH); ^{13}C NMR δ 162.35, 159.86, 148.95, 135.50, 133.69, 133.50, 131.34, 131.21, 126.62, 124.35, 120.79, 112.73, 102.78; *m/z* $[M]^+$ = 288.6, calcd. for $C_{15}H_{10}F_2N_2S$: 288.1.

Synthesis of 3-[4-(4-fluorothiophenoxy)phenyl]-pyrazole-1-carboxamide

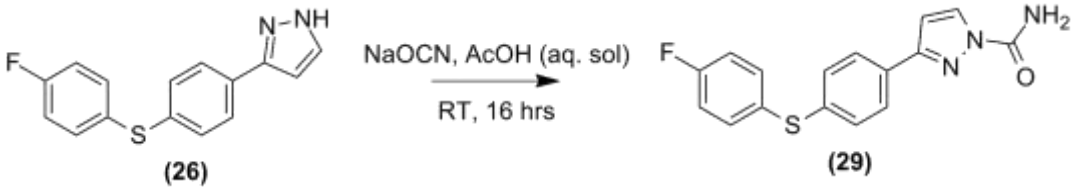

To a stirred solution of (**26**) (1.00 g, 3.70 mmol) in 90% aq. AcOH (30 mL) was added sodium cyanate (289 mg, 4.44 mmol) as an aq. suspension. The reaction mixture was stirred for 16 hours at RT. Distilled H_2O (20 mL) was added until a white precipitate formed and the product collected by suction filtration. The crude product was purified by CC (EtOAc/hexane; 1:2) giving (**29**) as a white solid (404 mg, 34.9%). ^{1}H NMR δ 8.17 (d, (J=2.8 Hz), 1H, **CH**-N-C=O), 7.69-7.65 (m, 2H, PhH), 7.39-7.32 (m, 2H, PhH), 7.24-7.18 (m, 4H, PhH), 6.62 (d, (J=2.8 Hz), 1H, **CH**=CH-N), 5.31 (s, 1H, NH); ^{13}C NMR δ 189.71, 164.03, 161.32, 153.88, 150.47, 138.33, 134.70, 134.62, 130.10, 129.59, 126.85, 116.68, 116.46, 106.39; *.m/z* $[M+H]^+$ = 314.0, calcd. for $C_{16}H_{13}FN_3OS$: 314.1, HRMS 314.0777, calcd. 314.3587; CHN C 61.38% H 3.77% N 13.12%, calcd. C 61.33% H 3.86% N 13.41%.

Synthesis of 3-[4-(4-nitrothiophenoxy)phenyl]-pyrazole-1-carboxamide[7]

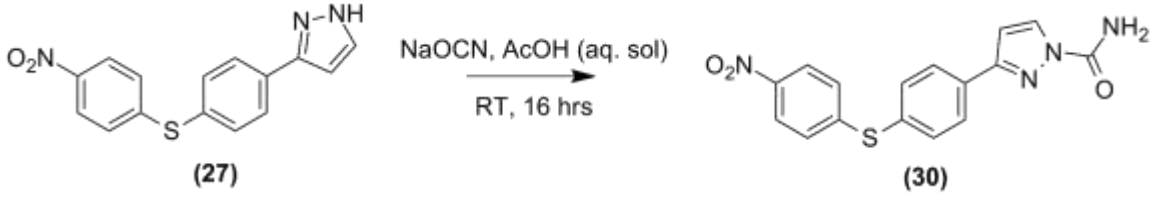

To a stirred solution of (**27**) (140 mg, 0.35 mmol) in 90% aq. AcOH (10 mL) was added sodium cyanate (28.0 mg, 0.42 mmol) as an aq. suspension. The reaction mixture was stirred for 16 hours at RT. Distilled H_2O (20 mL) was added until a white precipitate formed and the product collected by suction filtration. The crude product was purified by CC, (EtOAc/hexane; 1:2) giving (**30**) as a white solid (70 mg, 58.8%). ^{1}H NMR δ 8.31 (dd, (J=2.9, 1.1 Hz), 1H, **CH**-N-C=O), 8.11-8.03 (m, 2H, PhH), 7.98-7.84 (m, 2H, PhH), 7.59 (dt, (J=6.7, 1.2 Hz), 2H, PhH), 7.29-7.19 (m, 2H, PhH), 6.79 (dd, (J=3.0, 1.1 Hz), 1H, **CH**=CH-N); ^{13}C NMR δ 169.49, 155.91, 154.18, 147.79, 134.74, 133.13, 131.72, 129.67, 127.70, 127.17, 124.12, 107.49; *m/z* HRMS $[M+H]^+$ = 341.0206, calcd. for $C_{16}H_{14}N_4O_3S$: 341.0708.

Synthesis of 3-[4-(2,4-difluorothiophenoxy)phenyl]-pyrazole-1-carboxamide

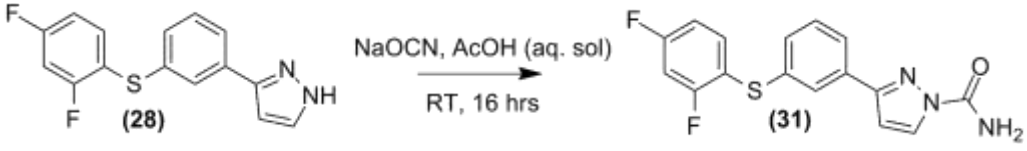

To a stirred solution of (**28**) (770 mg, 2.66 mmol) in 90% aq. AcOH (20 mL) was added sodium cyanate (207 mg, 3.19 mmol) as an aq. suspension. The reaction mixture was stirred for 16 hours at RT. Distilled H_2O (20 mL) was added until a pale yellow precipitate formed and the product collected by suction filtration. The crude product was purified by CC (EtOAc/hexane; 1:2) giving (**31**) as a pure cream solid (880 mg, 55.0%). ^{1}H NMR δ 8.28–8.26 (m, 1H, **CH**-N-C=O), 7.81–7.77 (m, 2H, PhH), 7.38–7.34 (m, 2H, PhH), 7.03–6.88 (m, 3H, PhH), 6.73–6.71 (m, 1H, **CH**=CH=NH), 5.45 (bs, 1H, NH); ^{13}C NMR δ 162.66, 160.17, 153.56,150.94, 135.39, 134.29, 134.14, 130.81, 130.61, 130.49, 130.13, 126.99, 124.32, 119.98, 119.80, 106.43; *m/z* HRMS $[M]^+$ = 331.1965, calcd. for $C_{16}H_{11}F_2N_3OS$: 331.3411; HPLC (method A), t_R = 10.1 minutes, purity >95%.

Syntheis of 3-(4-fluorophenyl)-1H-pyrazole

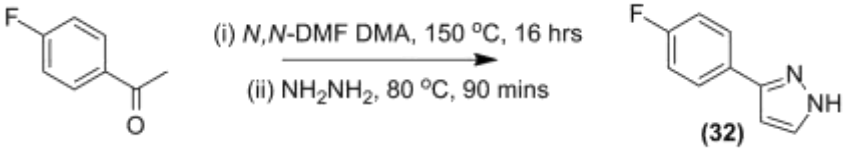

To a stirred solution of 4-fluoroacetophesssssnone (5.00 g, 44.6 mmol) in DMF (20 mL) was added *N*,*N*-dimethylformamide dimethylacetal (5.79 g, 49.0 mmol) the reaction was heated to 150 °C for 16 hours. The solution was cooled to RT and distilled H_2O (20 mL) was added over 20 minutes until a yellow precipitate formed. This solid was collected by suction filtration and washed with distilled H_2O (20 mL). The product was further dried by high vacuum at 25 °C for 4 hours. The precipitate was then dissolved in EtOH (20 mL) and 35% aq. hydrazine (1.57 g, 49.0 mmol) added dropwise. The mixture was heated to 80 °C for 90 minutes after which the solvent was removed by rotary evaporation. The crude product was then re-dissolved in EtOAc (20 mL) and washed with distilled H_2O (3 x 20 mL) and brine (20 mL). The organic layer was dried over $MgSO_4$ and the solvent removed *in vacuo*. The crude product was purified by CC (hexane/EtOAc; 1:2) giving **(32)** as a yellow solid (1.91 g, 32.0%). ^{1}H NMR δ 7.74 (dd, (J=8.5, 5.5 Hz), 2H, 2 x PhH), 7.61 (dd, (J=2.2, 0.9 Hz), 1H, **CH**=CH-NH), 7.14-7.06 (m, 2H, PhH), 6.58 (dd, (J=2.2, 0.9 Hz), 1H, **CH**-NH); ^{13}C NMR δ 163.89, 161.44, 127.61, 127.53, 115.79, 115.57, 102.57; *m/z* $[M]^+$

= 162.2, calcd. for $C_9H_7FN_2$: 162.1, HRMS $[M+H]^+$ = 163.0678, calcd. 163.0672; HPLC (method A), t_R = 8.1 minutes, 99% purity.

Synthesis of 3-(4-fluorophenyl)-pyrazole-1-carboxamide

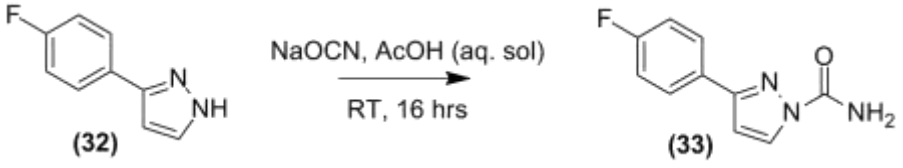

To a stirred solution of (**32**) (1.88 g, 14.0 mmol) in 90% aq. AcOH (15 mL) was added sodium cyanate (898 mg, 13.8 mmol) as an aq. suspension. The reaction mixture was stirred for 16 hours at RT. Distilled H_2O (20 mL) was added until a precipitate formed and the product collected by suction filtration. The crude product was purified by CC (EtOAc/hexane; 1:1) giving (**33**) as a pure cream solid (1.15 g, 45.9%). ^{1}H NMR δ 8.18 (d, (J=2.8 Hz), 1H, **CH**-N-C=O), 7.78-7.72 (m, 2H, PhH), 7.10-7.00 (m, 2H, PhH), 6.61 (d, (J=2.8 Hz), 1H, **CH**=CH=N), 5.54 (s, 1H, NH); ^{13}C NMR δ 164.52, 162.05, 153.51, 150.65, 130.15, 128.04, 127.96, 115.89, 115.67, 106.30; *m/z* $[M+Na]^+$ = 228.0, calcd. for $C_{10}H_8FN_3ONa$: 205.1, HRMS 228.0558, calcd. 228.1824; HPLC (method B), t_R = 7.9 minutes, > 95% purity.

Synthesis of 3-(4-((4-nitrophenyl)sulfonyl)phenyl)-pyrazole

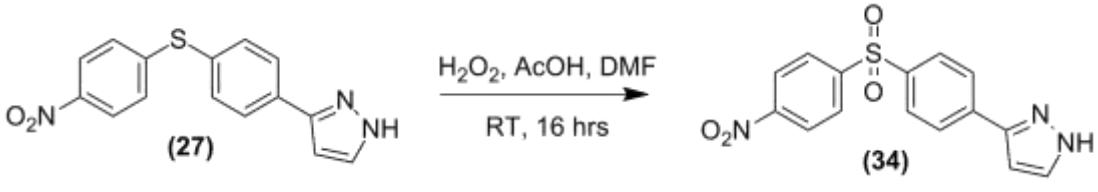

To a solution of **(27)** (120 mg, 427 µmol) in AcOH (5 mL) was added hydrogen peroxide (30% aq. solution) (435 µL, 12.8 mmol) in DMF (2 mL). The reaction was stirred for 16 hours at RT. The reaction was then diluted with distilled H_2O (10 mL) giving a yellow precipitate which was collected by suction filtration and dried on a high vacuum line. The product required no further purification yielding **(34)** as a yellow solid (99 mg, 70.5%). ^{1}H NMR δ 8.32 (dd, (J=2.0, 2.0 Hz), 2H, PhH), 8.12 (dd, 2H, PhH), 7.97 (m, 4H, PhH), 7.63 (d, (J=2.4 Hz), 1H, **CH**=CH-NH), 6.68 (d, (J=2.4 Hz), 1H, **CH**-NH); ^{13}C NMR δ 154.46, 151.45, 150.25, 146.55, 146.47, 145.95, 140.54, 128.91, 128.49, 126.15, 125.00; *m/z* $[M+H]^+$ = 330.1, calcd. for $C_{15}H_{12}N_3O_4S$: 330.1, HRMS 330.0530, calcd. 330.3383; IR 3426.0, 1640.2, 1521.2, 1410.6, 1347.5, 1304.0, 1155.8, 1069.7; HPLC (method B), t_R = 9.2 minutes, > 95% purity.

Synthesis of 3-(4-((4-nitrophenyl)sulfinyl)phenyl)-pyrazole-1-carboxamide

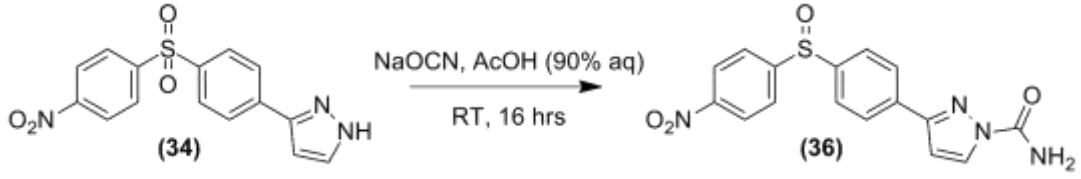

To a solution of **(34)** (99 mg, 301 µmol) in AcOH (90% aq. solution) (5 mL) was added NaOCN as an aq. solution (500 µL) and stirred at RT for 5 hours. A white precipitate formed which was collected by suction filtration and dried *in vacuo*. The residue was purified *via* CC (EtOAc/hexane; 2:1) to give **(36)** as a yellow solid (16 mg, 14.9%).^{1}H NMR δ 8.33-8.21 (m, 5H, PhH+ **CH**-N-C=O), 8.11-8.05 (m, 2H, PhH), 7.99-7.94 (m, 2H, PhH), 6.73 (d (J=3.0 Hz), 1H, **CH**=CH-N); ^{13}C NMR δ 168.35, 152.02, 149.41, 146.30, 138.98, 136.61, 128.89, 127.96, 127.61, 126.60, 123.55, 106.62; IR 2852.1, 1741.9, 1602.25, 1532.0, 1423.9, 1338.9, 1306.1, 1254.2, 1012.20 cm^{-1}; HPLC (method A), t_R = 12.0 minutes, purity <95%.

Synthesis of 3-(4-((4-fluorophenyl)sulfinyl)phenyl)-pyrazole

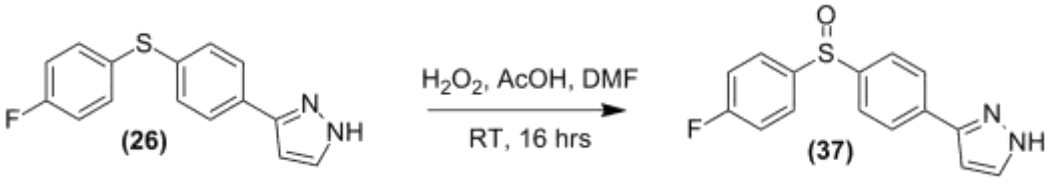

To a solution of **(26)** (239 mg, 884 µmol) in AcOH (5 mL) was added hydrogen peroxide (30% aq. solution) (30.1 µL, 884 µmol) in DMF (2 mL). The reaction was stirred for 16 hours at RT. The reaction was then quenched with distilled H_2O (5 mL) until a pale cream precipitate formed which was extracted into EtOAc (3 x 5 mL). The organic layer was dried over $MgSO_4$ and the solvent removed *in vacuo*. The crude product was purified by CC (hexane/EtOAc; 2:1) giving **(37)** as a yellow solid (93 mg, 36.7%). ^{1}H NMR δ 7.90 (m, 2H, PhH), 7.68-7.60 (m, 4H, PhH), 7.57 (dd, 1H,(J=2.6, 1.3 Hz), **CH**=CH-NH), 7.17-7.10 (m, 2H, PhH), 6.60 (dd, (J=2.8, 1.2 Hz), 1H, **CH**-NH); ^{13}C NMR δ 165.85, 163.42, 149.04, 144.33, 141.17, 136.30, 127.74, 127.65, 127.02, 125.66, 117.22, 116.99, 103.20; *m/z* $[M+H]^+$ = HRMS 287.0642, calcd. for $C_{15}H_{12}FN_2OS$: 287.3326; IR 3208.4, 1590.0, 1407.3, 1402.4, 1362.2, 1339.8, 1290.7, 1228.1, 1152.2, 1040.5, 924.4; HPLC (method B), t_R = 7.4 minutes, >95% purity.

Synthesis of 1-fluoro-2-tosyloxyethane[137]

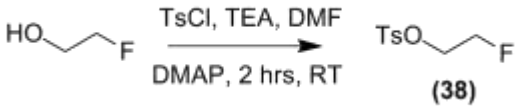

To a solution of 4-fluoroethanol (60.0 mg, 940 µmol) in anhy. DCM (2 mL) was added *p*-toluenesulphonyl chloride (270 mg, 1.41 mmol), triethylamine (200 µl, 1.41 mmol) and a catalytic amount of DMAP (13.0 mg, 110 µmol). The reaction mixture was stirred for 2 hours at RT. The mixture was then partitioned between 1M aq. HCl (10 mL) and DCM (20 mL). The organic layer was then washed with sat. aq. K_2CO_3 solution (10 mL), dried over $MgSO_4$, filtered and evaporated to dryness. The residue was purified by CC (hexane/EtOAc; 9:1) to give pure **(38)** as a colourless oil (200 mg, 98%). ^{1}H NMR δ 7.85 (d, (J=8.0 Hz), 2H, PhH), 7.38 (d, (J=8Hz), 2H, PhH), 4.66 (dt, (J=4.0, 4.0 Hz), **CH**-C-F), 4.54 (dt, (J=4.0, 4.0 Hz), **CH**-C-F), 4.33 (dt, (J=4.0, 4.0 Hz), **CH**-CH_2-F), 4.27 (dt, (J=4.0, 4.0 Hz), **CH**-CH_2-F), 2.45 (s, 3H, CH_3);^{13}C NMR δ 145.12, 132.74, 129.92, 127.98, 68.50, 68.29, 21.65; *m/z* $[M+Na]^+$ = 240.9, calcd. for $C_9H_{11}FO_3SNa$: 241.0, HRMS = 241.0300, calcd. 241.2321; HPLC t_R = (method A), 7.6 minutes, purity > 95%.

Synthesis of 3-(4-(2,4-difluorophenoxy)phenyl)-1-(2-fluoroethyl)-pyrazole

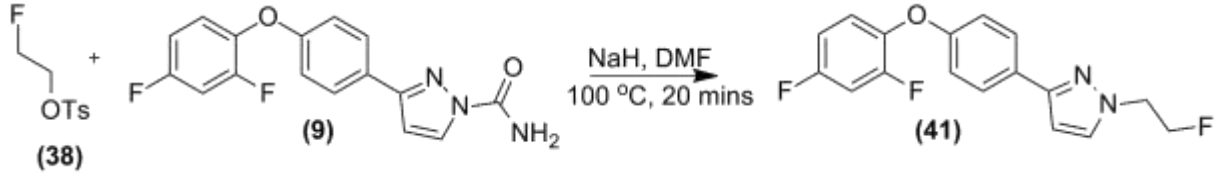

To a stirred solution of **(9)** (30.0 mg, 95.0 µmol) in DMF (3 ml) was added NaH (60% dispersion in mineral oil, 7.00 mg, 290 µmol) portion wise at RT. After ten minutes, a solution of **(38)** (14.0 mg, 67.0 µmol) in DMF (500 µL) was added to the reaction which was heated to 100 °C for 60 minutes. The reaction was then quenched with distilled H_2O (5 mL) and extracted into EtOAc (2 x 5 mL), dried with $MgSO_4$ and the solvent removed *in vacuo*. The crude mixture was then purified by preparative HPLC (method C), t_R =16.7 minutes. The product was extracted into EtOAc (3 x 5.00 ml) and dried with Na_2SO_4 giving **(41)** as a clear oil in (3.00 mg, 14.2%) yield, isomeric purity > 95%. ^{1}H NMR δ 7.69 (m, 2H, PhH), 7.41 (d, (J=2.4 Hz), 1H, CH-N), 7.00 (td, (J=5.5, 3.5 Hz), 1H, PhH), 6.92-6.85 (m, 3H, PhH), 6.81-6.75 (m, 1H, PhH), 6.44 (d,(J=2.4 Hz) 1H, **CH**=CH-N), 4.78 (t,(J=4.7 Hz), 1H, CH-F) 4.67 (t, (J=4.7 Hz), 1H, CH-F), 4.40 (t, (J=4.7 Hz), 1H, **CH**-CH_2-F), 4.33 (t, J=4.7 Hz), 1H, **CH**-CH_2-F); ^{13}C NMR δ 154.70, 152.75, 137.52, 131.60, 127.16, 122.47, 117.29, 111.37, 105.69, 103.22, 101.68, 82.81, 81.11, 52.64, 52.43; *m/z* $[M+H]^+$ =

319.3, calcd. for $C_{17}H_{14}F_3N_2O$: 319.1, HRMS = 319.1048, calcd. 319.3074; HPLC (method D), t_R = 11.9 minutes, >95% purity.

Synthesis of fluoroethylazide[137]

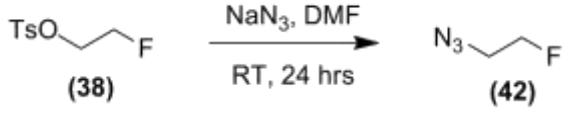

To a solution of **(38)** (200 mg, 2.25 mmol) in anhy. DMF (5 mL) was added sodium azide (439 mg, 6.75 mmol) under N_2 and the reaction was stirred at RT for 24 hours. Solid sodium tosylate was filtered off and **(42)** was isolated as a pale yellow oil as a DMF solution (0.23 M). Please note: **(42)** was not isolated as it is volatile and potentially explosive.

Synthesis of 4-(4-ethynylphenoxy)-1,2-difluorobenzene

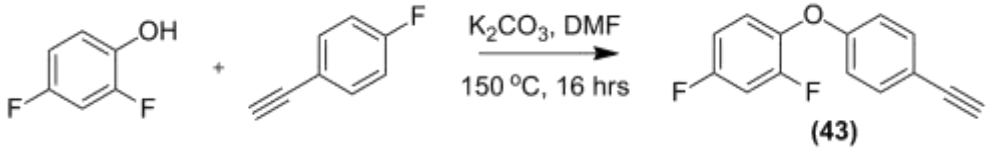

To a solution of 2,4 difluorophenol (595 mg, 4.58 mmol) in DMF (10 mL) was added potassium carbonate (518 mg, 3.75 mmol), shortly after, 1-ethynyl-4-fluorobenzene (500 mg, 4.17 mmol) was added and the solution was heated to 150 °C for 16 hours. The reaction was cooled to RT and diluted with DCM (20 mL). The organic layer was washed with 2M NaOH (2 x 20 mL) and brine (2 x 20 mL). The organic layer was dried over $MgSO_4$ and the solvent removed *in vacuo*. The crude mixture was purified by CC (hexane/DCM; 3:1) giving **(43)** as a white solid (117 mg, 12.0 %). ^{1}H NMR δ 7.36 (d, (J=9 Hz), 1H, PhH), 6.83-6.76 (m, 2H, PhH), 6.56-6.50 (m, 4H, PhH), 2.95 (s, 1H, CH); ^{13}C NMR δ 158.90, 156.49, 141.45, 141.33, 136.58, 136.55, 132.75, 115.72, 115.63, 115.31, 109.06, 108. 83, 103.39, 103.12; *m/z* $[M-F]^+$ = 212.0, calcd. for $C_{14}H_8FO$: 212.06; HPLC (method A), t_R = 13.8 minutes, 90% purity.

Synthesis of 4-(4-(2,4-difluorophenoxy)phenyl)-1-(2-fluoroethyl)-1,2,3-triazole

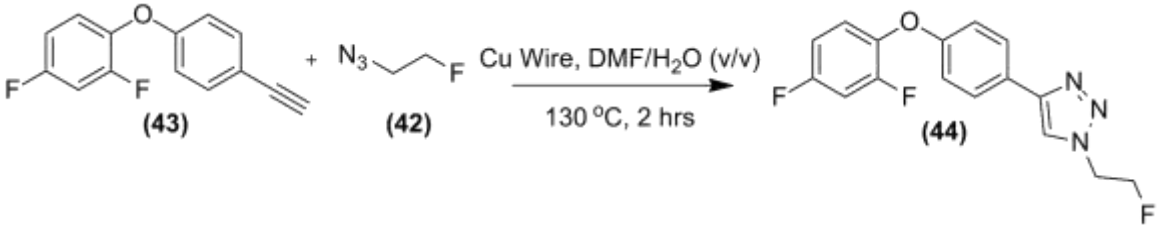

To a charged Wheaton vial containing copper wire (diameter 0.250 mm, 100 turnings) was added **(43)** (20.0 mg, 87.0 µmol) as a DMF/H_2O solution (1/1; 400 µL). To this was added **(42)** (380 µL,) as a 0.350 M solution in DMF. The reaction suspension was stirred for 2 hours at 130 °C. The reaction was then diluted with distilled H_2O (100 µL) and MeCN (500 µL) and the crude solution was purified by preparative HPLC (method E), t_R = 12.2 minutes The product was collected using a manual switch giving **(44)** in (6.60 mg, 24.0%) yield. ^{1}H NMR δ 7.75 (t, (J=1.1 Hz), 1H, CH-N), 7.71 (dq, (J=8.9, 1.1 Hz), 2H, PhH), 7.07-6.98 (m, 1H, PhH), 6.95-6.85 (m, 3H, PhH) 6.80 (dddd, (J=6.1, 3.5, 1.2 Hz), 1H, PhH), 4.82 (ddd, (J=6.1, 3.5, 1.2 Hz), 1H, CH-F), 4.69 (ddt, (J=9.2, 5.5, 3.7 Hz), 2H, CH-F + **CH**-CH_2-F), 4.63-4.57 (m, 1H, **CH**-CH_2-F); ^{13}C NMR δ 157.69, 147.65, 127.29, 125.56, 123.03, 122.93, 117.04, 111.57, 111.34, 105.79, 105.55, 105.53, 81.65, 50.63; *m/z* $[M+H]^+$ = 320.3, cald. for $C_{16}H_{13}F_3N_3O$: 320.1, HRMS 320.1027, calcd. 320.2955; CHN C 58.77%, H 3.73%, 12.79%, calcd. C 60.19% H 3.79%, N 13.16%; HPLC (method A), t_R = 11.1 minutes, purity >95%.

Synthesis of 2-azidoethanol

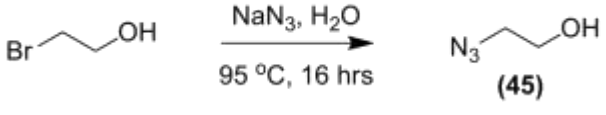

To a solution of bromoethanol (2.00 g, 16.0 mmol) in distilled H_2O (30 mL) was added NaN_3 (1.25 g, 19.2 mmol) and the solution was heated to 95 °C for 16 hours. The reaction was cooled to RT and diluted with DCM (20 mL). The organic layer was washed with distilled H_2O (2 x 20 mL) prior to drying over $MgSO_4$ and the solvent removed *in vacuo*. The product was not isolated as it is volatile and potentially explosive, therefore **(45)** was used as a crude product in the following step.

Synthesis of 2-azidoethyl 4-methylbenzenesulfonate

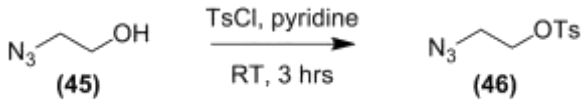

A solution of **(45)** (1.39 g, 16 mmol) in pyridine (1.94 mL) was cooled to 0 °C prior to addition of TsCl (4.57 g, 24 mmol). The solution was then warmed to RT and reaction was stirred for 3 hours before re-cooling to 0 °C. The reaction was diluted with ether (20 mL) prior to neutralising with aq. 2M HCl (5 mL). The product was extracted into ether (2 x 20 mL), dried over $MgSO_4$ and the solvent removed *in vacuo*. The crude mixture was purified by CC (ether/EtOAc; 5:1) giving **(46)** as a yellow oil (3.474 g, 90%). ^{1}H NMR δ 7.73 (d, (J=8 Hz), 2H, PhH), 7.33 (d, (J=8 Hz), 2H, PhH), 4.12 (t, (J=5 Hz), 2H, CH_2-O), 3.45 (t, (J=5 Hz), 2H, CH_2-N), 2.36 (s, 3H, CH_3); ^{13}C NMR δ 145.47, 132.41, 130.13, 127.97, 68.54, 49.59, 21.73; *m/z* $[M]^+$ = 241.00, calcd. for $C_9H_{11}N_3O_3S$: 241.05; HPLC (method A), t_R = 6.7 minutes, 90% purity.

Synthesis of 2-(4-(4-(2,4-difluorophenoxy)phenyl)-1,2,3-triazol-1-yl)ethyl-4-methylbenzene-sulfonate

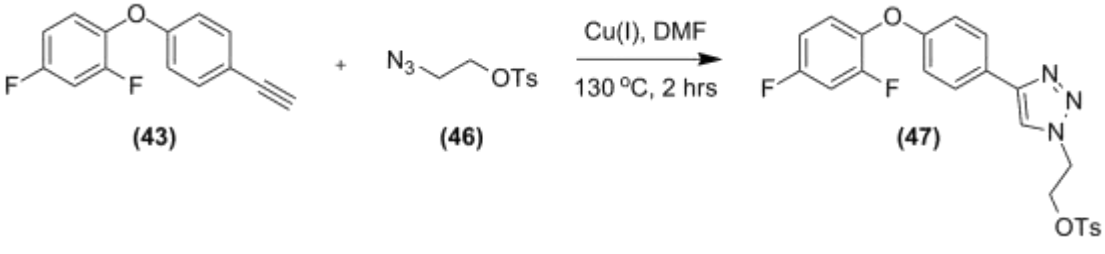

To a charged Wheaton vial containing copper wire (diameter 0.250 mm, 100 turnings) was added **(43)** (25.0 mg, 105 µmol) as a DMF/H_2O solution (1/1; 400 µL) and **(46)** (25 mg). The reaction suspension was stirred for 2 hours at 130 °C. The reaction was then diluted with distilled H_2O (100 µL) and MeCN (500 µL) and the crude solution was purified by preparative HPLC (method K), t_R = 22.5 minutes The product was collected using a manual switch giving **(47)** in (3 mg, 13.5%) yield. *m/z* $[M+H]^+$ = 472.19, calcd. for $C_{23}H_{19}F_2N_3O_4S$: 471.11; HPLC (method A), t_R = 12.5 minutes, 95% purity.

2.2 Radiochemistry

General procedure for manual drying of [^{18}F]fluoride

[^{18}F] fluoride (aq.) was dispensed into a Wheaton vial containing potassium carbonate (1M, 13.0 µmol), Kryptofix (10.0 mg, 30.0 µmol) and anhy. acetonitrile (1 mL). The mixture was azeotropically dried at 110 °C under a stream of nitrogen (0.4 mL/min). Two subsequent portions of anhy. acetonitrile (500 µL) were added and sequentially dried to give no-carrier-added [^{18}F]fluoride/Kryptofix®2.2.2./carbonate-complex as a white semi-solid residue.

Radiochemical yields

Radiochemical yields are all isolated non-decay corrected (n.d.c) values, calculated either from [^{18}F]fluoride or from a previous step (as indicated). Where yields are not given due to a product not being isolated, these reactions are measured as percent radiochemical purity using analytical HPLC.

Synthesis of ((4-^{18}F)fluorophenyl)(4-(trifluoromethyl)phenyl)methanone

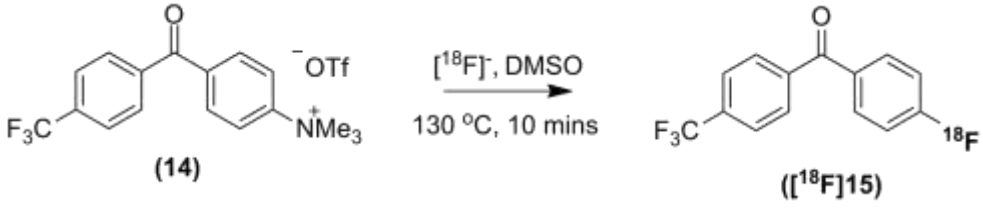

[^{18}F]Fluoride (aq.) (330-370 MBq) was dried as according to the general procedure and the vial cooled to RT. A solution of (**14**) (2.0 mg) in DMSO (200 µL) was added and stirred at 130 °C for 10 minutes before diluting with distilled H_2O (1.50 mL). The product was purified by trapping to a ^{t}C18 light Sep-pak cartridge pre-conditioned with EtOH (1 mL) and distilled H_2O (3 mL). The cartridge was dried over a stream of nitrogen for 15 minutes and the product was eluted off the cartridge with MeCN (100 µL) to afford **([^{18}F]15)** (132-167 MBq, 40-45% n.d.c. radiochemical yield in 70 minutes from [^{18}F]fluoride, n = 12). Analytical HPLC: (method A), t_R = 12.5 minutes, RCP > 99%.

Synthesis of (1-^{18}F)fluoro-4-bromobenzene

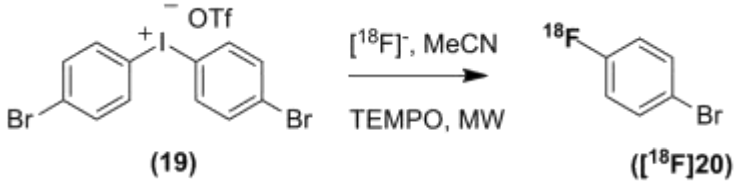

[^{18}F]Fluoride (aq.) (330-370 MBq) was dried as according to the general procedure and the vial cooled to RT. A solution of (**19**) (22.0 mg, 90.0 mmol) in DMF (200 µL) was added followed by a solution of TEMPO (10.0 mg, 60.0 µmol) in DMF (200 µL). The reaction was heated under microwave irradiation at 90 °C, 40 W for 30 secs. The reaction was diluted with distilled H_2O (300 µL) and MeCN (300 µL) prior to purification by semi-preparative HPLC, (method E), t_R = 10.2 minutes. The product was collected *via* a manual switch and diluted with distilled H_2O to a total volume of 20 mL, prior to loading to a ^{t}C18 light Sep-pak cartridge pre-conditioned with NMP (1 mL) and distilled H_2O (3 mL). The cartridge was dried over a stream of nitrogen for 20 minutes. The product was eluted off the cartridge with NMP (1 mL) to afford **([^{18}F]20)** (50-93 MBq, 15-25% n.d.c. radiochemical yield in 75 minutes from [^{18}F]fluoride, n = 19). Analytical HPLC: (method F), t_R = 10.2 minutes, RCP >99%.

Synthesis of 3-(4-((4-^{18}F)fluorophenyl))sulfinyl)phenyl)-1H-pyrazole

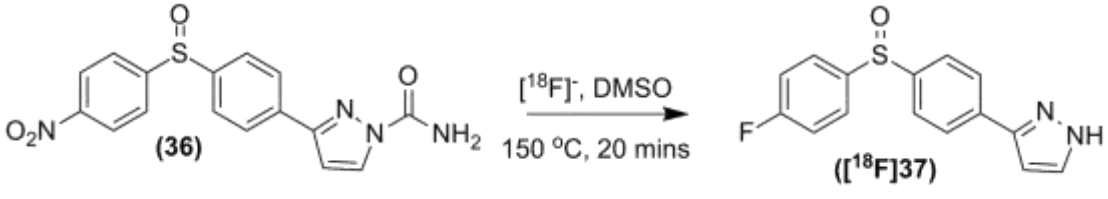

[^{18}F]Fluoride (aq.) (80-100 MBq) was dried as according to the general procedure and the vial cooled to RT. A solution of (**36**) (2.00 mg) in DMSO (200 µL) was added and the reaction was stirred at 150 °C for 20 minutes. The reaction was purified by semi-preparative HPLC: (method G), t_R = 14.8 minutes and the product isolated *via* manual switch to afford **([^{18}F]37) (**0.8-1 MBq, 1.0% n.d.c. radiochemical yield in 80 minutes from [^{18}F]fluoride). Analytical HPLC: (method B), t_R = 7.1 minutes, RCP > 99%.

Synthesis of (1-^{18}F)fluoroethyl tosylate

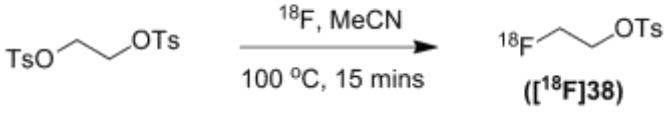

([^{18}F]38)

Manual: [^{18}F]Fluoride (aq.) (300-400 MBq) was dried as according to the general procedure and the vial cooled, to this was added a solution of ethyl ditosylate (5.00 mg, 100 µmol) in MeCN (500 µL). The reaction was stirred at 100 °C for 15 minutes. The reaction was then diluted with distilled H_2O (1.50 mL) and purified by semi-preparative HPLC: (method D), t_R = 13.2 minutes. The product was collected using a manual switch, diluted with distilled H_2O to a total volume of 20 mL, and loaded on to a ^{t}C18 light Sep-pak cartridge, pre-conditioned with DMF (1 mL) and H_2O (3 mL). The cartridge was dried over a stream of nitrogen for 15 minutes. The product was eluted off the cartridge with DMF (60.0 µL) to afford **([^{18}F]38)** (120-160 MBq, 30-40% n.d.c. radiochemical yield in 70 minutes from [^{18}F]fluoride, n = 13). Analytical HPLC: (method H), t_R = 11.0 minutes, RCP > 99%.

Automated synthesis via Tracerlab™ FX-N: [^{18}F]Fluoride (aq.) (2-4 GBq) was dried azeotropically in the reaction vessel using the same method as described in the general procedure section using the set-up as shown in Figure 2.1. To the dried [^{18}F]fluoride was added ethylene ditosylate (5.00 mg, 100 µmol) in MeCN (500 µL) through the manifold and the reaction was heated to 100 °C for 10 minutes before purifying *via* semi-preparative HPLC, (method I), t_R = 9.8 minutes. The product was collected *via* a manual switch and diluted with distilled H_2O to total volume of 20 mL and loaded on to a ^{t}C18 light Sep-pak cartridge, pre-conditioned with DMF (1 mL) and distilled H_2O (3 mL). The cartridge was dried over a stream of nitrogen for 15 minutes. The product was eluted off the cartridge with DMF (60 µL) to afford **([^{18}F]38)** (0.6 – 1.2 GBq, 20-30% n.d.c. radiochemical yield in 70 minutes from [^{18}F]fluoride, n=6). Analytical HPLC: (method H), t_R = 11.0 minutes, RCP > 99%.

Figure 2.1:GE Healthcare Tracerlab™ set-up for [^{18}F]fluoroethyl tosylate synthesis

Synthesis of 3-(4-(2,4-difluorophenoxy)phenyl)-1-(2-^{18}F)fluoroethyl))-pyrazole

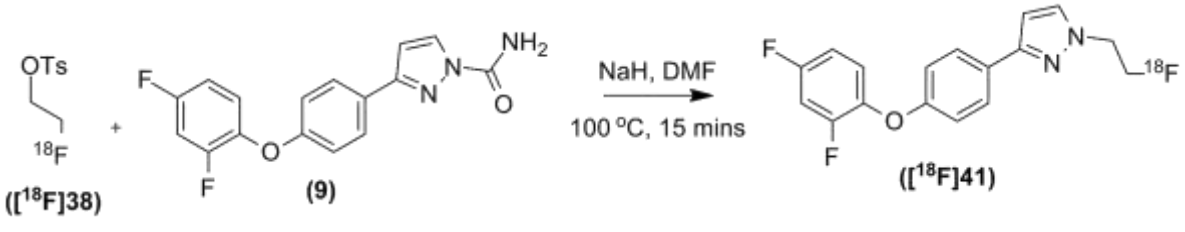

A solution of **(9)** (2.00 mg, 6.35 µmol) in anhy. DMF (100 µL) was added to a Wheaton vial followed by addition of NaH (60% dispersion in mineral oil, 1.50 mg, 62.5 µmol) at RT and stirred for 10 minutes. **([^{18}F]38) (**400 MBq**)** in DMF (approx. 300 µL) was added dropwise to the vial and subsequently heated at 100 °C for 15 minutes. The reaction was diluted with distilled H_2O (1.50 mL) and purified by reverse phase semi-preparative HPLC: (method J), t_R = 9.80 minutes. The product was collected using a manual switch, diluted with distilled H_2O to a total volume of 20 mL, and loaded on to a ^{t}C18 light Sep-pak cartridge, pre-conditioned with EtOH (1 mL) and distilled H_2O (3 mL). The cartridge was dried over a stream of nitrogen for 15 minutes. The product was eluted off the cartridge with EtOH (approx. 100 µL) to afford **([^{18}F]41)** (120 – 140 MBq, 30-35% n.d.c. radiochemical yield in 70 minutes from **([^{18}F]38)**, n = 8). Analytical HPLC: (method D), t_R = 9.8 minutes, >99% RCP. Specific activity: 3.48 GBq/µmol.

Synthesis of (1-^{18}F)fluoroethylazide

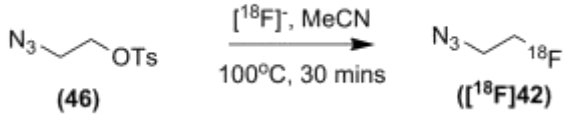

Automated synthesis via FASTlab™ module: [^{18}F]Fluoride (1-1.5 GBq) in [^{18}O]H_2O (0.1-1 mL) was trapped on to a QMA cartridge and eluted using a solution of Kryptofix 2.2.2 (10.0 mg, 27.0 µmol) and potassium hydrogencarbonate (5.00 mg, 60.0 µmol), in distilled H_2O (500 µL) and MeCN (1 mL) (Figure 2.2). [^{18}F]fluoride was then dried in the reaction vessel at 100 °C for 15 minutes. **(46)** (15.0 µL) in MeCN (2 mL) was added to the reactor through the central line and heated to 100 °C for 30 minutes. As the reaction progressed, the product was distilled from the cassette manifold to an external vial charged with DMF (100 µL) to trap **([^{18}F]42)** (300-450 MBq, 20-30% n.d.c. radiochemical yield in 60 minutes from [^{18}F]fluoride, n = 10). Analytical HPLC: (method A), t_R = 6.3 minutes, RCP >99%.

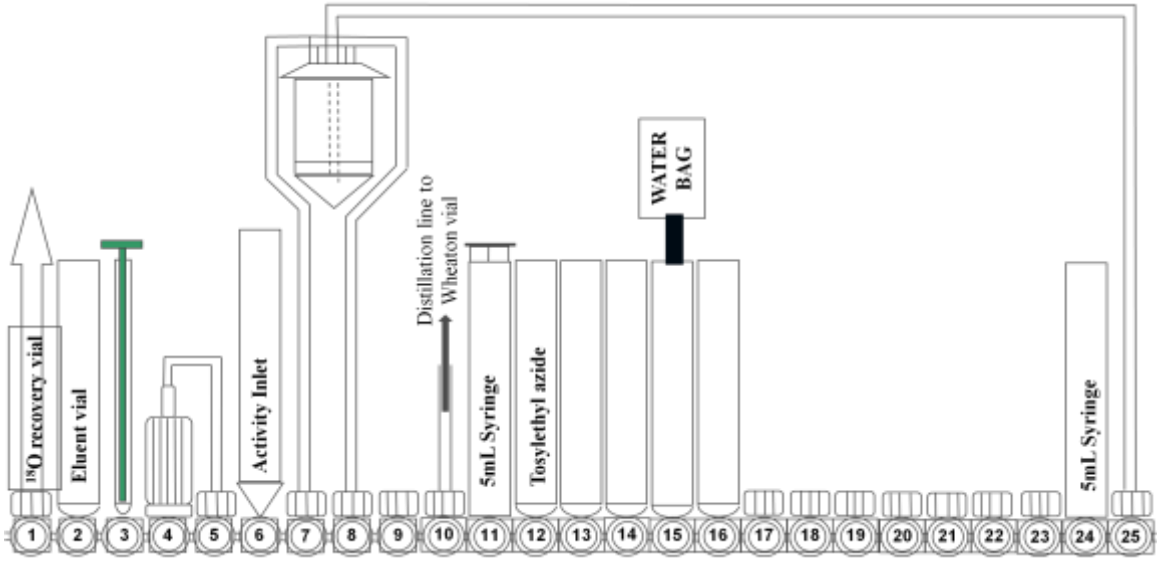

Figure 2.2: A prepared GE Healthcare FASTlab™ cassette set-up for synthesising [^{18}F]fluoroethyl azide

Synthesis of 4-(4-(2,4-difluorophenoxy)phenyl)-1-((2-^{18}F)fluoroethyl)-1,2,3-triazole

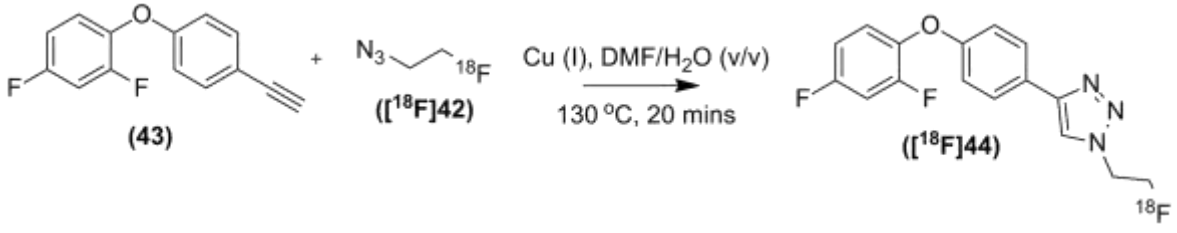

To a Wheaton vial was added distilled H_2O (100 µL) followed by copper (II) sulphate (4 eq.), sodium L-ascorbate (4.4 eq) and bathophenanthrolinedisulphonic acid disodium salt (4.4 eq.). The vial was purged with N_2 for 2 minutes prior to addition of **(43)** (2 eq.) in DMF (50 µL) followed by further N_2 purging for 2 minutes. A solution of **([^{18}F]42)** in MeCN (300-400 MBq, 200-300 µL) was added and the reaction proceeded at 130 °C for 15 minutes. The reaction was then cooled to RT and diluted with distilled H_2O (1.50 mL) before purification by semi-preparative HPLC: (method K), t_R = 23.4 minutes. The HPLC fraction was then collected *via* a manual switch and diluted with distilled H_2O to a total volume of 20 mL and loaded onto a ^{t}C18 light Sep-pak, which was subsequently dried over a stream of N_2 and the product eluted with EtOH (100 µL) affording formulated **([^{18}F]44)** (90-160 MBq, 30-40% n.d.c. radiochemical yield in 60 minutes from **([^{18}F]42)**. Overall **([^{18}F]44)** was achieved in 10% n.d.c. e.o.s. radiochemical yield from [^{18}F]fluoride (n=7) in 110 minutes with specific activity 0.2-16 GBq/µmol. Analytical HPLC: (method A), t_R = 11.3 minutes, RCP >99%.

2.3 Log P determination

The octanol/H_2O partition coefficients were determined using the shake flask method. Both solvents were presaturated with each other by shaking together for 5 minutes. To a solution of 0.5 mL of both octanol and distilled H_2O was added 1.0 mg of test compound. The mixture was shaken in a rotamixer for 5 minutes. After reaching equilibrium, the mixtures were centrifuged (5 minutes at 10,000 rpm) to achieve good separation. Samples from each layer (25 µL) were taken and dissolved in 25 µL of MeCN. Analytical HPLC of both the aqueous and octanol layers was performed to measure the UV absorbance region of interest (ROI). The absorbance was correlated to a calibration curve of known concentrations. Two further samples were prepared of the same concentration, and all samples analysed by analytical HPLC. Log P was calculated according to the formula:

$$\log P = \log (\text{ROI in octanol layer} / \text{ROI in } H_2O \text{ layer})$$

2.4 *In vitro* biology

2.4.0 Sharp intracellular microelectrode electrophysiology

Preparation and storage of brain slices.

Experiments were carried out using transverse, rostro-caudal slices of olfactory (piriform) cortex (450 µm thick; 6–10 slices per animal) prepared from adult male Wistar rats (150–200 g; either sex). Animals were sacrificed in accordance with the UK Animals (Scientific Procedures) Act 1986 by overdose with inhaled isoflurane, decapitated, hemisected and placed into ice-cold (4 °C) oxygenated Krebs' solution. Serial slices were then sectioned using a Campden Vibroslice/ tissue cutter (Campden Instruments, U.K.), and stored in oxygenated Krebs solution at 30 °C for at least 30 minutes, before transferring to a Perspex recording chamber, where they were superfused continuously (held completely submerged) at ~ 10 mL/min with pre-warmed oxygenated Krebs solution at 29–30 °C. The composition of the normal Krebs solution was (in mM): NaCl 118, KCl 3, $CaCl_2$ 1.5, $NaHCO_3$ 25, $MgCl_2$ 6, H_2O 1, NaH_2PO_4 2, H_2O 1.25 and D-glucose 11 (bubbled with 95% O_2 – 5% CO2, pH 7.4). [138]

Intracellular recording

Intracellular current-clamp recordings were made from the CA1 region of the hippocampus or periamygdaloid area of the piriform cortex slices within the piriform cortical cell layers II–III, using glass microelectrodes filled with 4M potassium acetate (tip resistances 60–80 MΩ) coupled to an Axoclamp 2B sample-and-hold preamplifier (2–3 kHz switching frequency, 50% duty cycle; Axon Instruments,CA, U.S.A.). Membrane input resistance and firing behaviour were assessed by injecting positive or negative current pulses of varying intensities (~ 0.25–3 nA; 160 ms), and the resulting electrotonic potentials or evoked action potentials recorded, respectively. First spike amplitudes were always measured (from baseline level) under 'bridge' recording mode to avoid sampling limitations of the discontinuous sample-and-hold preamplifier. In all experiments, the membrane potential was usually maintained at –70 mV (near firing threshold) by applying a steady depolarising current. The steady voltage level recorded at the soma following current step commands were always used to construct current–voltage (I–V) curves. Acceptable recordings

typically remained stable for periods of 1–5 hours. Sampled membrane voltage signals were monitored on a storage oscilloscope and a Gould TA240 Easygraf 2 channel chart recorder and also fed directly to a computer (Viglen Ltd, U.K.) *via* a Digidata 1322A analogue-to digital interface (Axon Instruments, CA, U.S.A.), using pCLAMP 10 software (Axon Instruments) for hard disk recording and off-line analysis. All measurements were made before, during and after bath superfusion (bath-exchange time 30 seconds) of pharmacological agents, so that each neurone served as its own control. Unless otherwise stated, each experimental sequence described below was repeated at least twice on different cells. Data are expressed as means ± s.e.m.

Compound applications

Research compounds were prepared as a 10 mM stock solution in either DMSO or EtOH, and were stored for up to 4 weeks at 4 °C without apparent loss of activity (analytical HPLC tested for decomposition). Compound solutions were subsequently diluted in Krebs solution immediately before use; the final bath concentrations of DMSO (up to 0.5%) or ethanol (0.1%) had no deleterious effects on membrane properties. The results presented in this thesis are based on recordings obtained from both pyramidal and cortical neurones in the hippocampus and piriform cortex respectively.

Data analysis

Electrophysiological traces of all recordings are reported to allow a qualitative report of the spike inhibition effects of each research compound at differing concentrations in each brain slice preparation.

2.4.1 Automated patch-clamp electrophysiology

Cell culture

Chinese hamster ovary (CHO) cells were stably transfected with specific Na^+ ion channel subtype cDNAs. Cells were cultured in Ham's F-12 supplemented with 10% fetal bovine serum, 100 U/mL penicillin G sodium, 100 μg/mL streptomycin sulphate, and the appropriate selection antibiotics. Before testing the cells, culture dishes were washed twice with Hank's Balanced Salt

Solution and treated with accutase for approximately 20 minutes. Immediately before use in the IonWorks Quattro™ system, the cells were washed with HB-PS to remove the accutase and re-suspended in approximately 3 mL of HB-PS.

Formulation of test articles

Chemicals used in solution preparation were purchased from Sigma-Aldrich (St. Louis, MO) unless otherwise noted and were of ACS reagent grade purity or higher. Stock solutions of test articles and the positive control (lidocaine.HCl, 3 mM) were prepared in dimethyl sulfoxide (DMSO) at 10 mM and stored frozen, unless otherwise specified. Test article and positive control concentrations were prepared fresh daily by diluting stock solutions into a HEPES-buffered physiological saline (HB-PS) solution (composition in mM): 137 NaCl, 4.0 KCl, 1.8 $CaCl_2$, 1 $MgCl_2$, 10 HEPES, 10 Glucose, pH adjusted to 7.4 with NaOH, which was prepared weekly and refrigerated until use. Since previous results have shown that ≤ 0.3% DMSO and 0.05% pluronic F-127 do not affect sodium channel currents, all test and control solutions contained 0.3% DMSO and 0.05% F-127. The test article formulations were loaded in a glass-lined 384-well compound plate, and placed in the plate well of IonWorks Quattro™ (Molecular Devices Corporation, Union City CA).

Test article treatment

All experiments were performed at ambient temperature. Each test article (TA) concentration was applied to naïve cells ($n \geq 2$, where n = the number cells/concentration) *via* steel needles of a 48-channel pipettor. Each application consisted of addition of 6 µL of 2 x concentrated test article solution to the total 12 µL of final volume of the extracellular well of the Population Patch Clamp™ (PPC) planar electrode. The addition was followed by mixing (3 times) of the PPC well content. To prevent test article cross-contamination where necessary, the pipettor was washed with 0.1 M NaOH (3 cycles) and PBS (3 cycles). Duration of exposure to each test article concentration was at least five minutes to cells expressing specific ion channels ($n \geq 6$, where n = the number cells). To verify the sensitivity of the assay to block, the positive control was applied to cells for five minutes ($n \geq 2$, where n = the number cells).

Electrophysiology recordings

In preparation for a recording session, intracellular solution comprising of as mM: KCl 130, $MgCl_2$ 4, EGTA 0.5, HEPES 10 was loaded into the intracellular compartment of the PPC planar electrode. Cell suspensions were pipetted into the wells of the PPC planar electrode. After establishment of a whole-cell patch-clamp configuration, membrane currents were recorded using the patch clamp amplifier within the IonWorks Quattro™ system. Before digitisation, the current records were low-pass filtered at one-fifth of the sampling frequency. Block of each Na_v channel sub-type was measured using a stimulus voltage pattern shown in Figure 2.3 (voltage potentials are indicated in Table 2.2). The pulse pattern was repeated twice: before and 5 minutes after TA addition and peak current amplitudes at three test pulses was measured (ITP_1, ITP_{11} and ITP_{12} [or TP_{13} or TP_{14}]).

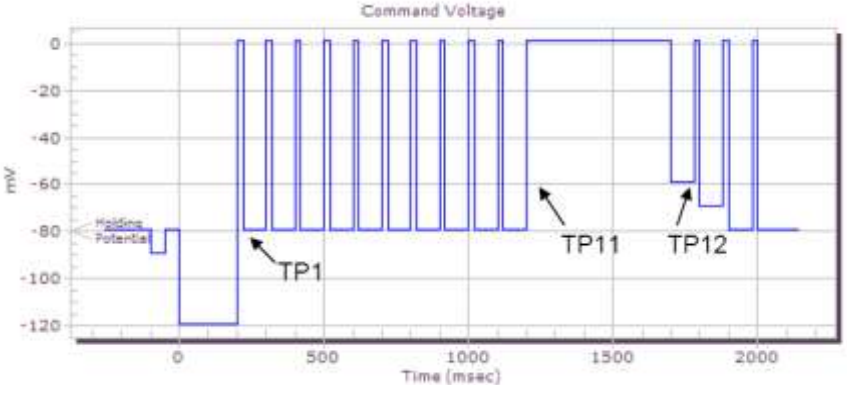

Figure 2.3: Voltage protocol Type I for $hNa_v1.x$ test procedure

Channel		Holding Potential (mV)	Pre-Pulse Potential (mV)	Test Pulse 1 - 10, 12-14 Duration (ms)	Test Pulse 11 Duration (ms)	Interpulse Duration (ms)	Test Pulse 1 -14 Potential (mV)
Nav1.1		-80	-120	20	500	80	0
Nav1.2		-80	-120	20	500	80	0
Nav1.3		-80	-120	20	500	80	0
Nav1.4		-80	-120	20	500	80	-10
Nav1.5		-80	-120	20	500	80	-10
Nav1.6		-80	-120	20	500	80	0
Nav1.7		-80	-120	20	500	80	0

Table 2.2: Voltage-protocol parameters for hNa_v 1.x channels

Data analysis

Data were stored on the ChanTest computer network (and backed-up nightly) for off-line analysis. Data acquisition and analyses were performed using the IonWorks Quattro™ system operation software (version 2.0.2; Molecular Devices Corporation, Union City, CA). Data were also corrected

for leak currents. The decrease in current amplitude after TA application was used to calculate the percent block relative to control.

The *tonic block* was calculated as:

% Block (Tonic) = (1 – ITP_1, TA / ITP_1, Control) x 100%,

where ITP_1, Control and ITP_1, TA are the inward peak Na^+ currents elicited by the TP_1 in control and in the presence of a test article, respectively.

The *frequency-dependent block* at stimulation frequency 10 Hz was calculated as:

% Block (10 Hz) = (1 – ITP_{11}, TA / ITP_{11}, Control)) x 100%,

where ITP_{11}, Control and ITP_{11}, TA are the inward peak Na^+ currents elicited by the TP_{11} in control and in the presence of a test article, respectively.

We define the *inactivation state block* as decrease in test pulse (TP_{12} [or TP_{13} or TP_{14}]*) current amplitude due to the conditioning depolarizing pulse (TP_{11}). The inactivation state block was calculated as:

% Block (inactivation state) = (1 – (ITP_{12}, TA / ITP_{12}, TA) x 100%,

where ITP_{12}, Control and ITP_{12}, TA are the inward peak Na^+ currents elicited by the TP_{12} in control and in the presence of a test article, respectively.

*TP_{13} or TP_{14} currents was analyzed instead of TP_{12} if insufficient current (<0.1 nA) at TP_{12}.

Concentration-response data for the blocks will be fit to an equation of the following form:

% Block = % VC + {(100 - % VC) - (100 -% VC) / [1 + ([Test] / IC_{50})N]},

where [Test] is the concentration of test article, IC_{50} is the concentration of the test article producing half-maximal inhibition, N is the Hill coefficient, % VC is the percentage of the current run-down (the mean current inhibition at the vehicle control) and % Block is the percentage of ion channel current inhibited at each concentration of the test article. Non-linear least squares fits was solved with the XL*fit* add-in for Excel 2003 (Microsoft, Redmond, WA).

2.4.2 Manual patch-clamp electrophysiology

Assay set-up

HEK-293 cells stably expressing Na_v 1.4 and 1.5 were cultured according to Scottish Biomedical standard operating system. They were plated onto 15 mm plastic dishes and incubated for 1-3 days in a 5% CO_2 incubator prior to cell perforated whole-cell patch clamp experiments. Cells were superfused at RT with a standard physiological solution containing (in mM) NaCl (140), KCl (4), CaCl (2), $MgCl_2$ (1), glucose (10), HEPES (10), pH 7.35 with NaOH. Patch pipettes were pulled from borosilicate glass and exhibited tip resistances of 2-5 MΩ when filled with the above solution. Internal (pipette) solution contained (in mM): NaCl (10), CsCl (50), CsF (60), $MgCl_2$ (2), EGTA (20), HEPES (10), (gramicidin) (0.1) pH 7.25 with CsOH, was used to study sodium channels without the interference of potassium currents.

Whole-cell patch clamp

Perforated patch-clamp technique (see Section 3.5.2) was carried out using an Axon 200B amplifier (Axon Instruments™) using the antibiotic gramicidin, to allow pore formation in the cell's membrane without rupturing the membrane, minimising cell's dialysis and allowing longer recording times (up to 60 minutes). The software program pClamp (version 10) was used to stimulate and record electrical activity using the two-pulse state-dependent protocol. A P/4 leak subtraction method was used for all experiments. Capacitative transients were compensated electronically from the recordings, however the voltage drop across the series resistance was generally less than 10 MΩ (n=76 cells), with a mean cell capacity of 30 ±5 pF. A two test pulse protocol was used to measure inhibition at rest and in an inactivated state (Figure 2.4). Starting from a holding potential of -90 mV, a test pulse was evoked for 10 ms pulses to 0 mV (P1; resting). Then, a 4 second pulse was applied to maintain the holding potential at -75 mV (P2; inactivation of channels). Prior to the assay, compounds were dissolved in 10 mM DMSO stock solution and then subsequently diluted in physiological solutions without exceeding 0.1% DMSO in the final solution of 0.1, 1, 10 and 30 µM. Perfusion of compounds only commenced when run-down of cells was <10% (within a 120 second control period for both P1 and P2). Cells with higher run-down were usually excluded from further analysis.

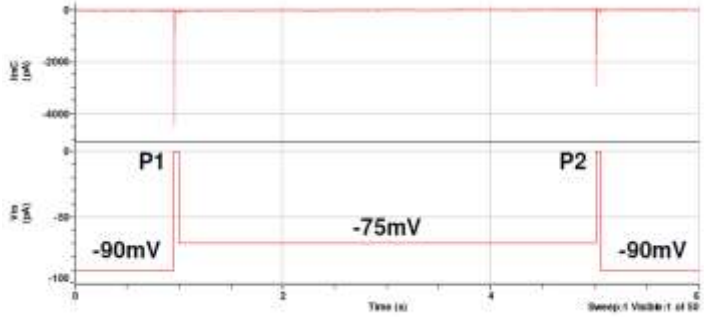

Figure 2.4: Two-pulse IV protocol to assay state-dependent inhibition of hNa$_V$ 1.5 and 1.4. Typical current traces evoked by 10 ms test pulses to 0 mV from a holding potential of –90 mV. The 2 pulse protocol is applied every 15 s. Peak 1 (P1) represents all channels available from the resting state, and Peak 2 (P2) evokes current after a 4 s prepulse to -75 mV, which inactivates ~50% of the channels.

Incubation time ranged from 2-5 minutes for control period, followed by 40 minutes incubation for each concentration. The effect of each compound on each channel was constantly monitored (for example, every 10 s), so that observation of steady-state inhibition was seen before experiment termination (40 minutes incubation time required).

Figure 2.5 shows an example of the hNa$_v$ 1.4 currents evoked by the I-V protocol as well as the average I-V curve and voltage-dependent parameters calculated from up to 6 cells. Inactivation and activation curves were always adequately fitted with single Boltzmann equations, indicating the presence of a single major sodium conductance. The rapid and complete inactivation of the currents were in line with published data. Currents begun to activate at -40 mV and typically reached a peak during test pulses to -10 mV, before reversing positive to +60 mV.

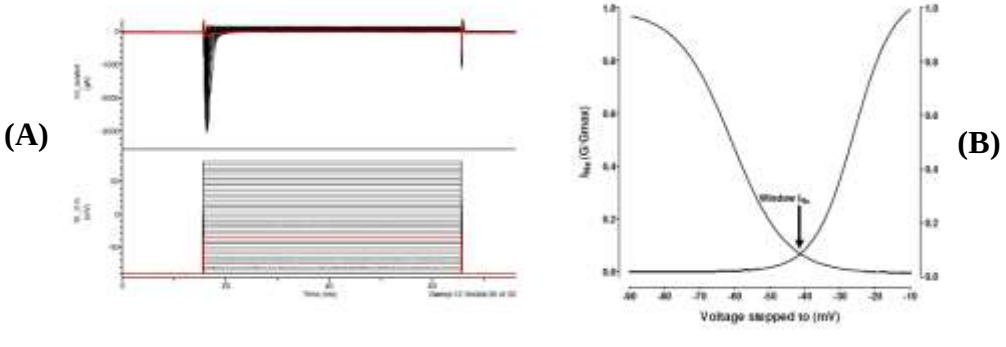

Figure 2.5: Voltage –dependent properties of hNa$_v$ 1.4 HEK-293 cell line. (A) example of current traces during an I-V protocol (50 ms test pulses from –90 mV in 10 mV increments). The -90 mV voltage pulse is highlighted by the red trace. (B): averaged activation and inactivation current data was used to plot the steady-state activation and inactivation curves, which are fit with single Boltzmann equations with values for Vh1/2 of -26±2 mV and V1/2 of -61±2 mV; slope factors were 6±2 and 8±2, respectively.

An example of the hNa_v 1.5 currents evoked by the I-V protocol is shown in Figure 2.6 below, as well as the average I-V curve and voltage dependent parameters calculated from up to 11 cells. Inactivation and activation curves were always adequately fitted with single Boltzmann equations, indicating the presence of a single major sodium conductance.

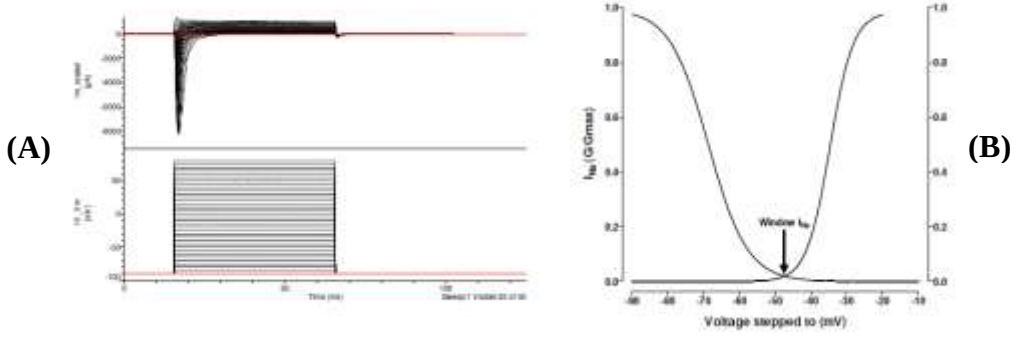

Figure 2.6: Voltage-dependent properties of hNa_V 1.5 HEK-293 cell line. (A) example of current traces during an I-V protocol (50 ms test pulses from –90 mV in 10 mV increments). The –90 mV voltage pulse is highlighted by the red trace. (B): averaged activation and inactivation current data was used to plot the steady-state activation and inactivation curves, which are fit with single Boltzmann equations with values for $Vh_{1/2}$ of -35 ±1 mV and $V_{1/2}$ of -69 ±1 mV; slope factors were 3 ±1 and 5 ±1,respectively.

TTX was used as positive control for both hNa_v 1.4 (Figure 2.7) and 1.5 (Figure 2.8). A calculated IC_{50} of 15 nM and 5 µM was obtained, respectively. hNa_v1.4 is regarded as the TTX sensitive channel and hNa_v 1.5 as the TTX resistant channel. The IV relationships recorded identified the correct expressed channel.

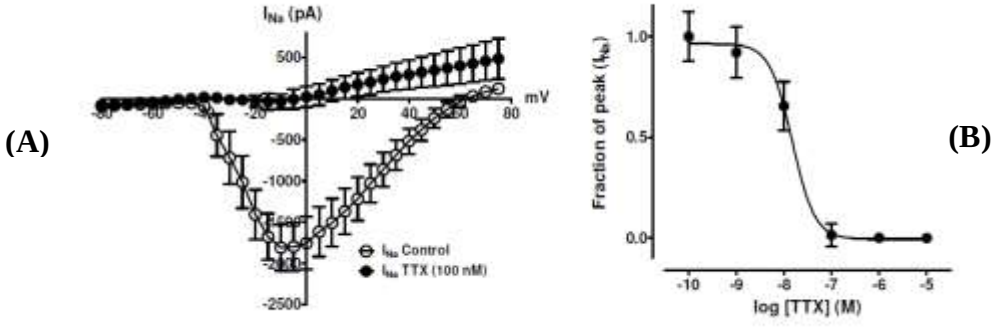

Figure 2.7: Block of hNa_V 1.4 by TTX on manual patch-clamp.(A): I-V relationships of I_{Na} expressed in terms of absolute current (pA), in the absence (open circles) and in the presence of TTX at 100 nM (solid circles; n=6).Values are means, with error bars denoting SEM. The holding potential was -90 mV up to+80 mV. (B): Concentration-dependent effects of TTX (0.1 nM-10 µM) on I_{Na} currents (pA) obtained from HEK-293 cells stable transfected with hNa_V 1.4. Cells were stimulated from a holding potential of -90 mV to +80 mV with 50 ms pulses at 1 Hz. The mean data points were fitted by a variable slope sigmoidal curve using the Hill equation.

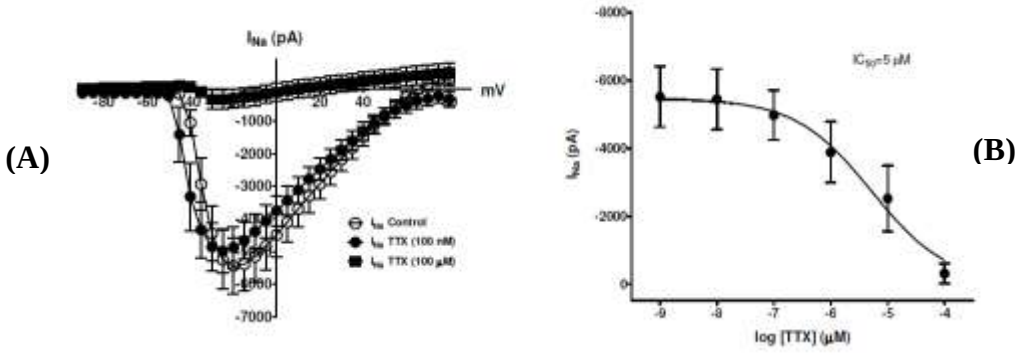

Figure 2.8: Block of hNa$_V$ 1.5 by TTX on manual patch-clamp.(A): I-V relationships of I_{Na} expressed in terms of absolute current (pA), in the absence (open circles) and in the presence of TTX at 100 nM (solid circles; n=11) and at 100 µM (solid squares; n=3). Values are means, with error bars denoting SEM. The holding potential was -90 mV up to + 80 mV. (B): Concentration-dependent effects of TTX (1 nM -100 µM) on I_{Na} currents (pA) obtained from HEK-293 cells stable transfected with hNa$_V$ 1.5. Cells were stimulated from a holding potential of -90 mV to -10 mV with 50 ms pulses at 1 Hz. The mean data points were fitted by a variable slope sigmoidal curve using the Hill equation.

Data analysis

Activation curves were created by transforming I-V current into conductance and normalising to the peak (G/Gmax). Single Boltzmann equations were used to fit the data by varying the V_{50} potential and slope (k) factors. The GraphPad Prism (version 5) software calculates the IC_{50} value and Hill slope co-efficient using a least squares regression algorithm, and constrained to allow 100% block at a large but unknown concentration and fixing 0% inhibition to the hNa_v peak current value in pre-drug control periods (0.1% DMSO throughout). The concentration of 0.1% DMSO did not lead to significant effects on the amplitude of either the fully activated (P1) or half-inactivated (P2) of each of the hNa_v channels tested, which generally remain stable during the duration of a typical manual whole-cell recording control period (up to 5 minutes). Concentration-response data for the effect of drugs on peak currents was fitted iteratively using a variable slope sigmoidal concentration-response curve and the calculated IC_{50} values were reported for the inactivation state.

2.4.3 In vitro autoradiography

Rat brains and hearts from naïve male Sprague Dawley rats were carefully removed and immediately frozen in 2-methylbutane cooled with dry ice. Briefly, coronal sections (10-15 µm thick) were cut in 3 regions of the brain (Regions 1, 2 and 4, see Figure 2.9) and 1 region of the heart (Figure 2.10). Frozen sections were thawed and pre-incubated for 20 minutes with 50 mM

TRIS buffer, pH 8.0, containing 138 mM NaCl and 2.7 M KCl, at RT. For determination of total binding, sections were incubated with a ~1.2 μM solution (100 μL containing 160 KBq) of **([^{18}F]44)** in the same buffer at RT for 60 minutes. Non-specific binding was determined in the presence of ~1.2 mM of cold **(44)**. After incubation, sections were washed twice for 2 minutes with 50 mM TRIS-HCl, pH 7.0, dipped briefly in ice-cold deionised water (5 seconds) and dried in a stream of cold air. Sections were exposed for 10-20 minutes to Kodak™ photographic film, which was developed using an Amersham Biosciences, Hyperprocessor™. One brain section (region 2) and one heart section (coronal) were imaged using a Biospace Mesures, Microimager™ for 2 hours. Images were digitised using a Photometrics CoolSnap™ and interpreted using MCID Elite™ 7.0 software.

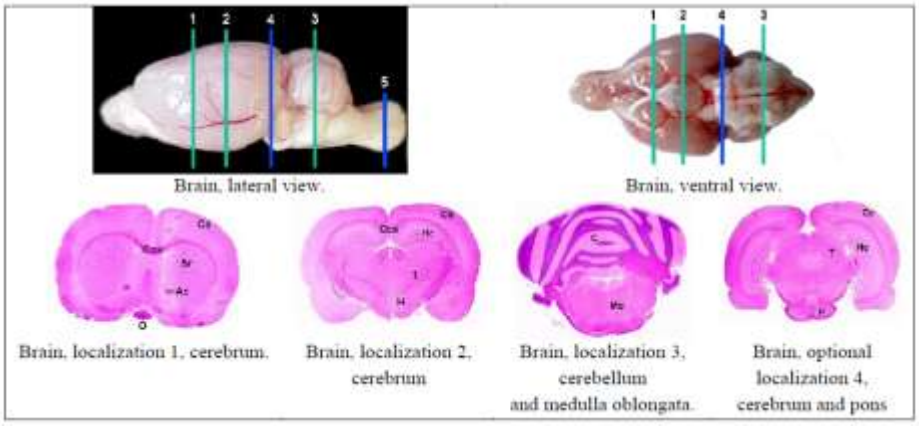

Figure 2.9: Slicing scheme. Abbreviations used in the above images: Ac: anterior commissure, C: cerebellum, Cc: cerebral cortex, Cca: corpus callosum, H: hypothalamus, Hc: hippocampus, Mo: medulla oblongata, O: optic chiasm, P: pons, Sr: striatum, T: thalamus.

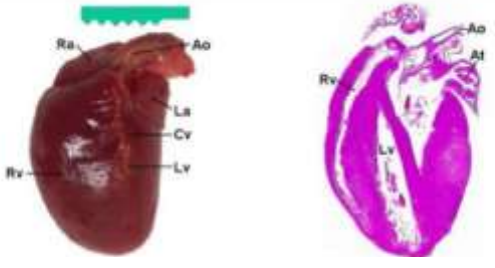

Figure 2.10: Schematic of rodent heart (left) and longitudinal section through both ventricles (right). Rv: right ventricle, Ra: right auricle, Ao: aorta, La: left auricle, Cv: conoventricular vein, Lv: left ventricle, At: atrium

2.4.4 Cell-culture of human breast cancer cell lines

MDA-MB-231 and MCF-7 cell lines

MDA-MB-231 cells obtained from ATTC (approx 1 x 10^6 cells) were thawed in a 37 °C water bath and then sprayed (70% EtOH) into a pre-cleaned category II tissue culture fumehood. The contents of the flask was added to a T75 flask (passage 0) containing 25 mL of fresh media RPMI media (developed by Roswell Park Memorial Institute), containing 5% FBS, 0.5% sodium pyruvate, 0.5% L-glutamine). Cells were cultured at 37 °C in a 5% CO_2 incubator. After 3 days the confluency of the flask had reached >70%. The flask was sprayed into a pre-cleaned category II tissue culture fumehood as before and the media removed prior to cell washing with 10 mL PBS. Trypsin (6 mL) was added to the flask and placed temporarily into the incubator (5 minutes). The cell suspension was then aliquoted into three T175 flasks (2 mL; passage 1) containing 50 mL of media and placed into the incubator. Subsequently, the cells were split on average every 3 days into T175 flasks; the split number depended upon the confluency of the flasks. After 5/6 passages, the cultured cells were used for *in vivo* inocculations.

MCF-7 cells were also obtained from ATTC and cultured using minimum essential amino acid media (containing 5% FBS, 0.5% minimum essential amino acid, 0.5% L-glutamine) following the same method as described above.

2.4.5 Radioligand cell binding assay

2.4.5.0 Seeded-cell assay

MDA-MB-231 and MCF-7 cells were separately harvested prior to seeding in flat-bottomed 96-well plates (following a similar method as described for cell culturing). The media was removed from each flask and all cells washed with PBS (5 mL) before addition of trypsin (6 mL per flask). The flasks were placed in a 37 °C incubator with 5% CO_2 for 5 minutes before being pooled into falcon tubes. The falcon tubes were placed in a centrifuge and spun for 5 minutes at 1000 rpm. The supernatant was removed and new media was added to the cell pellet to give a total concentration of: MDA-MB-231 cells: $1x10^5$ cells/mL and MCF-7 cells: $5x10^5$ cells/mL. To each of the wells was added 100 µL of each solution. The cells were seeded overnight in the incubator to attach to the plate.

Initially, 0.6 mL of PBS was added to ten eppendorf tubes (per cell line). Thereafter, 0.3 mL of prepared radiotracer (approx 1 µM) was added to tube one and then a 1:3 serial dilution produced nine different concentrations for testing.

Concentration	µM
1	1.6
2	0.53
3	0.18
4	0.059
5	0.019
6	0.0065
7	0.0022
8	0.00073
9	0.00027

Table 2.3: Serial dilutions of radiotracer for binding study

To measure block for specific binding, a 10 µL solution of cold standard (1 mM) was added to eighteen wells (per plate) prior to addition of radiotracer. Of each concentration (Table 2.3), 90 µL was added to each well containing cold standard, starting with the most dilute concentration in duplicate. In the remaining wells, 100 µL of each concentration was added in triplicate. Each 96-well plate was incubated for 60 minutes in a lead box at RT. The plates were washed with PBS twice to remove unbound radiotracer. Then, trypsin (100 µL) was added to each well and left for 5 minutes at RT to loosen the cells from the plate. Each plate was then transferred to a Micro 96 Harvester™. A printed glass fibre filter was moistened with PBS prior to removal of the cells from the plate and trapped to the filter using a standard washing cycle. The filter corresponding to each well was separated out and placed on a gamma counter.

2.4.5.1 Cell suspension assay

MDA-MB-231 and MCF-7 cells were separately harvested by trypsination and centrifuged for 5 minutes at 1,000 rpm prior to suspending in PBS (5×10^5 cells/mL). The cells were divided into 16 eppendorf tubes (0.5 mL) per cell line to give an initial starting number of 2.5×10^5 cells. Initially, 5 µL of **(44)** (1 mM) was added to 6 eppendorf tubes per cell line to give an overall concentration of 10 µM for "blocking". The cells were incubated for 5 minutes at RT. To two of

the "block" tubes was added **([^{18}F]44)** (50 µL) and then the same amount was added to two blank tubes, giving concentration one as 100 nM. Then, to two of the "block" tubes was added **([^{18}F]44)** (5 µL) and then the same amount was added to two blank tubes, giving concentration two as 10 nM. All the cells were incubated for 60 minutes at RT. The tubes were then centrifuged for 5 minutes at 1,000 rpm. The supernatant was carefully removed and the cell pellet resuspended in PBS (0.5 mL) before further centrifugation (5 minutes, 1,000 rpm). The supernatant was carefully removed and further PBS (0.5 mL) was added. Again, all samples were centrifuged as before and cells resuspended in PBS (0.5 mL). Finally, all the samples were transferred to a Wallach™ counter for recording. To monitor cell viability, cells with just "block" and blank cells which underwent the assay were tested. Tryphan blue (200 µL) was added to an aliquot of cells (200 µL) and counted using a haemocytometer, cells which showed active removal of the chemical were counted.

2.5 *In vivo* biology

2.5.0 Biodistribution study

The [^{18}F] sodium channel tracer was injected intravenously as a bolus *via* the tail vein of non-anaesthetised mice, in a volume of no more than 5 mL/kg. Each animal was injected with between 1-3 MBq. Following injection of the "labelled substance" the animals were placed in short-term metabolism cages as appropriate. All voided urine and faeces were collected. At the appropriate time points, animals were anesthetised and killed by cervical dislocation (non-schedule 1). Inhalational isoflurane anaesthetic was used for all the biodistribution experiments (2% alveolar concentration). Key tissues (as decided for each study) were dissected, weighed, counted and expressed as % ID and % ID/g. Each study was performed at n ≥1 (see each study for more exact details).

For näive studies, tracer concentrations were sampled at 2, 15, 20, 60 and 120 minutes. For tumour-bearing mice, see each study for exact details.

Biodistribution studies were kindly performed by the *in vivo* biology team, GE Healthcare, Amersham.

2.5.1 Metabolism study

Initially, [^{18}F] sodium channel tracer was injected intravenously as a bolus *via* the tail vein of non-anaesthetised mice, in a volume of no more than 5 mL/kg. Each animal was injected with between 1-3 MBq. Following injection of the "labelled substance" the animals were placed in short-term metabolism cages as appropriate. All voided urine and faeces were collected. Animals were anesthetised and killed by cervical dislocation (non-schedule 1) at 2, 15 and 60 minutes. Inhalational isoflurane anaesthetic was used for all the biodistribution experiments (2% alveolar concentration). Plasma, brain and heart tissue was extracted at each time point and the protein precipitation method was used to extract parent and non-parent radiotracer from each tissue sample.

Initially, the 2 minute plasma sample was selected and a 100 µL aliquot of plasma was extracted and added to an eppendorf tube in duplicate (for measuring on the Wallach counter at the end of the study). To the remaining plasma sample was added 5 mL of ice-cold acetonitrile and centrifuged for 3 minutes at 1000 rpm. The supernatant was removed and collated in a 100 mL round bottom flask. The total volume of supernatant was recorded and 100 µL aliquoted into an eppendorf tube for measuring at the end of the study in duplicate. The plasma pellet was also placed onto the Wallach counter to measure the efficiency of the centrifugation step. The remaining supernatant was put on the rotary evaporator to remove the acetonitrile and resuspended in 2 mL (40% MeCN and 60% H_2O) mobile phase. A 100 µL aliquot of the mobile phase solution was taken for counting in duplicate. Of the remaining mobile phase solution, 1 mL was injected onto a semi-preparative HPLC. The eluent was collected to ascertain the efficiency of the HPLC purification. This procedure was then repeated for each sample over the three time points.

This study was kindly assisted by the *in vivo* biology team, GE Healthcare, Amersham.

2.5.2 Inoculations of MDA-MB-231 and MCF-7 cells

MDA-MB-231 cells

MDA-MB-231 tumour cells in PBS (100 µL; 1 x 10^7 cells/mL) were inoculated subcutaneously into the right second mammary fat pad area of up to six anaethetised SCID female mice and the tumours allowed to grow for up to six weeks or until they reached a maximum size of 12.5 mm.

A secondary group of SCID female mice were also inoculated, 5 x 10^7 cells/mL in 1/1 PBS/Matrigel™ (100 µL), subcutaneously into the right second mammary fat pad area and allowed to grow over the same time scale.

Inoculations studies were kindly performed by Dr S Hoppmann, GE Healthcare, Amersham.

MCF-7 cells

MCF-7 tumour cells were implanted at 1x10^7 cells/mL in PBS (100 µL) subcutaneously into the inner right thigh of up to six anaesthetised female mice and the tumours allowed to grow for up to six weeks or until they reached a maximum size of 10 mm. As MCF-7 cells are oestradiol dependent, mice were implanted subcutaneously into the nape of the neck with a 60-day slow release pellet (17β-oestradiol, 1.7 mg/pellet) obtained from Innovative research of America (cat number, SE-121).

Inoculations were kindly performed by Dr S Hoppmann and Ms R Lear, GE Healthcare, Amersham.

2.5.3 PET/CT imaging

Each animal was placed in a warming box at 37 °C to ensure the tail vein was visible to aid injection. Animals were placed in a humane perspex restrainer and injected with 100 µL of the radiotracer (5-10 mBq). The animal was then placed on the imaging bed and maintained under inhalation anaesthesia (isoflurane) throughout the duration of the study (60 minutes). Immediately, DYNAMIC PET scanning was commenced using a MicroPET-P4 scanner (Siemens Inc). Respiration and body temperature was monitored using the BioVET system. Following the emission acquisition a transmission scan was acquired. The imaging bed was then transferred to a MicroCT II (Siemens) scanner and a CT scan acquired. The animal was either recovered for use in a further study or sacrificed by cervical dislocation (non-Schedule 1).

PET/CT imaging was kindly carried out by the *in vivo* biology team, GE Healthcare, Amersham.

3. Results and Discussion

Design, synthesis and bioevaluation of 3-(3-(4-R-phenoxy)phenyl)-pyrazole-1-carboxamides

3.0 Synthesis of 3-(4-R-phenoxy)phenyl pyrazoles

3-(4-R-Phenoxy)phenyl pyrazoles, first reported by Yang and co-workers (Scheme 3.1), were shown to be potent state-dependent VGSC ligands through *in vitro* studies.[7] They reportedly gave good efficacy in animal models of neuropathic pain. In-fact, they were shown to be nearly 10 times as efficacious as carbamazepine (a known anti-convulsant). Inhibition of VGSC currents were recorded in HEK-293 cells stably expressing hNa_v 1.4. The inhibitory effects of these compounds were reported to be highly sensitive to the holding voltage, indicating that they bind more efficiently to VGSCs in their inactivated states (measured as K_i), and show ~100 times weaker potency towards resting states (measured as K_r). This class of compounds were chosen as a platform to develop a novel fluorine-18 labelled PET ligand targeting VGSCs. They were selected due to their good binding affinity and its structure amenable to multiple potential radiolabelling strategies.[7]

Initially, the three most potent compounds were selected from the library of 3-(4-R-phenoxyphenyl) pyrazoles (**(7)** – **(9)**, Scheme 3.1). These compounds were synthesised following a three step procedure.

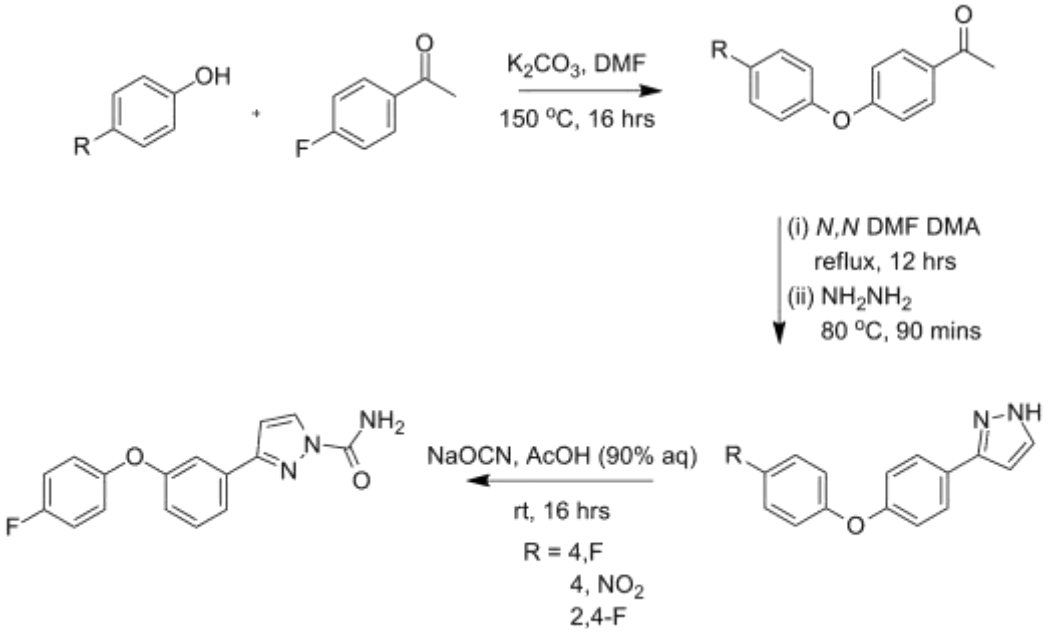

Scheme 3.1: Synthesis of 3-(4-substituted-phenoxy)phenyl pyrazoles [7]

The first step followed a Williamson ether synthesis (Scheme 3.2). Deprotonation of the phenol allowed for nucleophilic attack on 4-fluoroacetophenone with loss of KF. Following reaction completion as monitored by tlc, each reaction was quenched with

2M NaOH and the product was extracted into EtOAc. The crude products were continued onto the following step without further purification. However, a small sample from each reaction (**(1)-(3)**) was purified by CC (1:1; hexane:EtOAc) for product identification by nuclear magnetic resonance spectroscopy (NMR) and gas chromatography mass spectrometry (GCMS).

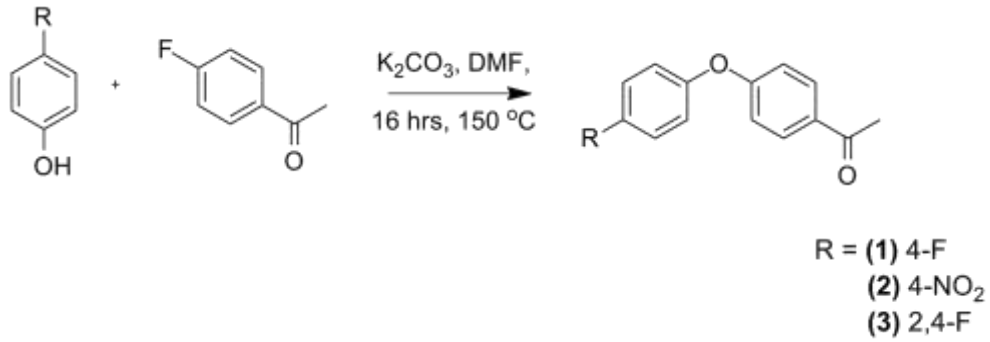

Scheme 3.2: Formation of ether bridge

The pyrazole ring was formed by a one-pot two-step ring closure (Scheme 3.3). Addition of N,N dimethylformamide dimethylacetal (N,N DMF DMA) allowed carbon-carbon bond formation through a base catalysed aldol reaction. Attack at the terminal carbonyl gave a reactive enolate intermediate, which then reacted with the carbonyl of dimethylacetal dimethylformamide giving an α,β-unsaturated ketone intermediate as a yellow precipitate. The addition of hydrazine drove the ring closure through a 1,4 Michael addition.

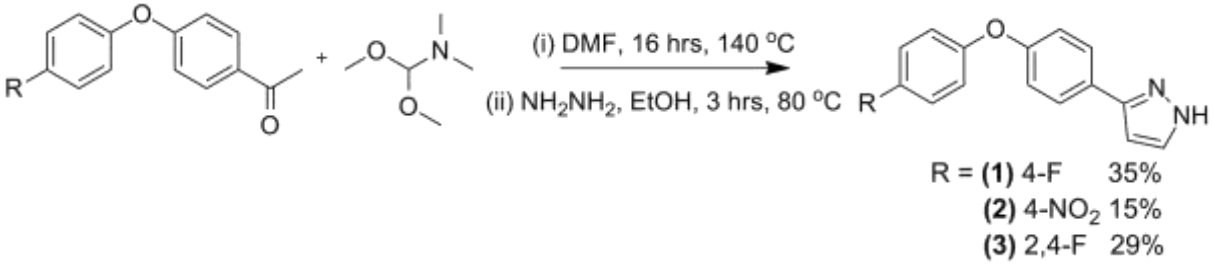

Scheme 3.3: Pyrazole ring closure

In the final step, addition of sodium cyanate in AcOH (90% aq.), allowed for formation of the terminal carboxamide through nucleophilic attack on the pyrazole (Scheme 3.4). The product precipitated out of solution without further purification. **(7)**, **(8)** and **(9)** were isolated in 68%, 25% and 78% yield respectively.

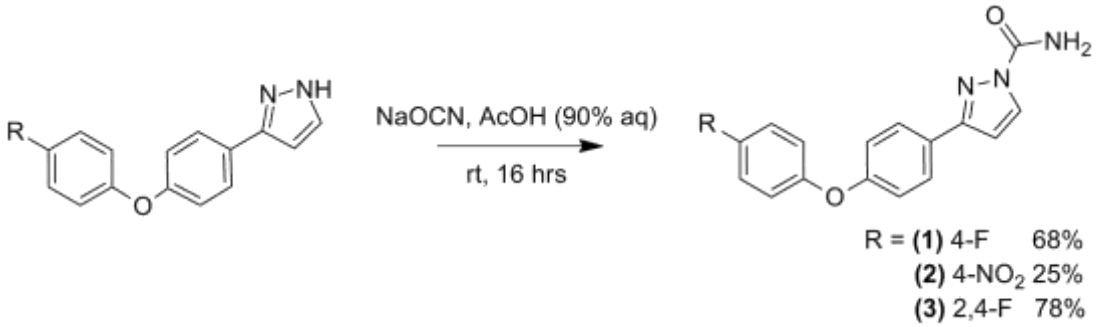

Scheme 3.4: Formation of terminal carboxamide

Product identity was confirmed by ^{1}H, ^{13}C, COSY and NOSEY NMR and liquid chromatography mass spectrometry (LCMS) under electrospray ionisation. Data was consistent with the structures shown, and with literature reports.[7]

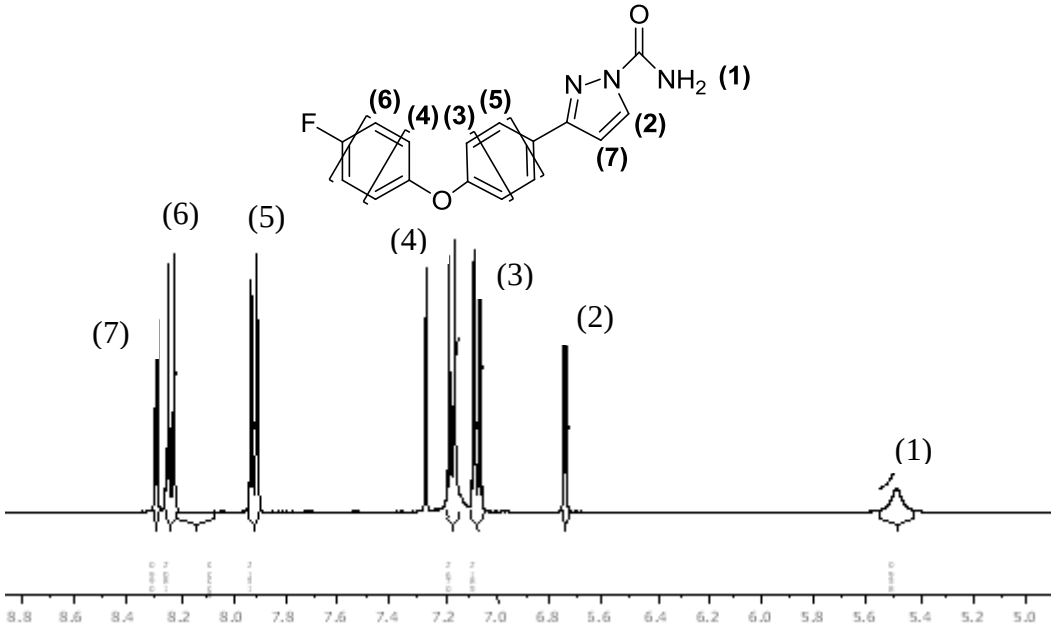

*Figure 3.1: ^{1}H NMR spectrum of **(7)** in $CDCl_3$*

The three literature compounds were produced in variable yields with purity > 95%. The NMR spectrum of **(7)** (Figure 3.1) was compared to the data reported by Yang *et. al.*, and showed to be consistent with literature characterisation.

The next steps were to ascertain a reproducible radiolabelling process to produce a fluorine-18 labelled analogue of the 3-(4-R-phenoxy)phenyl pyrazoles. Thereafter, these potential radiotracers were going to be used in radioligand binding studies to afford the B_{max} and K_d values and ultimately the binding potential (B_{max}/K_d). As discussed previously (Section 1.5), this would need to be ≥10 to afford a good signal to noise ratio. Tritiation of the compounds could have allowed these radioligand binding studies to be achieved earlier; unfortunately, funds were not available to allow this, so the

compounds were evaluated for radiolabelling studies with fluorine-18 in the first instance.

3.1 General [^{18}F] radiolabelling strategies

Fluorine-18 produced from a proton accelerator cyclotron was delivered as an aqueous solution by irradiation of an [^{18}O] H_2O liquid target. In aqueous solution, [^{18}F]fluoride is relatively unreactive, due to being highly diluted and strongly solvated, thus steps are taken to provide a reactive nucleophilic reagent.[139-140] Firstly, a large organic soluble cation is added. Caesium and tetralkylammonium salts have been used, but more commonly a potassium salt complexed by a cryptand such as Kryptofix (2.2.2)™ (4,7,13,16,21,24-hexaoxa-1,10-diazabicyclo[8.8.8]-hexacosane). This step is often performed by adsorbing the target water containing [^{18}F]$^-$ on a short anion exchange resin cartridge and eluting with a solution of the chosen cation in a water/solvent mixture, *e.g.* an aqueous solution of potassium carbonate with Kryptofix™ (Figure 3.2). Secondly, [^{18}F]$^-$ has to be dried. This step is completed by azeotropic distillation of the aqueous solution with a solvent, commonly acetonitrile. The azeotropic drying of [^{18}F]$^-$ typically takes from 10 to 30 minutes in an automated radiosynthesis process.[141]

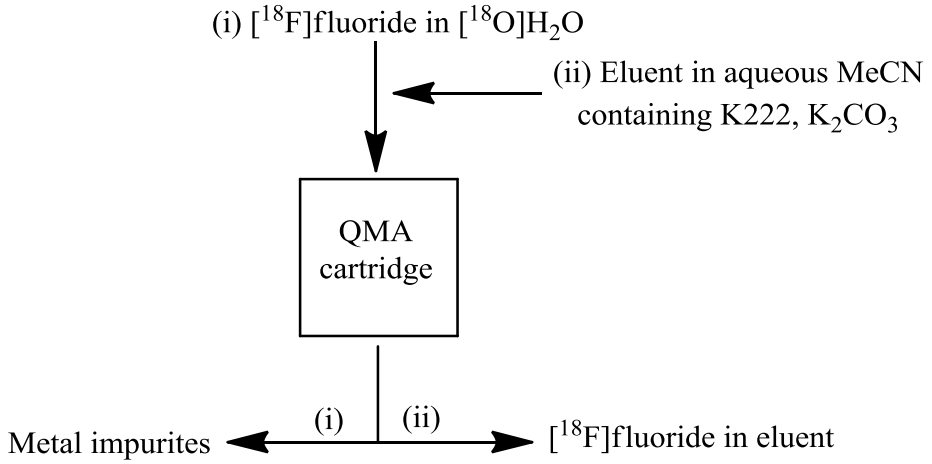

Figure 3.2: Diagram to represent the purification of [^{18}F]fluoride on a QMA cartridge

There are two established methods for radiolabelling compounds with fluorine-18:

Direct labelling incorporates fluorine-18 in a one-step method through nucleophilic aromatic substitution (S_NAr) for example, or other displacement reactions. This type of labelling allows for short synthesis times, but has limitations with molecules that do not allow for direct labelling due to incompatible functionalities present on the molecule.[142-143]

Indirect labelling makes use of synthon chemistry; the molecule is broken down into "fragments" through disconnecting certain bonds following the rules for retrosynthetic analysis. Initially, a small "fragment" is labelled, and subsequently bound to the remainder of the target molecule.[144]

In the context of PET radiochemistry, it is important to minimise reaction times, to avoid unnecessary decay of the radioisotope. [^{18}F] has a half-life of 110 minutes and [^{18}F]-labelled tracers for PET are therefore ideally synthesised and purified within one half-life. It is also important to note that the concentration of fluorine-18 present is so low, that it is not possible to incorporate fluorine-18 into multiple positions.

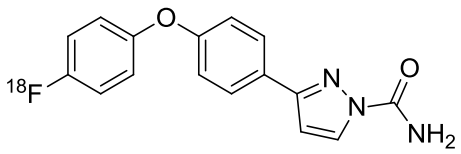

Figure 3.3: Structure of ***([^{18}F]7)***

Of the three VGSC ligands, **([^{18}F]7)** (Figure 3.3) was selected to be the first PET tracer of this class to be prepared.

3.1.0 Direct fluorine-18 labelling

There is much information in the literature about devising radiolabelling strategies and problems which may arise due to side and competition reactions; this knowledge allowed for different radiolabelling routes to be planned and implemented. For direct labelling to proceed, any base labile functional groups on the molecule require protecting first, as [^{18}F]fluoride can act as a base. The carboxamide group is a base labile functional group, where [^{18}F]fluoride could de-protonate and cleave the whole functional group, stopping the desired S_NAr reaction from occurring. The protecting group used needed to be base stable but acid labile to remove the group at the end of the synthesis. Di-*tert*-butyl dicarbonate (Boc) is a common protecting group used, as it is base stable but cleaved easily with concentrated trifluoroacetic acid (TFA).

To produce **([^{18}F]7)**, **(10)** was synthesised as labelling precursor *via* a boc protection of the terminal carboxamide of **(7)**. This was carried out in the presence of TFA and boc in anhydrous DCM at rt for 24 hrs. The product was purified by CC (4:1; hexane: EtOAc)

giving **(10)** in 10% yield. Characterisation was achieved *via* ^{1}H and ^{13}C NMR and high-resolution mass spectroscopy (HRMS).

Fluorine-19 for fluorine-18 isotopic substitution of **(10)** (Scheme 3.5) was assessed as a high-risk radiolabelling strategy to model whether direct labelling of this compound was possible. As discussed in section 2.1, the concentration of fluorine-18 in comparison to the concentration of precursor is so low that there will always be a significant amount of fluorine-19 compound remaining, giving low specific activity (amount of activity divided by the mass of material, usually expressed in GBq/µmol). Although radiolabelling by isotopic exchange gives poor specific activity, it does allow for an indication of whether radiolabelling is possible. Blom *et. al.,* reported using isotopic exchange for radiolabelling a series of compounds including fluorobenzophenones, 1-(4-fluorophenyl)ethanone and various activated and deactivated fluoro benzenes. They reported the best general conditions for isotopic exchange to be: DMSO, 150 °C, 25 minutes giving an average specific activity of 0.58 GBq/µmol.[145]

Initially the isotopic exchange of **(10)** was performed using the conditions in Table 3.1 and Table 3.2.

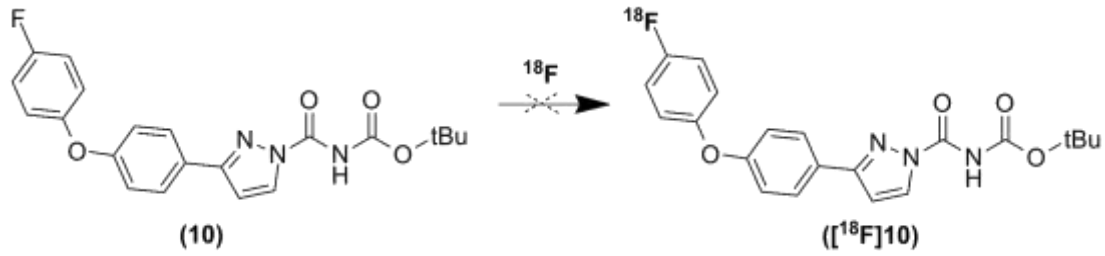

*Scheme 3.5: Attempted radiolabelling of **(10)** through isotopic exchange*

Solvent	Temperature (°C)	Reaction Time (minutes)	Radiochemical Purity (%)
DMSO	150	45	0
DMSO	150	75	0
MeCN	100	25	0
MeCN	110	15	0
DMF	110	30	0
DMF	140	15	0

*Table 3.1: Attempted isotopic exchange of **(10)** via conventional heating*

Solvent	Set Temperature (°C)	Power (W)	Reaction Time (seconds)	Radiochemical Purity (%)
DMSO	80	50	30	0
DMF	100	50	60	0

*Table 3.2: Attempted isotopic exchange of **(10)** via microwave irradiation*

Though many different reaction conditions were tested, no labelling of **(10)** was observed. From the HPLC radio chromatograms, it was seen that the activity remained as unreacted [^{18}F]fluoride. Despite the literature precedent for this reaction, we could not replicate isotopic exchange on our compounds.[145] Interestingly, when comparing UV chromatograms (Figure 3.4), **(5)** was identified as a side-product of this reaction. It was surprising that cleavage of the boc and carboxamide group was seen, as the boc group had been added to protect this type of reaction from occurring. El Kazzouli *et. al.*, however published results showing that bases can in fact cleave boc groups.[146] Their findings were that boc is very labile in the presence of sodium carbonate. It was therefore concluded that the presence of potassium carbonate required in the azeotropic drying of [^{18}F]fluoride, was causing deprotection of **(10)**.

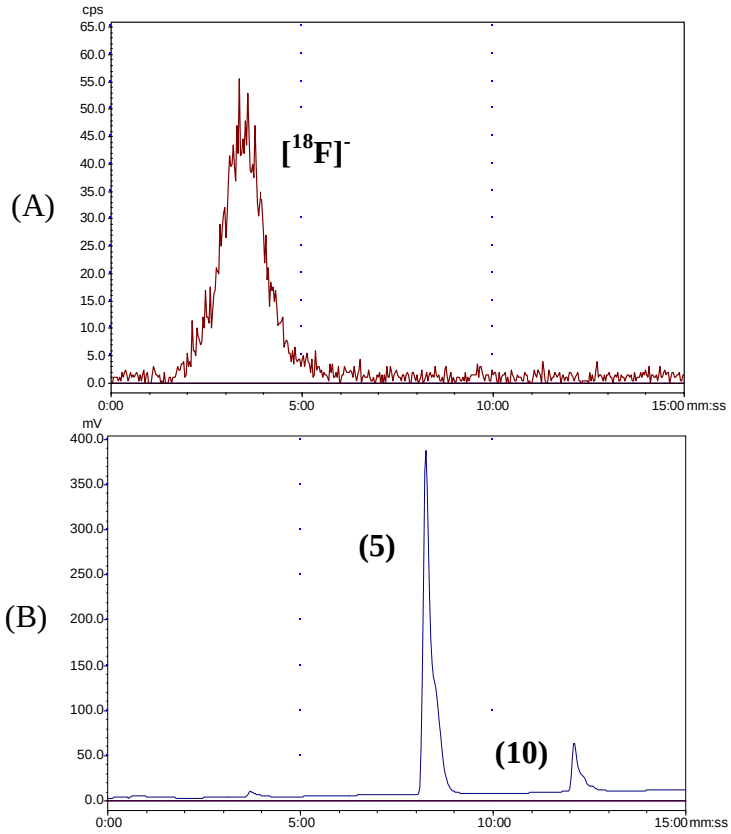

*Figure 3.4: HPLC (a) radio and (b) UV chromatogram of radiolabelling of **(10)***

As protection of the carboxamide had shown to be ineffective, the synthetic route was altered to add the carboxamide with sodium cyanate after fluorination to afford **([^{18}F]7)**. Therefore, radiolabelling of **(5)** was subsequently tested through a nucleophilic aromatic substitution reaction of the *para*-nitro group with fluorine-18. This compound contains no labile terminal carboxamide and as the NH is only weakly acidic, we initially did not protect this group (Scheme 3.6). The results under various conditions are shown in Table 3.3.

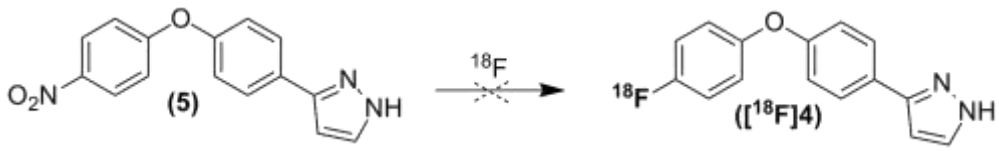

*Scheme 3.6: Attempted radiolabelling of **(5)***

Solvent	Temperature (°C)	Reaction Time (minutes)	Radiochemical Purity (%)
MeCN	90	30	0
MeCN	110	45	0
DMF	145	20	0

*Table 3.3: Attempted radiolabelling of **(5)** via conventional heating*

Once again S_NAr chemistry, for directly labelling proved unsuccessful. The main reason was thought to be due to the electron donation from the oxygen atom (forming the ether bridge), causing de-activation of the ring towards S_NAr chemistry. To activate radiolabelling, additional electron withdrawing groups for example CF_3 and NO_2 were investigated. It was proposed that addition of the electron withdrawing groups would stabilise the positively charged ring intermediate, thus drive the $[^{18}F]^-$ nucleophilic attack and S_NAr reaction forward. Therefore, based on the reported information that **(9)** is the most potent of the three compounds by 6 nM, and that isotopic exchange does not occur, we proposed the modification of **(8)** by adding in a fluorine *meta* to the nitro (Scheme 3.7; **(11)**). Although electron withdrawing groups in the *meta* position would not directly activate this ring for S_NAr chemistry, it was thought that adding the extra electron withdrawing group into the *ortho* positon might change some pharmacological properties of the molecule. By adding the fluorine in the *meta* position, we were able to maintain the structure of **(9)**. Also, the terminal carboxamide was added to protect the NH group to avoid concerns over deprotontation with fluorine-18.

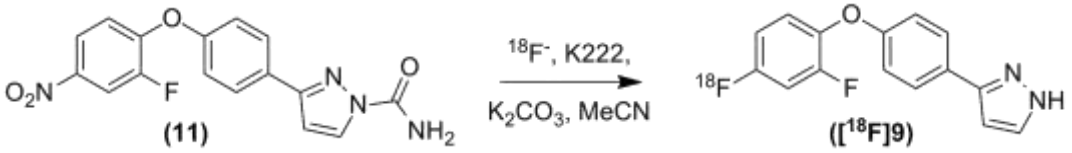

*Scheme 3.7: Proposed synthesis of **([^{18}F]9)***

The synthesis of **(11)** was undertaken using the same procedure as described in (Scheme 3.1). 2-Fluoro-4-nitrophenol in the presence of base was added 4-fluoroacetophenone to undergo a Williamson reaction (Scheme 3.8). Following thin layer chromatography (tlc) monitoring, no product was seen, even after 16 hours at 140 °C.

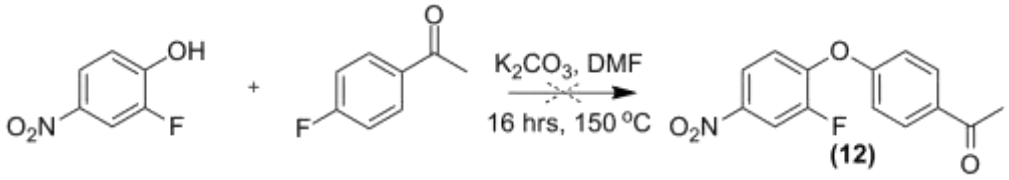

*Scheme 3.8: Attempted synthesis of **(12)***

The reaction was worked-up and the crude mixture purified by CC (4:1; hexane: EtOAc) to identify whether any undesired side-products had formed. An NMR spectrum of each product was taken, and only starting materials (2-fluoro-4-nitrophenol and 4-fluoroacetophenone) and DMF (presumably polymerised) were identified. This was unexpected, as **(9)** was successfully synthesised which also has two electron-withdrawing groups on the phenolic starting material in the same positions. Stronger base was used encase the limitation was deprotonation of the phenol. Potassium hydroxide was used under the same reaction conditions but also after 16 hours at 140 °C, no product was seen. Again, the reaction mixture was purified by CC (4:1; hexane:EtOAc) and following NMR of each fraction, only starting material and DMF were found.

It was unusual that this reaction did not work even after the addition of a stronger base. We hypothesised that perhaps the phenol was being deprotonated by both bases, (in accordance with previous results (compounds **(1)** – **(3)**), but the anion formed, was stabilised by delocalising the charge into the benzene ring, thereby inhibiting the Williamson reaction.

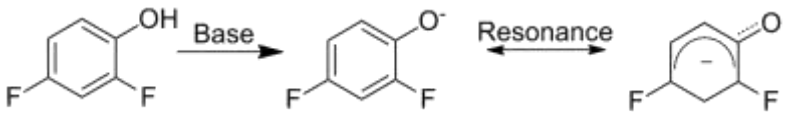

Scheme 3.9: Stability of 2,4 difluorophenol under basic conditions by inductive effect

The presence of the second fluorine, as in 2,4-difluorophenol is likely to increase stability of the phenolate formed during deprotonation of the phenol by stabilising the electron density over the ring (Scheme 3.9).

We proposed that the combination of *ortho*-fluorine and *para*-nitro group stabilised the anion better than the other phenols previously used. This could also be one reason why the yields were so low for previous reactions. Also, nitro is a better electron-withdrawing group than fluorine, and could better stabilise an anion intermediate, hence why this reaction did not proceed, but the synthesis of **(3)** did. To test this hypothesis, we used 2,4 dinitrophenol under standard Williamson conditions (Scheme 3.10) to afford **(13)**. We also found this reaction was unsuccessful. The reaction was monitored hourly by tlc, but after 9 hours no reaction was occurring. Tlc showed only starting material in the crude reaction mixture and the reaction was subsequently abandoned. We proposed that the anion of 2,4-dinitrophenol and 2-fluoro-4-nitrophenol were too stable to undergo a Williamson reaction due to the stabilising effect of the nitro group.

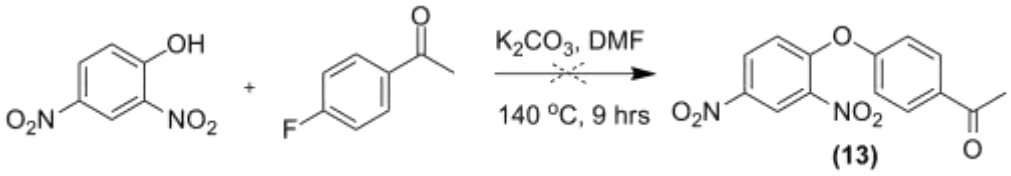

*Scheme 3.10: Attempted synthesis of **(13)***

Finally, the use of iodonium salts was proposed to afford a precursor for use in a one step labelling process. An iodonium salt of **(7)** was initially sought (Figure 3.5), utilising a modified Koser's reagent to afford a 4-methoxy moiety on the terminal phenyl ring. It was hoped that the *p*-methoxy moiety would direct fluorination onto the opposite ring and leave 1-iodo-4-methoxy benzene as the by-product, together with **([^{18}F]7)**

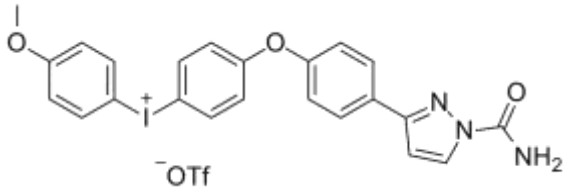

*Figure 3.5: Proposed iodonium salt of **(7)***

The initial synthesis of the modified Koser's reagent (Figure 3.6) however, proved challenging and was not achievable. Previous reports have shown that modifying the traditional Koser's reagent is difficult to do and only exothermic decomposition is seen.[147-148]

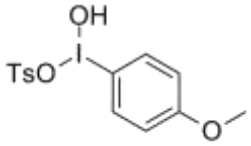

Figure 3.6: 4-methoxy derivative of Koser's reagent

We set out to develop an iodonium salt to afford a precursor for use in a one-step labelling process. However, it was not possible to find a reliable procedure to undertake this work and as such, this route was discarded in favour of following an indirect labelling process.

3.1.1 Indirect fluorine-18 labelling

As fluorination *via* direct radio-fluorination proved unsuccessful, multi-step routes were investigated to produce **([^{18}F]7)**. Firstly a retrosynthetic analysis was used to identify possible synthons for indirect labelling protocols.

3.1.1.0 Retrosynthetic analysis

Through retrosynthetic analysis two synthons were identified, (4-^{18}F)fluorophenol and (1-^{18}F)fluoro-4-bromobenzene (Scheme 3.11).[133, 149-150] Both synthons have literature precedent for their synthesis and could be conjugated to the rest of the molecule in a short synthetic pathway.

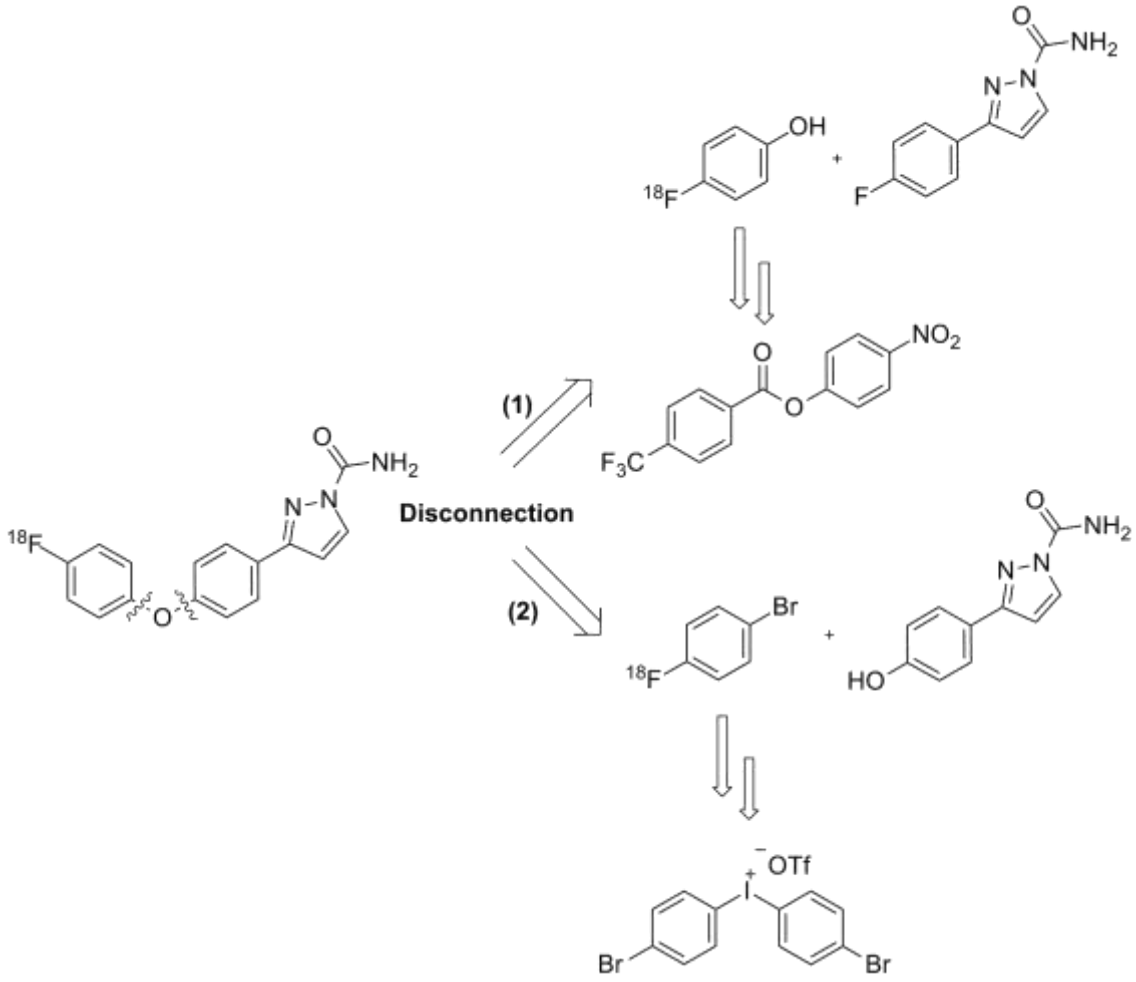

Scheme 3.11: Retrosynthetic analysis of target molecule

The two strategies outlined show feasible pathways to produce the desired compound **([^{18}F]7)**. Following the synthesis of (1-^{18}F)fluorophenol, a Williamson reaction would complete the synthesis of the target molecule (Scheme 3.12). Following route two, (1-^{18}F)fluoro-4-bromobenzene would undergo a copper catalysed Ullmann coupling to afford **([^{18}F]7)**.

3.1.1.1 Synthesis of (1-^{18}F)fluorophenol

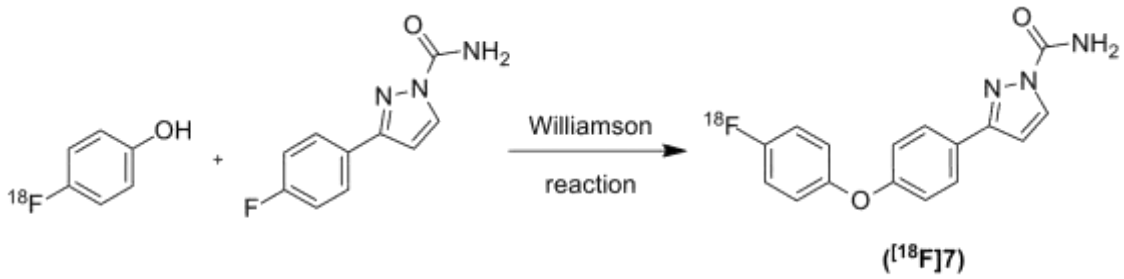

*Scheme 3.12: Proposed scheme to afford **([^{18}F]7)** using a Williamson reaction with 4-[^{18}F]fluorophenol*

Coenen and co-workers reported the synthesis of (1-^{18}F)fluorophenol in 60% radiochemical yield (RCY) from [^{18}F]fluoride (Scheme 3.13). Starting from the diaryl ketone **(14)**, they carried out their radiolabelling to give **([^{18}F]15)** and performed a Baeyer-Villiger oxidation to prepare **([^{18}F]16)**. Lastly, hydrolysis of the ester with sodium hydroxide, yielded n.c.a. [^{18}F]4-fluorophenol and trifluoromethyl benzoic acid.[133]

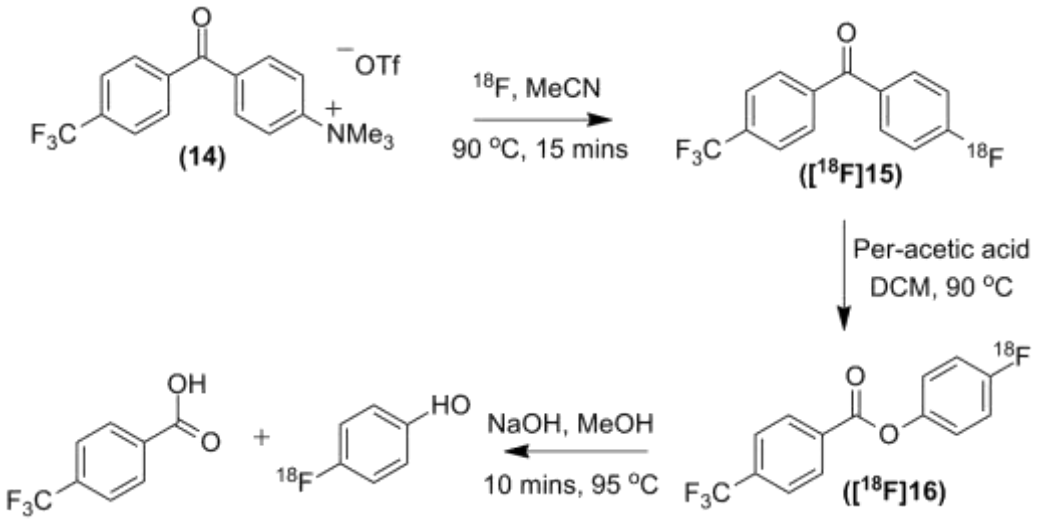

Scheme 3.13: Proposed synthesis of (1-^{18}F)fluorophenol[133]

This procedure was followed to synthesise (1-^{18}F)fluorophenol. To synthesise the radiolabelling precursor **(14)**, a three step procedure by the same group was used. Initially a Friedel-Crafts acylation between 4-fluorobenzene and 4-(trifluoromethyl)-benzoyl chloride afforded **(15)**. In the first instance, 1 equivalent of $AlCl_3$ was used to catalyse the reaction, however no desired product was observed by ^{1}H NMR. Literature searches showed the original procedure published by Pews *et. al.* followed a similar procedure but used an excess of $AlCl_3$.[151] After adding 1.2 equivalents of $AlCl_3$, the reaction, still proved unsuccessful. An improved method published by Noriyuki *et. al.*,

used 0.5 equivalents of TfOH instead of $AlCl_3$, as they stated that "CF_3-bearing aryl fluorophenyl ketones are rarely obtained using $AlCl_3$". After 6 days at 100 °C, the Noriyuki group reported yields of 64%.[132] In my hands, **(15)** was obtained in 56% yield after 4 days as tlc monitoring showed no further reaction occurring. The synthesis of **(17)** (Scheme 3.14), returned to the literature procedure by Coenen and co-workers. The displacement of fluorine with dimethyl amine hydrochloride, afforded **(17)** in 86% yield with no purification required. Lastly, the trimethylammonium group was produced *via* a methylation reaction with methyl triflate. The triflate salt precipitated out of solution after 1 hour and was recrystallised from hot ether giving **(14)** in 85% yield.

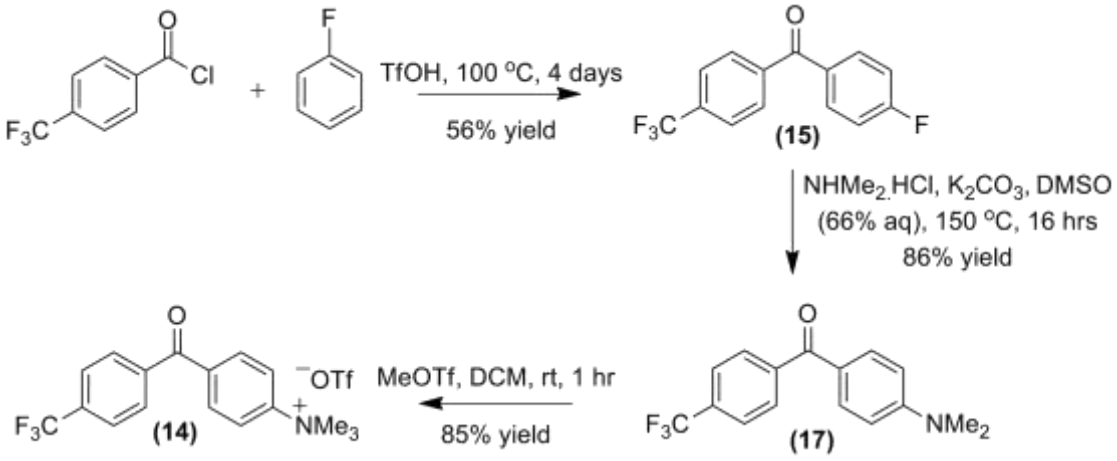

*Scheme 3.14: Synthesis of (4-(trifluoromethyl)phenyl)benzoyl-4-trimethylammonium triflate **(14)***

Radiolabelling of **(14)** was tested as shown in Scheme 3.15 following the procedure by Coenen and co-workers.[133]

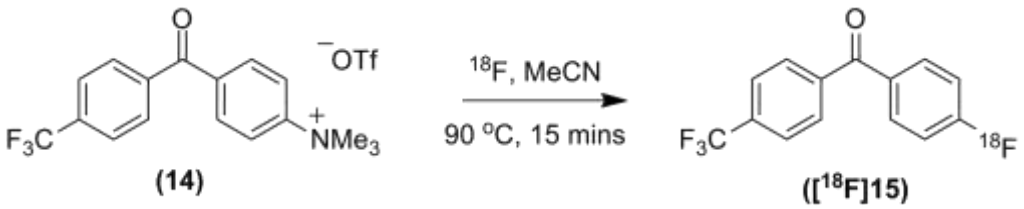

*Scheme 3.15: [^{18}F] radiolabelling **(14)***

The synthesis of **([^{18}F]15)** in acetonitrile at 90 °C for 15 minutes, gave 40% non-decay corrected (n.d.c.) radiochemical yield from [^{18}F]fluoride after purification by semi-preparative HPLC. This procedure was not optimised further due to the adequate yield produced. After formation of **([^{18}F]15)**, the acetonitrile was removed by distillation prior to the oxidation step. The procedure by Coenen and co-workers used hydrogen peroxide in the presence of acetic acid, acetic anhydride, and sulphuric acid, generating

per-acetic acid *in-situ* for the Baeyer-Villiger oxidation step (Scheme 3.16). The oxidation was further investigated using *m*CPBA (Table 3.4 and Table 3.5).

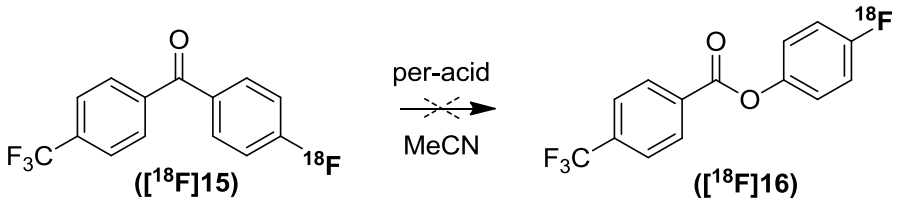

*Scheme 3.16: Attempted synthesis of **([^{18}F]16)***

Per-acid H_2O_2 (60% aq.) (0.5 mL) *m*-CPBA (40 mg)	**Temperature (°C)**	**Reaction Time (mins)**	**Radiochemical Purity (%)**
H_2O_2	80	45	0
H_2O_2	90	45	0
H_2O_2	100	45	0
H_2O_2	120	60	0
m-CPBA	85	15	0
m-CPBA	90	30	0
m-CPBA	130	60	0
m-CPBA (100 mg)	130	30	0

*Table 3.4: Attempted Baeyer-Villiger oxidation of **([^{18}F]15)** via conventional heating*

Per-acid H_2O_2 (60% aq.) (0.5 mL) *m*-CPBA (40 mg)	**Temperature (°C)**	**Power (W)**	**Reaction Time (secs)**	**Radiochemical Purity (%)**
H_2O_2	90	50	90	0
***m*-CPBA**	60	60	130	0
***m*-CPBA (100 mg)**	60	60	30	0
***m*-CPBA (150 mg)**	100	50	120	0

*Table 3.5: Attempted Baeyer-Villiger oxidation of **([^{18}F]15)** via microwave irradiation*

After multiple attempts, the Baeyer-Villiger oxidation did not proceed.

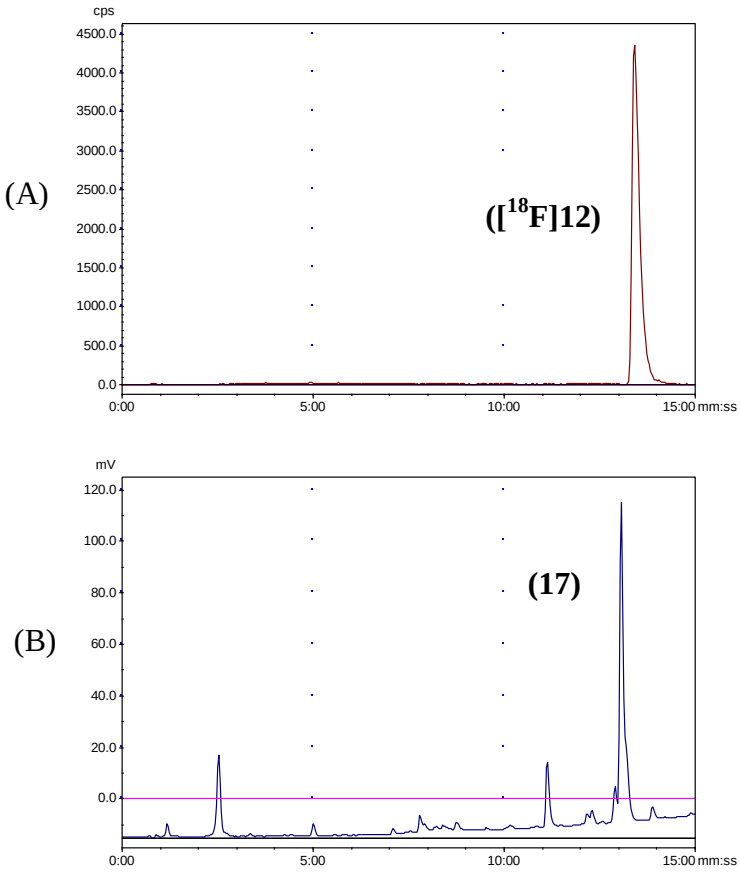

*Figure 3.7: HPLC (a) radio and (b) UV chromatogram of oxidation of **([18F]15)***

From the HPLC UV chromatogram of the reaction mixture (Figure 3.7), there was a high residual concentration of **(17)** (the decomposition product of **(14)**. It was hypothesised that perhaps this was oxidising preferentially over the reaction with **([18F]15).** However, after evaluating HPLC chromatograms, the peak corresponding to **(17)** never diminished whilst under oxidation conditions. Thus it was concluded that neither compound was reactive towards a Baeyer-Villiger oxidation under these conditions. To determine the progression of oxidation in the absence of **(17)**, **(15)** was used to model the radiochemistry (Scheme 3.17). Again, the different per-acids were used (*in-situ per*-acetic acid and *m*-CPBA). Analytical HPLC chromatograms were acquired to monitor the progress of each reaction.

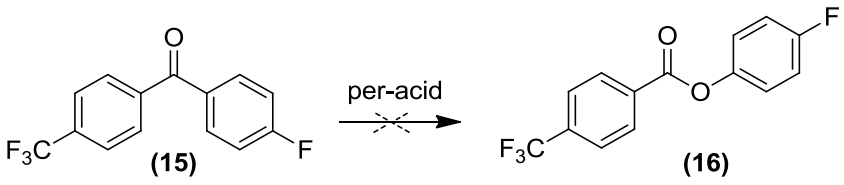

*Scheme 3.17: Attempted synthesis of **(16)***

After 12 hours of heating each reaction under reflux, **(15)** was still present with no peak corresponding to **(16)** observed. It was therefore concluded that **(15)** was unreactive towards oxidation.

In conclusion, the synthesis of (1-^{18}F)fluorophenol initially seemed straightforward, however, the Baeyer-Villiger oxidation did not proceed as expected and this pathway was consequently abandoned. Other pathways to afford (1-^{18}F)fluorophenol were investigated.

Independently Gouverneur *et. al,* published a manual synthesis of (1-^{18}F)fluorophenol starting from 4-*tert*-butylphenol in the presence of [^{18}F]TBAF, using the oxidant *p*-iododiacetoxy benzene under acidic conditions in dichloromethane at RT for 20 minutes. They reported an integrated analytical HPLC yield of 4-6% (or as it should be known, radiochemical purity).[19] Due to the low radiochemical purity and no isolated yield reported, we chose not to reproduce this work.

The synthon (1-^{18}F)fluoro-4-bromobenzene (Section 3.1.1.2) was pursued. This synthon can in principle be conjugated in a similar manner as (1-^{18}F)fluorophenol, using a copper catalysed Ullmann coupling to produce **([^{18}F]7)**.

3.1.1.2 Synthesis of (1-^{18}F)fluoro-4-bromobenzene

Different methods were considered for the synthesis of (1-^{18}F)fluoro-4-bromobenzene as discussed by Ermert *et al.*, who compared various pathways.[152]

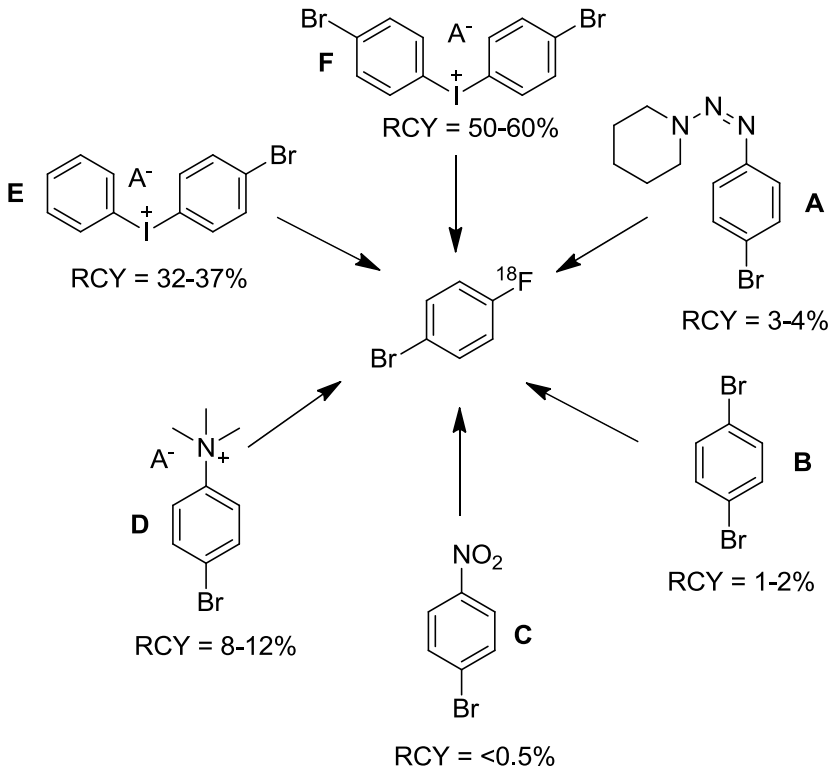

Scheme 3.18: One-step reactions to n.c.a (1-^{18}F)fluoro-4-bromobenzene

The Wallach reaction (Scheme 3.18, pathway **A**), even using a wide variety of conditions (temperature, concentration of precursor, ^{19}F carrier, solvent, different sulfonic acids for decomposition), only provided 3-4% radiochemical yield.

Pathway **B** followed a direct nucleophilic aromatic substitution reaction using ^{18}F-for-halide exchange.[153-154] The bromines simultaneously act as weak activating and leaving groups. However, only 1-2% radiochemical yield was reported.

In pathway **C**, 1-bromo-4-nitrobenzene was used for halogen activated ^{18}F / NO_2 exchange. Only 0.5% radiochemical yield was reported.[155] The major product was [^{18}F]1-fluoro-4-nitrobenzene in > 40% radiochemical yield.[155]

Pathway **D** used trimethyl ammonium substitution for [^{18}F] weakly activated with a *para* bromo, leading to only 8-15% radiochemical yield.[156-157]

Pathway **E** and **F** both made use of diaryl iodonium salts. They react with nucleophiles by interacting with, in this case [^{18}F]fluoride, to form a trigonal bipyramidal complex which undergoes *syn* elimination to give an [^{18}F]fluoroaryl and iodoaryl species.[158] Numerous diaryliodonium salts have been synthesised and radiolabelled with [^{18}F].[159-161]

In pathway **E** the synthesis of (1-^{18}F)fluoro-4-bromobenzene is preferred to the formation of (1-^{18}F)fluorobenzene, as labelling is directed to the more electronegative arene. Unfortunately however, this pathway only allows a maximum 50% yield. In comparison, pathway **F** offers a higher yielding reaction (50-60% radiochemical yield), due to both arenes possessing an electron-withdrawing *para*-bromine.[152]

Consequently pathway **F** was selected as it allowed the highest possible yields of [^{18}F]1-bromo-4-fluorobenzene. Consequently, 1-bromo-4-iodobenzene was acetylated to give (**18**) in 17% yield, followed by acidic coupling with bromobenzene *via* an iodoso species giving (**19**) in 47% yield (Scheme 3.19).[134-135]

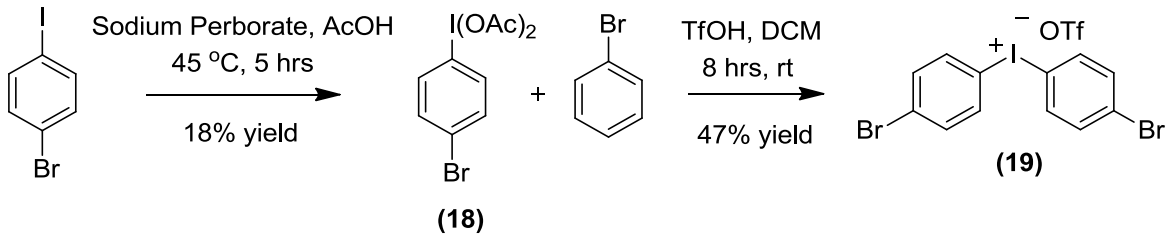

*Scheme 3.19: Synthesis of **(19)***

Radiolabelling of **(19)** yielded (1-^{18}F)fluoro-4-bromobenzene **([^{18}F]20)** (Scheme 3.20; Table 3.6 and Table 3.7), which was characterised by comparing retention times with 1-bromo-4-fluorobenzene on analytical HPLC. Reaction concentration was calculated based on amount of **(19)** and isolated yields are given after purification by semi-preparative HPLC.

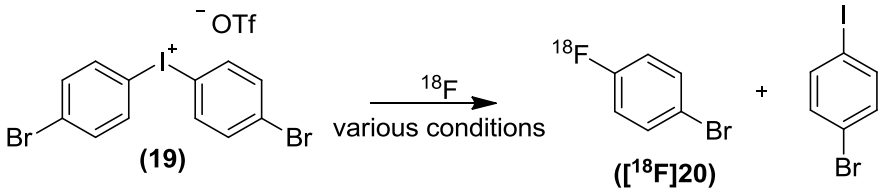

*Scheme 3.20: Proposed radiolabelling of dibromodiphenyliodonium triflate **(19)***

Solvent	Concentration (mmol/L)	Temperature (°C)	Reaction Time (minutes)	Radiochemical Yield n.d.c (%)
MeCN	25	90	15	0.2
MeCN	25	95	30	0.3
DMF	90	130	30	3.1
DMSO	90	140	30	0

*Table 3.6: Radiolabelling of **(19)** via conventional heating*

Solvent	Temperature (°C)	Power (W)	Reaction Time (seconds)	Radiochemical Yield n.d.c (%)
DMF	100	40	50	2.0
DMF	130	50	100	3.5
DMF	120	50	60	2.6
DMF	100	40	35	7.0
DMF	90	40	30	6.4
*DMF	90	40	30	3.0
**DMF	90	40	30	19.8
**DMF	90	40	30	20.7

*[^{18}F]Fluoride purified with a QMA pre-drying step

**[^{18}F]Fluoride purified with a QMA pre-drying step plus addition of TEMPO

*Table 3.7: Radiolabelling of **(19)** via microwave irradiation (concentration 90 mmol/L)*

(A)

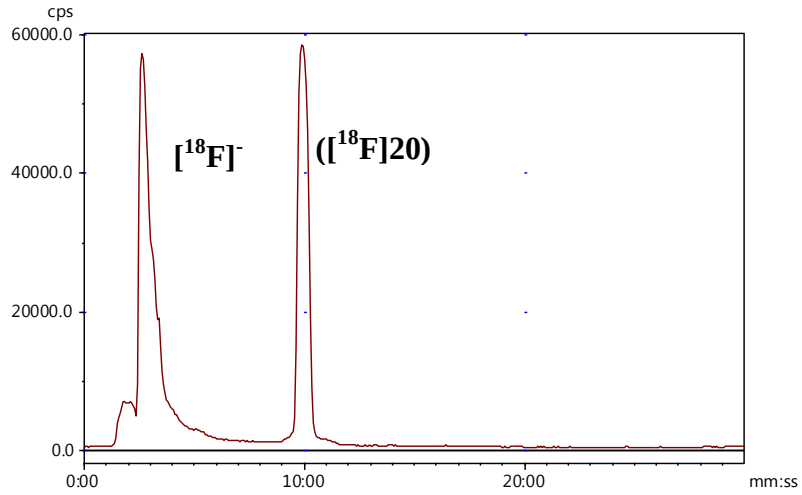

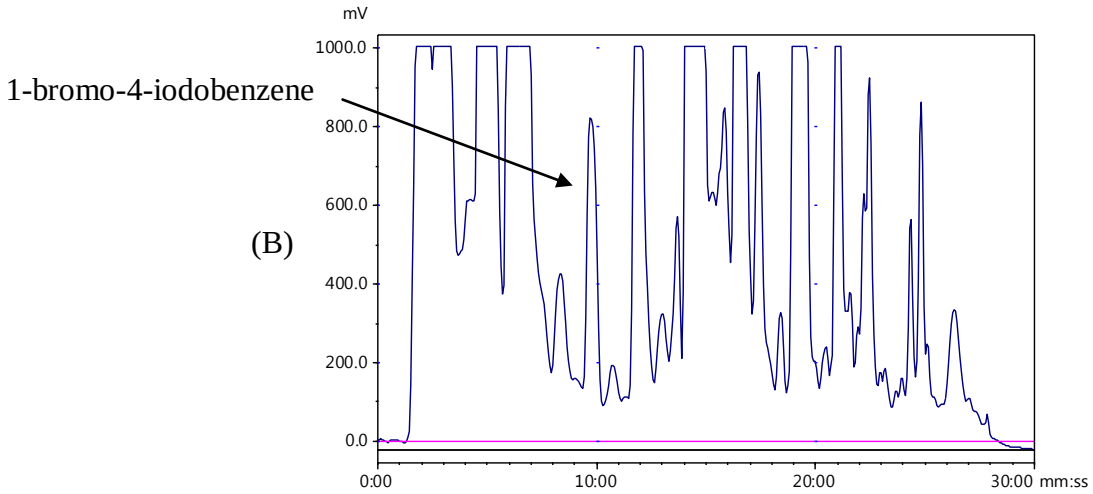

Figure 3.8: Semi-preparative HPLC (a) radio and (b) UV chromatogram of the synthesis of ***([^{18}F]20)***

Initial radiolabelling of **(19)** showed little incorporation of fluorine-18. This was possibly due to decomposition of **(19)** from free radical reactions and metal impurities from the cyclotron source. To reduce the likelihood of side reactions, [^{18}F]fluoride was purified prior to use. Fluorine-18 in aqueous solution was trapped to a quaternary ammonium cartridge, allowing cations, water and other impurities to pass through the cartridge. Thereafter, [^{18}F]$^{-}$ was cleanly eluted with kryptofix™, K_2CO_3 and MeCN, and azeotropically dried. TEMPO, a radical scavenger was added to the precursor to prevent side reactions.[162] Subsequent reactions after purification of fluorine-18 and addition of TEMPO gave n.d.c. radiochemical yields of approximately 20% after purification by semi-preparative HPLC. This satisfactory yield allowed progression onto the Ullman coupling to prepare the target molecule (Scheme 3.21).

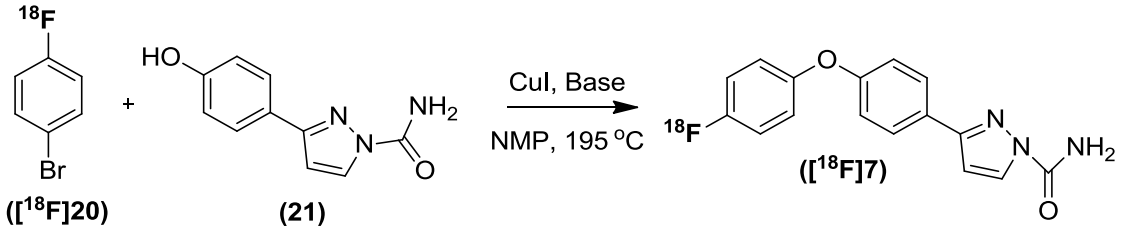

Scheme 3.21: Proposed synthesis of 3-[4-(4-[^{18}F]fluorophenoxy)phenyl]-1H-pyrazole-1-carboxamide ***([^{18}F]7)***

The classic copper-catalysed Ullman coupling allows for synthesis of both symmetrical and unsymmetrical biaryls. As a model to test reaction conditions for radiochemistry, 2-napthol was coupled with (**20**) (Scheme 3.22), following the procedure by Sperotto and co-workers.[136] The reaction was catalysed by ligand free CuI in low catalytic amount (3.5 mol% wrt to the phenol).

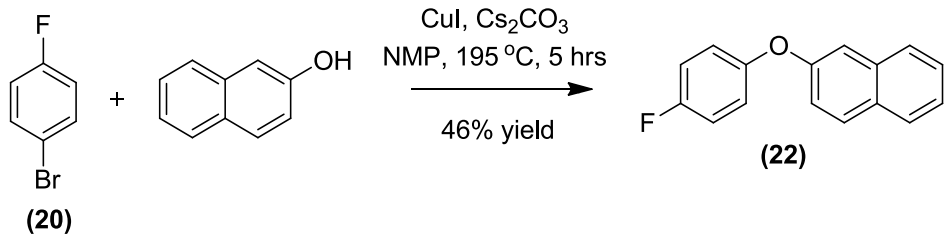

*Scheme 3.22: Synthesis of 2-(4-fluorophenoxy)naphthalene **(22)***

This reaction was monitored by analytical HPLC and after five hours **(22)** was isolated following CC (*n*-hexane) purification in 47% yield. As this proof-of-concept reaction proceeded in moderate yield, radiolabelling studies with **([^{18}F]20)** commenced (Scheme 3.23; Table 3.8 and Table 3.9) using the same reaction conditions.

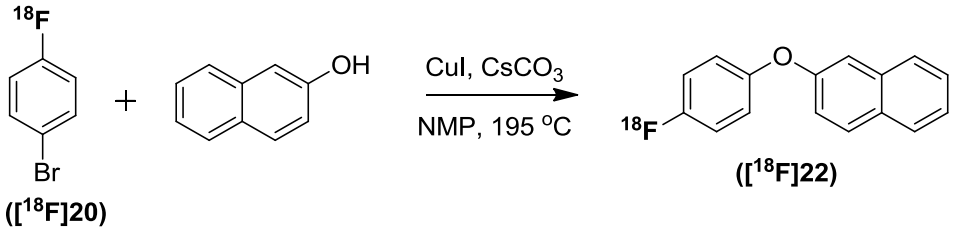

*Scheme 3.23: Proposed synthesis of **([^{18}F]22)** through an Ullman coupling reaction*

Solvent	Temperature (°C)	Reaction Time (mins)	Radiochemical Purity (%)
NMP	195	40	0
NMP	195	70	0
NMP	195	80	0

Table 3.8: Ullmann coupling via conventional heating

Solvent	Temperature (°C)	Power (W)	Reaction Time (secs)	Radiochemical Purity (%)
NMP	180	60	180	0

Table 3.9: Ullmann coupling via microwave irradiation

Initial radiochemistry showed no coupling. One explanation for this could be the presence of a large amount of the by-product 1-bromo-4-iodobenzene co-eluting with **([^{18}F]20)** upon semi-preparative HPLC purification. This by-product exhibited the same retention time as **([^{18}F]20)** making it difficult to separate even using various gradients and mobile phase conditions. 1-Bromo-4-iodobenzene can react with copper iodide, thus it was believed, that this competing reaction prevented the radiochemical reaction

from progressing. A strategy to overcome this problem was to add a higher concentration of copper iodide and heat prior to the addition of napthol and caesium carbonate. It was thought this should allow a complex to form between **([^{18}F]20)** and copper iodide.

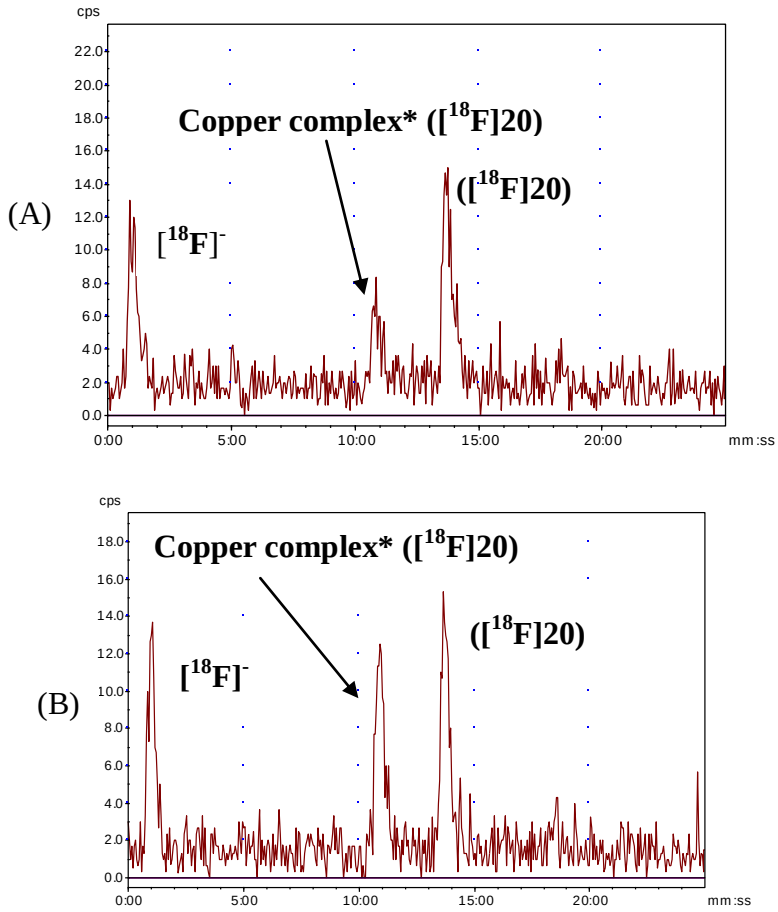

*Figure 3.9: HPLC (A) radio chromatogram after 40 minutes heating and (B) radio chromatogram after 90 minutes heating during the synthesis of **([^{18}F]20)***

The HPLC radio chromatogram showed a new radiochemical peak (Figure 3.9A) that did not correlate to the correct retention time for the product nor any previously identified side-products. It was hypothesised that this peak might be a copper complexed intermediate. Heating was continued for a further 50 minutes after the addition of napthol and caesium carbonate, but no peak corresponding to **([^{18}F]22)** was seen (Figure 3.9B) only the relative ratio of the new peak to **([^{18}F]20)** changed. Subsequently, microwave irradiation was used but this proved unsuccessful also.

Despite the Ullmann reaction showing promising results with the fluorine-19 analogue to produce **(22)**, this reaction could not be reproduced radiochemically.

After attempting numerous routes to produce **([^{18}F]7)** both directly and in-directly, radiolabelling proved unsuccessful. It was demonstrated that these molecules have a cleavable site and are unreactive towards a variety of chemistries. Alternative compounds were therefore pursued.

3.2 Synthesis of 3-(4-((4-R-phenyl)thio)phenyl)-pyrazoles

The closely related (arylthiooxy)aryl semicarbazones (Figure 3.10),[163] were reported by Dimmock *et. al.,* during their quantitative structure activity relationship (QSAR) study of the arylsemicarbazones. They reported that the optimum linker between the phenyl rings to maintain binding to VGSCs could be either an oxygen or sulphur, however, if the linker were changed beyond this, the effects were detrimental. The thioether linker was also attractive as sulphur is less electron donating than oxygen, thus it was hoped this structural alteration would remove the previous problems with S_NAr chemistry for radiolabelling. Furthermore, there is literature precedent that by oxidising the thioethers to aromatic sulphones and sulphoxides, the system may be sufficiently activated for fluorination. The semi-carbazone moiety was replaced with the pyrazole ring as previously discussed (Section 3.0).

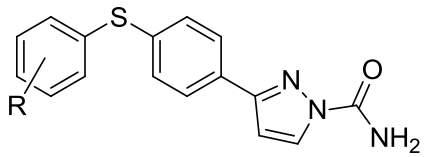

R = **(29)** 4, F
(30) 4, NO_2
(31) 2,4 F

Figure 3.10: Structure of 3-(4-((4-R-phenyl)thio)phenyl)-pyrazoles-carboxamides

The synthesis of these compounds followed the same procedure as (Scheme 3.1; Section 3.0), to afford compounds **(29)**, **(30)** and **(31)** (Scheme 3.24).

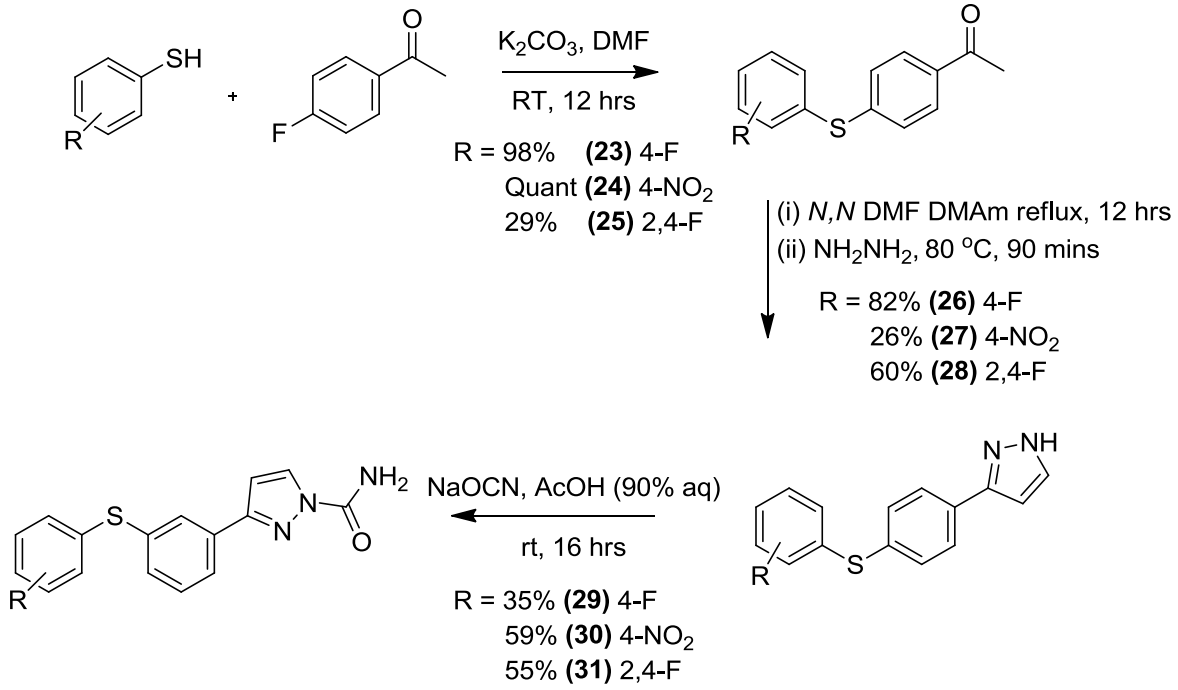

Scheme 3.24: Synthesis of 3-(4-((4-R-phenyl)thio)phenyl)-pyrazoles

Compounds **(23)** – **(25)**, the products of the Williamson reaction, were not isolated and carried onto the next step as crude material.

The pyrazole ring closure gave mixed yields with **(25)** produced in the lowest yield (26%). The subsequent carboxamide formation gave generally moderate yields to afford **(29)**, **(30)** and **(31)** (35-55%). All compounds were characterised by NMR and HRMS. Subsequently this class of compounds were evaluated for radiolabelling with fluorine-18.

3.3 General [^{18}F] radiolabelling strategies

Compound **(30)** was selected for radiolabelling initially, to determine whether our hypothesis was correct: is a thioether linker less deactivating towards S_NAr chemistry than an ether. Nitro was used as the leaving group and the carboxamide group was used to protect the secondary NH.

3.3.0. Direct fluorine-18 labelling

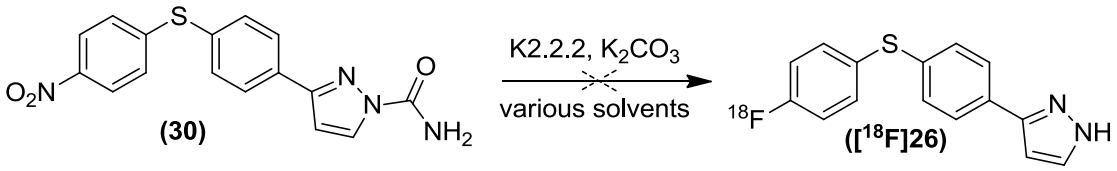

*Scheme 3.25: Attempted radiolabelling of **(30)***

Different reaction conditions were tested for labelling of **(30)** and incorporation of fluorine-18 was monitored by analytical HPLC (Table 3.10). **([^{18}F]26)** was the assumed product, due to previous results showing efficient cleavage of the amide under radiolabelling conditions.

Solvent	Temperature (°C)	Reaction Time (mins)	Radiochemical Purity (%)
DMSO	150	40	0
MeCN	100	40	0

*Table 3.10: Attempted radiolabelling of **(30)** via conventional heating*

Many different radio peaks were seen in the HPLC radio chromatogram; however, following co-injection of **(26)**, no correlation was seen. We considered the thioether bridge may have been a site of cleavage caused by attack of [$^{18}F^-$], but comparison with HPLC standards **(32)** and **(33)**, showed that neither was the radiolabelled product (Figure 3.11).

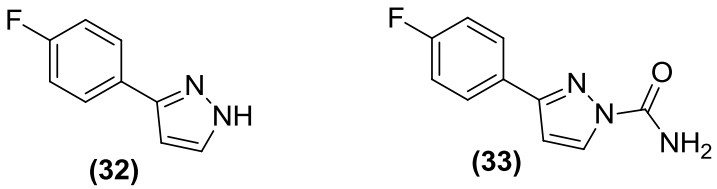

*Figure 3.11: Structure of **(32)** and **(33)***

Unfortunately, we were unable to identify any of the radioactive species. It was presumed that under the radiolabelling conditions, the molecule was unstable and decomposed.

Subsequently, the thioether bridge moiety was oxidised using hydrogen peroxide to afford a sulphone (Scheme 3.26) linker.[164] It was proposed this would stabilise the thioether bridge allowing incorporation of fluorine-18 and following reduction using sodium borohydride, cede the desired product **([^{18}F]26)**. There is precedent for this

method in the literature, Elmaleh *et. al.*, reported using a sulphone to initiate labelling of their molecule in MeCN at 140 ^{o}C, followed by reduction of the sulphone to the thioether.[165] A yield was not reported for this; as this step was the first of a multiple step pathway.

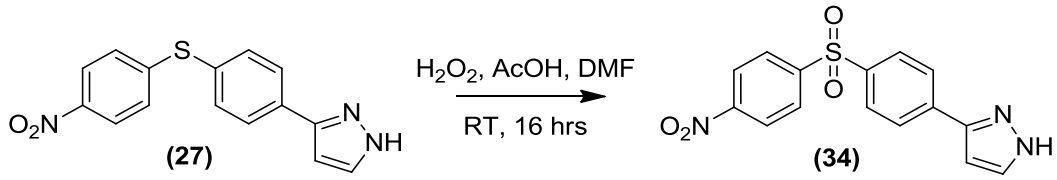

*Scheme 3.26: Synthesis of **(34)** [164]*

Following the procedure by Liu *et. al.*, oxidation of **(27)** was achieved using 29 equivalents of hydrogen peroxide in glacial acetic acid at RT. After 16 hours the reaction was quenched by addition of water which followed precipitation of the crude product and collection *via* suction filtration. Compound **(34)** was isolated and observed *via* NMR and HRMS before following onto the next step. To complete the synthesis of the precursor **(35)**, **(34)** was reacted with sodium cyanate in acetic acid (90% aq.), allowing for formation of the terminal carboxamide (as described in section 3.0).

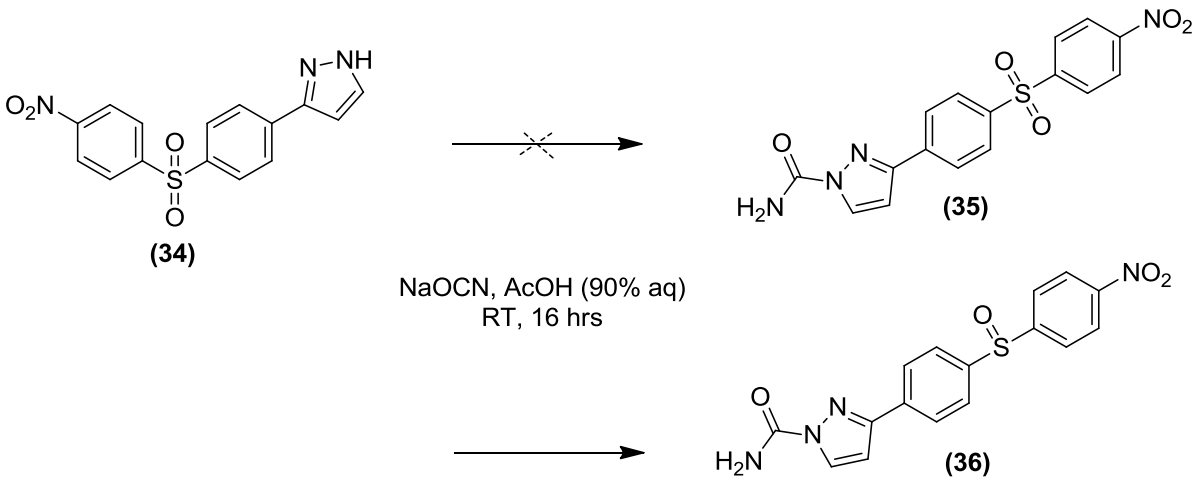

*Scheme 3.27: Attempted synthesis of **(35)***

Compound **(35)** was not identified as the product of the reaction (Scheme 3.27). From ^{1}H NMR, the terminal carboxamide was seen, characterised by the upfield shift in the pyrazole CH adjacent to the carboxamide. Infrared spectroscopy (IR) spectroscopy confirmed that a sulphoxide, rather than a sulphone had been formed. The S=O stretch band for sulphoxides was identified at 1012 cm^{-1}, whereas bands at 1325 ± 25 and 1140 ±20 cm^{-1}, characteristic of sulphones, were absent. It was not possible to characterise

this compound further. Although high resolution mass spectroscopy (HRMS) spectra were compared, **(35)** did not ionise very well under electro spray ionisation. Presumably, the acidic reaction conditions caused reduction of the sulphone affording **(36)** as the by-product in 15% yield. Although we were unable to produce a radiolabelling precursor possessing the sulphone moiety, we used **(36)** as a platform to investigate radiolabelling of sulphoxides with fluorine-18, as to the best of our knowledge there was no literature precedent for this reaction.

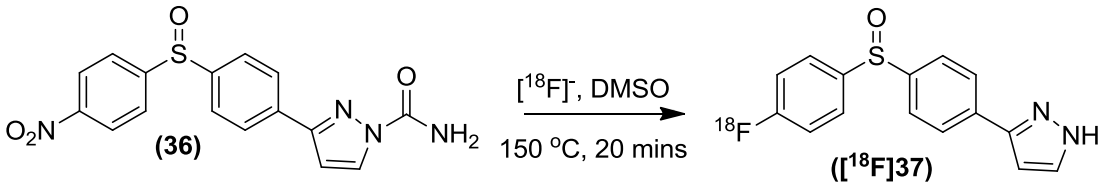

*Scheme 3.28: Radiolabelling of **(36)***

Labelling of **(36)** commenced using similar conditions to the work reported by Elmaleh *et. al.* (Scheme 3.28). DMSO instead of MeCN was used as heating the reaction 50 °C above the boiling point of MeCN might cause pressure problems within the sealed reactor. The reaction was monitored *via* analytical HPLC and a new product was seen, following co-injection of **(37)**, the product was identified as **([^{18}F]37)**. After 15 minutes no further reaction was observed, the product was purification and isolated by semi-preparative HPLC (10-95% using MeCN/H_2O over 25 minutes) affording **([^{18}F]37)** in 1.0 % n.d.c. yield.

The low isolated yield meant that using **([^{18}F]37)** as a synthon for subsequent modifications to yield **(7)** was not feasible. Very harsh conditions had been required to produce even this low yield. As a result of this work radiolabelling of the 3-(4-((4-R-phenyl)thio)phenyl)-pyrazole-carboxamides was abandoned.

3.4 Conclusion of radiolabelling studies

Following an in-depth look into the chemistry of the 3-(4-R-phenoxy)phenyl pyrazole-1-carboxamides, these compounds were shown to be difficult to label for a variety of reasons. It was proposed that S_NAr chemistry with fluorine-18 was inhibited due to the electron donating ether bridge. Secondly, we found the terminal carboxamide labile to cleave under basic conditions, even when protected with base stable protecting groups.

Consequently radiolabelled synthons such as (1-^{18}F)fluorophenol and (1-^{18}F)fluoro-4-bromobenzene (which the latter was successful) was produced, for use in in-direct labelling strategies, but were unable to utilise these synthons to produce the desired products.

Lastly, we modified the molecule to contain a thioether link between the two phenyl rings to reduce electron donation into the aromatic ring. However, this caused further problems; the molecule became so unstable that multiple radiolabelled products formed. Only one product was identified in minimal yield.

In summary, we were unable to produce a PET tracer using the given structures by Yang *et. al.*, and Dimmock *et. al*.[7, 131]

3.5. *In vitro* electrophysiological characterisation

Although we were unable to produce a fluorine-18 labelled PET tracer of 3-(3-(4-R-phenoxy)phenyl)-pyrazole-1-carboxamides and its thio derivative (Section 3.0 and 3.2), it was still important to improve our knowledge of the physiological properties of these compounds. The report by Yang *et. al.*, described limited electrophysiological data, therefore by studying these compounds in more detail, we were able to more fully characterise their biological properties. Moreover, by studying these compounds using a quantified technique, we were then able to compare with analogues produced later on (Chapter 4 and 5) in this thesis.

3.5.0. Overview of sharp microelectrode electrophysiology

Electrophysiology is the study of the electrical properties of biological cells and tissues. It involves measurements of changes in voltage or current in response to stimuli. In neuroscience, it includes measurements of the electrical activity of neurones, and particularly action potentials through commonly whole-cell patch clamp or sharp microelectrode electrophysiology.

The sharp microelectrode technique uses a thin tipped micropipette allowing the pipette to pierce the membrane, thereby recording the potential inside the cell. Due to the thinner tip (<0.5 μm), there is little ion exchange between the intracellular fluid and the

electrolyte in the pipette. The resistance of the micropipette is normally in the range of 80-100 MΩ, allowing small currents to be measured and applied.

3.5.0.0 Results

Sharp microelectrode electrophysiology was performed by Dr Andrew Constanti (UCL School of Pharmacy). This was intended to be a preliminary screen of compounds in order to provide a basis for further quantitative evaluation of potency and sub-type selectivity using automated and manual patch clamp assays. Each result presented here was confirmed in at least two neurones in different brain slice preparations. Compound **(9)** (Figure 3.12) was chosen as a "reference standard" for the development of further analogues, moreover, Yang *et. al.*, showed this compound to be the most potent with a K_i of 25 nM.[12]

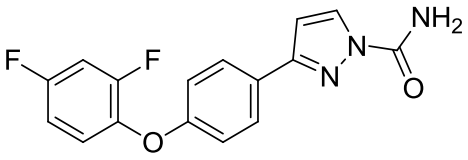

*Figure 3.12: Structure of **(9)***

Initially, recordings were taken from the hippocampus region of the brain. The hippocampus is located in the medical temporal lobe of the brain; it is part of the limbic system and plays a role in the consolidation of information in the short-term to long-term memory and spatial navigation. It contains two main interlocking parts; *Cornu Ammonis* (CA) and the dentate gyrus (DG). This area of the hippocampus is thought to contribute to the formation of new memories. The DG receives excitatory input from the entorhinal cortex; this activates pyramidal cells among the CA. CA4 and CA3 pyramidal cells *via* the Schaffer collaterals contact CA1 pyramidal cells, allowing the DG to control the flow of information within the hippocampus.[23]

The electrophysiological characterisation of **(9)** was initiated within the CA1 region of the hippocampus, an area known to be densely populated with neurones and has been reported to express Na_v 1.6.[166] The pyramidal cells were chosen as they are larger and more able to be impaled for sharp electrophysiology studies. Brain slices were obtained from Sprague-Dawley rats as previously described by Whalley *et. al.*[167] Briefly, The brain was rapidly removed following decapitation, hemisected and placed in ice-cold

oxygenated Kreb's solution at 4 °C. Transverse slices were cut 450 µm thick using a vibrating tissue slicer in ice-cold Kreb's medium. Once the slices had been cut, they were transferred to a Kreb's solution (as described in Materials and Methods) warmed to 29 °C for 1 hour to recover.

A pyramidal cell of the CA1 region was impaled and held at -70 mV (Figure 3.13). Control recordings were taken and a solution of **(9)** at 1 µM was applied for 60 minutes.

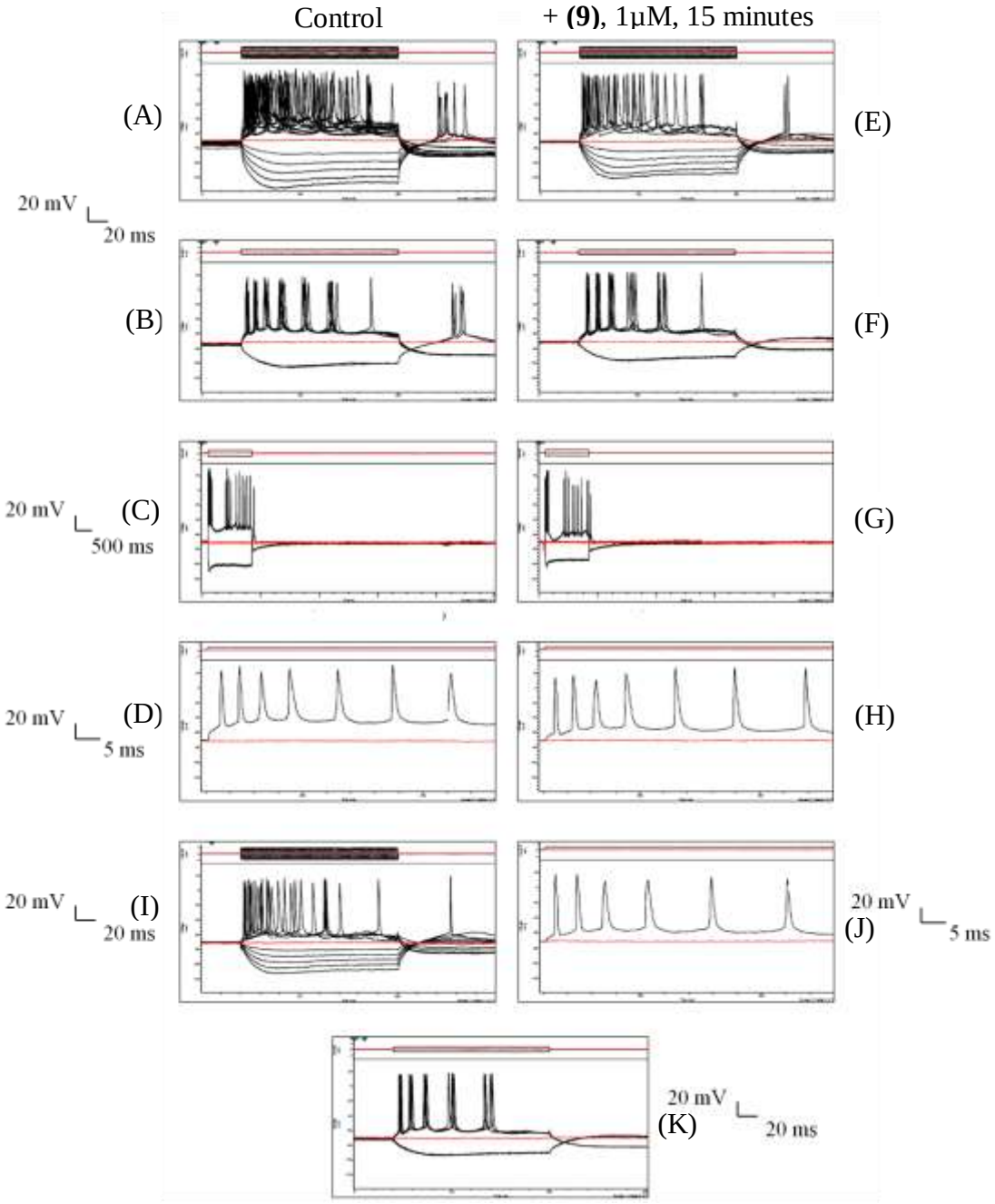

*Figure 3.13: Hippocampal CA1 neurone held at -75 mV (maintained by steady current injection). (A): Control IV relationship (± 0.2 nA steps, duration 160 ms). (B): Control positive/negative step in control (± 0.5 nA step, duration 160 ms). (C) Control long sweep (+ 0.8 nA / -0.5 nA step, duration 1.5 s). (D) Stretch of control long sweep recording from (C). (E) IV relationship (± 0.2 nA steps, duration 160 ms) showing no change in neuronal firing with **(9)** (1 µM; 15 minutes). (F) Positive/negative step (± 0.5 nA step, duration 160 ms) showing no change in neuronal firing with **(9)** (1 µM; 15 minutes). (G) Long sweep (+ 0.8 nA / -0.5 nA step, duration 1.5 s) with **(9)** (1 µM; 15 minutes). (H) Stretch of long sweep recording from (G). (I) IV relationship (± 0.2 nA steps, duration 160 ms) after 30 min washout.(J): Stretch of long sweep recording after 30 min washout. (K): Positive/negative step (± 0.5 nA step, duration 160 ms) after 30 min washout.*

In total, neuronal activity was recorded over 1 hour (30 minute traces shown; Figure 3.13), during which, no obvious changes in neuronal firing patterns nor resting membrane potential was seen.

Recording of pyramidal cells in the CA1 region was then repeated with a ten-fold higher concentration of **(9)** (Figure 3.14). A pyramidal cell of the CA1 region was also impaled and held at -70 mV. Control recordings were acquired before applying **(9)** at 10 μM for 45 minutes.

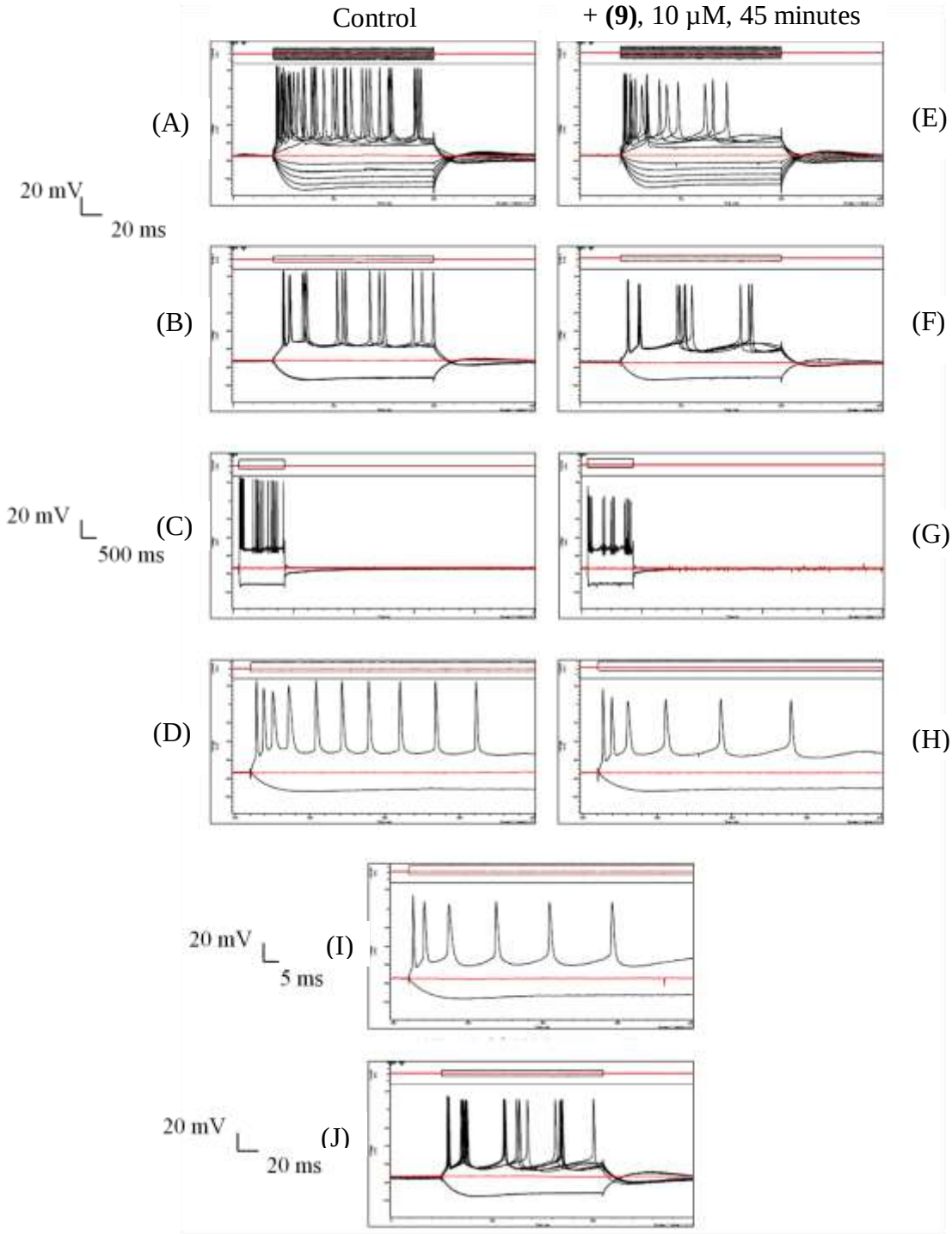

*Figure 3.14: Hippocampal CA1 neurone held at -70 mV (maintained by steady current injection). (A): Control IV relationship (± 0.2 nA steps, duration 160 ms). (B): Control positive/negative step (± 0.5 nA step, duration 160 ms). (C) Control long sweep (+ 1.0 nA / -0.5 nA step, duration 1.5 s). (D) Stretch of control long sweep recording from (C). (E) IV relationship (± 0.2 nA steps, duration 160 ms) showing inhibition of later action potentials with **(9)** (10 µM; 45 minutes). (F) Positive/negative step (± 0.5 nA step, duration 160 ms) showing clear inhibition of spikes with **(9)** (10 µM; 45 minutes). (G): Long sweep (+ 0.8 nA / -0.5 nA step, duration 1.5 s) after 45 minutes showing a change in the neuronal firing pattern. (H): Stretch of long sweep recording from (G) showing noticeable diminishing in the spike amplitude and considerable decline in the number of spikes. (I): Stretch of long sweep recording after 45 min washout. (J): Positive/negative step (± 0.5 nA step, duration 160 ms) after 45 min washout.*

At 15 minute intervals, recordings were taken to monitor the drug effect. At 45 minutes the drug effect peaked (Figure 3.14E-H). The number of action potentials and the peak spike amplitude after the first spike decreased dramatically. For example, the amplitude of the 4^{th} spike decreased by 12 mV from 65 mV in control (Figure 3.14D) to 53 mV after application of **(9)** (Figure 3.14H). After 45 minute washout, the spike amplitude showed some recovery, returning to 60 mV. The time between spikes also increased due to the longer spike after-hyperpolarizations (AHPs), most likely due to opening of more calcium channels and subsequent activation of Ca^{2+} activated K^{+} channels. The time between action potentials 4 and 5 is 20 milliseconds in control (Figure 3.14D), whereas after application of **(9)** at 10 µM for 45 minutes, this gap doubled to 40 milliseconds (Figure 3.14H). After washout, this time did not change remaining at 40 milliseconds (Figure 3.14I), indicating **(9)** had not washed out after 45 minutes. Meanwhile, the resting membrane potential remained steady and there was no change in slow inward rectification currents or input resistance. Having raised the drug concentration 10-fold, **(9)** had now exhibited reversible binding to the pyramidal cells of the CA1 with some slow washout seen after 45 minutes.

To compare these results with VGSC inhibition elsewhere in the brain, recordings were taken from pyramidal cells within layers II- III of the piriform cortex (PC). The PC lies to the posterior of the hippocampus and is associated with the generation and propagation of forebrain (limbic type) seizures.[168] To begin with, a 1 µM solution of **(9)** (1:99 EtOH/Kreb's) (Figure 3.15) was tested. The piriform cortex was studied due to good neuronal activity in this area. A pyramidal cell of the PC was impaled and held at a membrane potential of -70 mV (Figure 3.15). Control recordings were then taken, followed by application of **(9)** at 1 µM for 15 minutes.

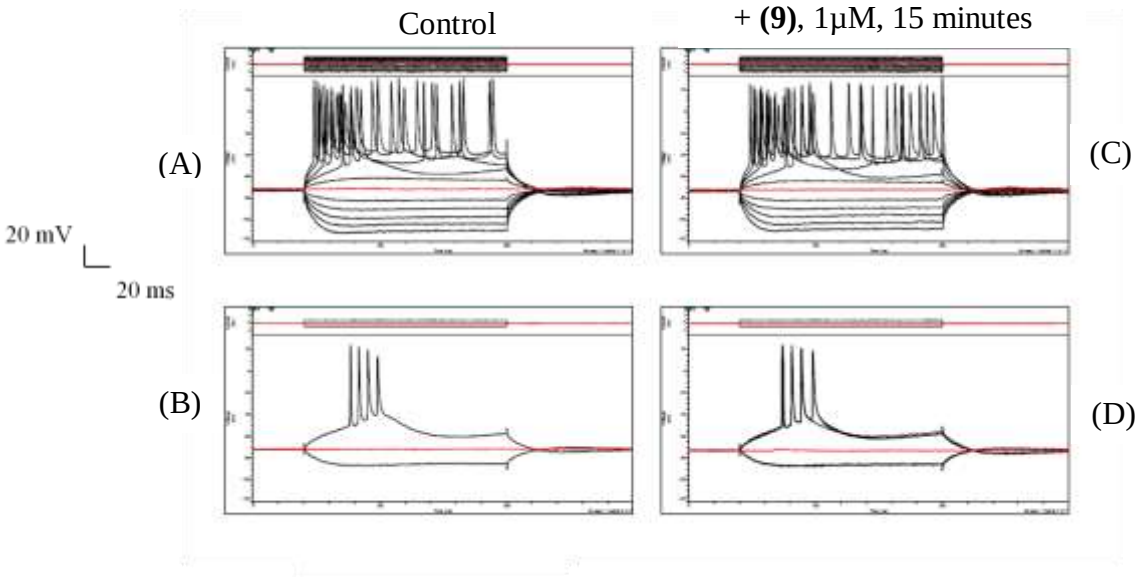

*Figure 3.15: Piriform cortex neurone held at -70 mV (maintained by steady current injection). (A): Control current/voltage (IV) relationship (± 0.2 nA steps, duration 160 ms). (B): Control positive/negative step (± 0.4 nA step, duration 160 ms). (C) IV relationship (± 0.2 nA steps, duration 160 ms) showing no change in neuronal firing with **(9)** (1 µM; 15 minutes). (D) Positive/negative step (± 0.4 nA step, duration 160 ms) showing no change in neuronal firing with **(9)** (1 µM; 15 minutes).*

On comparing the control recordings with recordings after application of **(9)** over 15 minutes, no change in neuronal firing was seen, whilst resting membrane potential remained steady and no change in input resistance occurred. No washout was recorded due to the lack of effect. Unfortunately, no data are reported about VGSC isoform expression in the PC. It was hypothesised however, that there is a difference in the isoform expression between the PC and CA1 to explain these results.

With **(9)** at 1 µM having no obvious efficacy in the PC region, we increased the concentration ten-fold to see the effect this higher concentration would have.

A pyramidal cell of the PC was impaled and held at a membrane potential of -70 mV. Control recordings were then taken, followed by application of (9) at 10 µM for 30 minutes. Still, no change in neuronal firing was seen (traces not shown), so the concentration of (9) was increased to 20 µM (Figure 3.16) whist stimulating the same pyramidal cell.

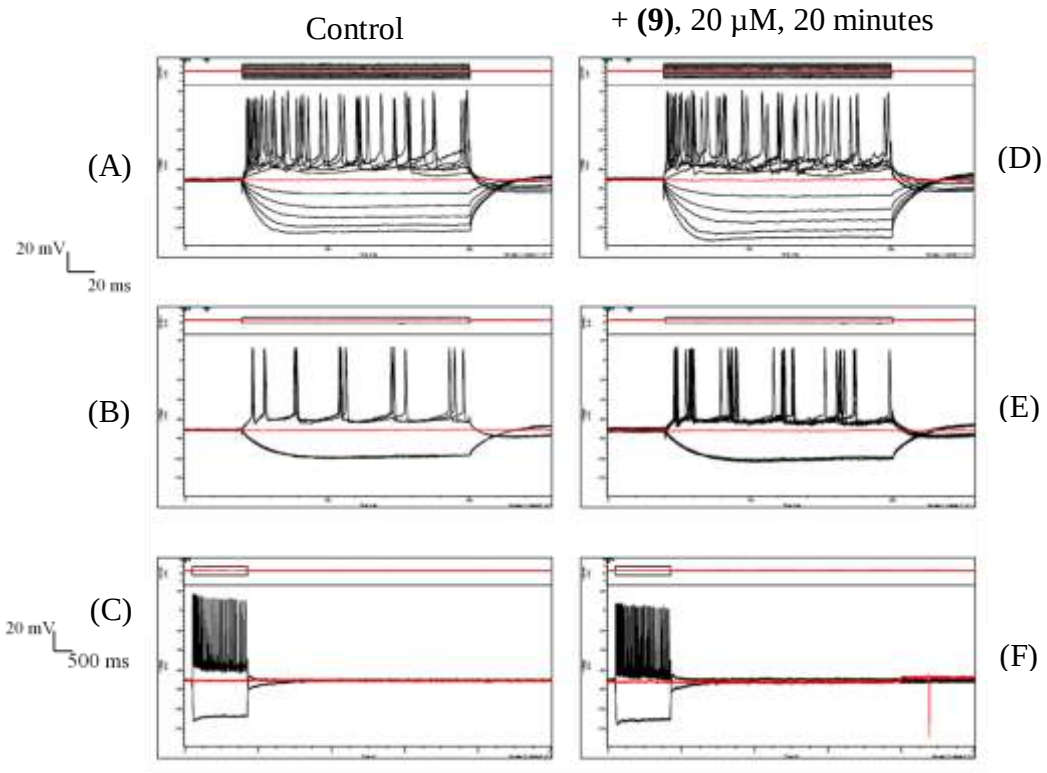

Figure 3.16: Piriform cortex neurone held at -70 mV (maintained by steady current injection). (A): Control current/voltage (IV) relationship (± 0.2 nA steps, duration 160 ms). (B): Control positive/negative step (± 0.5 nA step, duration 160 ms). (C) Control long sweep (+ 0.8 nA / -0.5 nA step, duration 1.5 s). (D) IV relationship (± 0.2 nA steps, duration 160 ms) showing no change in neuronal firing with (9) (20 µM; 15 minutes). (E) Positive/negative step (± 0.5 nA step, duration 160 ms) showing no change in neuronal firing with (9) (20 µM; 20 minutes). (F) Long sweep (+ 0.8 nA / -0.5 nA step, duration 1.5 s) after 20 minutes showing no change in the neuronal firing pattern.

After increasing the concentration of (9) to 20 µM, there was still no strong change in neuronal firing frequency nor resting membrane potential. When comparing traces from Figure 3.16C and F showing the long sweep, there is a slight diminishing of the spike amplitude. The lack of effect was anticipated to be an indication of VGSC subtype selectivity. No further concentrations were tested; having concluded this drug is inactive within the low micromolar concentration range in this brain region.

Upon completion of intial testing of **(9)**, **(25)** was studied using the same procedure and in the same brain region for direct comparisons. Subsequently, **(25)** was tested also beginning in the CA1 region of the hippocampus. A pyramidal cell of the CA1 region was impaled and held at -70 mV. Control recordings were taken and a solution of **(25)** at 10 µM was applied for 30 minutes (traces not shown). During this time, no change in neuronal firing nor membrane potential was seen. The concentration of **(25)** was then increased to 20 µM whilst stimulating the same pyramidal cell. However, the neuronal firing pattern remained steady (traces not shown) even at this increased concentration.

Finally, the drug concentration was increased to 30 µM and the same pyramidal cell was stimulated for a further 70 minutes (Figure 3.17).

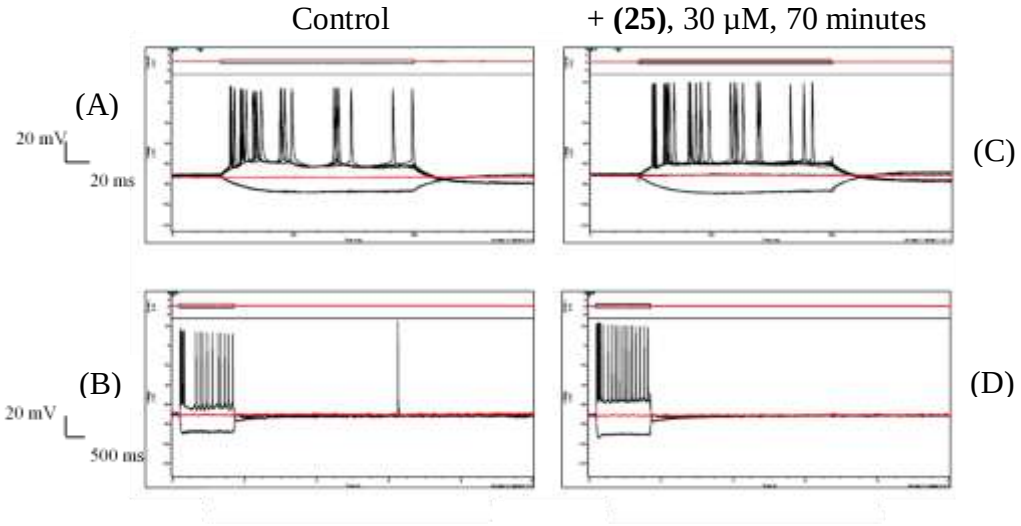

*Figure 3.17: Hippocampal (CA1) neurone held at -70 mV (maintained by steady state injection). (A) Control positive/negative step (± 0.5 nA step, duration 160 ms). (B) Control long sweep (+ 0.8 nA / -0.5 nA step, duration 1.5 s). (C) Positive/negative step (± 0.5 nA step, duration 160 ms) showing no change in neuronal firing with **(25)** (30 µM; 70 minutes). (D) Long sweep (+ 0.8 nA / -0.5 nA step, duration 1.5 s) after 70 minutes showing no change in the neuronal firing pattern.*

At this highest concentration, **(25)** showed minimal effect in the CA1 region (maximum concentration 30 µM; 70 minutes incubation). Upon comparison of the control and drug traces, traces with drug showed a slightly faster firing rate. Currently, **(25)** has not been assessed in the PC region.

3.5.0.1 Discussion

Initially, **(9)** was studied in both the CA1 region of the hippocampus and in the PC. This compound showed a good effect in the CA1 region of the brain (up to 10 µM) to reduce spike amplitude and repetitive firing, whereas in the PC little effect was noticed (only slight reduction in the spike amplitude up to 30 µM). It has been reported that there is a high expression of Na_v 1.6 in the hippocampus, with respect to Na_v 1.1, 1.2 and 1.3 also found in the brain. [166] However, nothing could be found on the relative expression of VGSCs in the PC, thus it was difficult to tell whether Na_v 1.6 was also found in the PC or not. It was inferred from the electrophysiology that perhaps there is a lack of this sub-type expressed in this region. Thus, it was proposed that **(9)** was showing some selectivity for Na_v1.6.

Subsequently, **(25)** was studied to ascertain whether the alternative thioether link increased or decreased potency towards VGSCs. After testing at numerous concentrations in the CA1 (up to 30 µM), no change in neuronal firing was exhibited, nor was there any change to the resting membrane potential. Thus, **(25)** was shown to be inactive at the concentrations tested (30 µM maximum concentration). It was concluded that the introduction of the thioether link was the most likely cause of the lack of potency. Although, Dimmock *et. al.,* described these compounds as potent VGSC blockers, our studies showed them to be inactive.[131]

As a result of initial data, **(9)** was evaluated further in an automated patch clamp study using cultured cells expressing Na_v 1.1 to 1.7 (Section 3.5.1) to ascertain if any, VGSC subtype selectivity. **(25)** was also included as a negative control to moderate the results between the two electrophysiological studies, but also to see if **(25)** showed binding to any non-CNS expressed VGSC.

3.5.1 Overview of automated electrophysiology

Compounds **(9)** and **(25)** were screened to highlight VGSC sub-type selectivity following some initial positive electrophysiological evaluation on brain tissue. As only certain VGSC isoforms are expressed in different tumours, we also needed to ascertain which VGSCs (if any), this family of compounds were selective for. These two compounds were screened by ChanTest® US, using their automated IonWorks Quattro™ patch clamp system on transfected CHO (Chinese hamster ovary) cells stabling expressing Na_v1.1 – 1.7 from the organism *Cricetulus griseus*. They screened 8 different concentrations (0.01-30 µM) to obtain a dose-response relationship and lidocaine (3 mM) was used as the positive control drug to block all sodium currents at the end of each experiment. The IC_{50} of both **(9)** and **(25)** was evaluated in three experiments: tonic block (no stimulation applied), frequency-dependent block (following 10 Hz frequency stimulation) and inactivated state block (following a conditioning depolarising pulse).

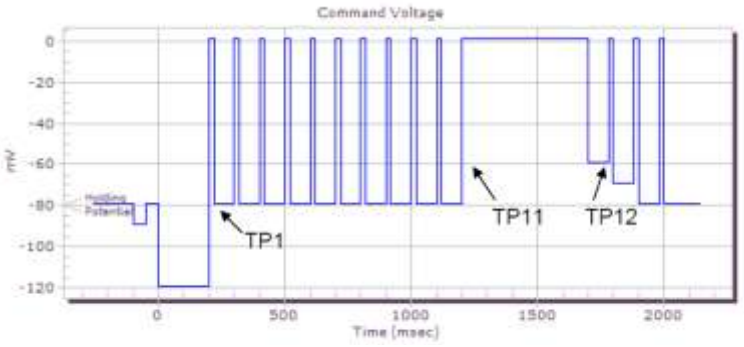

Figure 3.18: Voltage step protocol for hNa$_v$1.x test procedure

Three protocols were used to study binding to Na_v 1.1-1.7; tonic, frequency dependent block and inactivated state block.

Tonic block was ascertained by measuring binding at -80 mV (resting membrane potential), the measurement was calculated as follows:

$$\text{Tonic block (\%)} = (1\text{-}ITP_1,TA/ITP_1,control) \times 100\%$$

Where ITP_1, control and ITP_1, TA are the peak inward sodium currents elicited by the test pulse (TP_1) in control and in the presence of each compound.

Frequency dependent block was ascertained by increasing the stimulation frequency to 10 Hz, this protocol highlighted whether the compounds were only binding to the channels under a strong stimulation. Frequency dependent block was calculated as follows:

$$\text{10 Hz block (\%)} = (1\text{-}ITP_{11},TA / ITP_{11},control) \times 100\%$$

Where ITP_{11}, TA and ITP_{11},control are the peak inward sodium currents elicited by the TP_{11} in control and in the presence of a test article.

Inactivated state block, was measured by holding 500 ms stimulation to 0 mV, this established all the channels in the inactivated state. Inactivated block was calculated as follows:

$$\text{Inactivation state block (\%)} = (1\text{-}ITP_{12},TA / ITP_{12},control) \times 100\%$$

Where ITP_{12}, TA and ITP_{11}, control are the peak inward currents elicited by the TP_{12} in control and in the presence of the test article.

Concentration-response data with standard error for the blocks was fit to an equation of the following form:

$$\text{Block} = \%\ VC + \{(100 - \%\ VC) - (100 - \%\ VC) / [1 + ([Test] / IC_{50})^{N}]\}$$

where [Test] was the concentration of test article, IC_{50} was the concentration of the test article producing half-maximal inhibition, N was the Hill coefficient, % VC is the percentage of the current run-down (the mean current inhibition at the vehicle control) and % Block is the percentage of ion channel current inhibited at each concentration of the test article. Nonlinear least squares fits were solved with the XLfit, (model 201) add-in for Excel 2003 (Microsoft, Redmond, WA). In case of maximal blocking effect less than 50% or minimal blocking effect greater than 50%, the IC_{50} value was not calculated.

3.5.1.0 Results

Following automated patch clamp experiments on Na_v 1.1-1.7 in CHO cells, **(9)** was shown to be a state-dependent blocker of VGSCs. In particular **(9)** was shown to be most potent for Na_v 1.5 (IC_{50} = 0.78 ±0.29 µM) followed by Na_v 1.4 (IC_{50} = 1.26 ± 0.29 µM) and then Na_v 1.2 (IC_{50} =1.53 ± 0.49 µM). **(25)** however, was shown not to block VGSCs over the concentrations tested (maximum concentration tested 30 µM) in any isoform. Results are detailed in Table 3.11.

In each block, the test pulse (Figure 3.18) was repeated twice; before and 5 minutes after compound addition. Peak current amplitudes at three test pulses were measured (ITP_1, ITP_{11} and ITP_{12}).

No	Type of block	IC_{50} (µM)						
		Nav 1.1	Nav 1.2	Nav 1.3	Nav 1.4	Nav 1.5	Nav 1.6	Nav 1.7
(9)	Tonic	>30	>30	>30	>30	>30	>30	>30
	10 Hz	>30	>30	>30	>30	6.37 ± 2.71	>30	>30
	Inact.	5.46 ± 0.49	1.53 ± 0.49	6.82 ± 3.3	1.26 ± 0.29	0.78 ± 0.29	2.84 ± 0.95	>30
(25)	Tonic	>30	>30	>30	>30	>30	>30	>30
	10 Hz	>30	>30	>30	>30	>30	>30	>30
	Inact.	>30	>30	>30	>30	>30	>30	>30

*Table 3.11: Summary of **(9)** and **(25)** IC_{50} values with Na_v 1.1-1.7*

3.5.1.1 Discussion

This study highlighted the sub-type selectivity of **(9)** and confirmed that **(25)** is not a VGSC blocker under these test conditions used. Upon comparison of these results with Yang and co-workers reported findings on **(9)**, this compound appeared to be less potent. They showed **(9)** to have a K_i of 25 nM in human skeletal muscle (hSkM) tissue (expressing Na_v 1.4) but our study found the IC_{50} for Na_v 1.4 to be 1.26 ± 0.29 µM. This automated study did not measure binding kinetics of **(9)** and **(25)**, only IC_{50} values were afforded. Thus, we cannot directly compare K_i to our IC_{50} data, although one would expect the values to be similar. These results were unexpected, but the protocol used only stimulated the channels twice and each compound was only allowed to superfuse for 5 minutes (this protocol was not changeable). Through sharp microelectrode electrophysiological recordings reported in Section 3.4.0.1, we showed that it took at least 20 minutes for **(9)** to have a full effect on neuronal activity. In conclusion, our study indicated that **(9)** binds to all Na_v 1.1 -1.6 at <7 µM. It was most selective for Na_v 1.5, while potency for Na_v 1.4 and Na_v 1.6 were in the same order of magnitude.

The next step was to identify a more accurate IC_{50} value for both Na_v 1.4 and Na_v 1.5 for comparison with analogues of **(9)** (Chapter 4 and 5) and with literature reported values. As a result of these data, **(25)** however, was not incorporated into further studies.

3.5.2 Overview of patch clamp electrophysiology

Patch clamp techniques allow the study of single or multiple ion channels in cells under current clamp. There are different variations of patch clamp techniques, for example cell-attached recordings, whole-cell recordings, outside-out patch, inside-out patch and perforated patch clamp. These techniques use a glass micropipette with an open tip of diameter (0.5-1 μm), a size enclosing a membrane surface area or "patch" that often contains just one or a few ion channels. This technique requires the micropipette to seal onto the surface of the cell membrane rather than insert through it, as in traditional sharp microelectrode recordings. The interior of the pipette is filled with a solution matching the ionic composition of the cell interior. A chlorided silver wire is placed in contact with this solution and conducts electric-current to the recording amplifier. The micropipette is pressed against a cell membrane and suction is applied to assist in the formation of a high resistance seal between the glass and the cell membrane. This is known as a "gigaohm seal" (10^9 Ω), since the electrical resistance of the seal is in excess of a gigaohm. The high resistance of this seal makes it possible to electronically isolate the currents measured across the membrane with little noise competing, as well as providing mechanical stability for the recordings.

Perforated patch clamp was used in the proceeding study. In this variation of whole-cell recordings, a gigaohm seal forms, but no suction is required to rupture the patch membrane. Instead, the electrode solution contains small amounts of an antifungal or antibiotic agent, such as amphothericin-B, nystatin, or gramicidin. As the molecules diffuse into the membrane patch, they create small perforations in the membrane, providing access to the cell interior. This technique reduces the dialysis of the cell that occurs in whole-cell recordings allowing longer drug incubation time. This method also has several disadvantages associated with it. First, the access resistance is higher (access resistance being the sum of the electrode resistance and the resistance at the electrode-cell junction). The high resistance decreases electrical access and thus current resolution, which increases recording noise, and magnifies any series resistance error. Secondly, it can take a significant amount of time for the antibiotic to perforate the membrane (10–30 minutes, though this can be reduced with thin tipped electrodes). Thirdly, the membrane under the electrode tip is weakened by the perforations formed by the antibiotic and can rupture. If the patch ruptures, the recording is then in whole-cell mode, with antibiotic contaminating the inside of the cell.

Patch-clamp studies were undertaken on $Na_v1.4$ and 1.5 channels only, due to earlier results highlighting **(9)** as binding preferentially to these channels (Section 3.5.1.0). The I-V relationship was used to calculate half-inactivation potential (IC_{50}), and 500 milliseconds pre-pulses used to create inactivation curves for estimation of channel availability (hα); all experiments were conducted using a holding potential of -90 mV to ensure maximum channel availability and block of the resting state; and half-inactivation between -80-60 mV was used to ensure block of the inactivated state. The rapid kinetics and complete inactivation of the currents were in line with published data.[18]

3.5.2.0 Results

$hNa_v1.4$ and 1.5 were stably expressed in HEK-293 cells, **(9)** was tested at 4 concentrations (0.1, 1, 10 and 30 µM) to ascertain an accurate IC_{50} value. These concentrations were chosen based on previous electrophysiological work which indicated an approximate IC_{50} in the low micromolar range. Using the resting and inactivated state protocol (Section 2.4.2), **(9)** showed a preference for binding to the inactivated state.

Following testing in hNa_v 1.4, **(9)** had approximately 5000-fold higher affinity for P2 (inactivated) compared to P1 (resting), with an IC_{50} 2 nM vs 10 µM, respectively. The maximal inhibitory response (I_{max}) of **(9)** was approximately 98% total block at the maximal concentration of 30 µM in P2, whilst only 62% was seen in P1. No standard error is reported for the IC_{50} value. The dose-response curve (Figure 3.19) indicated that all concentrations tested gave >50% block. Therefore, the IC_{50} value quoted was reported using a non-linear regression fit algorithm (GraphPad Prism version 5.0) to extrapolate the data. The graph below shows the trough of a standard inhibition dose response curve.

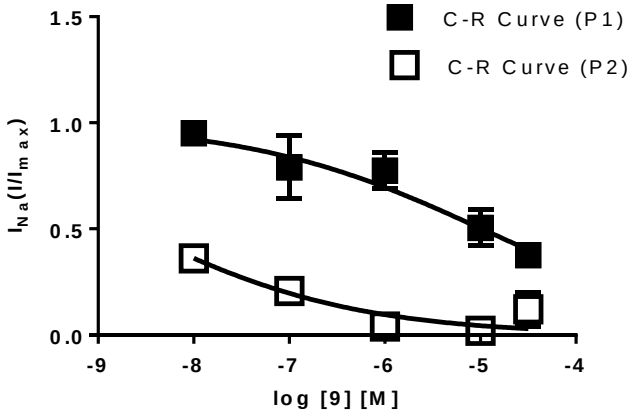

*Figure 3.19: Dose response curve of hNa$_v$ 1.4 of **(9)** (0.1-30 µM) under P1 and P2 conditions.*

Following testing on hNa$_v$ 1.5, **(41)** also showed a higher affinity for P2 compared to P1 (Figure 3.20). The IC$_{50}$ for P2 was calculated as 41 nM, however, an IC$_{50}$ for P1 at the highest concentration of 30 µM could not be afforded, due to its limited inhibitory activity at resting state. The maximal inhibitory response (I$_{max}$) of **(9)** on hNa$_v$ 1.5 current was approximately 94% of control for P2 and 14% of control for P1 at the maximum concentration tested of 30 µM.

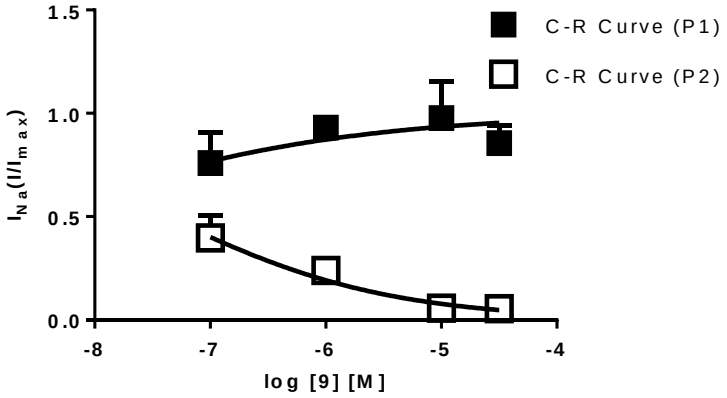

*Figure 3.20: Dose response curve of hNa$_v$ 1.5 of **(9)** (0.1-30 µM) under P1 and P2 conditions.*

The dose-response curve for these results (Figure 3.20) is similar to that seen for hNa$_v$ 1.4. It also highlights the trough section of a dose response curve. Block saturation was seen at 10 µM and but all concentrations again afforded >50% block. No standard error is given as described for hNa$_v$ 1.4 due to the high variance with extrapolating data. The value afforded is the best estimate of the IC$_{50}$ according to the non-linear regression best fit algorithm.

3.5.2.1 Discussion

This assay showed **(9)** to be highly selective for the skeletal muscle sodium channel (Na_v 1.4; IC_{50} = 2 nM *vs* Na_v 1.5; IC_{50} = 41 nM). Whereas in the previous assay, there was approximately equal selectively between the two channels (when including error variance). The estimated IC_{50} values quoted for each channel here, indicated that **(9)** is far more potent than was initially established (Section 3.5.1.0). Moreover, the concentrations tested were based on those previous results, but it appeared that the automated electrophysiological screen was inaccurate in indicating likely IC_{50} values. The values quoted here, are three orders of magnitude more potent. Although there is a high margin of error associated with these extrapolated values, this study showed that **(9)** has an IC_{50} around the low nanomolar range on both channels.

The most likely reason for the difference in potency between these results and the automated electrophysiology results is the incubation time allowed. When developing a protocol for the automated electrophysiology, the incubation time used was not changeable. Therefore all compounds were screened for 5 minutes in each state (resting, frequency dependent and inactivated). The main concern about the inaccuracy of those data, was that the maximum effect at each concentration was not being seen within 5 minutes. This study aimed to minimise that error by incubating the cells until a steady state effect was reached (approximately 20-30 minutes). Therefore these results are more precise. Unfortunately it could not be foreseen that the potency of these compounds would be quite so different from that indicated previously. The dose response curves shown, gives a true indication of inhibition at each concentration, but future work will require lower concentrations being tested to get an exact determination of the IC_{50} value. Overall, **(9)** is more potent than previously established and these data appear to corroborate to the potency values reported by Yang *et. al.*

Following electrophysiology studies undertaken, a binding study would normally be the next step to afford values of B_{max}, K_d and ultimately binding potential using **[^{3}H](9) (**as it was not possible to label with fluorine-18). This would have allowed an estimation of whether **(9)** was worth pursuing in further radiochemical studies, and also, whether an analogue of this compound would be suitable as a radiotracer for VGSCs. After consulting numerous companies who perform trituration and radioligand binding assays, we were unable to find a company which could perform binding assays on cell lines expressing Na_v 1.4 and 1.5.

Although it was not ideal that binding studies had not been performed on these compounds, the electrophysiology data suggested that this class of compounds could serve as a good basis for future analogue development.

However, to allow an approximation of the binding potential of **(9)** to Na_v 1.5, data from [^{3}H]BTX studies on cardiomyocytes was used, to give an approximation of VGSC B_{max}. Sheldon and co-workers reported that the B_{max} for [^{3}H]BTX in cardiomyocytes was 6.6 µM. We assume, as BTX is a potent VGSC ligand, that this B_{max} value could be used as an approximate indication of the VGSC expression in the heart. In order to afford an estimation of the binding potential for **(9)**, the approximate IC_{50} value for Na_v 1.5 (41 nM) was used as a substitute for K_d.[169]

Therefore:

Binding Potential = B_{max} / K_d

= 6.6 µM / 41 nM

= 160

Whilst it is noted that the assumptions made in the above calculation only allow for a very approximate indication of binding potential, this figure is ten times greater than the suggested minimum value. Thus, **(9)** appears to be a promising compound and it is unfortunate that a labelling pathway could not be found. Additioanlly though, this value does highlight that pursuing this class of compound is warranted.

3.6 *In vivo* characterisation

3.6.0 Naive biodistribution

In previous work conducted by Arstad,[170] **(9)** was tritiated by GE Healthcare, Amersham and studied through naive mouse biodistribution.

3.6.0.0 Results

This naive biodistribution (Figure 3.21) is the only historical *in vivo* data reported to show the behaviour of **(9)** in an animal model. Therefore we show here for comparison with data presented in Chapters 4 and 5. Unfortunately as this biodistribution used low energy tritium [^{3}H] and not [^{18}F], it was not possible to directly compare these data with fluorine-18 labelled analogues. However, it is interesting to note the uptake and clearance trend of **([^{3}H]9)** for general comparison.

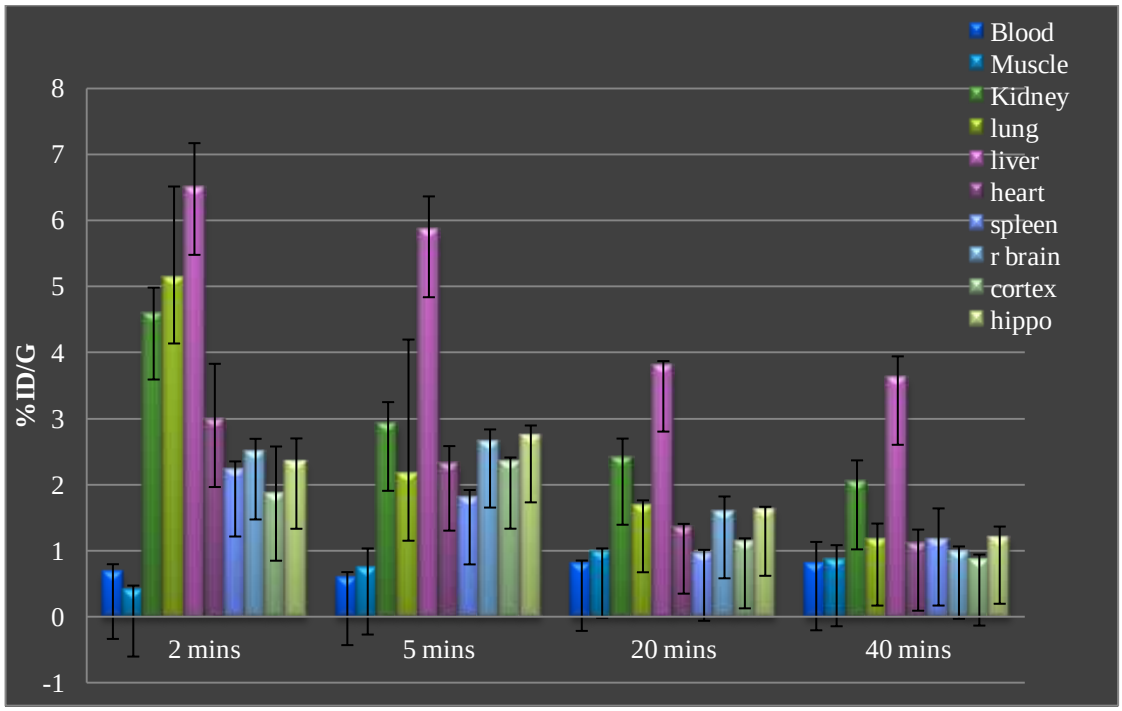

*Figure 3.21: Naive biodistribution graph for **([^{3}H]9)***

Good uptake was seen in the (whole) brain (total brain; 6.65% id/g) and heart (2.96% id/g) at 2 minutes which decreased to (whole) brain (total brain; 3.02% id/g) and heart (1.09% id/g) by 40 minutes, consistent with reversible uptake. Little uptake was seen in the muscle (0.4% id/g), which was surprising as Yang *et. al.*, and recent data showed this compound to have good efficacy for Na_v 1.4 (expressed in the skeletal muscle) [7]. High uptake was seen in the kidney (4.59% id/g), lung (5.13% id/g) and liver (6.48% id/g) at 2 minutes whilst after 20 minutes levels in the kidney (2.39% id/g) and liver (3.80% id/g) remained high, suggesting the compound is metabolised in the liver and cleared through the renal system.

Although the brain biodistribution was separated into right, cortex and hippocampus, here, the % id/g is quoted as total brain. In subsequent studies, the brain was not separated in this way, so the values of total brain are more important here.

3.6.0.1 Discussion

It was difficult to draw too many conclusions from these data as this was the first indication of the compounds behaviour *in vivo*. It appears that there was good uptake of **([^{3}H]9)** and this was reversible within 40 minutes. However, *in vivo* stability cannot be inferred as with fluorine-18 labelled compounds, where fluorine uptake in the bone can indicate *in vivo* stability (with respect to de-fluorination). In summary, this biodistribution has given an insight into the uptake profile of this compound for use as a general trend for comparison with analogues of **(9)** labelled with fluorine-18, presented later.

3.7 Conclusions of chapter 3

In summary, **(9)** was shown to be a potent sub-type selective VGSC blocker. Following numerous pathways to radiolabel this compound with fluorine-18, we were unable to find any success in our pursuits. Subsequently, we were able to offer a more detailed characterisation of **(9)** through both sharp electrode and patch-clamp electrophysiology. We showed that **(9)** selectively binds to the cardiac sodium channel (Na_v 1.5) and SkM sodium channel (Na_v 1.4). This result was interesting, as previously reported work had only been carried out on Na_v 1.4, our work allowed for a more detailed and wider analysis of **(9)**.[7]

Following on, **(25)** showed no binding to any VGSC subtype over the concentrations tested, this was in contrast to previous reports.

As **(9)** had shown to be a promising VGSC ligand through initial evaluation, analogues of **(9)** were pursued to overcome the problems of radiolabelling.

4. Results and Discussion

Design, synthesis and bioevaluation of [^{18}F]3-(4-(2,4-difluorophenoxy)phenyl)-1-(2-fluoroethyl)-pyrazole

4.0 Rationale for novel tracer

Due to the difficulties surrounding the labelling of the 3-(4-(4-R-phenoxy)phenyl)-pyrazole-1- carboxamides with fluorine-18 (chapter 3), strategies were developed to generate analogues of the 3-(4-phenoxyphenyl)pyrazole-1-carboxamides, to provide more reliable radiolabelling pathways. A well known reaction for introducing fluorine-18 is the base activated fluoroalkylation with [^{18}F]fluoroethyltosylate **([^{18}F]38)** (Scheme 4.1). [^{18}F]Fluoroethyl tosylate is a reliable radiochemical synthon and has been used in the synthesis of many PET ligands and reactions generally proceed in high yields.[171-175]

4.1 Synthesis of 3-(4-(2,4-difluorophenoxy)phenyl)-1-(2-fluoroethyl)-pyrazole

In initial studies, we proposed a fluoroalkylation of the terminal carboxamide of **(9)** with fluoroethyl tosylate **(38)** to afford **(39)** (Scheme 4.1). Various bases and conditions were employed to optimise this chemistry (Table 4.1).

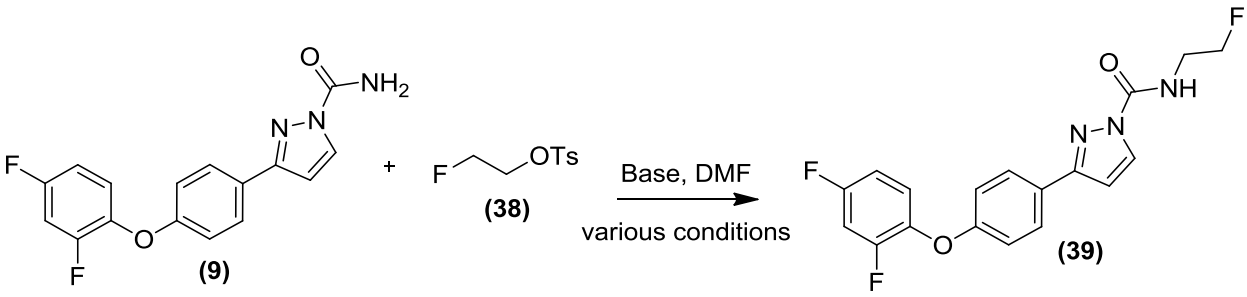

*Scheme 4.1: Proposed fluoroalkylation of **(9)***

Base	Temperature (°C)	Reaction Time (hrs)	Product
Cs_2CO_3	55	12	(6)
DIPEA	100	2	(6)
NaH	rt/50	1	(6) + (40) + (41)
DBU	Rt	1	(6)
$KHCO_3$	50	4	(6)

*Table 4.1: Conditions for fluoroalkylation of **(9)***

During our testing of reaction conditions using various bases, total cleavage of the carboxamide was seen without any product formation. Production of **(6)** and remaining **(38)** however, was seen in high concentration.

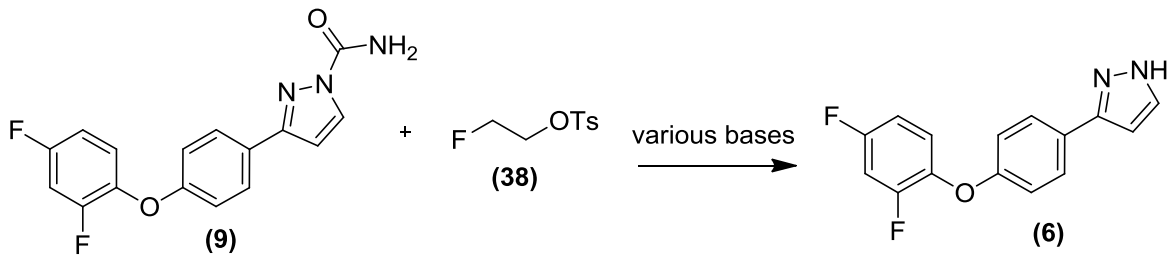

*Scheme 4.2: Cleavage of carboxamide during fluoroalkyation of **(9)***

As shown in Table 4.1, only the mild base potassium bicarbonate did not cause cleavage of the carboxamide, but no product was obtained either. It was serendipitously found through using sodium hydride, that alkylation does proceed on the pyrazole NH following cleavage of the carboxamide. Two products were found during HPLC purification in the ratio of approximately 9:1. Subsequently, NOESY and COSY NMR studies identified that the major product was the isomer **(41)** in 27% yield. It was proposed that the minor product was **(40)**. 2D NMR studies on **(40)** were unable to determine the structure due to minimal compound isolated (<5% yield). When scaling up this reaction to isolate a larger amount, HPLC purification became unable to separate the two isomers and CC was also unable to separate the stereo isomers.

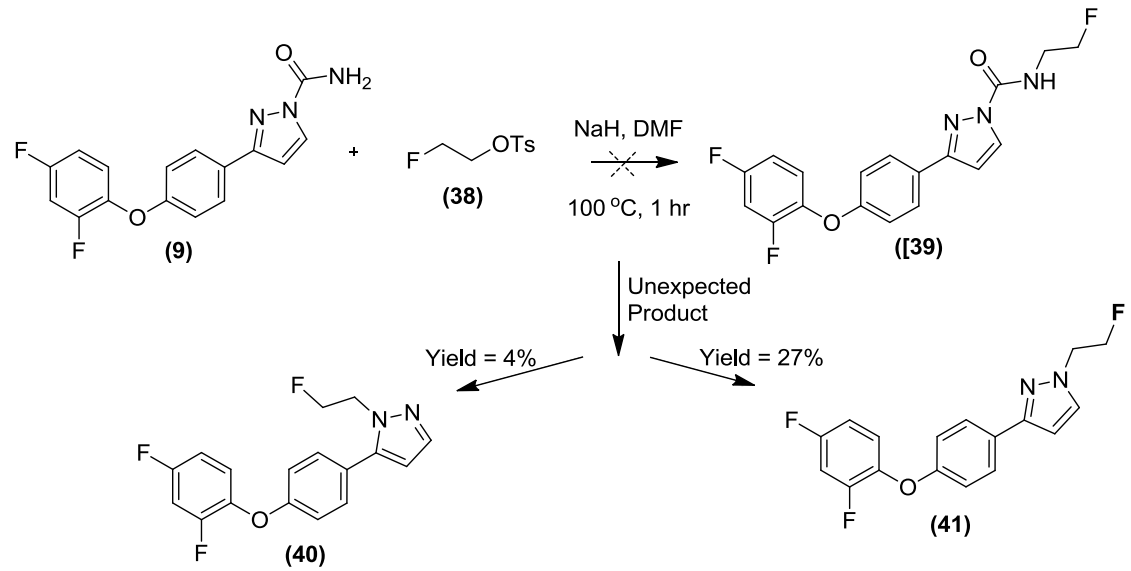

Scheme 4.3: Unexpected products of the fluoroalkylation reaction

Although the terminal carboxamide of **(9)** was cleaved during the course of this reaction, the biological properties and radiochemistry of **(41)** was still of interest. In particular, whether the same mixture of isomers would be formed and in what ratio. Yang *et. al.*, reported replacing the carboxamide with a methyl group and they afforded

a K_i of 0.69±0.18 µM. Hogenkamp *et. al.*, reported the use of aryl substituted pyrazoles for use as VGSC ligands, finding the IC_{50} values of their compounds to be approximately 100 µM or less in hSkM VGSCs expressed in HEK 293 cells .[176] These previously reported data were used as a basis to further investigate **(41)** as a potential novel VGSC ligand.

4.2 Synthesis of ([^{18}F]41)

Using the conditions as outlined in Scheme 4.3 we investigated the radiolabelling of **(9)** with **([^{18}F]38)**.

To generate **([^{18}F]38)** we started from commercially available ethylene di(*p*-toluenesulfonate).

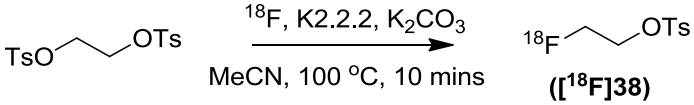

*Scheme 4.4: Synthesis of **([^{18}F]38)***

([^{18}F]38) was synthesised following the procedure by Block and co-workers (Scheme 4.4).[177] Ethylene di(*p*-toluenesulfonate) was added to a solution of pre-dried [^{18}F]fluoride in acetonitrile at 100 °C for 10 minutes. The reaction mixture was then cooled to RT and purified by preparative HPLC (40-80% MeCN/H_2O over 25 minutes), **([^{18}F]38)** was isolated in 30% n.d.c. yield from [^{18}F]fluoride.

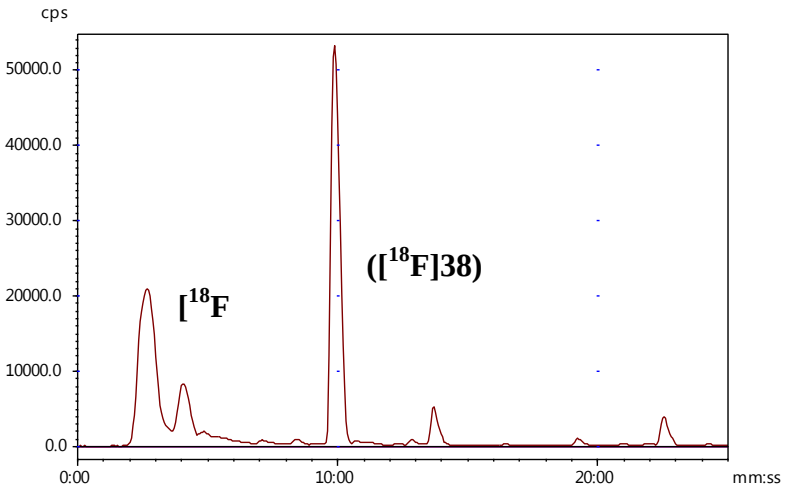

*Figure 4.1: HPLC radio chromatogram of **([^{18}F]38)***

Using the conditions employed in Scheme 4.5, sodium hydride was added to a solution of **(9)** in DMF (100 µL) shortly followed by addition of **([^{18}F]38)** as a DMF solution (200-300 µL). The reaction was then heated to 50 °C for 15 minutes. Following analytical HPLC analysis, some **([^{18}F]38)** remained, but after heating the reaction to 100 °C for a further 15 minutes all **([^{18}F]38)** was consumed. Consequently, the crude product was purified by semi-preparative HPLC (40-80% MeCN/H_2O over 25 minutes). **([^{18}F]41)** was identified to be the major isomer in 30% isolated n.d.c. yield from **([^{18}F]38)**. Overall, **([^{18}F]41)** was produced in 11% isolated e.o.s. n.d.c. yield from [^{18}F]fluoride within 2.5 hrs, in 90-95% radiochemical purity (n=10). Whilst **([^{18}F]40)** was produced minimally owing to < 1% n.d.c. yield (Scheme 4.5 and Figure 4.2).

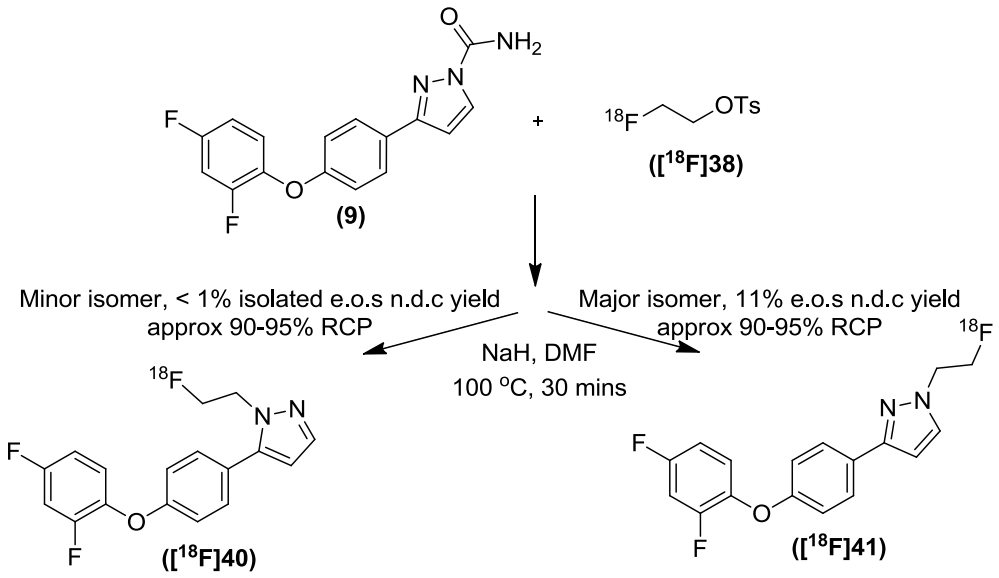

*Scheme 4.5: Synthesis of **([^{18}F]40)** and **([^{18}F]41)***

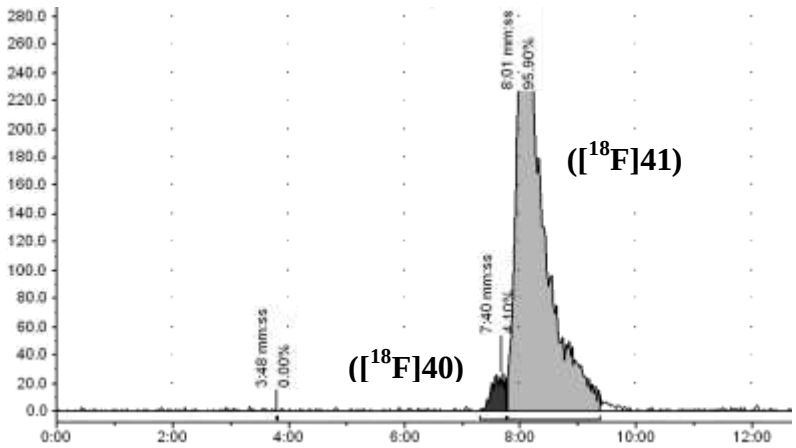

*Figure 4.2: Analytical HPLC chromatogram of **([^{18}F]40)** and **([^{18}F]41)***

This two-step reaction to yield **([^{18}F]41)** was repeated a number of times to assess its reproducibility. Following numerous experiments (n=10) which all showed good yields,

this chemistry was applied to an automated module. This allowed a higher starting activity of [^{18}F]fluoride to be used, whilst minimising personal dose. Initially, the synthesis of **([^{18}F]38)** was automated using a Tracerlab™ FX F-N module (GE Healthcare) with HPLC purification. The azeotropic drying of [^{18}F]fluoride followed the same method as mentioned in Section 3.1 and the labelling of ethylene di(*p*-toluenesulfonate) was performed under the same conditions. After the preparation of **([^{18}F]38)**, the crude product was purified by semi-preparative HPLC (50-80% ammonium acetate / methanol over 25 minutes). The isolated product was then diluted in water (20 mL) and trapped to a reverse phase silica gel cartridge (C-18 Sep-Pak; Waters). The cartridge was dried over a stream of nitrogen and the product was eluted with DMF (300-400 µL). The automated synthesis of **([^{18}F]38)** afforded on average 25% n.d.c. isolated yield from [^{18}F]fluoride (n = 4).

The fluoroalkylation step however, was unable to be automated due to the harsh conditions required. Namely, using sodium hydride produced a pH 9 reaction solution; this basic solution is unsuitable to be used on an automation module.

Following the successful development of **([^{18}F]41)** and semi-automated synthesis, the next steps were to characterise the fluorine-19 standard **(41)**, to ascertain whether this compound behaves as a potent VGSC ligand.

4.3 *In vitro* electrophysiological characterisation

Evaluation of **(41)** commenced with 'sharp' intracellular microelectrode and patch-clamp electrophysiology studies (as outlined in section 3.5). These results were compared with the literature compound **(9)** and other analogues (Chapters 3 and 5).

4.3.0 Sharp microelectrode electrophysiology

For a general overview of sharp electrode electrophysiology, see Section 3.5.0.

4.3.0.0 Results

As depicted in Section 3.5.0.0, sharp microelectrode electrophysiology was performed by Dr Andrew Constanti (UCL School of Pharmacy). This was intended to be a

preliminary screen of compounds in order to provide a basis for further quantitative evaluation of potency and sub-type selectivity using automated and manual patch clamp assays. Each result presented here was confirmed in at least two neurones in different brain slice preparations. Evaluation of **(41)** began in the CA1 region of the hippocampus as discussed previously for **(9)**. A pyramidal cell in the CA1 region was impaled and held at -70 mV membrane potential with steady positive current (Figure 4.3); control recordings were taken and a 10 µM solution of **(41)** in Kreb's medium was bath-applied for 30 minutes. During this time, no obvious reduction in spike amplitude or evoked firing was seen, and the resting membrane potential remained steady at -70 mV (traces not shown). Consequently, the concentration of **(41)** applied was increased to 20 µM and the same pyramidal cell was stimulated (traces not shown). Still, no change in neuronal firing was seen. Finally, the concentration was increased to 30 µM and the cell was monitored further (Figure 4.3).

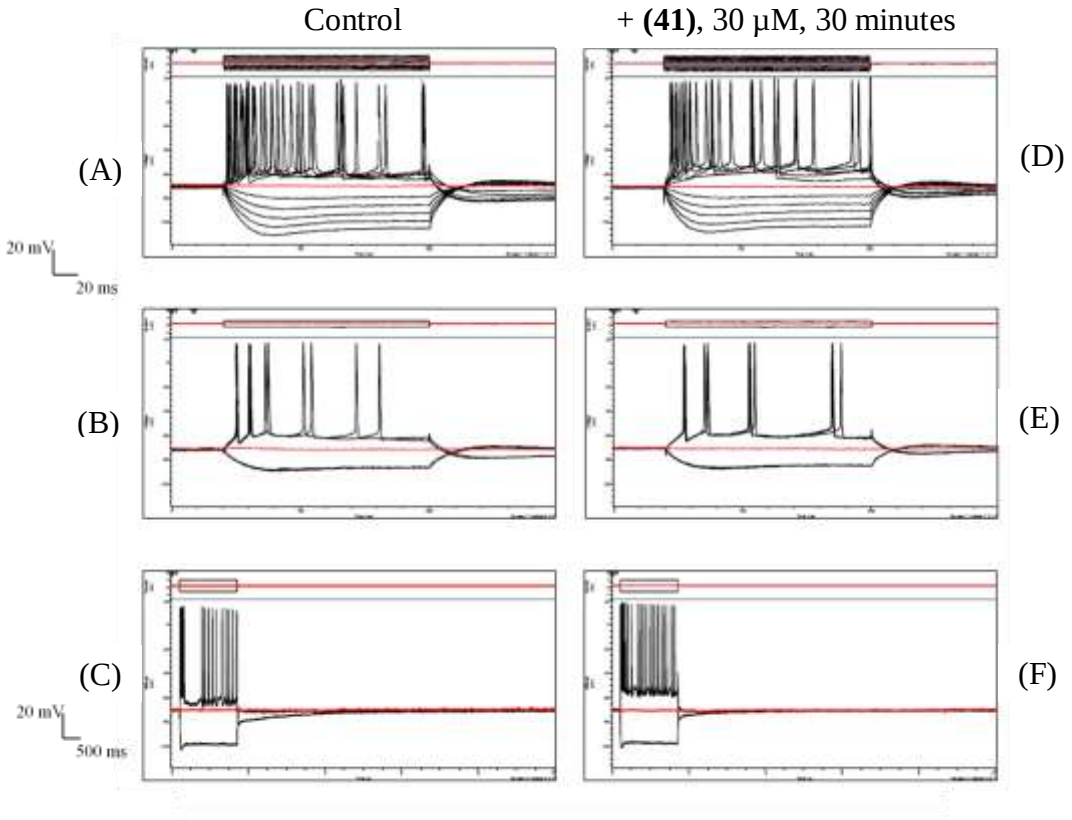

*Figure 4.3: Hippocampal CA1 pyramidal cell held at -70 mV (maintained by steady current injection). (A): Control current/voltage (IV) relationship (± 0.2 nA steps, duration 160 ms). (B): Control positive/negative step (± 0.5 nA step, duration 160 ms). (C) Control long sweep (+ 0.8 nA / -0.5 nA step, duration 1.5 s). (D) IV relationship (± 0.2 nA steps, duration 160 ms) showing no change in neuronal firing with **(41)** 30 µM; 30 minutes). (E) Positive/negative step (± 0.5 nA step, duration 160 ms) showing no change in neuronal firing with **(41)** (30 µM; 30 minutes). (F) Long sweep (+ 0.8 nA / -0.5 nA step, duration 1.5 s) after 30 minutes showing a reduction in the after hyperpolarisation slow bursting*

After increasing the drug concentration to 30 µM for 40 minutes, the neuronal firing pattern showed a small change (Figure 4.3E) indicated by a decrease in the number of spikes initiated by the short depolarising current pulse step (8 spikes reduced to 7). Interestingly, when a longer (1.5 second) and larger ((+ 0.8 nA / -0.5 nA) current step was injected, a reduction in the slow afterhyperpolarisation following a spike burst, resulted in an apparent increase in the firing frequency (Figure 4.3F). However, this increase in neuronal firing is not well represented in the IV traces or positive/negative current step.

4.3.0.1 Discussion

Compound **(41)** was shown through sharp microelectrode electrophysiology to be mostly inactive in the CA1 region of the hippocampus. It was only at higher concentrations (30 µM) (Figure 4.3E) that a slight effect on firing rate was seen with no apparent change in spike amplitude or duration. Reduction of the slow afterhyperpolarisation was also seen, which resulted in an increase in the neuronal firing frequency during the longer current step in Figure 4.3F.

Normally, the repolarisation phase of an action potential increases the membrane potential, due to opening of slow-inactivating (delayed rectifier) potassium channels. Also, slow calcium-activated potassium channels (SK channels), open in response to the influx of calcium ions during the action potential burst. The permeability to potassium causes the membrane potential to be driven closer to the potassium equilibrium potential, causing an undershoot of the resting membrane potential (after-hyperpolarisation). It is possible that **(41)** was having an inhibitory effect on these slow inactivating potassium channels and/or on cell calcium entry, but this was not confirmed. However, it was shown that **(41)** was not behaving like a classical VGSC blocker in this brain region at the concentrations tested.

Due to this compound showing minimal effect in the hippocampal slices, **(41)** was not selected for further testing in the CNS. Nevertheless, **(41)** went on to be tested in a VGSC isoform selectivity screen to ascertain its full potential as a VGSC ligand.

4.3.1 Automated electrophysiology

For details on the protocol used for this study, see Section 3.5.1. The results described in this section were provided by Chantest®, US.

4.3.1.0 Results

The same conditions and measurements were used as first detailed (Section 3.5.1), but a ten-fold higher concentration of **(41)** was tested (Table 4.2) than previously used, due to this compound appearing to have lower potency towards VGSCs than **(9)**, following sharp microelectrode studies.

No	Type of block	IC_{50}						
		Na_v 1.1	Na_v 1.2	Na_v 1.3	Na_v 1.4	Na_v 1.5	Na_v 1.6	Na_v 1.7
(41)	Tonic	>300	>300	>300	>300	>300	>300	>300
	10 Hz	>300	>300	>300	>300	75.9 ± 27.2	>300	>300
	Inact	138 ± 56.7	113 ± 28.9	189 ± 74.6	44.2 ± 3.50	15.1 ± 6.6	193 ± 81.5	>300

*Table 4.2: Summary of IC_{50} values with **(41)** on Na_v 1.1-1.7*

Firstly, it should be noted that **(41)** seemed to have the same binding characteristics as **(9)**, namely, that it bound preferentially to the inactivated state of the Na^+ channels. These data indicated preferential binding to specifically Na_v 1.5 (IC_{50} = 15.1 ± 6.6 µM) and Na_v 1.4 (IC_{50} = 44.2 ± 3.5 µM). Although **(9)** showed higher potencies for Na_v 1.5 (IC_{50} = 0.78 ± 0.29 µM) and Na_v 1.4 (IC_{50} = 1.26 ± 0.29 µM), **(41)** emerged to be more selective, 2.9 times more selective for Na_v 1.5 compared with **(9)**, showing 1.6 times selectivity. Poor potency was seen in the tonic and frequency dependent block protocols, with no IC_{50} value established at the concentrations tested, except Na_v 1.5, where an IC_{50} of 75.9 ± 27.2 µM was determined (maximum concentration 300 µM). Although the overall binding profile appeared similar to **(9)**, **(41)** was one order of magnitude less potent in these tests.

4.3.1.1 Discussion

Compound **(41)** was highlighted as a semi-potent sub-type selective VGSC blocker. Although the potency of this compound was revealed to be less than **(9)**, this study only allowed for an indication of potency. As **(41)** along with **(9)** is a state-dependent blocker, with preferential affinity for the inactivated state, it was likely to require more time under stimulation to see the maximum effect, than was allowed in the protocol. Furthermore, a longer stimulation period would have been more in-line with physiological conditions. In conclusion, this assay showed our compound to be sub-type specific but was unable to accurately depict the potency within the confines of this assay. **(41)** was therefore also screened through manual patch clamp experiments (courtesy of Scottish Biomedical®) specifically testing for inactivated state block in expressed Na_v 1.4 and 1.5 channels.

4.3.2 Patch-clamp electrophysiology

The results described in this section were provided by Scottish Biomedical®, UK. $hNa_v1.4$ and 1.5 were stably expressed in HEK-293 cells, **(41)** was tested at 4 concentrations (0.1, 1, 10 and 30 µM). Incubation time of drug varied depending on time taken to reach maximum inhibition at each concentration.

4.3.2.0 Results

Using the P1-P2 protocol (see Section 2.4.1), **(41)** showed a preference for binding to the inactivated state, inducing a significant reduction in control response across both cell lines.

Following testing in hNa_v 1.4, **(41)** had approximately 160-fold higher affinity for P2 (inactivated) compared to P1 (resting), with an estimated IC_{50} 40 nM *vs* 6 µM, respectively. The maximal inhibitory response (I_{max}) of **(41)** was approximately 93% total block at the maximal concentration of 30 µM in P2, whilst 67% was seen in P1. Figure 4.4 shows the trough of a dose response curve. At -5 log [M] (10 µM), the rising part of the curve is beginning to show.

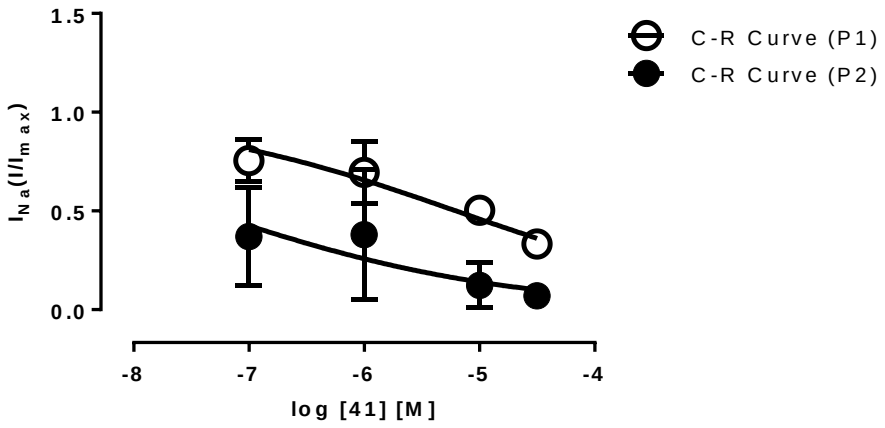

*Figure 4.4: Dose response curve of hNa$_v$ 1.4 of **(41)** (0.1-30 µM) under P1 and P2 conditions*

Following testing in hNa$_v$ 1.5, **(41)** had approximately 145,000-fold higher affinity for P2 (inactivated) compared to P1 (resting), with an estimated IC_{50} 0.2 nM *vs* 29 µM, respectively. The maximal inhibitory response (I_{max}) of **(41)** was approximately 94% total block at the maximum concentration of 30 µM in P2, whilst 54% was seen in P1.

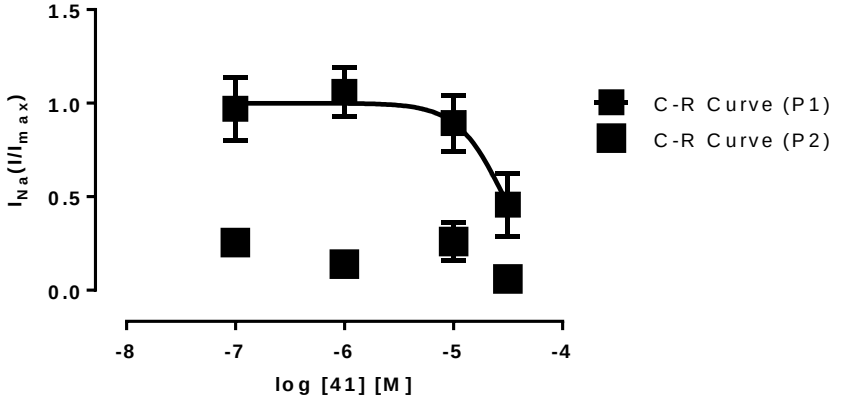

*Figure 4.5: Dose response curve of hNa$_v$ 1.5 of **(41)** (0.1-30 µM) under P1 and P2 conditions*

The dose-response curves for **(41)** indicated that all concentrations tested gave >50% block across both cell lines. The IC_{50} value was therefore reported using a non-linear regression fit algorithm (GraphPad Prism version 5.0) to extrapolate the data.

4.3.2.1 Discussion

The estimated IC_{50} values quoted for both channels indicated that **(41)** is more potent than was initially established (Section 4.3.1.0). Applying each concentration of **(41)** for longer, showed a marked difference in the reported inhibition values. All concentrations

tested gave >50% block. These results mirror that seen with **(9)**. The IC_{50} values quoted here, are four orders of magnitude more potent when comparing Na_v 1.5 IC_{50} (0.2 nM) with the IC_{50} value obtained for Na_v 1.5 (15.1 µM) in the automated electrophysiology screen. As described previously, there is a high margin of error with these results, but it is likely that **(41)** has an IC_{50} around the low to sub nanomolar range. Interestingly, these results also indicated a higher degree of selectivity between the two channels (40 *vs* 0.2 nM; 1.4 *vs* 1.5) than was seen before.

Overall, the potency of **(41)** has been shown to be much higher in this study. In order to gain confidence in these values, lower concentrations are needed to be tested, but it was not possible within the confines of the research grant to commission a further external study.

In order to put these values in context, calculations were carried out using the same approximate B_{max} (6.6 µM) as mentioned in Section 3.5.2.1. To indicate the binding potential, the calculation used the approximate IC_{50} of 0.2 nM as K_d **(41)** giving a binding potential of 33,000. Again, caution must be used when interpreting this value as this should be used as a guide only. However, this value does imply that the binding potential is possibly much higher than the minimum recommended value of 10.

In vitro work showed **(41)** to be a promising VGSC ligand, more work was needed to establish its exact efficacy and binding kinetics but it was important to identify the *in vivo* characteristics of **([^{18}F]41)**. A näive biodistribution of **([^{18}F]41)** was carried out to ascertain whether this radiotracer was able to show uptake, retention and then clearance in key tissues.

4.4 *In vivo* characterisation

All *in vivo* studies described in this section were kindly performed by the *in vivo* biology team, GE Healthcare, Amersham.

4.4.0 Log P determination

Lipophilicity can indicate compound properties such as non-specific binding and metabolic stability.[130, 178-179] Therefore, before any *in vivo* work was carried out, the lop P of **(41)** was determined.

The distribution coefficient (Log-P) was measured experimentally using the shake-flask method (see Section 2.3). Briefly, known concentrations of **(41)** were added to a mixture of octanol and water (0.5 ml; 1/1) in an eppendorf tube. The tube was vortexed for 10 minutes to allow for even distribution of **(41)** before being centrifuged for 5 minutes at 10 000 *xg*. The amount of **(41)** in the octanol and water layer was measured using HPLC and the area of the solute was evaluated against a calibration curve of known concentrations run on the same day. (Ideally, known concentrations of **([^{18}F]41)** would have been used but access to fluorine-18 was not available at that time).

The Log P was found to be 2.03 which is within the range 2 < logP < 3.5 typically identified as optimal.

4.4.1 Näive biodistribution

([^{18}F]41) was assessed through a näive biodistribution study to determine whether this tracer could show uptake and retention in key tissues and clear from these tissues within 2 hours.

4.4.1.0 Results

([^{18}F]41) was delivered in 11% n.d.c. e.o.s. yield from [^{18}F]fluoride at 30.3 MBq/mL, as a phosphate buffer /ethanol solution (9:1), with specific activity 3.48 GBq/µmol. 3.3 MBq (100 µL) was injected i.v. *via* the tail vein to each CD1 näive male mouse. The radiotracer was sampled at five time points over 2 hours and three animals were sacrificed at each time point (Figure 4.6 and Table 4.3).

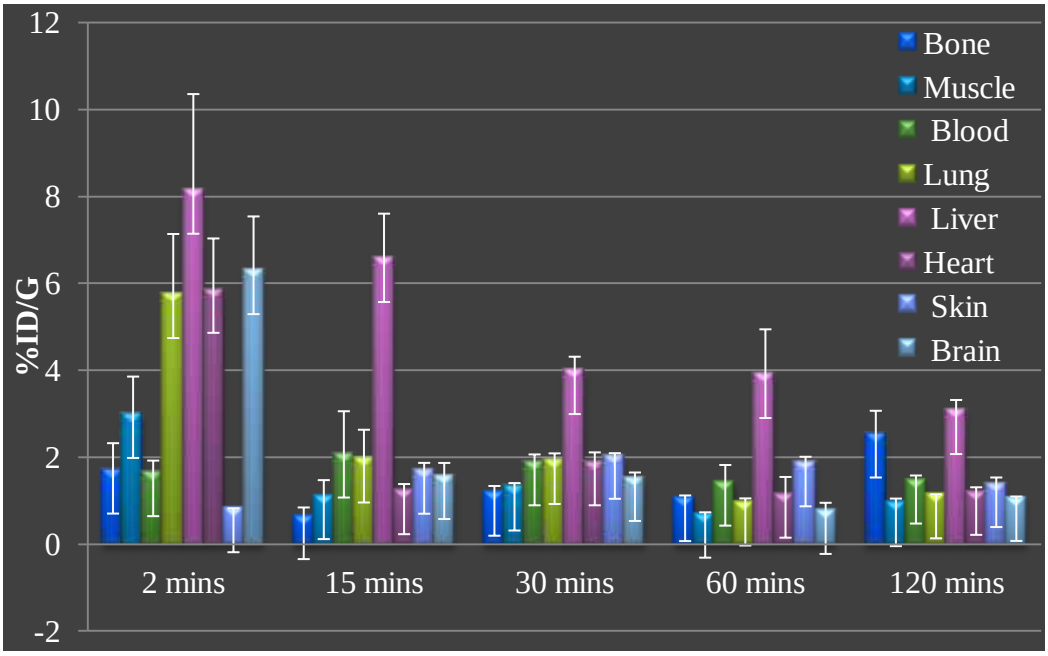

Figure 4.6: Näive biodistribution graph for ***([18F]41)***

Tissue	2 minutes	15 minutes	30 minutes	60 minutes	120 minutes
			Mean %ID/G ±SD (n=3)		
Bone	1.70 ±0.62	0.65 ±0.19	1.19 ±0.14	1.07 ±0.05	2.53 ±0.54
Muscle	2.98 ±0.87	1.11 ±0.36	1.31 ±0.09	0.68 ±0.04	0.95 ±0.09
Blood	1.64 ±0.28	2.07 ±0.99	1.89 ±0.17	1.42 ±0.40	1.47 ±0.11
Lung	5.74 ±1.39	1.95 ±0.67	1.92 ±0.17	0.96 ±0.09	1.13 ±0.01
Liver	8.15 ±2.21	6.57 ±1.03	3.99 ±0.32	3.90 ±1.04	3.07 ±0.24
Heart	5.86 ±1.17	1.23 ±0.15	1.89 ±0.22	1.14 ±0.40	1.21 ±0.09
Skin	0.81 ±0.01	1.70 ±0.17	2.04 ±0.05	1.87 ±0.14	1.39 ±0.14
Brain	6.29 ±1.25	1.57 ±0.29	1.53 ±0.12	0.77 ±0.18	1.07 ±0.02

Table 4.3: Näive biodistribution data of ***([18F]41)*** *in key tissues*

In general, the biodistribution indicated little retention of radioactivity in most tissues; clearance was primarily through the hepatobiliary system (39.84% id at 120 minutes). In more detail, the biodistribution showed initial brain uptake at 2 minutes to be 6.3 ± 1.3% id/g and heart at 2 minutes, 5.9 ± 1.2% id/g. The radioactivity cleared rapidly from these tissues, (brain: 1.5 ±0.1% id/g; heart: 1.8 ±0.2% id/g) within 30 minutes. Little retention of radioactivity was seen in the muscle. Initial uptake of 2.98 ± 0.9% id/g at 2 minutes within the muscle rapidly cleared to (1.11 ± 0.4% id/g) after 15 minutes. Lowest blood levels were seen at 2 minutes (1.64 ± 0.3% id/g), whilst subsequent time points showed higher levels, consistent with rapid uptake of radiotracer into tissues and

later, diffusion of radioactivity out of tissues and into the systemic system. For example, the muscle level dropped from 2.98 ± 0.9% id/g to 1.11 ± 0.4% id/g from 2 to 15 minutes. Interestingly, the skin level (skin known not to contain VGSCs), although low at 2 minutes at 0.81 ±0.01% id/g, increased to 2.04 ± 0.05% id/g within 30 minutes before decreasing. This could be due to contamination from blood, which appeared to follow a similar pattern. The lung showed uptake comparable to the heart and brain at 2 minutes (5.75 ± 1.4% id/g) and sharply decreased by 15 minutes to 1.95 ± 0.2% id/g. Uptake in the lung is likely to be consistent with dispersion of radioactivity which quickly diffuses back into the blood. Bone level remained low throughout the time course of the study (average 1.15 ± 0.3% id/g in the first 60 minutes) until the last time point at 120 minutes, the radioactivity level increased to 2.53 ± 0.5% id/g. All three animals were consistent (2.56 ±0.6% id/g) so it was not thought that the sudden increase was due to contamination, but more likely, free [^{18}F]fluoride binding which has been released during metabolism of the tracer.

4.4.1.1 Discussion

The näive biodistribution study for **([^{18}F]41)** showed somewhat unpredicted results. *In vitro* data suggested this compound would show greater binding to Na_v 1.4 (expressed in skeletal muscle) and Na_v 1.5 (expressed in the heart), although uptake was seen in these tissues it was not retained, suggesting little specific uptake. *In vitro* data also showed less selectivity towards Na_v 1.1-1.3 and 1.6 (found in the brain), but higher uptake of **([^{18}F]41)** was seen in the brain (than in the heart or muscle) at the initial time point (6.29 ± 1.3% id/g; 2 minutes).

Overall, the biodistribution profile showed little retention of **([^{18}F]41)** in all tissues, implying minimal binding, whilst most of the radioactivity was cleared through the hepatobiliary system.

Although there was not a known fluorine-18 labelled VGSC PET tracer to compare our biodistribution data with, it was important to put our figures into context in terms of indicating whether uptake, retention and clearance were noteworthy.

The NMDA receptor (as first mentioned in Section 1.4) is an ionotropic glutamate receptor distributed widely within the brain, which also exhibits voltage-dependent activation, allowing the flow of sodium and calcium ions into the cell and potassium out of the cell. PET tracers to target the NMDA receptor have now been developed.[180] The

NMDA PET tracer [^{18}F]memantine was studied through a näive mouse biodistribution. Samnick *et. al.*, reported initial brain uptake of 2.50% id/g ± 0.13 at 5 minutes, subsequently this increased to 3.76% id/g ± 0.45 at 30 minutes before decreasing.[180] Using these data as a rough guideline of uptake for comparison, our tracer appeared to have greater initial uptake in our expressing tissue (heart; 5.86 ±1.17% ID/g), but not as good retention. Although no strong comparisons can be drawn, it was interesting to understand what percentage uptake in a key tissue (high expression of receptor) is common for an ion channel PET tracer.

It is also important to consider the low specific activity afforded. To-date, it has not been possible to determine accurate values of B_{max} (and K_d). Without this, we are not sure if the concentration of available receptors for binding is high or low. It could be that the administered mass of **(41)** or (an unidentified compound which elutes at the same retention time) is blocking the an unknown amount of VGSCs and therefore, inhibiting the binding of **([^{18}F]41)**. Currently, not enough is known regarding the concentration of sodium channels or more accurately the B_{max}. However, the low specific activity afforded here, will need to be improved, if later studies confirm that there is a high VGSC saturation at this concentration.

4.5 Conclusions of Chapter 4

Initial *in vitro* data (Section 4.1) highlighted **(41)** as a semi-potent sub-type selective VGSC ligand. It was further investigated through a näive biodistribution study to characterise its *in vivo* biodistribution profile. It was known that removing the terminal carboxamide might have an effect on the compound's affinity for VGSCs, but it was not known to what extent and therefore still important to ascertain how this compound behaved *in vivo*. Moreover, as Yang *et. al.*, had not performed *in vivo* studies on their compounds, our study was adding to the field of knowledge. It was important to note, that after injecting **([^{18}F]41)** into näive CD1 mice for the biodistribution study, all animals suffered no measurable ill effects from this tracer. Although it showed little retention in key tissues, initial uptake was good, *in vivo* stability was inferred from the low bone uptake and the tracer showed signs of clearing within 2 hours. As a result of this work **([^{18}F]41)** was not selected for further development. Using the data from this chapter, our next analogue of the 3-(4-(4-R-phenoxy)phenyl)-pyrazole-1- carboxamides was developed.

5. Results and Discussion

Design, synthesis and bioevaluation of [^{18}F]4-(4-(2,4-difluorophenoxy)phenyl)-1-(2fluoroethyl)-triazole

5.0 Rationale for novel tracer

Following on from work described in Chapter 4, **([^{18}F]41)** was highlighted to have some efficacy for VGSCs, but it's *in vivo* characteristics indicated that it was not suitable for use as a PET tracer. Moreover, the biodistribution appeared to indicate that the terminal carboxamide was indeed important for binding. However, due to this group's lability towards cleavage under basic conditions as discussed in Chapter 3, a bioisostere was sought to replace the terminal amide. A 1,4-substituted triazole produced by the Hüisgen 1,3-cycloaddition reaction between an azide and a terminal alkyne had been previously reported to act as a bioisostere for an amide.[181] The Hüsigen 1,3-cycloaddition, a so called "click chemistry" reaction is well reported with [^{18}F]2-fluoroethylazide and a variety of terminal alkynes, whilst the copper (I)-catalysed reaction gives exclusively the 1,4-product.[182] Subsequently, the structure was altered further with the removal of the pyrazole ring (Figure 5.1). The purpose of this ring as reported by Yang *et. al.*, was simply to conjugate the second phenyl ring to the terminal amide whilst being metabolically stable. There was no other rationale for its presence.[181] The exclusion of the pyrazole ring also reduced the molecular weight and size of the molecule, making it closer to the original 3-(4-phenoxyphenyl) pyrazole-1-carboxamides.

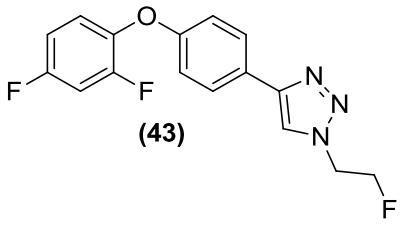

(43)

*Figure 5.1: Structure of **(43)***

5.1 Click chemistry

Over the last decade there has been an ever increasing demand for pharmaceutically active molecules to be produced in high purity and yield. A powerful synthetic tool that fulfils these requirements is click chemistry. The term was first coined by Sharpless in 1999 at the 217th American Chemical Society annual meeting. He then followed on this work with his 2001 review defining click chemistry as a group of reactions that "... *must be modular, wide in scope, give very high yields, generate only inoffensive by products that can be removed by nonchromatographic methods, and be stereospecific. The*

required process characteristics include simple reaction conditions, readily available starting materials and reagents, the use of no solvent or a solvent that is benign, allowing easy product isolation. Purification, if required, must be by non-chromatographic methods, such as crystallisation or distillation, and the product must be stable under physiological conditions".[183] These reactions include cycloadditions; primarily this refers to 1,3-dipolar cycloadditions including hetero Diels-Alder cycloadditions.[184] Other reactions also come under the umbrella of click chemistry, for example, nucleophilic ring-openings,[184] carbonyl chemistry involving non-aldol chemistrys and addition to C-C multiple bonds.[184-185]

5.1.0 The Hüisgen 1,3 cycloaddition

The Hüisgen 1,3-cycloaddition has found much synthetic utility since it is extremely reliable and easy to use. The reaction is very atom economic as the combined formula of the reactants equals the formula of the product. No σ-bond connection is broken during the reaction, therefore the solvent is not coordinated to the starting material during product formation, allowing the reaction to be solvent independent. The reaction exclusively forms a 1,4-substituted product when copper catalysed, making it regiospecific and the catalysed route significantly improves the rate of reaction (> 10^7 times faster). It can be performed in a wide range of solvents including aqueous. Azides and terminal alkynes are fairly easy to install and are tolerant to a range of conditions commonly encountered in synthesis. Aliphatic azides may decompose in a thermodynamically favoured reaction. However, in the cycloaddition reaction, a kinetic barrier to decomposition allows them to form a stable complex.[184-187]

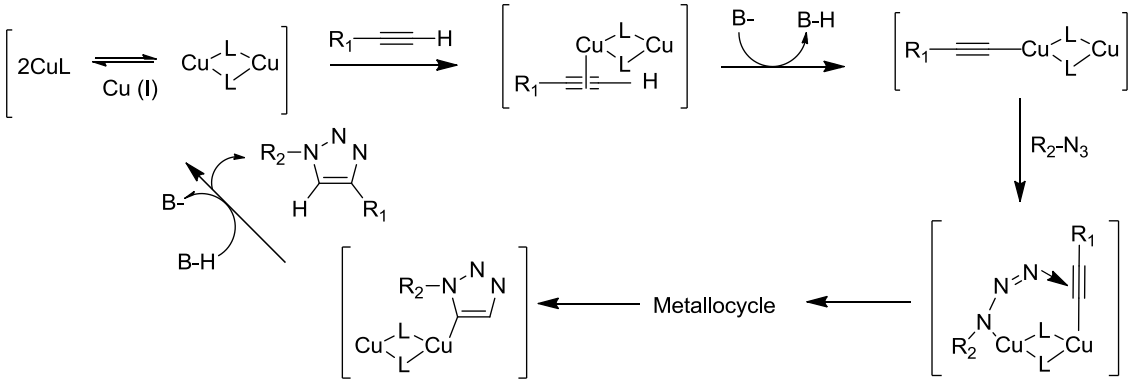

Figure 5.2: General mechanism for Hüisgen 1,3-cycloaddition

This cycloaddition proceeds *via* a stepwise reaction pathway based on Cu(I) insertion into terminal alkynes. It seems most likely that the first step of the reaction is the π-complexation of a Cu(I) dimer to the alkyne *via* a Cu_2L_2 complex.[184-185] After this, the deprotonation of the terminal alkyne occurs to form a Cu-acetylide.[184-185] There are many forms of this complex that exist; only one is shown above. The π-complexation of Cu(I) reduces the *pKa* of the terminal alkyne by nearly 10 units allowing the deprotonation to occur in aqueous solution without the need for a base (if the reaction were to be performed in an organic solvent then a suitable base such as *N,N*-diisopropylethylaminutes (DIPEA) would need to be added). In the following step the internal nitrogen of the azide attaches to the free copper (not bonded to the acetylide) forming an "activated" metallo complex. The external nitrogen on the azide now acts as a nucleophile and can attack the adjacent alkyne carbon due to the close proximity and electronic factors. The metallocycle contracts when the lone pair on the nitrogen attacks the alkyne forming the respective triazole ring. Once this complex has been formed the copper dimer then dissociates from the triazole and complexes to a second terminal alkyne. This occurs *via* protonation of the triazole.[184-187]

The general method for the formation of the Cu(I) catalyst is mixing copper (II) sulphate with a reducing agent such as sodium ascorbate, although this is not the only reducing agent that can be used. The production of the catalyst using this method is very cheap and can be performed in aqueous solution. The only drawback to this method is that Cu(II) can be reduced to Cu(0) from Cu(I) in a disproportionation reaction.[184-187] However, recently the use of copper wire and copper powder has been reported, which overcomes this problem.[188]

5.2 Synthesis of 4-(4-(2,4-difluorophenoxy)phenyl)-1-(2-fluoroethyl)-triazole

(44) was produced through a Hüisgen 1,3-cycloaddition between **(42)** and **(43)** (Scheme 5.3). Initially, **(42)** was afforded in a 2-step procedure (Scheme 5.1). Treating 2-fluoroethanol with tosyl chloride (TsCl) under basic conditions with triethylamine (TEA) catalysed by dimethylaminopyridine (DMAP) afforded **(38)** in 98% yield. The tosyl group was displaced using sodium azide in DMF to yield **(42)**. Due to the instability of **(42)**, it was kept as a solution in DMF with concentration 0.23 M.

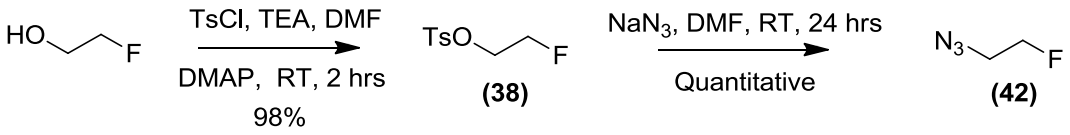

*Scheme 5.1: Synthesis of **(42)***

Subsequently, **(43)** was produced by reaction of 2,4-difluorophenol with 1-ethynyl-4-fluorobenzene undergoing a Williamson reaction, giving **(43)** in 15% yield (Scheme 5.2). The low yield was perhaps related to the stability of 2,4-difluorophenol under basic conditions as discussed in Section 3.1.1.

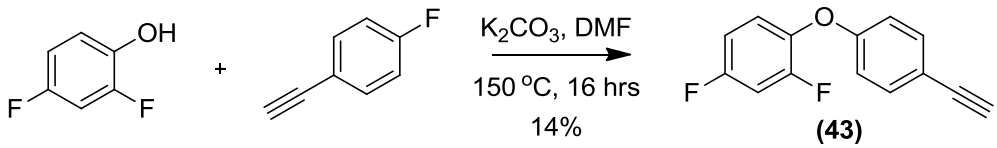

*Scheme 5.2: Synthesis of **(43)***

The subsequent Hüisgen 1,3-cycloaddition reaction between **(42)** and **(43)** was catalysed using copper wire (where copper (I) is present on the surface) in DMF, affording **(44)** as the exclusive isomer in 24% yield (

Scheme 5.3). Copper wire was introduced as catalyst instead of using the reduction of copper sulphate to minimise any disproportionation reactions.

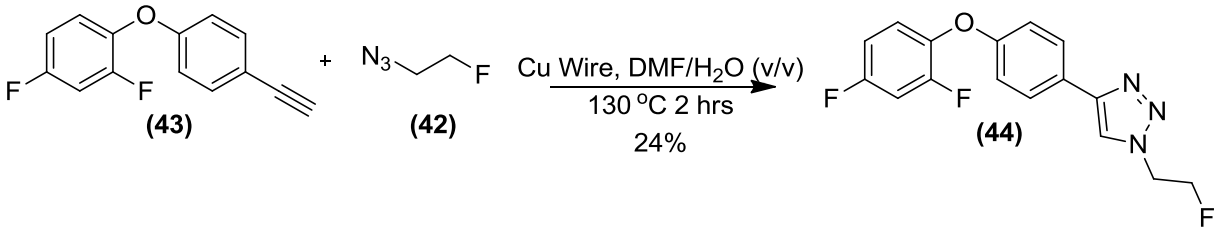

*Scheme 5.3: Synthesis of **(44)** via a Huisgen 1,3 cycloaddition*

The low yield was attributed to precipitation of starting materials under reaction conditions. However, using a more dilute reaction solution did not improve the yield of the rate of reaction.

5.3 General [^{18}F] radiolabelling strategies

Following on from the successful synthesis of **(44)**, radiolabelling studies commenced incorporating fluorine-18 by using **([^{18}F]42)** (Scheme 5.5).

5.3.0 Indirect fluorine-18 labelling

The precursor for **([^{18}F]42)** was produced in a two-step synthesis. 2-Bromoethanol underwent an S_N2 reaction with sodium azide in DMF at RT for 24 hrs affording **(45)** **(**Scheme 5.4**)**. Due to the volatile nature of **(45)**, this compound was not isolated. Subsequently, pyridine and tosyl chloride were added at 0 °C and the reaction proceeded at RT to yield **(46)** in 90% yield.

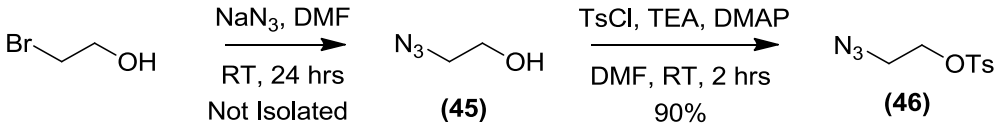

*Scheme 5.4: Synthesis of **(45)** via an S_N2 reaction*

The synthesis of **([^{18}F]42)** was carried out using an automated manifold. Recently, its synthesis on a GE Healthcare FASTlab™ was reported by Iddon *et. al.,* who distilled the product in 30-40% n.d.c. yield starting from **(46)**.[188]

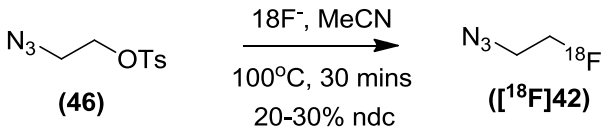

*Scheme 5.5: Automated synthesis of **([^{18}F]42)** on a FASTlab™*

A FASTlab™ cassette was assembled (Section 2.2). Initially a solution of $KHCO_3$ and kyrptofix® in MeCN was used to elute [^{18}F]fluoride from the QMA cartridge in the first processing step. Following drying of [^{18}F]fluoride in the reactor vessel, **(46)** in MeCN was added and heated at 100 °C for 30 minutes to yield **([^{18}F]42)**. Owing to the volatility of **([^{18}F]42)**, it was distilled out of the central manifold into an external vial charged with 100 µl of DMF as a simple and effective purification. As the labelling proceeded, **([^{18}F]42)** was trapped in DMF affording this synthon in 20-30% n.d.c. yield.

Following on from the successful synthesis of **([^{18}F]42)**, the Hüisgen 1,3-cycloaddition was attempted under manual labelling conditions (Scheme 5.6).

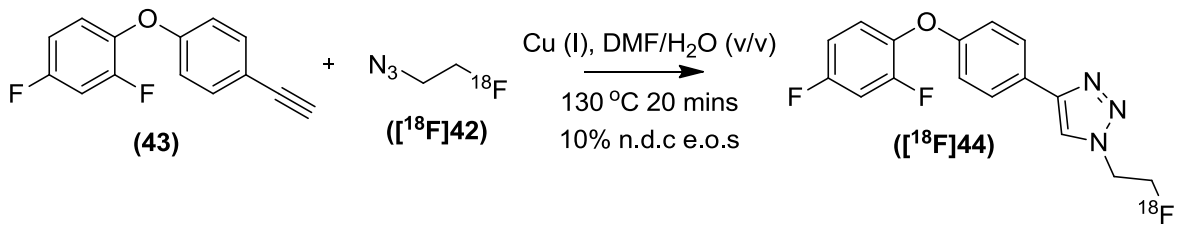

Scheme 5.6: Manual synthesis of ***([18F]44)***

Instead of using copper wire to catalyse the reaction as previously discussed, copper (I) was produced under the classic reduction of copper(II)sulphate with sodium ascorbate in water. Copper wire was reported by Iddon *et. al.*, to be unsuccessful in catalysing the Hüisgen 1,3-cycloaddition in reactions with fluorine-18 using alkyne functionalised peptides.[188] Following reduction of copper sulphate by sodium ascorbate in a Wheaton vial under aqueous conditions; the copper ligand bathophenanthroline (BPDS) was added to enhance the rate of reaction as reported by Glaser *et. al.*[137] The vial was purged with nitrogen to prevent oxidation of copper and thereafter **(43)** was added as a DMF solution. The solution was again purged with nitrogen and left to complex with the copper for 5 minutes. Lastly, **([18F]42)** as a MeCN solution was added and the reaction was heated to 130 °C for 20 minutes. **([18F]44)** was purified by semi-preparative HPLC (10-95%; MeCN/H_2O over 25 minutes) and isolated in 37% n.d.c yield, giving **([18F]44)** overall in 10% e.o.s n.d.c. yield from [^{18}F]fluoride (n=7).

A one-step synthesis of **([18F]44)** was attempted using a fluorine-18 for tosylate displacement using **(47)** as precursor (Scheme 5.7). **(47)** was produced through a copper catalysed Hüisgen 1,3-cycloaddition between **(46)** and **(43)** in the presence of copper (I) to yield **(46)** in 12.5%. Due to the minimal yield, **(47)** was characterised by low resolution MS only.

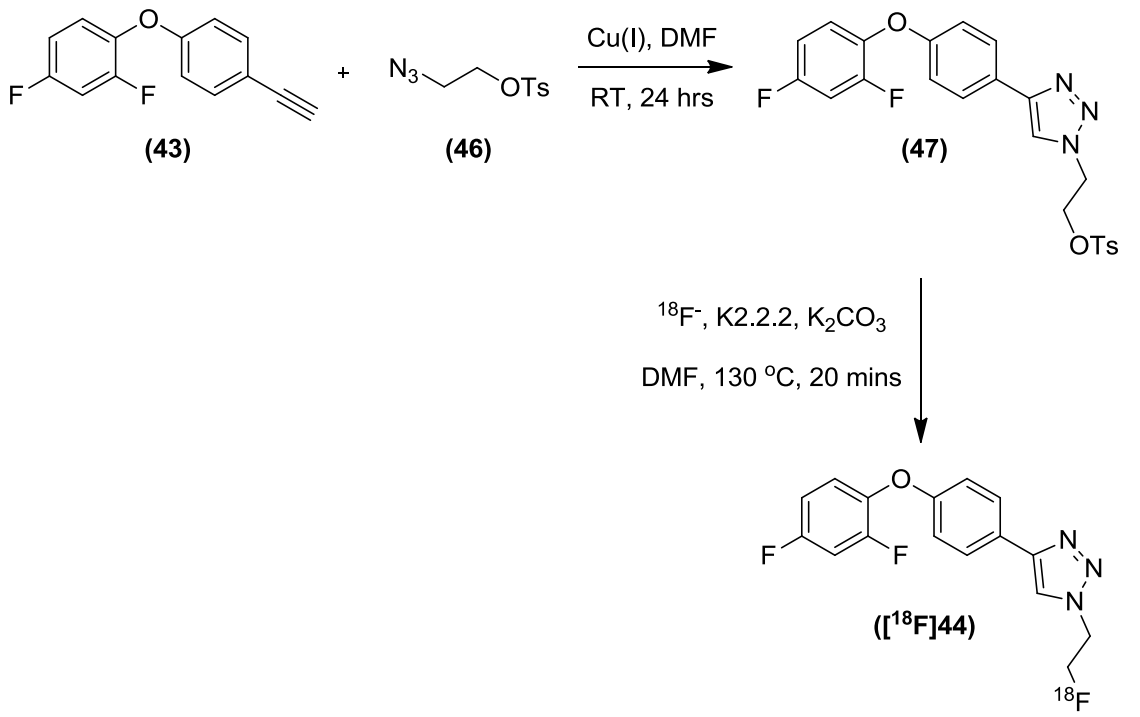

*Scheme 5.7: Synthesis of **(46)** and attempted radiolabelling of **([^{18}F]44)***

Subsequently, [^{18}F]fluoride was dried manually as per normal procedure (Section 3.0.1) and **(47)** was added as a DMF solution and heated to 130 °C for 20 minutes (Scheme 5.7). The reaction mixture was subsequently purified by semi-preparative HPLC (10-95%; MeCN/H_2O over 25 minutes) to identify **([^{18}F]44)**.

From the radiochemical chromatogram, most of the activity remained as "free" [^{18}F]fluorine while 2 minor peaks were seen each accounting for <0.5% integrated yield, but neither were product. Unfortunately, it was not possible to identify these peaks.

The next step was to trial this radiochemistry using the FASTlab™ module, as previously introduced. To date, the total automation to synthesise **([^{18}F]44)** has not been achieved due to laboratory time constraints and synthesis of **(47)** has not been scaled up as yet. For more details see Future Work (Section 8).

5.4 Conclusion of radiolabelling experiments

A new tracer **([^{18}F]44)** was successfully produced in a two-step semi-automated procedure using click chemistry. An alternative one-step procedure was attempted

manually which had so far proved unsuccessful. The two-step procedure was used herein to prepare this tracer for a series of *in vitro* and *in vivo* studies.

5.5 *In vitro* electrophysiological characterisation

Initially, **(44)** was assessed through a series of electrophysiological studies and compared with the literature compound **(9)** and other analogues.

5.5.0 Sharp microelectrode electrophysiology

For a general overview of sharp microelectrode electrophysiology, see Section 3.5.0.

5.5.0.0 Results

As depicted in Section 3.5.0.0, sharp electrode electrophysiology was performed by Dr Andrew Constanti (UCL School of Pharmacy). Classification of **(44)** commenced with a 10 µM solution (1:99; EtOH/Kreb's) (Figure 5.3) applied to pyramidal cells of the CA1 hippocampal region *in vitro*. This region and concentration was first studied to see whether there was a similar effect in this area, as shown with **(9)**.

A CA1 pyramidal neurone was impaled and held at -70 mV membrane potential. Control recordings were taken and the drug solution bubbled with oxygen 95% / CO_2 5% applied *via* the bathing medium. Neuronal activity was monitored and recorded.

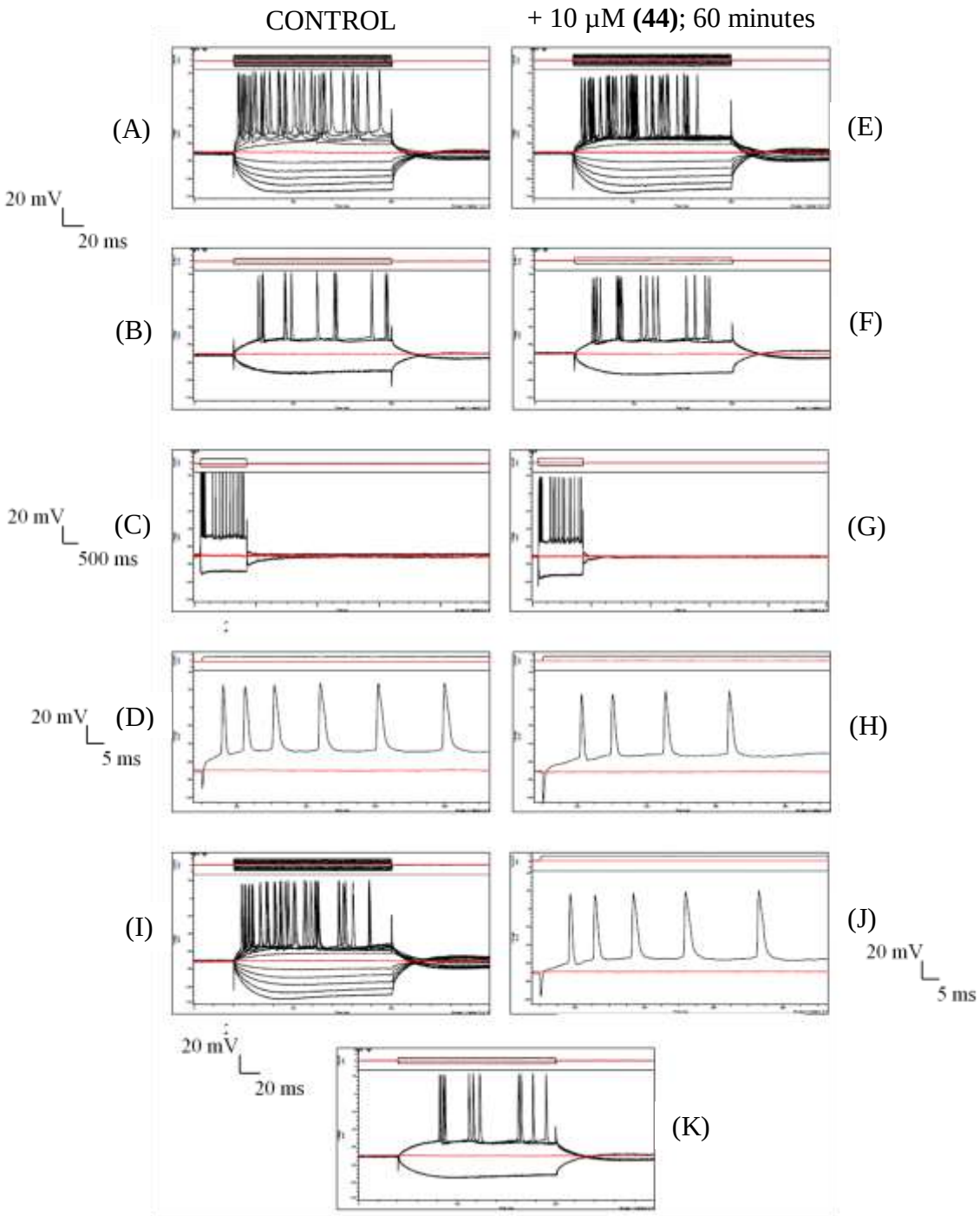

Figure 5.3: Hippocampal CA1 neurone held at -70 mV (maintained by steady positive current injection). (A): Control IV relationship (± 0.2 nA steps, duration 160 ms). (B): Control positive/negative step (± 0.5 nA step, duration 160 ms). (C) Control long sweep (+ 0.8 nA / -0.5 nA step, duration 1.5 s). (D) Stretch of control long sweep recording from (C). (E) IV relationship (± 0.2 nA steps, duration 160 ms) showing inhibition of later action potentials after (44) was applied (10 µM; 60 minutes). (F) Positive/negative step (± 0.5 nA step, duration 160 ms) showing clear inhibition of spikes with (44) (10 µM; 60 minutes). (G): Long sweep (+ 0.8 nA / -0.5 nA step, duration 1.5 s) showing a change in the firing pattern after (44) applied (10 µM; 60 minutes). (H): Stretch of long sweep recording from (G) showing slight diminishing in the spike amplitude. (I) IV relationship (± 0.2 nA steps, duration 160 ms) after 30 min washout. (J) Stretch of long sweep (+ 0.8 nA / -0.5 nA step, duration 1.5 s). (K) Positive/negative step (± 0.5 nA step, duration 160 ms) after 30 min washout.

After 60 minutes, very little effect was seen on neuronal activity. It was anticipated that **(44)** might be less potent than **(9)** due to the structural modifications made. From (Figure 5.3E), it can be seen that some later action potentials were dropping out. This is quantified in Figure 5.3D and H. The time between the third and fourth spike in control was 12 ms (Figure 5.3D) which increased to 19 ms after application of **(44)** (Figure 5.3H). Interestingly, the peak amplitude of the spikes was not changed, remaining at 65 mV throughout (Figure 5.3D and H). After 30 minutes washout (Figure 5.3K), those action potentials recovered and thus the gap decreased to 15 ms. The drug concentration was then doubled to 20 µM and recordings repeated using the same cell.

A CA1 pyramidal neurone was held at -70 mV, control recordings taken before and after **(44)** was applied (Figure 5.4). A 20 µM solution of **(44)** (2:98; EtOH/Kreb's) bubbled with oxygen 95% / carbon dioxide 5% was applied to the system and neuronal activity was monitored.

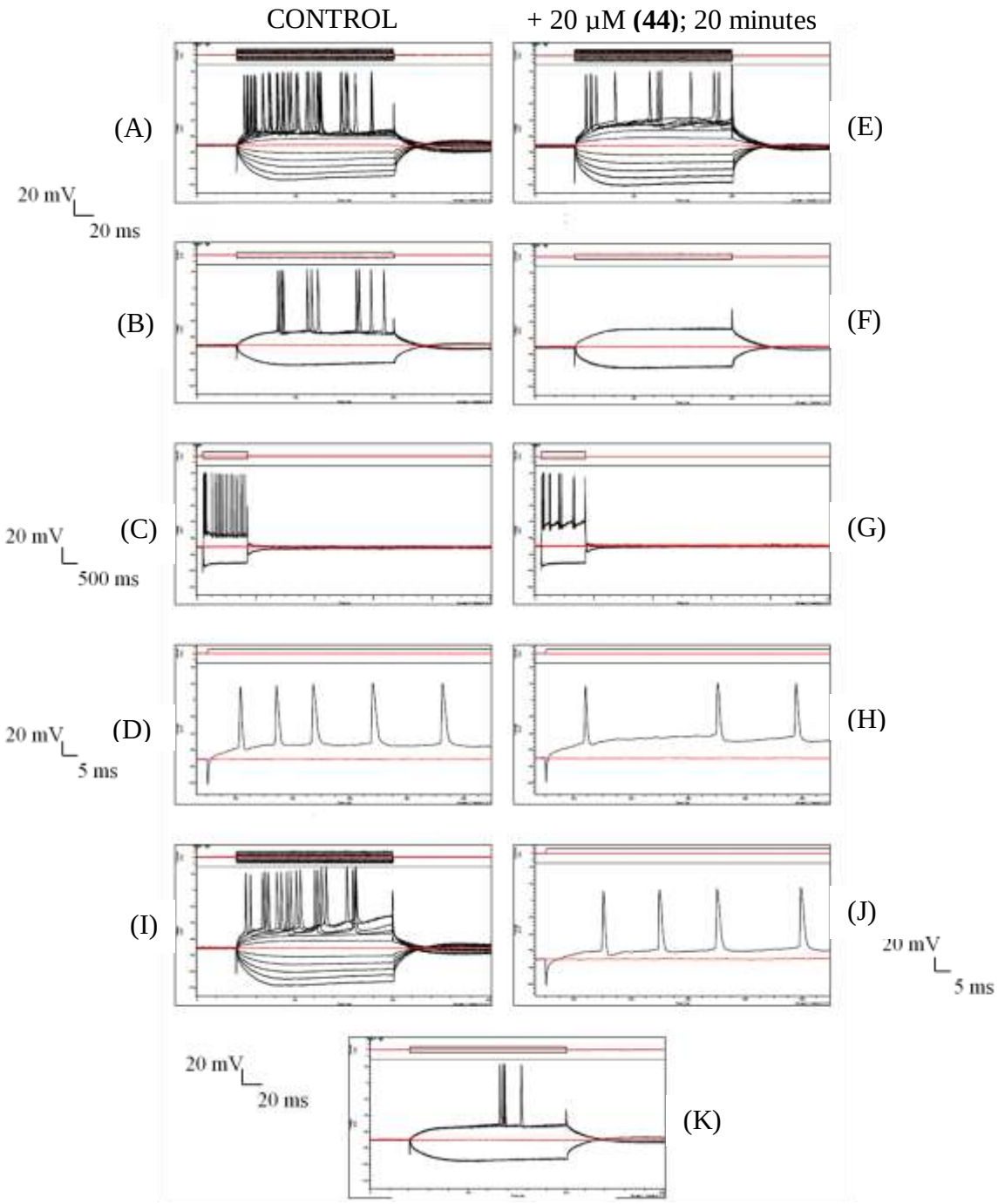

*Figure 5.4: Same hippocampal CA1 neurone as in Figure 5.3, held at -70 mV (maintained by steady current injection). (A): Control IV relationship (± 0.2 nA steps, duration 160 ms). (B): Control positive/negative step (± 0.5 nA step, duration 160 ms). (C) Control long sweep (+ 0.8 nA / -0.5 nA step, duration 1.5 s). (D) Stretch of control long sweep recording from (C). (E) IV relationship (± 0.2 nA steps, duration 160 ms) showing some inhibition of action potentials with **(44)** (20 µM; 15 minutes). (F) Positive/negative step (± 0.5 nA step, duration 160 ms) showing total neuronal block with **(44)** (20 µM; 20 minutes). (G): Long sweep (+ 0.8 nA / -0.5 nA step, duration 1.5 s) showing little neuronal firing with **(44)** (20 µM; 20 minutes). (H): Stretch of long sweep recording from (G) showing diminished spike frequency. (I) IV relationship (± 0.2 nA steps, duration 160 ms) after 20 minutes washout. (J) Stretch of long sweep (+ 0.8 nA / -0.5 nA step, duration 1.5 s) after 30 min washout. (K) Positive/negative step (± 0.5 nA step, duration 160 ms) after 20 minutes washout showing some recovery of neurones.*

Recordings were taken 20 minutes after drug application. After 7 minutes, a clear drop in the number of action potentials fired was observed. It is interesting to note that only a very slight drop in the spike amplitude was seen (65 mV to 60 mV) (Figure 5.4 D and H), whilst spike AHPs were again increasing due to opening of calcium channels. Within 20 minutes, total block of all action potentials were seen (Figure 5.4F). When applying the long pulse (1.5 seconds) some action potentials were seen (Figure 5.4G) indicating reversible binding with longer stimulation. Figure 5.4 proved that **(44)** had affinity for blocking neuronal firing in the pyramidal cells of the CA1 region at 20 µM, however, it is not as potent as previously reported **(9)**. Interestingly, a different onset of action for **(44)** at 20 µM, than was seen with **(9)** at 10 µM.

Consequently, recordings were taken from pyramidal cells of the PC to monitor any differences in action and therefore indicate any subtype selectivity

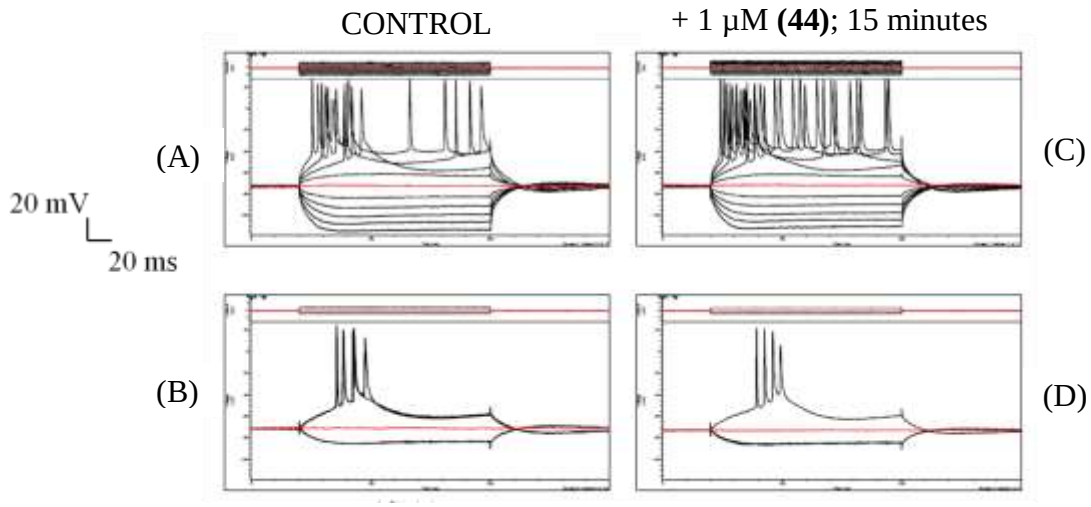

*Figure 5.5: PC neurone held at -70 mV (maintained by steady current injection). **(A)** Control IV relationship (± 0.2 nA steps, duration 160 ms). **(B)** Control positive/negative step (± 0.5 nA step, duration 160 ms). **(C)** IV relationship (± 0.2 nA steps, duration 160 ms) showing no inhibition of action potentials after application of **(44)** (1 µM; 15 minutes). **(D)** Positive/negative step (± 0.5 nA step, duration 160 ms) after **(44)** (1 µM; 20 minutes) applied, showing no inhibition of spikes.*

The recordings with **(44)** applied at 1 µM in PC corroborated with the results of **(9)** (Section 3.5.0.0.) at the same concentration. The traces appeared virtually identical between drug and control. Due to no effect seen, no washout was recorded. These results further suggested that these compounds have a lack of binding affinity for the PC neurones at this concentration.

5.5.0.1 Discussion

Compound **(44)** appeared to act like a traditional Na^+ channel pore blocker; inhibiting action potentials without causing an effect on the spike amplitude. This is reminiscent of the site 1 blocker tetrodotoxin (TTX). Compound **(9)** in contrast, showed use-dependent characteristics (Section 3.5.0.0). Compound **(44)** may thus be a novel inhibitor of neuronal firing exhibiting TTX-like characteristics, although not as potent. Moreover, as exhibited with **(9)**, **(44)** showed a good inhibitory effect in the hippocampal CA1 region but no effect was shown in the PC, possibly indicating some neurone type/brain area selectivity. **(44)** was thus considered to be an interesting compound warranting further investigation, therefore, it was also tested in the VGSC selectivity screen.

5.5.1. Automated electrophysiology

For a general background to the study performed see Section 3.5.1. The results described in this section were provided by Chantest®, US.

5.5.1.0 Results

Following automated patch clamp experiments on Na_v 1.1-1.7 channels expressed in CHO cells, **(44)** was shown to be a state-dependent blocker of VGSCs (Table 5.1).

Type of block	**IC_{50}**						
	Na_v 1.1	Na_v 1.2	Na_v 1.3	Na_v 1.4	Na_v 1.5	Na_v 1.6	Na_v 1.7
Tonic	>30	>30	>30	*>100	*>100	>30	>30
10 Hz	>30	>30	>30	*74.6 ± 21.7	*52.0 ± 17.05	>30	>30
Inactivated	>30	>30	>30	*34.3 ± 12.6	*15.6 ± 16.3	>30	>30

*Maximum concentration tested was 100 µM to ascertain accurate IC_{50} values

*Table 5.1: IC_{50} values of **(44)** with Na_v 1.1-1.7 provided by Chantest®*

In particular, **(44)** was shown to be most potent for Na_v 1.5 (IC_{50} = 15.6 ± 16.3 µM) followed by Na_v 1.4 (IC_{50} = 34.3 ± 12.6 µM) in the inactivated state. Higher concentrations of **(44)** were tested in these cell lines only to more accurately measure the IC_{50}. At the increased concentrations, the IC_{50} for frequency dependent block (10

Hz) was also afforded. Although, it was shown that **(44)** did not bind as well under these conditions, when comparing the raw data, Na_v 1.1-1.3 and 1.6-1.7 sodium currents showed minimal inhibition of sodium currents at up to 30 µM. Therefore, it was felt that testing higher concentrations in these cell lines was not necessary as these concentrations adequately demonstrated the lack of potency toward these channels.

5.5.1.1 Discussion

Compound **(44)** was shown from the automated electrophysiology assay to be a cardiac sub-type selective VGSC blocker in the low µM range. It was also shown to be somewhat less potent than **(9)**, but it was recognised in Section 3.5.1.1 that automated electrophysiology does not give an accurate representation of potency, because of the limitations in the procedure (low incubation time) and thus the potency of **(44)** was expected to be higher than reported. On comparison with **(41)**, **(44)** was shown to be equally potent for the cardiac sodium channel. **(44)** then went on to be studied in a manual patch-clamp study to afford a more accurate IC_{50} for Na_v 1.4 and 1.5 channels.

5.5.2 Patch-clamp electrophysiology

For information of the procedure used for this study, see section 2.4.2. The results described in this section were provided by Scottish Biomedical®, UK. As described earlier, $hNa_v1.4$ and 1.5 stably expressed in HEK-293 cells were tested at 4 concentrations (0.1, 1, 10 and 30 µM) of **(44)** to ascertain an IC_{50} value. (These concentrations were chosen based on previous electrophysiological work which indicated an approximate IC_{50} in the low micromolar range.)

5.5.2.0 Results

Compound **(44)** showed a preference for binding to the inactivated state, inducing a significant reduction in control response.

Following testing in hNa_v 1.4, **(44)** had approximately 30,000-fold higher affinity for P2 (inactivated) compared to P1 (resting), with an IC_{50} 4 nM *vs* 126 µM, respectively. The maximal inhibitory response (I_{max}) of **(44)** was approximately 98% total block at the

maximal concentration of 30 µM in P2, whilst only 30% was seen in P1. Figure 5.6 shows the trough of the dose response curve only.

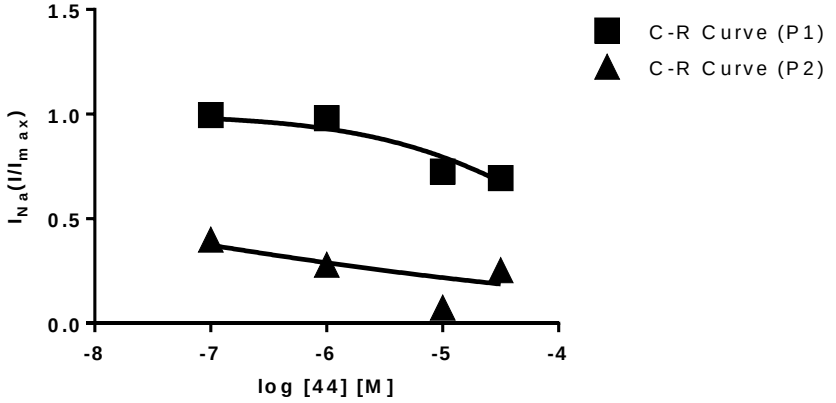

*Figure 5.6: Dose response curve of hNa$_v$ 1.4 of **(44)** (0.1-30 µM) under P1 and P2 conditions*

Following testing in hNa$_v$ 1.5, **(44)** had a higher affinity for P2 (inactivated) compared to P1 (resting), with IC$_{50}$ 3 nM. No IC$_{50}$ could be calculated for P1 at the maximum concentration tested due to its limited inhibitory activity. The maximal inhibitory response (I$_{max}$) of **(44)** was approximately 69% total block at the maximal concentration of 30 µM in P2, whilst only 22% was seen in P1. The data points from Figure 5.7 show the trough of the dose response curve only.

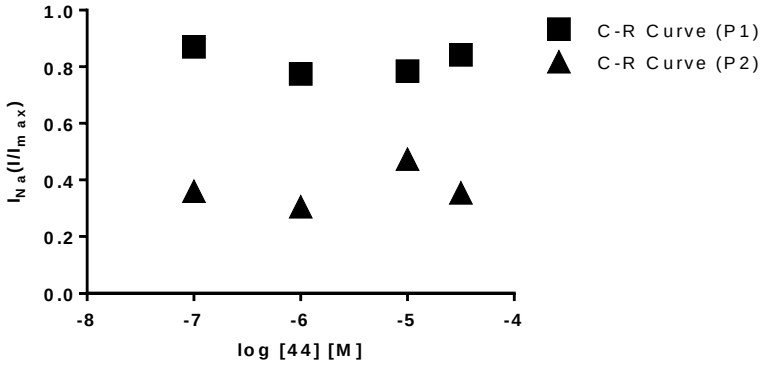

*Figure 5.7: Dose response curve of hNa$_v$ 1.5 of **(44)** (0.1-30 µM) under P1 and P2 conditions*

5.5.2.1. Discussion

The estimated IC$_{50}$ values quoted for each channel indicated that **(44)** is far more potent than was initially established (Section 5.5.1.0). The values quoted here, are four orders of magnitude more potent (comparing Na$_v$ 1.5, IC$_{50}$ 3 nM *vs* 15.6 µM). Although there is a high margin of error associated with these values. Interestingly, these results

highlighted a narrower degree of selectivity between the two channels (4 *vs* 3 nM; 1.4 *vs* 1.5), than was seen before, highlighting **(44)** to be equally potent for Na_v 1.4 and 1.5. As mentioned previously, there is a high error associated with this assay. All concentrations showed maximal blocking as was seen in results from **(9)** and **(41)**.

Overall, this second assay has allowed for a better insight into the potency of this novel VGSC ligand, but due to the unexpected high potency of this compound, only an approximate IC_{50} was afforded. This compound will require further testing at lower concentrations, but it was not possible within the confines of the research grant to commission a further external study.

To give an indication of the possible binding potential of **(44)** (as calculated previously for **(41)** and **(9)**) the IC_{50} of 3 nM for Na_v 1.5 was used as an approximation of the K_d. Again, 6.6 µM was taken as an indication of the B_{max}. Therefore, the estimated binding potential for **(44)** is 2,200. Again, caution must be applied to this value; however, it is above the minimum recommended value of 10.

The next steps were to establish the *in vivo* characteristics of **([^{18}F]44)** through a biodistribution study. Namely, to ascertain whether this compound was able to show uptake, retention and clearance in key tissues.

5.6 *In vivo* studies

All *in vivo* studies were kindly performed by the *in vivo* biology team, GE Healthcare, Amersham.

5.6.0 Log P determination

As outlined in Section 4.4.0, Log P was measured using the shake-flask method to indicate potential lipophilicity and infer some metabolic stability. The measured value was 3.05, which is inside the range 2 <logP< 3.5 typically identified as optimal.

5.6.1 Näive mouse biodistribution

We initially characterised **([^{18}F]44)** through a näive mouse biodistribution study (Figure 5.8) to ascertain whether the triazole moiety (which replaced the amide), offered a more suitable *in vivo* profile then **([^{18}F]41)** (Chapter 4).

5.6.1.0 Results

([^{18}F]44) was delivered in 10% n.d.c. e.o.s. yield from [^{18}F]fluoride, as a phosphate buffer /ethanol solution (9:1; 1/1) at 25.0 MBq per ml, with specific activity 16.8 GBq/µmol. 2.5 MBq (100 µl) were injected *via* the tail vein to each CD1 näive male mouse. The radiotracer concentration was sampled at 2, 15, 30, 60 and 120 minutes, three animals were sacrificed at each time point.

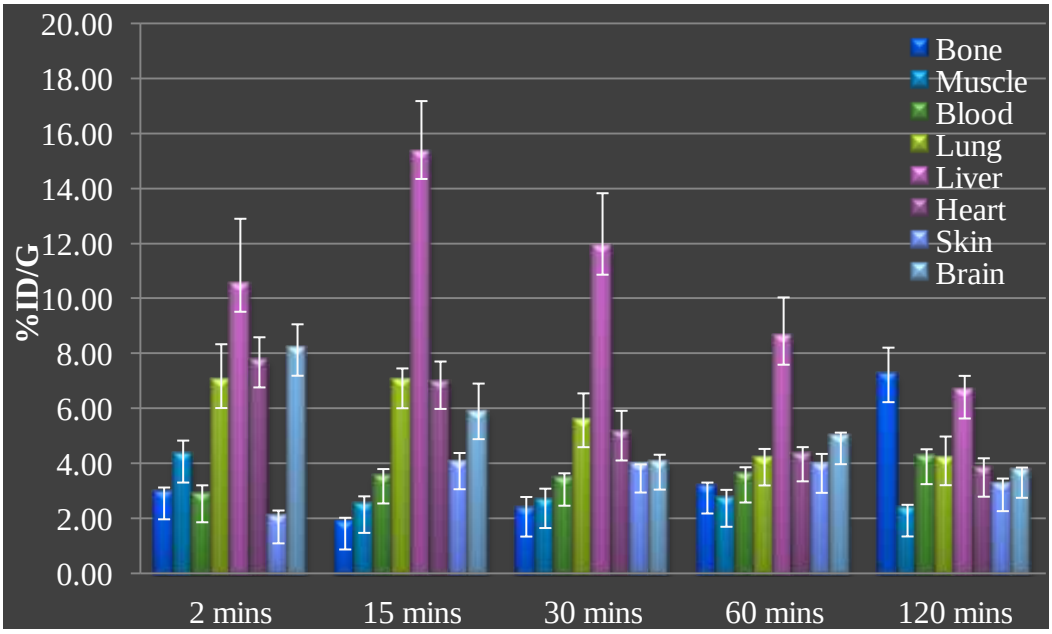

*Figure 5.8: Naive biodistribution graph of **([^{18}F]44)***

Tissue	2 minutes	15 minutes	30 minutes	60 minutes	120 minutes
			Mean %ID/G ± SD (n=3)		
Bone	2.98 ± 0.16	1.88 ± 0.15	2.35 ± 0.44	3.19 ± 0.12	7.24 ± 0.98
Muscle	4.32 ± 0.53	2.49 ± 0.33	2.66 ± 0.43	2.71 ± 0.34	2.36 ±0.15
Blood	2.87 ± 0.34	3.56 ± 0.25	3.48 ± 0.18	3.59 ± 0.28	4.26 ± 0.27
Lung	7.02 ± 1.32	7.02 ± 0.45	5.60 ± 0.96	4.21 ± 0.33	4.22 ± 0.77
Liver	10.52 ± 2.38	15.35 ± 1.83	11.87 ± 1.96	8.60 ± 1.45	6.65 ± 0.55
Heart	7.77 ± 0.82	6.99 ± 0.72	5.12 ± 0.81	4.36 ± 0.24	3.80 ± 0.40
Skin	2.11 ± 0.19	4.07 ± 0.32	3.95 ± 0.02	3.94 ± 0.41	3.28 ± 0.19
Brain	8.20 ± 0.87	5.89 ± 1.02	4.06 ± 0.27	4.98 ± 0.15	3.76 ± 0.10

*Table 5.2: Näive biodistribution data of **([^{18}F]44)** in key tissues*

The radiotracer showed good initial uptake in the brain (8.2 ± 0.9% ID/g, 2 minutes) and heart (7.8 ± 0.8% ID/g, 2 minutes) unlike **([^{18}F]41)**, where clearance from these organs was almost complete after 30 minutes. Here, after 30 minutes there was a much

higher degree of radiotracer retention in the brain (4.0 ± 0.3% ID/g) and heart (5.1 ± 0.8% ID/g) whilst after 120 minutes the tracer appeared to have potentially cleared (brain: 3.8 ± 0.1% ID/g *vs* heart: 3.80% ID/g). Clearance of the tracer was mainly through the hepatobiliary system (27.7 ± 0.2% ID; 120 minutes) and some through the renal system (7.2 ± 0.4% ID; 120 minutes). Muscle also showed some retention although not much initial uptake was seen (4.3 ± 0.5% ID/g, 2 minutes *vs* 2.4 ± 0.2% ID/g 120 minutes). As mentioned in Section 4.4.1.0, uptake in the muscle was presumed to be consistent with binding to Na_v 1.4 (known to be expressed in the muscle). Lowest blood levels were seen at 2 minutes (2.9 ± 0.3% ID/g); subsequent time points showed higher levels, which may indicate diffusion of radiotracer or its metabolite into the systemic system. Interestingly, the skin level (skin known not to contain VGSCs) although low at 2 minutes at 2.11 ± 0.2% ID/g, increased to 3.95 ± 0.02% ID/g within 30 minutes. This could be reasoned by contamination from blood which also followed a similar pattern. The lung showed uptake consistent with dispersion of radioactivity into the tissue which quickly diffuses back into the blood. Bone level remained low throughout the time course of the study (average 2.60 ± 0.3% ID/g in the first 60 minutes) until the last time point at 120 minutes, the radioactivity level increased to 7.24 ± 1.0% ID/g. All three animals were fairly consistent, so it was not thought that this was due to contamination from other tissues, but more likely, free [^{18}F]fluoride binding which has been released during metabolism of the tracer.

5.6.1.1 Discussion

This biodistribution showed good initial uptake in both the brain and heart, with enhanced retention seen in the heart suggesting some specific binding here. Although **([^{18}F]44)** was shown to be less selective towards Na_v 1.1-1.3 and 1.6, good initial uptake in the brain was seen, but less of this uptake was retained, therefore, corroborating *in vitro* results that this tracer is not particularly active in the CNS.

On comparing **([^{18}F]44)** and **([^{18}F]41)**, it appears that **([^{18}F]44)** shows a more positive uptake and retention profile, whilst showing some clearance from major organs within 120 minutes. Without having **(9)** radiolabelled with fluorine-18, it was difficult to assess whether this biodistribution profile was better or worse than **([^{3}H]9)**.

On comparison of **([^{18}F]44)** with the CNS expressing NMDA receptor PET tracer [^{18}F]memantine (as first discussed in Section 4.4.1.0), this tracer showed much higher initial uptake in the heart (2 minutes, 7.8 ± 0.8% ID/g) (where our channel is expressed), compared with 2.50 % ± 0.13% ID/g in the brain at 5 minutes reported for [^{18}F]memantine.[180]

In addition, it is important to note the specific activity of 16.8 GBq/µmol. As discussed in the previous chapter, the relative concentration (B_{max}) of VGSCs in each tissue is still unknown. Therefore, it is difficult to appreciate whether there is a saturation of VGSCs from binding of **(44)**. Future work will require the B_{max} of VGSCs to be determined in all expressing tissues to allow a greater understanding of how much VGSC binding is occurring from 'cold' by-products, and how many VGSCs are still available for **([^{18}F]44)** to bind to.

5.6.1 Näive mouse metabolism

To complement the results of the biodistribution, a metabolism study was performed to demonstrate the stability of **([^{18}F]44)** *in vivo* (2-60 minutes). Cellular protein was removed by precipitation using ice-cold acetonitrile (see Section 2.5.1).

Before the metabolism study was performed, an extraction efficiency test was executed using a 0.6 mL plasma sample with 6 MBq of **([^{18}F]43)**. The percentage recovery of radiotracer associated with this method was checked at each step (Table 5.3). Each percentage reported is with respect to the previous step.

Sample	% Recovery (n.d.c.)
Post centrifugation supernatant	96
Post centrifugation pellet	4
After removal of solvent	86
After filtration of HPLC sample	64
HPLC eluent waste	100

Table 5.3: Percent recovery (n.d.c.) from protein precipitation method

This method gave good recovery of the radiotracer into the supernatant with little **([^{18}F]44)** remaining in the pellet (4% recovery) and washes. However, some radiotracer was retained during filtration of samples prior to the HPLC injection, so this step was omitted in the subsequent metabolism study. Each sample was quickly injected onto a semi-preparative HPLC system and co-injection of **(44)** was performed. All solvent

waste from the HPLC was collected and measured, showing that all radiotracer was efficiently eluted from the column. Having shown this method to afford good recoveries, this procedure was used to carry out the metabolism study.

5.6.1.0 Results

([^{18}F]44) was delivered in 7.3% n.d.c. e.o.s. yield from [^{18}F]fluoride at 104 MBq/mL as a phosphate buffer /ethanol solution (9:1; 1/1), with 0.187 specific activity GBq/µmol. 10.4 MBq (100 µl) was injected *via* the tail vein to each C57BL/6 näive male mouse. Unfortunately, the specific activity was not as high as normal, but as interest was only in the metabolism of **([^{18}F]44)** and not of the cold impurities, it was thought this would not affect any results. The radiotracer concentration was sampled at three time points (2, 15 and 60 minutes) in the heart and plasma and at 15 minutes only in the brain. One animal was sacrificed at each time point (except 60 minutes, where two animals were sacrificed and their tissue combined due to little activity remaining at later time points). Once the tissue was extracted at each time, the tissue samples were cleaned, homogenised and separated using the protein precipitation method as discussed previously. Table 5.4 shows the percentage parent *vs* non-parent for each time point in the heart and plasma. A 15 minute brain sample was taken to see whether the uptake shown in the brain during the biodistribution was due to uptake of parent or non-parent.

Tissue	Time (min)	% Parent Compound	Parent %ID	Parent %ID/G	Non-parent %ID/G
Heart	2	100	0.98	7.77	-
	15	93	0.85	6.5	0.49
	60	56	0.33	2.44	1.92
Brain	15	94	3.81	5.54	0.35
Plasma	2	100	5.61	2.87	-
	15	71	4.57	2.53	1.03
	60	14	0.94	0.5	3.09

Table 5.4: Raw data of percent metabolite and percentage injected dose as parent (n=1)

([^{18}F]44) showed good overall in vivo stability. It is interesting to note that percentage parent in the brain (94%) (Figure 5.9A) and in the heart (93%) (Figure 5.9B) was very

similar at 15 minute time point. While in the plasma (Figure 5.9C), less parent was seen (71%) at the same time point.

(A)

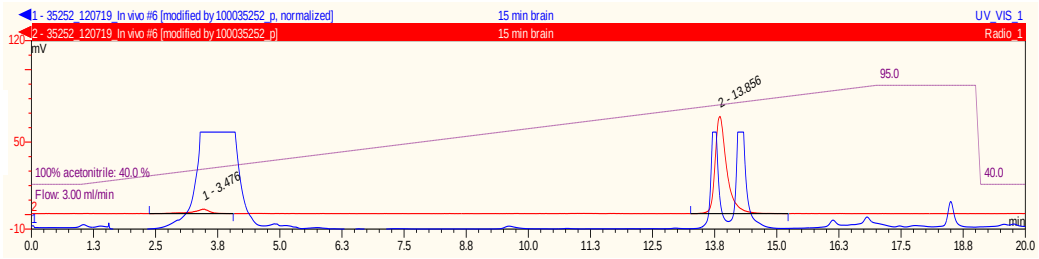

(B)

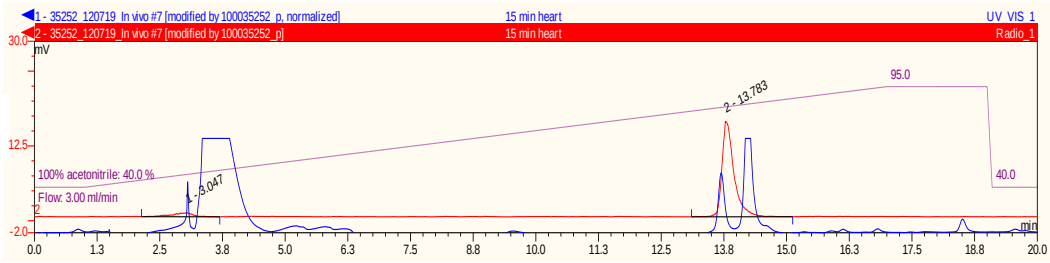

(C)

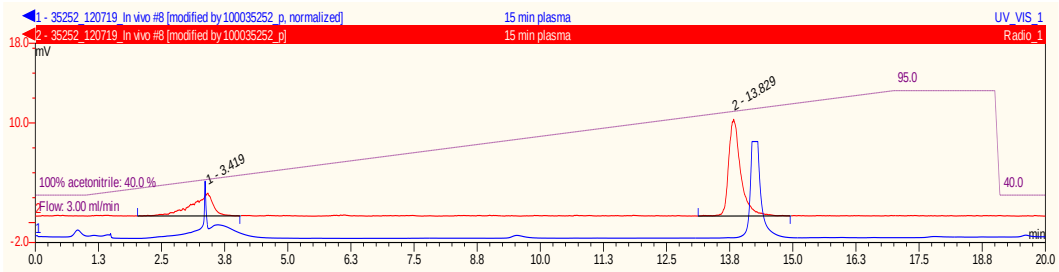

Figure 5.9: Radio chromatogram of labelled parent molecule and labelled metabolites at 15 mins post iv injection (red trace) in (A) brain, (B) heart and (C) plasma overlaid with UV chromatogram with "cold" ***(44)*** *co-injected (blue trace).*

After 60 minutes, further metabolism of the tracer was observed. A hydrophilic metabolite was observed in the heart and plasma (Figure 5.10). In the plasma, the percentage non-parent was much larger than in the brain and heart.

(A)

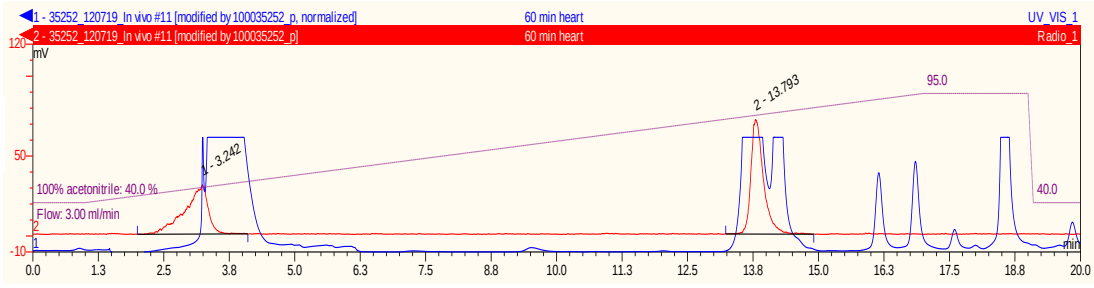

(B)

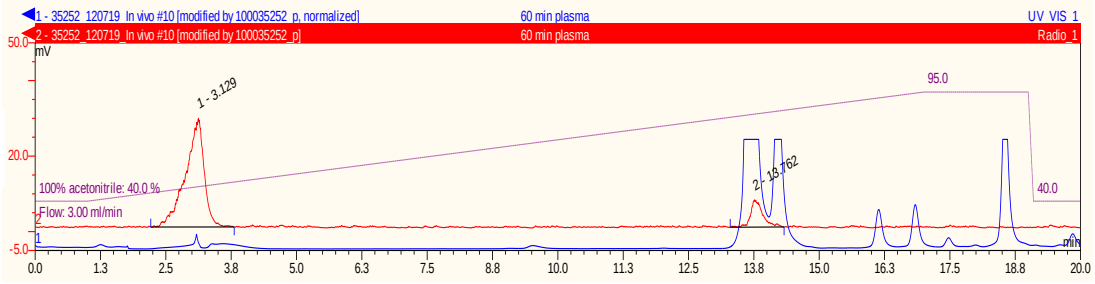

Figure 5.10: Radio chromatogram of labelled parent molecule and labelled metabolites at 60 mins post iv injection (red trace) in the (A) heart and (B) plasma overlaid with UV chromatogram with "cold" ***(44)*** *co-injected (blue trace),*

In order to give an indication of the possible active metabolite(s), the structure of **(44)** was analysed using Meteor™ software (Lhasa limited). This software produces structures of the most plausible metabolites using reasoning from phase I and II metabolism processes and published reports of metabolites based on similar structures. Meteor™ inferred a 5-hydroxylation of the trisubstituted distal phenyl ring as a possible phase I metabolism product. However this is not a plausible structure as the metabolite(s) eluted from the HPLC in the solvent front. Therefore, the metabolite(s) are hydrophilic species. From the naive biodistribution, the bone uptake remained low at 60 minutes, thus, it is unlikely that one of the metabolites was [^{18}F]fluoride. One possible suggestion is cleavage of the triazole ring, either re-forming (1-^{18}F)fluoroethyl azide or potentially (1-^{18}F)Fluoroethane. The metabolites will need to be determined in future work.

5.6.1.1 Discussion

Overall, the study showed that uptake in the heart and brain is mainly parent radiotracer (at 2 and 15 minutes) and not a metabolite (Table 5.4). While after 60 minutes the amount of parent radiotracer decreases and more metabolite is seen, which is consistent with the biodistribution data, as the signal in these tissues decreases after 60 minutes. It is likely that the metabolite would not be an active VGSC ligand, which may explain why the signal from the brain and heart decreases. Although not as many time points were studied here as in the biodistribution (due to laboratory time constraints and tracer decay), this metabolism study indicates adequate *in vivo* stability of **([^{18}F]44)** and allowed for further investigations of this tracer in a disease model.

5.7 Conclusions of Chapter 5

In summary, this chapter has shown that **([^{18}F]44)** was successfully synthesised in moderate yield through a copper catalysed Hüisgen 1,3-cycloaddition. Thereafter, **(44)** was characterised through a series of electrophysiological studies to ascertain its potency and selectivity for VGSC sub-types. These studies showed **(44)** to be both potent and sub-type selective, but an accurate IC_{50} value was not determined. Automated electrophysiology results showed **(44)** to have less than ideal affinity, with IC_{50} 15.6 µM for Na_v 1.5. Manual patch clamp results indicated the potency to be rather lower, with all concentration (100 nM lowest) showing >50% inhibition of sodium currents. Further work is now required to test this compound at <100 nM in both Na_v 1.4 and 1.5.

Consequently, we evaluated this tracer *in vivo* through a näive biodistribution and metabolism study. The data showed **([^{18}F]44)** to have good uptake in key tissues while clearance was seen through the hepatobiliary system over the 2 hour time course studied. The metabolism study corroborated that uptake seen in the biodistribution during early time-points (2-15 minutes) was consistent with parent rather than non-parent uptake. Whereas at 60 minutes, metabolised product was seen in higher concentration, especially in the plasma. Overall, early näive pre-clinical studies highlighted this tracer as a promising candidate for PET imaging. As a result of this data, **([^{18}F]44)** was selected for studying in two types of breast cancer, metastatic (MDA-MB-231 cell lines) and non-metastatic (MCF-7 cell lines) (Chapter 6).

Autoradiography was performed on brain and heart slices (Appendix 5.8) to ascertain specific binding using a 1000-fold higher concentration of **(44)** *vs* **([^{18}F]44)** for blocking. However, these results were inconclusive. At the time of this study, we received electrophysiology data from Chantest, US that confirmed there was no or little binding in the tonic (resting) state. Although some specific binding had been inferred for these data, it was then highlighted that binding of our compound occurs in a physiological dependent state, so the data shown was not be a fair representation of the possible specific binding that may occur *in vivo*. For interest, these images are disclosed but are not put forward as evidence of specific binding. Following the termination of this study, literature research was undertaken to outsource a binding study. Studies available to screen novel potential VGSC ligands centred around automated and patch-clamp electrophysiology as previously performed (Section 5.5), with binding studies

available on homogenised cerebral cortex (site of Na_v 1.1-1.3 and 1.6 expression) tissue. Moreover, it was not possible to find a study which used homogenised heart tissue to measure specific binding. Additionally, as this tracer was hoped to potentially target the neo-natal splice variant of the cardiac sodium channel (expressed in B Ca), it was thought it would be more beneficial to measure specific binding in that variant. There are seven amino acids differences between the neo-natal and adult channel affecting DI: TMS3, most of DI:TMS4, and DI:TMS3-S4. As it was not known how, or if binding of **(44)** would be altered in the neo-natal splice variant, the next study was invaluable.

5.8 Appendix

Autoradiography was performed on brain and heart slices. **([^{18}F]44)** was delivered in 6 MBq/mL as a PBS/EtOH solution (9:1; v/v), with specific activity 3.53 GBq/µmol.

Frozen heart and brain tissue were sliced (10-15 microns) and placed on glass microslides. All slices were incubated with **([^{18}F]44)** (100 µL) for 60 minutes at RT. In order to perform a blocking study, a 1000-fold concentration of **(44)** was added to one set of slices, prior to addition of **([^{18}F]44)**. All slices were then washed with PBS three times to remove all non-bound radiotracer, and then exposed to Kodak™ film for 20 minutes before developing the films. The films were digitised and interpreted using MCID software to measure radiotracer uptake. Specific binding (sb) was measured by using digitised non-blocked slices and subtracting total uptake from digitised blocked slices (see Section 2.4.3).

As mentioned previously, this study was not included in the main chapter, as during this work, results received showed that **(44)** binds in a physiological dependent state (Section 5.5.1). Nevertheless, the images were analysed to complete this section of work.

Brain

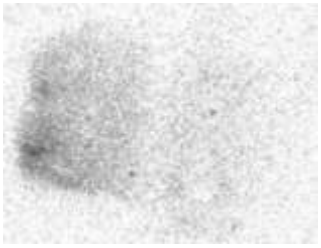

Olfactory bulbs

(sb 30-40%)

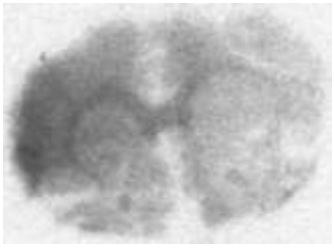

Frontal cortex

(sb 30-40%)

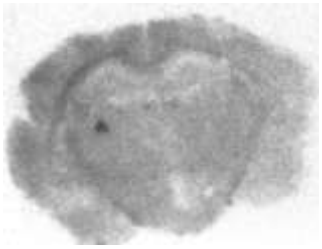

Dorsal hippocampus

(sb 50-60%)

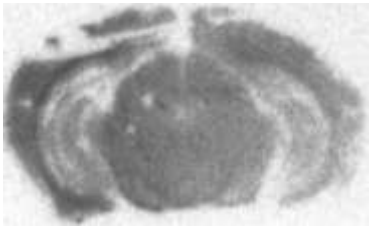

Ventral hippocampus

(sb 60-70%)

Mid-brain

(sb 50-60%)

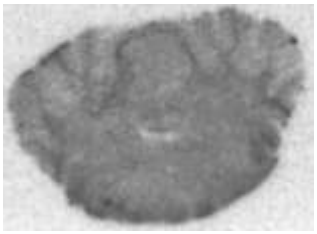

Cerebellum

(sb 30-40%)

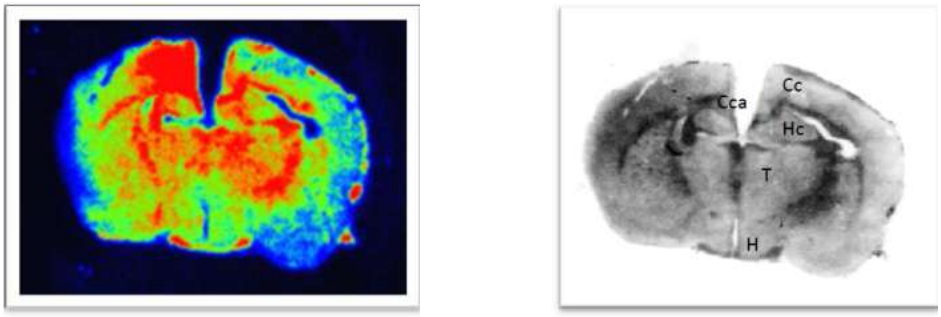

Dorsal Hippocampal slice imaged on a Microimager™ (no sb measured)

Figure 5.11: Autoradiography images of brain slices

These images highlighted some specific binding in the brain, particularly in the hippocampal region. Possibly this is due to some binding to Na_v 1.6 (expressed in the hippocampus) in the resting state.

Heart

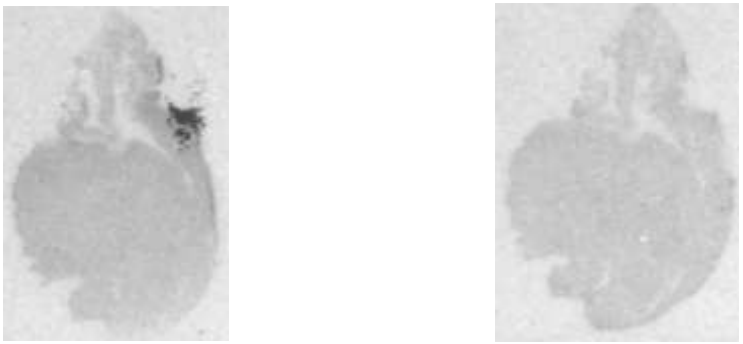

Mid-heart (sb 20-25%) Mid-heart (sb 20–30%)

Figure 5.12: Autoradiography of heart slices

Little specific binding was seen in the cardiac tissue, presumably due to the tracer being unable to bind to the tissue.

In summary, this study did not allow for accurate measurement of specific binding. Additionally, a cell binding assay was used to monitor specific binding (Section 6.1.0).

6. Results and Discussion

Preliminary application of [^{18}F]4-(4-(2,4-difluorophenoxy)-phenyl)-1-(2-fluoroethyl)-triazole in PET imaging of breast cancer

6.0 Rationale for metastatic breast cancer study

After the successful synthesis and initial näive bioevaluation of **([^{18}F]44)**, the next steps were to apply this potential PET radiotracer for *in vitro* and *in vivo* assessment in a tumour model. The aim of this study was to assess if **([^{18}F]44)** could image highly metastatic tumours.

As described in chapter 1, high VGSC expression is associated with increasing metastatic potential of various tumours. Importantly, it was shown that neo-natal Na_v 1.5 is associated with the strongly metastatic model of breast cancer MDA-MB-231, showing 1800-fold higher mRNA expression than the weakly metastatic model (MCF-7), which shows little or no expression.[54, 59, 189-190] *In vitro* work (Chapter 5), highlighted **([^{18}F]44)** as a moderately selective VGSC ligand with highest affinity for Na_v 1.4 and 1.5. Crucially, there was good uptake in the heart during näive biodistribution studies and the *in vivo* characteristics were similar to that required for a PET radiotracer.[191-193] Namely, the radiotracer requires good uptake in key tissues above background, with pharmacokinetics that allow reversible binding and clearance within 2 hours.

In order to obtain an understanding of the binding of this tracer to the neo-natal cardiac sodium channel, cultured MDA-MB-231 cells (stably expressing neo-natal Na_v 1.5), were used to undertake a radioligand binding assay. Cultured MCF-7 cells were used as a negative control. The autoradiography described in Chapter 5 was not useful in providing accurate binding data due to **(44)** binding in a state-dependent manner. Cultured cells however, are dynamic systems, with functionally active sodium channels. We wanted to identify binding specifically to the neo-natal isoform of Na_v 1.5 expressed in metastatic breast cancer. There is however, significant sequence similarity between the adult and neo-natal isoforms, with only seven amino acids differing between the two. It is currently thought that these differences do not affect binding site 1, the most likely binding site for our tracer as briefly described in Section 5.5.0.

6.1 *In vitro* biology

Following previous findings by Djamgoz *et. al.*, that MDA-MB-231 cells display neo-natal Na_v 1.5 expression and MCF-7 cells low or no expression,[190] these cells were cultured for cell binding studies. Two variations of a standard radioligand binding assay

were carried out. Initially, a seeded-cell method was used, where cells were cultured in 96-well plates 24 hours prior to assay, and secondly, a cell suspension method. For more details see section 2.4.5.

Work described in this section was aided by the *in vitro* biology team at GE Healthcare, Amersham.

6.1.0 Cell binding study in MDA-MB-231 and MCF-7 cell lines

6.1.0.0 Results

Initially, MDA-MB-231 and MCF-7 cells (approx 1 x 10^4 cells) were seeded onto 96 well plates 24 hrs before assay commenced to create a monolayer of cells in the corresponding media (100 µL).

([^{18}F]44) was delivered in 6.0 MBq/mL as a phosphate buffer /EtOH solution (9:1; v/v), with specific activity 4.2 GBq/µmol.

Nine serial dilutions of **([^{18}F]44)** was prepared to give a wide concentration range (Table 6.1). A 10.6 µM solution of **(44)** (100-fold excess concentration of **([^{18}F]44)**), was prepared for the blocking study and added to a set of cells (for each tracer concentration), in duplicate. These cells were left for 5 minutes at RT to incubate prior to addition of each tracer concentration. **([^{18}F]44)** was added to all cells giving n=2 for the blocking study and n=3 for the binding study, at each concentration, per cell line. All cells were left to incubate for 60 minutes at RT. The cells were then washed with PBS and subjected to cleavage with trypsin for 5 minutes at RT. These cells were then washed, harvested and trapped to a printed glass fibre filter. The washed 96 well plates were monitored under a microscope to check that all cells were removed from the wells. The filter paper corresponding to each well was removed and activity counted using a gamma counter.

Dilution Number	Concentration (nM)
1	1600
2	530
3	180
4	59
5	19
6	6.5
7	2.2
8	0.73
9	0.27

*Table 6.1: Concentrations of **([^{18}F]44)** to measure specific binding*

Following completion of the assay the activity observed on the filters was found to be within background levels. Assessment of the 96 well plates with a beta counter detector showed significant activity, suggesting that the activity and by extension the tracer, remained on the plates. This indicated a high degree of non-specific binding to the plastic composite. Due to this issue, this assay method was not repeated.

To overcome this problem, a cell suspension radioligand binding assay was undertaken. **([^{18}F]44)** was delivered in 5.0 MBq/mL as a phosphate buffer/EtOH solution (9:1; v/v), with specific activity 3.7 GBq/µmol.

MDA-MB-231 cells (2.5 x 10^5 cells) and MCF-7 cells (2.5 x 10^5 cells) were aliquoted into twelve eppendorf tubes per cell line. Figure 6.1 details the assay set-up per cell line. Briefly, two concentrations (100 nM and 10 nM) of **([^{18}F]44)** were prepared from a stock solution, to measure binding. To estimate specific binding, a 10 µM concentration of **(44)** was applied to block VGSCs prior to addition of **([^{18}F]44)**. After addition of **([^{18}F]44)**, all cells were incubated for 60 minutes at RT. Cells were pelleted by centrifugation (1000 rpm, 5 minutes) and supernatant removed. To wash the cells, PBS (0.5 mL) was added and cells pelleted. This wash procedure was carried out twice. After washing, the cells were re-suspended in PBS (0.5 mL) for counting. In order to remove contamination due to non-specific binding associated with the eppendorf tubes, the cell suspensions were added to fresh tubes before counted overnight (Wallac counter).

([^{18}F]44) (100 nM)	**([^{18}F]44)** (10 nM)	Blank	**(44)** (10 µM) + **([^{18}F]44)** (100 nM)	**(44)** (10 µM) + **([^{18}F]44)** (10 nM)	**(44)** (10 µM)
([^{18}F]44) (100 nM)	**([^{18}F]44)** (10 nM)	Blank	**(44)** (10 µM) + **([^{18}F]44)** (100 nM)	**(44)** (10 µM) + **([^{18}F]44)** (10 nM)	**(44)** (10 µM)

Figure 6.1: Radioligand binding assay set-up, per cell line

Two controls were used to measure cell viability in the assay: cells without any **([^{18}F]44)** (media only), and cells with only **(44)** applied (block control). These cells underwent the whole procedure and cell viability was monitored at the end using a standard tryphan blue test to give an indication of active cell numbers (Table 6.2).

	MCF-7 cells	**MDA-MB-231 cells**
	Average cell viability (%)	
Blank	52 (61, 42)	52 (40, 63)
Block	40	44 (47, 42)

Table 6.2: Cell viability after assay (n=1/2)

Following cell viability test of the two cell lines, both gave approximately 52% viability on the blank cells (n=2), whilst slightly higher viability was seen in the MDA-MB-231 cells (44 *vs* 40%) incubated in 10 µM **(44)**, implying some toxicity at this concentration.

Following counting of all cell samples, all results were decay-corrected (d.c.) back to formulation time and expressed as a function of cell viability (Table 6.3).

Concentration of ([^{18}F]44)	**MCF-7 cells**	**MDA-MB-231 cells**
	Average d.c. cpm/viable cell (n=2)	
100 nM	921 (995, 849)	1084 (989, 1180)
10 nM	93 (104, 82)	243 (456, 30)
100 nM +**(44)** (10 µM)	1183 (1044, 1323)	1898 (2186, 1611)
10 nM +**(44)** (10 µM)	129 (141, 119)	329 (342, 440)

Table 6.3: Decay-corrected values of cpm/cell (per cell line).

These results suggested slightly increased binding of **([^{18}F]44)** to the MDA-MB-231 cells when compared to the MCF-7 cells, on average 1084 *vs*. 921 cpm/viable cell, respectively. Furthermore, the data from the MCF-7 cells suggested that the difference in cpm/viable cell was proportional to the two tracer concentrations tested (100 *vs* 10

nM). The MDA-MB-231 cells did not show this proportional correlation, which could be attributable to a saturation effect.

The blocking study showed no reduction in cpm for either cell line, implying a high degree of non-specific binding. In fact, when **([^{18}F]44)** (100 nM) was combined with **(44)** (10 μM) in the MDA-MB-231 cells, there was a 75% increase in cpm/viable cell (1898 *vs* 1084). However, at the lower concentration of 10 nM, this was not apparent (within error). The MCF-7 cells displayed a similar profile, but higher cpm/viable cell was seen at both concentrations.

6.1.0.1 Discussion

Initially, a standard seeded-cell radioligand binding study was performed to measure binding to the neo-natal channel in high and low expressing cell lines. Unfortunately, no binding was observed above background in either cell line and thus no difference was seen between the cells with block applied. A high degree of non-specific binding was observed to the well plate itself. These 96 well plates are made of a polystyrene composite treated with an enhanced cell binding surface, to aid cell attachment by incorporating more oxygen into the cell culture surface, rendering it more hydrophilic and with better surface stability. The plate washes were not extracted for counting, so it was not possible to determine whether there was no possible binding or whether no binding was due to no access of **([^{18}F]44)** to the cells.

Non-specific binding of highly lipophilic radiotracers to plastic is common and method validation to produce an optimised binding assay is time consuming and highly labour intensive. In order to overcome this issue in a timely manner, a cell-suspension radioligand assay was undertaken.

In contrast, the cell suspension assay afforded some useful information. Importantly, the assay was performed with little binding to the eppendorf tubes themselves. Although some activity remained bound to the eppendorf tubes, much of the activity was associated with the cell suspension.

Importantly, this assay highlighted uptake in the MDA-MB-231 cells to be 15% higher than the MCF-7 cells (n=2). This indicated a binding differential between the VGSC expressing (MDA-MB-231 cells) and non-expressing (MCF-7 cells). Also, a potential saturation effect was noted with the MDA-MB-231 cells over the two concentrations tested (Table 6.3). Where the concentration of **([^{18}F]44)** was increased 10-fold (10 nM

to 100 nM), a ten-fold increase in binding was not seen. Due to the minimal concentration range tested here, further investigations are warranted to assess this effect over a greater concentration range. The blocking study however, did not show expected results. The addition of a 100 and 1000-fold block of **(44)** did not inhibit binding of the radiotracer and in fact, these data suggested binding was slightly enhanced. This high non-specific binding indicated that perhaps **([^{18}F]44)** is not suitable as a PET tracer for targeting VGSCs in tumour cells. Another possible explanation for these data could be due to the low cell viability encountered. The cell viability test showed that only 50% of cells (approximately) were still functional at the end of the assay. This high cell death showed that the conditions employed were not able to maintain a high level of living cells. Cell death was probably due to permealisation of the cell membrane causing release of cellular debris. It is plausible that excess cell debris gave rise to non-specific interactions with both **(44)** and **([^{18}F]44)**. In order to discount this reasoning, an improved assay method is required which affords higher cell viability. It would also be interesting to see if a higher concentration of **(44)** would make any difference to the blocking effect, or whether the concentration used was having a toxic effect.

Nevertheless, this study was the first time a novel VGSC PET tracer was assessed for specific binding to metastatic tumour cells. This tracer is highly lipophilic, so some non-specific binding was anticipated. The next step would be to repeat this assay using a variety of conditions and with a greater range of concentrations of both **(44)** and **([^{18}F]44)**. Due to the time constraints of this study and increasing personal radiation dose, it was not possible to develop this assay further. To summarise, this assay provided useful results over two concentrations and most importantly, a difference between uptake in the MCF-7 and MDA-MB-231 cells was shown.

Although it was not possible to fully complete this assay and obtain the required binding data, an estimation of the required sodium channel density (B_{max}) can be calculated, if the binding potential is set to the generally accepted minimum value of 10. Using the approximate IC_{50} for **(44)** (Na_v 1.5; 3 nM) as the K_d, the approximate required B_{max} of Na_v 1.5 in breast tumour cells to give appropriate signal to noise ratio is ≥30 nM. Future work on VGSCs in breast cancer will require the relative expression of VGSCs to be determined.

6.2 *In vivo* biology

Alongside *in vitro* study, MDA-MB-231 and MCF-7 cells were inoculated into immune compromised mice to allow growth of tumours with high and low expression of neo-natal Na_v 1.5, respectively.[54, 59, 189-190] Full details see section 2.5.2

Initially an immunohistochemistry study (IHC) of the tumour tissue was planned using a non-commercial neo-natal Na_v 1.5 antibody to measure relative expression of the channel in our model prior to any further studies. Sourcing of the antibody through an academic collaboration however, proved unsuccessful. Thus this study was altered to an imaging and biodistribution study to ascertain *in vivo* uptake of **([^{18}F]44)** in a disease model.

Following reported work on neo-natal Na_v 1.5 expression levels by Djamgoz *et al.,* on MDA-MB-231 and MCF-7 cell lines,[190] and clinical evidence of channel expression in metastatic breast tissue,[194] tumours were grown with an assumed but not determined expression level.

Both MDA-MB-231 and MCF-7 tumours were grown post-inoculation for six weeks after which imaging and biodistribution studies were carried out to determine if **([^{18}F]44)** could detect metastatic breast cancer. Tumours grown from MCF-7 cells were imaged as a negative control experiment, as this cell line is associated with little or no VGSC expression.[190]

All *in vivo* data described in this section was kindly carried out by the *in vivo* biology team at GE Healthcare, Amersham.

6.2.0 Tumour growth and PET imaging of metastatic breast tumours

Briefly, MDA-MB-231 cells (1 x 10^6 cells in PBS; 100 µL) were inoculated into the mammary fat pad of six female severely combined immunodeficiency (SCID) mice. Following slow tumour growth over an initial six week pilot study, only five mice displayed tumours (average weight 42.3 ± 19.7 mg, post-dissection). [From herein, these animals are referred to as group #1 for imaging and biodistribution studies].

To increase tumour growth, an adjustment to the protocol was sought. Colleagues at Stanford University reported faster and larger tumour growth using a higher

concentration of cells.[195] Thus, 5 x 10^6 cells in PBS and Matrigel™ (100 µL; v/v) were injected into the mammary fat pad of SCID mice. Following a six week growth period, four tumours grew. They were slightly larger using this method (average weight 53.6 ± 38.4 mg, post-dissection), however they were not so consistent in size. [From herein, these animals are referred to as group #2].

Group Number	PET/CT imaging (number of studies)	Biodistribution (number of studies)
Group #1	2	3
Group #2	1	3

Table 6.4: MDA-MB-231 study outline

6.2.0.0 Results - study #1 / group #1

A tumour bearing mouse was selected for PET/CT imaging. **([^{18}F]44)** was delivered in 8.5% n.d.c. e.o.s. yield from [^{18}F]fluoride in 180 minutes at 59.0 MBq/mL, as a phosphate buffer /ethanol solution (9:1; v/v), with specific activity 0.68 GBq/µmol. 100 µL was iv injected *via* tail vein to a MDA-MB-231 tumour bearing SCID female mouse (tumour size approx. 4.7 mm x 3.6 mm, measured 6 hrs pre-imaging).

The animal was placed on a microPET scanner bed after tail-vein radiotracer injection. PET imaging commenced 6 minutes pi and ended 66 minutes pi. The animal was maintained under inhalation anaesthetic during the imaging and respiration rate monitored.

Imaging was assessed in three planes: transverse, coronal and sagittal to give an overview of binding and clearance.

A microCT scan was performed post PET imaging. CT images were used to determine anatomical information. During analysis, ROIs were positioned over key tissues with PET data overlaid to give functional data.

During the first 2 minutes of the PET imaging, the animal regained consciousness from anaesthetic producing motion distortion of the images. This made it difficult to overlay the PET and CT data accurately, therefore, images from 6-11 minutes pi were not analysed. The first PET imaging was analysed at 12 minutes pi (Figure 6.2).

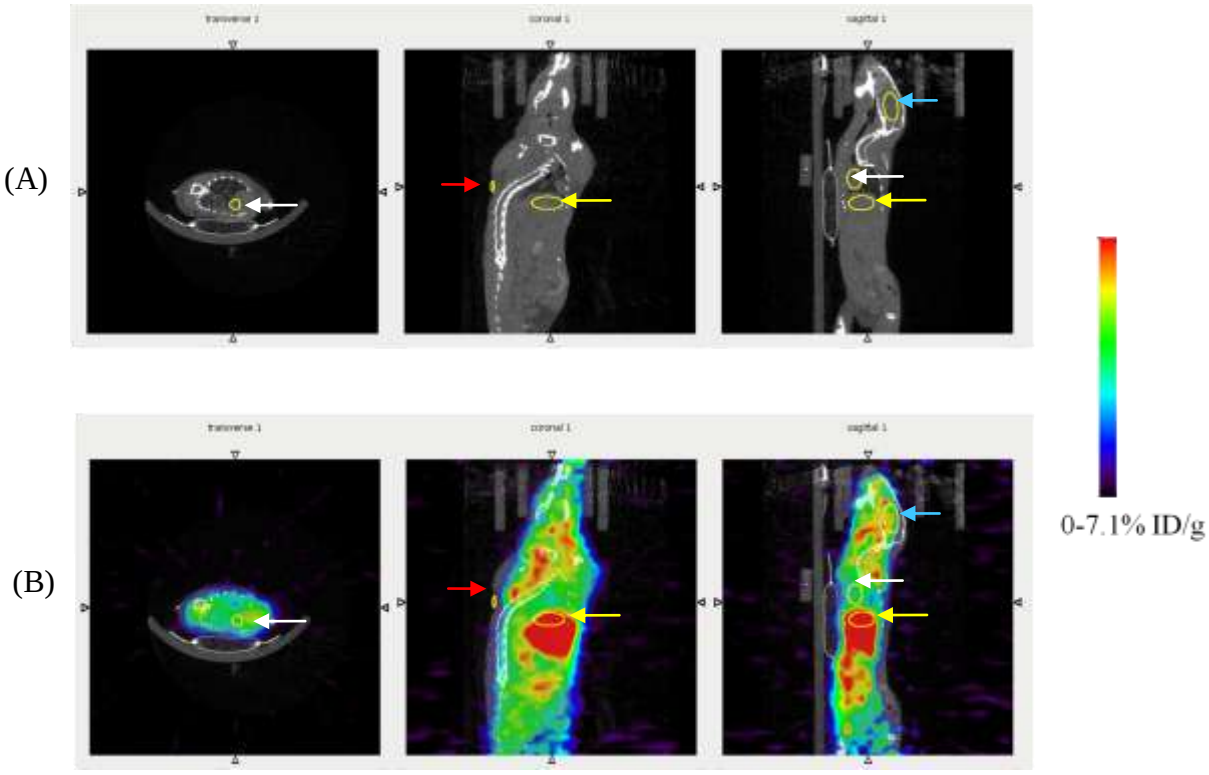

Figure 6.2: Dynamic PET image 12-14 minutes pi: ROIs for tumour (coronal view, red arrow), brain (sagittal view, blue arrow), heart (transverse and sagittal view, white arrow) and liver (coronal and sagittal views, yellow arrow). (A) CT image (B) PET/CT image. PET calibration bar indicating 0-7.1% ID/g

Radiotracer uptake was apparent in the liver and brain, with the heart showing no radiotracer uptake above background (Figure 6.2). Some motion distortion still affected these images, so the alignment of the PET and CT data was not exact, hence why the tumour imaged by CT does not overlay with the PET data.

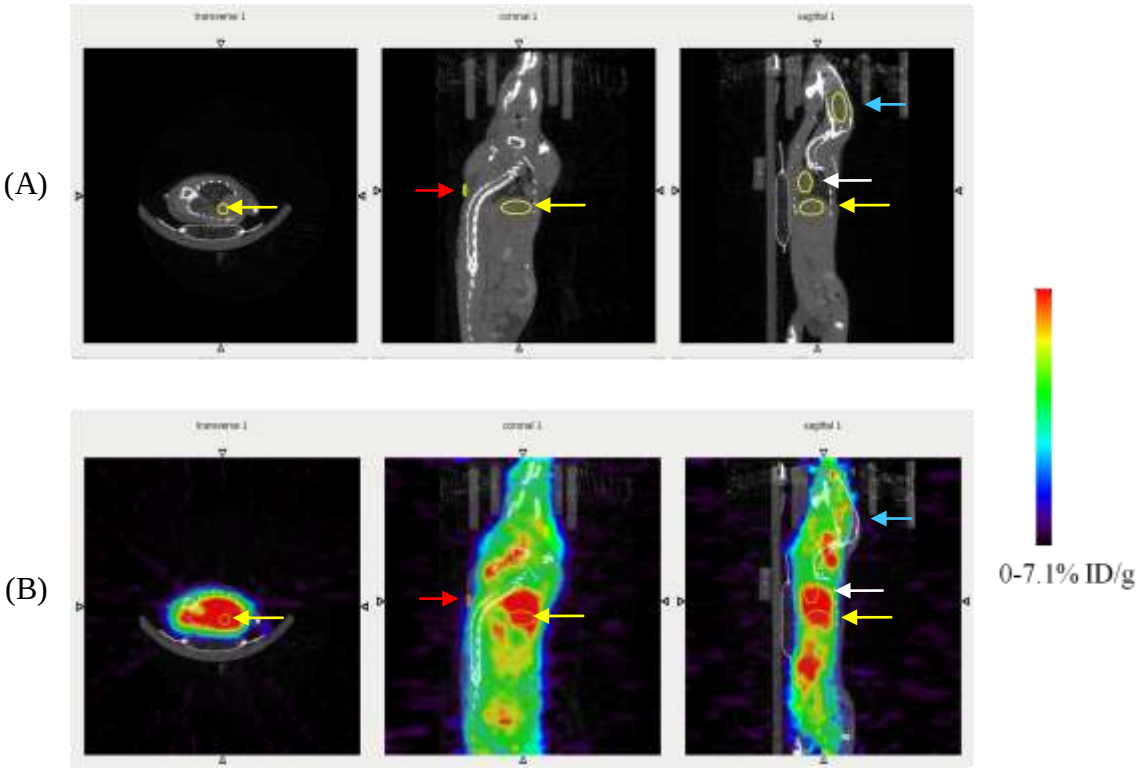

Figure 6.3: Dynamic PET image 31-32 minutes pi: ROIs for tumour (coronal view, red arrow), brain (sagittal view, blue arrow), heart (sagittal view, white arrow) and liver (coronal and sagittal views, yellow arrow). (A) CT image (B) PET/CT image. PET colour indicating 0-7.1% ID/g

The latter time points of the imaging (31-32 minutes pi) showed more exact overlay between the PET and CT images. Radiotracer concentration in the brain appeared to decrease and uptake in the heart is now apparent (Figure 6.3), but could not be resolved from radiotracer concentrations in the liver.

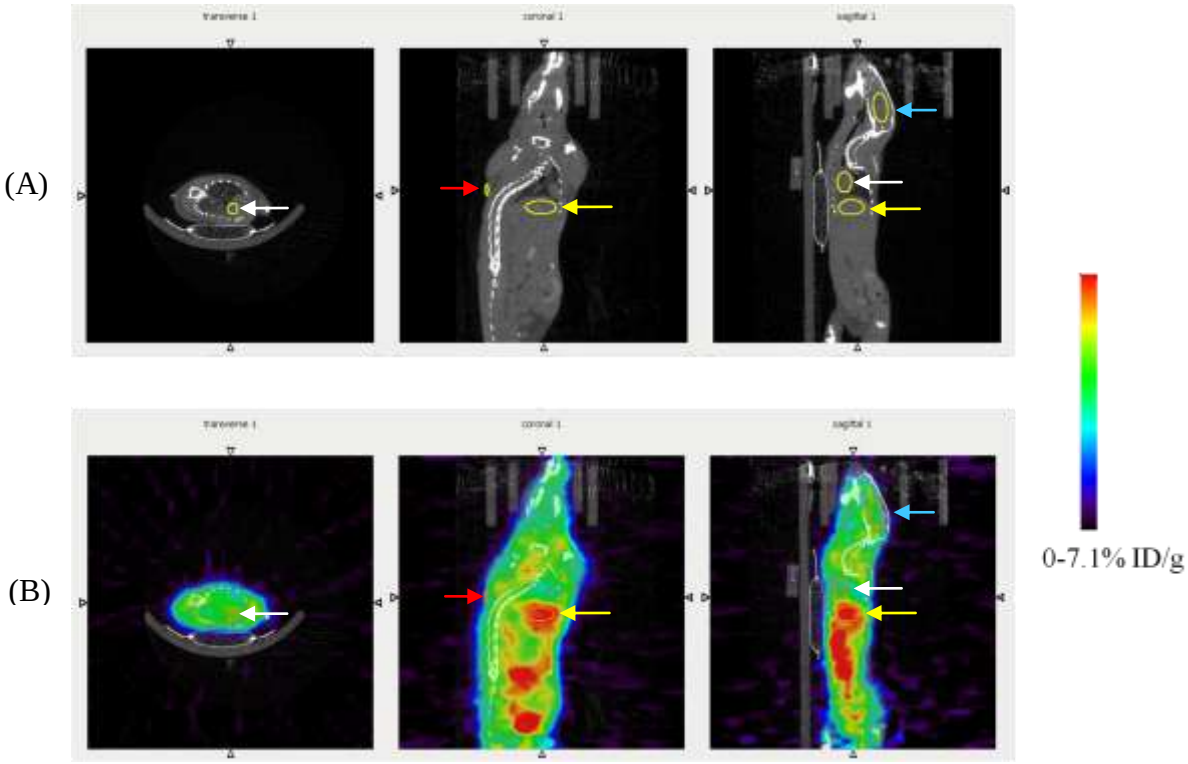

Figure 6.4: Dynamic PET image 65-66 minutes pi: ROIs for tumour (coronal view, red arrow), brain (sagittal view, blue arrow), heart (sagittal view, white arrow) and liver (coronal and sagittal views, yellow arrow). (A) CT image (B) PET/CT image. PET colour indicating 0-7.1% ID/g

The last minutes of the imaging (Figure 6.4) showed high levels of radioactivity in the liver and bladder while radioactivity seen earlier in the heart and brain had cleared.

During the last minute of the PET image. The animal's respiration deteriorated without recovery. It was not clear what caused this effect. The PET radiotracer was examined and the solution had turned slightly cloudy (90 minutes post formulation). The precipitate likely to be an impurity co-eluting with **([^{18}F]44)**. Although no ill effects were seen during radiotracer administration, the radiotracer was discarded and an improvement to the purification of the radiotracer was sought.

Compounds used in the synthesis of **([^{18}F]44)** were analysed as possible contaminants using analytical HPLC. Alkyne **(42)**, 2,4-difluorophenol and 4-fluorophenylacetylene were checked for co-registration of retention times with the unknown contaminant. Following analytical HPLC, 4-fluorophenylacetylene was shown to have the same retention time as **([^{18}F]44)** (gradient: 5-95% MeCN / H_2O over 15 minutes), t_R = 11.3 minutes. However, this compound was not present in the alkyne starting material **(42)**. Overall, it was not possible to identify the contaminant.

A time course of the PET data was plotted to monitor the biodistribution of **([^{18}F]44)** commencing from 12 minutes pi (Figure 6.5). Activity concentrations from ROIs of key tissues were measured from the PET data and converted to %ID/mL. Earlier time points were not plotted as motion distortion (when the animal regained consciousness) made it difficult to assign accurate ROIs. Alongside the PET imaging, radiotracer concentrations from a biodistribution study (section 6.2.1) using three tumour bearing mice from the five that grew [group #1], were also carried out to measure radioactivity levels at 15 minutes (n=3) and an animal was also imaged 74 minutes (n=1) after administration of **([^{18}F]44)**. Biodistribution studies measured radiotracer concentration in % ID/g whereas the PET time curve was measured in % ID/mL, it was assumed that the ratio of g:mL was one, so the biodistribution and PET data could be compared.

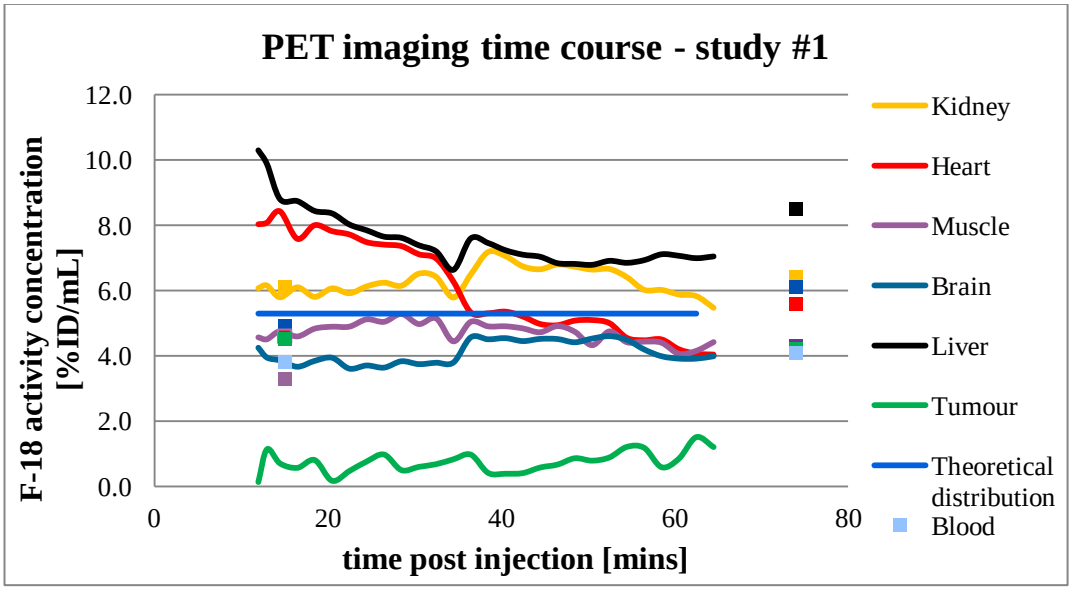

Figure 6.5: PET imaging time course (12-66 minutes pi) in key tissues (lines) and biodistribution data (points)

Overall, the PET imaging time course showed some clearance of radiotracer from the liver and heart, while uptake in other tissues (brain and muscle) appeared not to reverse. More specifically, highest uptake was seen in the liver, which started to clear over the first 30 minutes of the imaging to give a consistent 6.5 ± 0.3% ID/mL in the later time points. The heart however, showed continual clearance of radiotracer over the 60 minute imaging. The kidney gave a consistent level of radiotracer (5.9 ± 0.3% ID/mL) until approximately 38 minutes pi where an increase was seen and then some clearance in the final 20 minutes of the imaging. In contrast, the muscle, brain and tumour were quite consistent in their concentration of radiotracer indicating little clearance over the 60

minute time course, with tumour uptake the low throughout the imaging. The uniform theoretical distribution line and blood data points (biodistribution data) were used to indicate background radiotracer concentration. The theoretical distribution line (from PET data) assumes there is no specific uptake of the tracer and that instead the tracer distributes evenly throughout the body. Of course usually this is not the case, even for a non-binding compound clearance through specific organs starts straight away, giving an uneven distribution. This marker therefore, is a crude threshold for targeted binding. Here, **([^{18}F]44)** does appear to distribute evenly throughout the body so the uniform distribution is indicated, to allow comparison against this "surrogate" background level.

The liver, kidney and heart were all above the distribution line at early time points with the muscle, brain and tumour remaining below at all time points. When comparing with the blood level however, (which itself remained consistent at the two time points, 15 and 74 minutes, pi) then all tissues except muscle fall above background.

The imaging results showed little consistency with the biodistribution results at 15 minutes pi. A significant difference in tumour uptake was seen (4.5 *vs* 0.7% ID/mL; 15 minutes), with the imaging indicating the lower value. The brain also showed lower uptake in the imaging than the biodistribution. In contrast, the imaging indicated higher levels (than the biodistribution) in both the muscle and heart (*NB*: biodistribution point masked by tumour point). Almost exact alignment was seen in the kidney. The liver point (25.5% ID/mL; biodistribution 15 minutes pi) was not plotted as it was significantly higher than the 0-12% ID/mL range.

The biodistribution results at 74 minutes pi also highlighted a different pattern to that seen at the end of the imaging (66 minutes). The biodistribution showed higher levels of radiotracer in the liver, brain, heart, kidney and tumour than was reported at the end of the imaging. However, the muscle showed a very similar level.

6.2.0.1 Discussion

In summary, the first PET images of the MDA-MB-231 tumours gave no evidence that **([^{18}F]44)** is able to highlight ion channel activity in metastatic breast tumours.

Firstly, it is important to note that the tumours themselves were slow to grow over a six week period, which indicated these tumours probably were not aggressive in their

nature. It is well established that the metastatic potential and aggressiveness of these tumours is directly correlated to the expression of VGSCs; therefore its likely these tumours expressed little neo-natal Na_v 1.5. Moreover, it was not possible to determine the relative expression of VGSCs within the tumour cells due to the neo-natal Na_v 1.5 antibody not being available.

The time course of the PET imaging was plotted and overlaid with results from a biodistribution study of MDA-MB-231 tumour bearing mice. This indicated the accuracy of using ROI points to infer actual radiotracer uptake. Little correlation was seen. For example, there was little uptake in the tumour throughout the imaging, while actual tumour uptake in the biodistribution (15 minutes pi), showed levels to be somewhat higher. Similar inconsistencies were seen throughout all tissues studied.

In summary, the PET imaging showed below background (using theoretical uniform distribution) uptake in the tumour throughout the imaging. It was unclear whether other factors to do with the morphology and growth of the tumour tissue were the key limitations or more over, whether our radiotracer was not binding to the neo-natal VGSCs.

Only two time points were studied in the biodistribution. A greater breadth of time points are needed for overlaying with the imaging data, before any firm conclusions regarding how inaccurate assigning of ROIs is for interpreting radiotracer uptake.

Following this initial study, another tumour bearing mouse was selected for imaging.

6.2.0.2 Results - study #2 / group #1

A second tumour bearing mouse was selected for PET/CT imaging. **([^{18}F]44)** was delivered in 8.0% n.d.c. e.o.s. yield from [^{18}F]fluoride in 120 minutes at 61.0 MBq/mL, as a phosphate buffer / ethanol solution (9:1; v/v), with specific activity 0.98 GBq/µmol. 100 µl was iv injected *via* the tail vein to a MDA-MB-231 tumour bearing SCID female mouse (tumour size approx. 6.4 x 5.2 mm, measured 6 hrs pre-imaging).

The animal was placed on a microPET scanner bed after tail-vein radiotracer injection. PET imaging commenced 6 minutes pi and ended 66 minutes pi. The animal was maintained under inhalation anaesthetic during the imaging and respiration rate monitored.

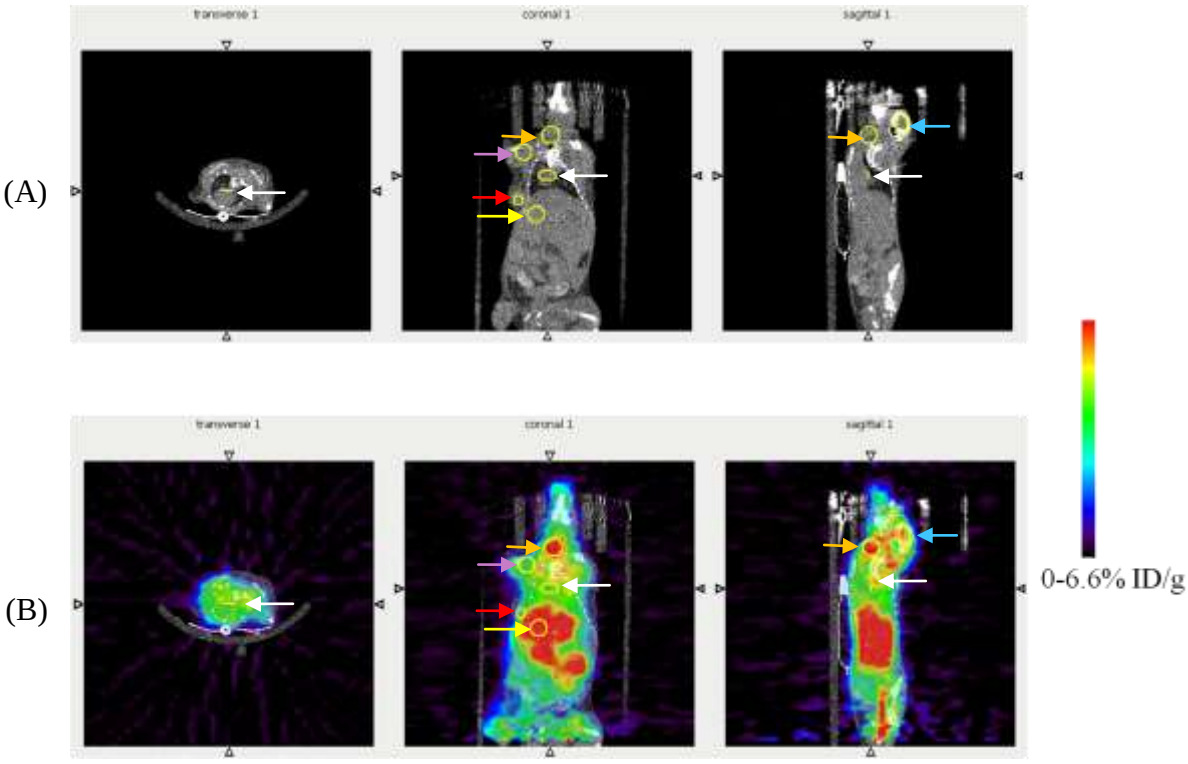

Figure 6.6: Dynamic PET image 6-7 minute pi: ROIs for tumour (coronal view; red arrow), liver (coronal view; yellow arrow), throat (coronal and sagittal view; orange arrow), front leg muscle (coronal view; purple arrow) and heart (transverse, coronal and sagittal view, white arrow). (A) CT image (B) PET/CT image. PET colour indicating 0-6.6% ID/g

Uptake of **([^{18}F]44)** was evident in the heart, brain and liver at 6-7 minutes pi (Figure 6.6; first minute of PET imaging). Uptake in the tumour however, was not above background; but it was difficult to resolve tumour uptake from the high uptake spreading from the liver. Radiotracer concentration in the front leg muscle appeared to be within background level. Interestingly, these images showed high uptake in the throat area, which had not been seen previously (Figure 6.6).

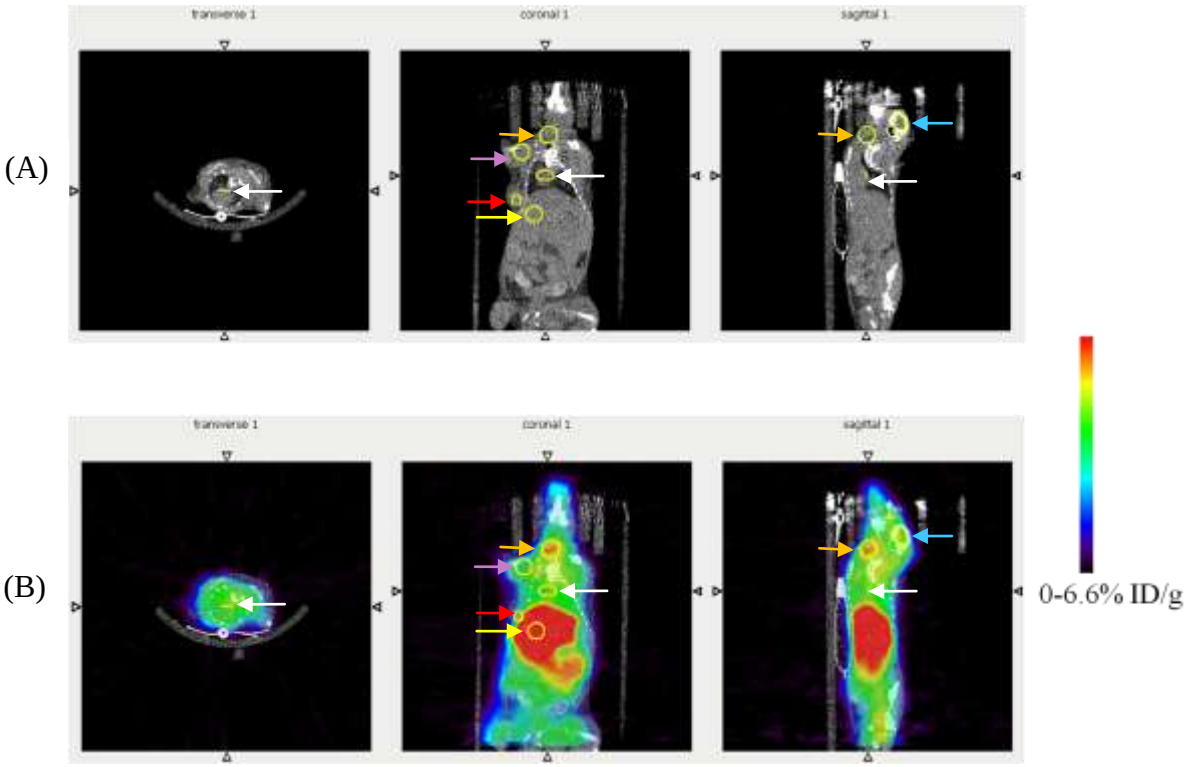

Figure 6.7: Dynamic PET image 15-16 minute pi. ROIs for tumour (coronal view; red arrow), liver (coronal view; yellow arrow), throat (coronal and sagittal view; orange arrow), front leg muscle (coronal view; purple arrow) and heart (transverse, coronal and sagittal view, white arrow). (A) CT image, (B) PET/CT image. PET colour indicating 0 - 6.6% ID/g

The 15th minute of the imaging showed uptake in the heart and brain to have cleared to within background levels (Figure 6.7). Radiotracer concentration in the throat had decreased from earlier time points, while uptake in the liver appeared to be increasing. Although it was difficult to distinguish radiotracer levels in the tumour from increasing liver uptake, it appears there was not uptake above background in the tumour.

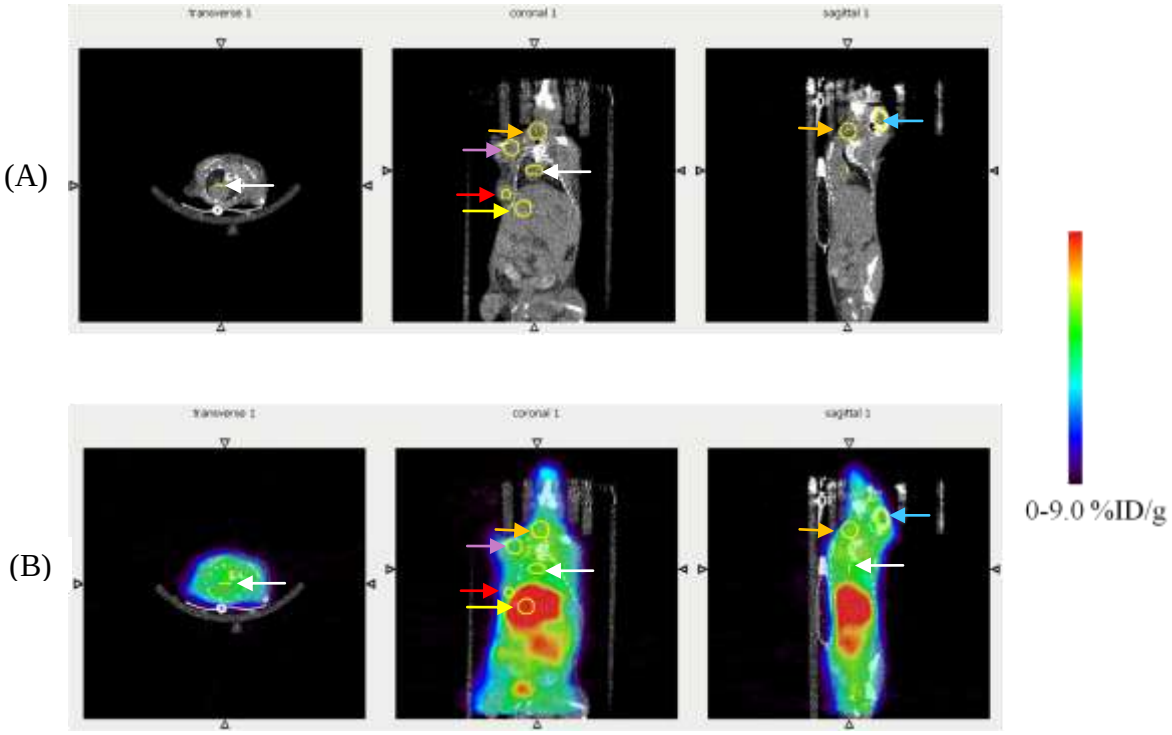

Figure 6.8: Dynamic PET image 65-66 minute pi. ROIs for tumour (coronal view; red arrow), liver (coronal view; yellow arrow), throat (coronal and sagittal view; orange arrow), front leg muscle (coronal view; purple arrow) and heart (transverse, coronal and sagittal view, white arrow). (A) CT, (B) PET/CT image. PET colour indicating 0 - 9.0% ID/g

The last minute of the imaging (65-66 minutes pi; Figure 6.8) showed **([^{18}F]44)** to be present mainly in the liver and bladder. Previous uptake in the throat had now reversed to background levels. The PET calibration was decreased to improve resolution (0–9.0% ID/g) between the bladder, kidneys and liver. Overall, the imaging study was completed with no measurable ill effects to the animal. Post imaging this animal underwent a biodistribution study to afford a late time point data set (74 minutes pi).

A time course of the PET data was plotted as described in the previous section and data points from a biodistribution study were overlaid as before (15 and 74 minutes pi).

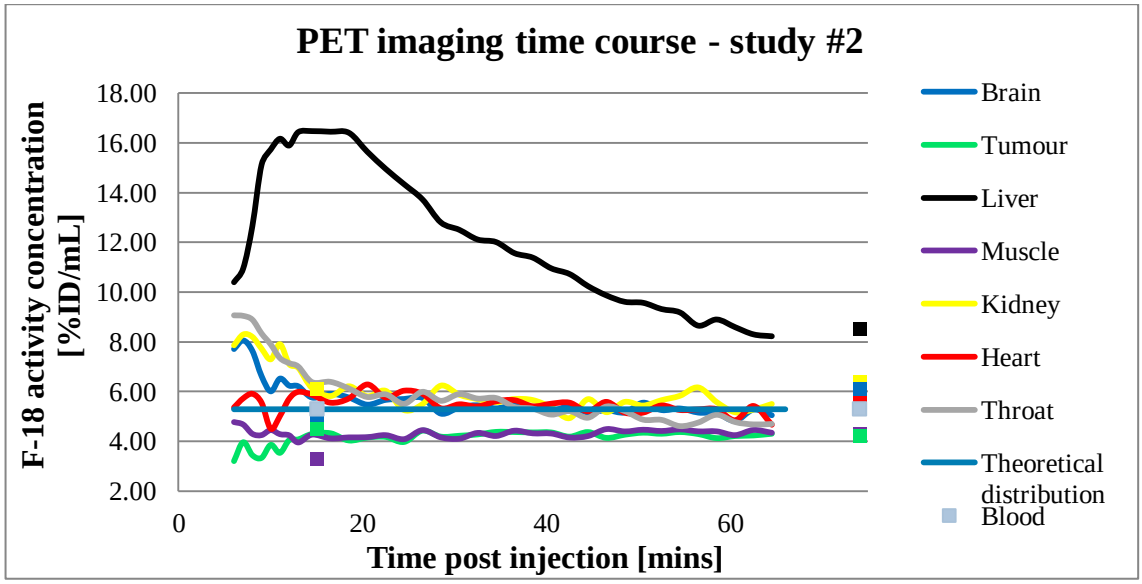

Figure 6.9: PET imaging time course (6-74 minutes, pi) in key tissues (lines) and biodistribution data (points). All tissues are colour coded the same between the PET and biodistribution data.

The PET imaging time course showed highest early (6 minutes, pi) uptake in the liver (10.4% ID/mL) which increased before reaching a plateau at 20 minutes, and then decreased over the remaining 40 minutes imaged. Strangely, the throat showed significant (9.0% ID/mL; 6 minutes pi) uptake at early times points, which cleared rapidly to below the theoretical distribution line but remained above blood level (indicated at 15 and 74 minutes pi). The kidney also showed high uptake (7.7% ID/mL); 6 minutes pi) which was quick to clear. The same initial uptake in the kidney was seen in the brain, which also displayed a similar clearance profile (to kidney), throughout the imaging. Radiotracer uptake in the heart appeared early on to fluctuate above and below the theoretical distribution line, but after 30 minutes the % ID/mL remained consistent. The muscle and tumour uptake was the lowest across the tissues sampled and remained below the theoretical distribution throughout. In muscle, an initial decrease from 4.7-4.0% ID/mL was reported over 6-13 minutes. Thereafter, a consistent level of 4.1% ID/mL was seen. Interestingly, there was a slight increase in tumour uptake from 6-16 mins of 3.2-4.3% ID/mL which plateaued, leaving a consistent level of uptake which overlapped with the time curve for muscle for the remaining time points.

Overall, the PET imaging time curve showed some uptake and clearance of radiotracer at early time points (6-20 minutes), after which levels remained consistent for all tissues sampled (except the liver). This suggested little clearance of radiotracer from these tissues (brain, heart, muscle and tumour) within 66 minutes pi. Using blood level from

the biodistribution data points as background, all tissues were above this level at 15 minutes and then at end of the time course, all tissues except the liver were nearing this background level. The theoretical distribution level co-registered with the blood level almost exactly.

Upon comparison of the imaging and biodistribution data, it was evident that the PET data appeared to indicate slightly higher radiotracer concentrations (in most tissues) than was actually sampled (biodistribution data) at the earliest time point (15 minutes pi).

Initial biodistribution data from the liver (15 minutes pi) was not plotted on this graph, due it being significantly higher than this scale (25.5% ID/mL). At the latest time point, the PET imaging data for the liver (8.3% ID/mL; 66 minutes) correlated well to the biodistribution data at 74 minutes (8.5% ID/mL). Alignment of PET data and biodistribution data was seen in the kidney (15 minutes pi), while the 74 minute pi data point (biodistribution) showed higher radiotracer concentration than was indicated by the last PET data point (66 minutes; 6.4 *vs* 5.4% ID/mL), respectively. In the heart, PET data showed higher uptake than was sampled (15 minutes biodistribution) but it is not possible to see the data point due to masking by data from the brain and tumour. The radiotracer concentration seen at end of the PET imaging (66 minutes pi) was shown to be slightly higher at 74 minutes pi (biodistribution). Again, the PET data overestimated the uptake in the brain at 15 minutes pi and then underestimated at the 75 minutes pi (compared to biodistribution). In contrast to this, good alignment was seen in the muscle and tumour tissues with just the muscle biodistribution data point (15 minutes pi), showing some lower radiotracer concentration. Throat tissue was not sampled in the biodistribution; it was felt that the uptake here was unlikely to be repeated.

6.2.0.3 Discussion

These images of a second mouse bearing a slightly larger tumour (6.4 x 5.2 mm), correlated well to our previous data (Section 6.2.0.1). A time course of the imaging was reported and overlaid with data from a later biodistribution study. The time course clearly showed lowest levels in the tumour and muscle with higher uptake in the brain and heart. The biodistribution data also supported these findings. The higher uptake in

the brain was quick to clear suggesting little retention of radiotracer, while the heart showed little clearance of radiotracer suggesting binding was not reversed.

The differences seen when overlaying the PET time course and the biodistribution data is likely to be due namely, to the low n numbers used in these studies providing no error bars associated for this data. Importantly, the PET data is dependent upon the efficiency of the detector and also the manipulation of the data to afford an accurate time course. For example, bleeding of radioactivity between tissues, makes it difficult to distinguish between different tissues. Importantly, the accurate assignment of voxels when manipulating the PET data is vital in order to get a precise time course. In the biodistribution however, all the tissues are separated quickly but some contamination can occur. Therefore, although there are differences in tracer concentration between the biodistribution and PET data, without an understanding of the associated error, it is not clear if the differences seen are significant or not.

This study indicated **([^{18}F]44)** was not able to highlight metastatic breast cancer tissue above background levels. These data corroborate with data from study #1 (Section 6.2.0.0). It is likely our compound is not able to bind to the VGSCs but also the morphology of the tumour tissue was questioned. Moreover, due to their slow growth, suggesting little aggressive or metastatic behaviour it was inferred that the level of VGSC expression was low. It was not possible to determine the VGSC expression level so the next steps were to use tumour bearing mice from [group #2] which grew slightly larger tumours for the following imaging and biodistribution study.

6.2.0.4 Results - study #3 / group #2

After imaging two of five MDA-MB-231 tumour bearing mice [group #1], our studies then turned to imaging of a slightly larger tumour from the second group of SCID mice inoculated with MDA-MB-231 cells.

([^{18}F]44) was delivered in 3.7% n.d.c. e.o.s. yield in 150 minutes from [^{18}F]fluoride at 7.0 MBq/mL, as a phosphate buffer /ethanol solution (9:1; v/v), with specific activity 4.0 GBq/µmol. 100 µL was injected iv *via* the tail vein to a MDA-MB-231 tumour bearing SCID female mouse (size approx. 7.89 x 6.44 mm). As before, PET imaging was performed over 60 minutes with CT imaging afterwards.

At 6 minutes pi, PET imaging commenced and the image acquired from the first minute was analysed (Figure 6.10).

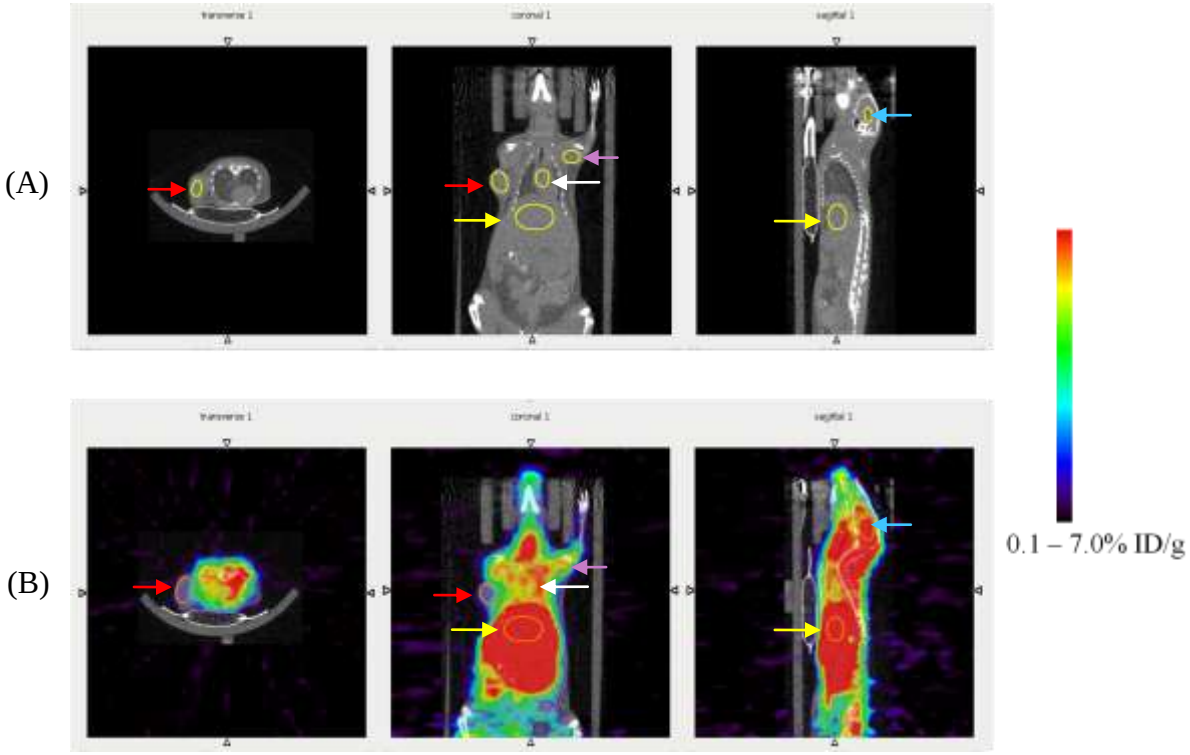

Figure 6.10: Dynamic PET image 6-7 minute pi: ROIs for tumour (transverse and coronal view, red arrow), heart (coronal view, white arrow), liver (coronal and sagittal views, yellow arrow) and muscle (coronal view, purple arrow). (A) CT image (B) PET/CT image. PET colour indicating 0.1-7.0% ID/g

The tumour from this animal grew on the right shoulder allowing improved resolution of tumour tissue. The tumour is clearly visible in the CT scan but with the PET data overlaid, the tumour has decidedly low uptake, well below background. Initial high uptake was seen in the heart, brain and liver, with little activity in the muscle (Figure 6.10).

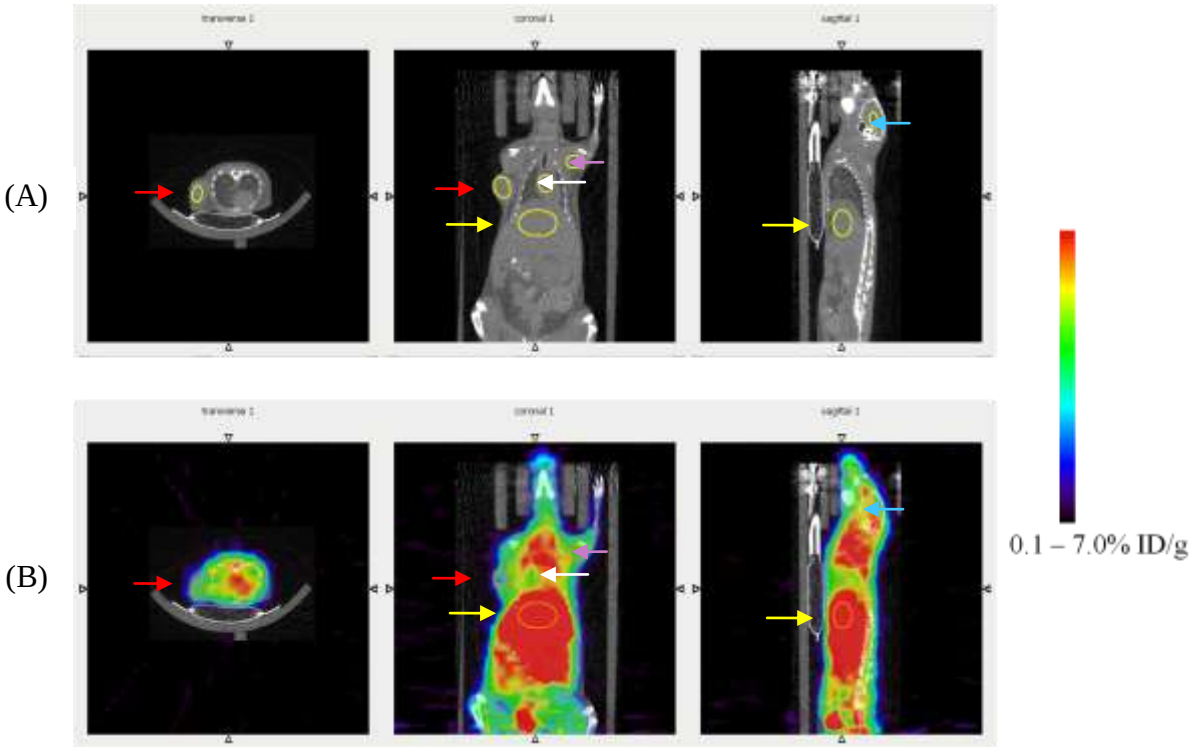

Figure 6.11: Dynamic PET image 16-18 minute pi: ROIs for tumour (transverse and coronal view, red arrow), heart (coronal view, white arrow), liver (coronal and sagittal views, yellow arrow) and muscle (coronal view, purple arrow). (A) CT image (B) PET/CT image. PET colour indicating 0.1-7.0% ID/g

At 16 minutes pi, uptake in the tumour appeared to show some increase, although it seemed not above background (Figure 6.11). As previously seen (study #1 and #2; group #1), early uptake in the brain cleared rapidly, while concentration of radiotracer in the heart was retained. The uptake in the liver and kidneys is shown to be bleeding into each another causing a large central mass of radiotracer concentration and some clearance *via* the bladder is now evident.

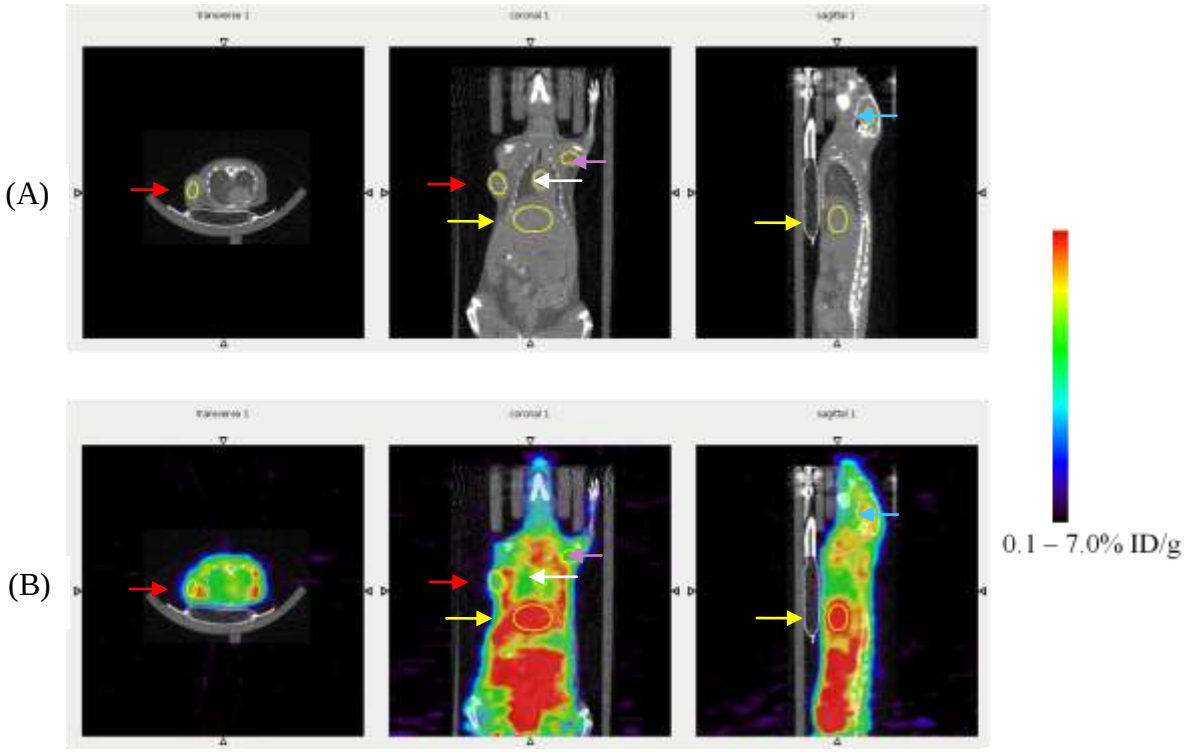

Figure 6.12: Dynamic PET image 63-65 minute pi: ROIs for tumour (transverse and coronal view, red arrow), heart (coronal view, white arrow), liver (coronal and sagittal views, yellow arrow) and muscle (coronal view, purple arrow). (A) CT image (B) PET/CT image. PET colour indicating 0.1-7.0% ID/g

At 63-65 minutes, (Figure 6.12) activity in the heart, kidney and liver cleared to the intestines and bladder. These high levels in the intestine and bladder are indicative of hepatobiliary and urinary excretion. The tumour level, although appearing to increase during the time course, remained within background levels.

A time course of the PET data was plotted as described in the previous section and data points from a later biodistribution study were overlaid as before (15 minutes pi). A 74 minute post-imaging data point was not afforded for this biodistribution study. The animal imaged here, was recovered for studying in the biodistribution study at 15 minute pi, due to it exhibiting the largest tumour in this group of animals (however this animal was removed from the study a short time later, as discussed below).

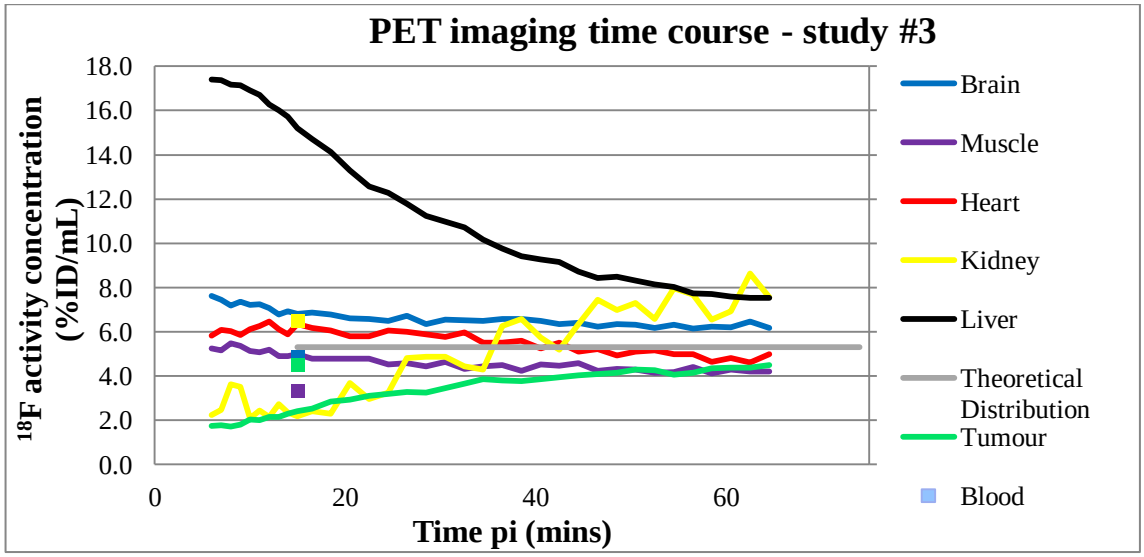

Figure 6.13: PET imaging time course (6-74 minutes, pi) in key tissues (lines) and biodistribution data (15 minutes pi, points). All tissues are colour coded the same between the PET and biodistribution data.

The PET time curve (Figure 6.13) indicated increasing uptake of radiotracer in tumour and kidney tissue throughout the time course, whilst the liver, heart, brain and muscle all showed clearing of tracer.

More specifically, the tumour showed a large increase in uptake over the 60 minutes imaged (1.7-4.5% ID/mL) equating to a 265% increase. Although this increase remained below theoretical distribution and blood level (taken from the biodistribution at 15 minutes; 4.45% ID/mL). Due to overlap of data points the blood point cannot been seen.

The high liver uptake (17.4% ID/mL, 16 minutes pi), continued to clear over the 60 minute imaging, whilst in the kidney, increasing uptake was seen (2.2-7.5% ID/mL, 6-66 minutes pi). The brain, heart and muscle remained consistent across all time points indicating little clearance of tracer. The heart and brain remained above theoretical distribution and blood level, whilst the muscle and tumour uptake remained below these thresholds.

In terms of accuracy of PET data with respect to biodistribution values, the imaging overestimated uptake in the heart, brain and muscle, whilst the actual tumour uptake was higher than imaging indicated.

This animal was recovered post-imaging for a later biodistribution study, however, 16 hours post-imaging, the animal was found unwell and was removed from the study. The

remaining radiotracer solution remained clear and HPLC analysis of the decayed radiotracer did not show a change in the UV profile.

6.2.0.5 Discussion

A modification to the procedure for inoculating the MDA-MB-231 cells into animals of group #2 was made to produce larger tumours. However, this was found not to be the case. The tumours were only slightly larger by weight and only four tumours grew from six inoculated, whereas before [group #1], five tumours grew. While tumour growth was limited, the imaging of these tumours was important to corroborate our previous results (Study #1 and #2), as only low uptake in the tumours was seen before.

The tumour imaged from this study (tumour size 7.89 x 6.44 mm) was located on the right shoulder which aided in resolution between the cardiac and tumour tissue, whereas previously, the tumour had grown more centrally. The PET/CT images for this study (Figure 6.10, Figure 6.11, Figure 6.12) allowed for a more accurate picture of tumour uptake. These data showed low initial tumour uptake but a high increase (265%) throughout the imaging time course. Interestingly, patch-clamp electrophysiology results showed that it took a minimum of 30 minutes for **(44)** to have a maximum effect at each concentration tested. As this tracer is a state-dependent VGSC blocker, binding to the channel in the inactivated state nearly exclusively, the channels are not available for binding instantly. This increasing uptake over 60 minutes could be aligned to the fact that this tracer requires a long incubation period to afford maximum effect.

As seen before, rapid uptake in the brain and heart was evident and clearance of the radiotracer was through the hepatobiliary system and renal system. These results were co-registered with a biodistribution study (Figure 6.13) and correlation of PET imaging to actual levels was shown to be less accurate than data produced in study #1, group #1. The difference in tracer concentration when overlaying the PET time course and the biodistribution data is likely to be due namely, to the low n numbers used in these studies (as mentioned in the previous section). The low n numbers afforded no error bars, therefore, although there are differences in tracer concentrations between the biodistribution and PET data, without an understanding of the associated error, it is not clear if the differences seen are significant or not. Importantly, the PET data is dependent upon the efficiency of the detector and also the manipulation of the data to

afford an accurate time course. For example, much bleeding of radioactivity was seen in the PET images making it difficult to distinguish between different tissues. In the biodistribution however, all the tissues are separated quickly but some contamination can occur. Future work will need to study more biodistribution time points to give greater overlay with PET data, thus affording firmer conclusions to be drawn when comparing the two techniques.

6.2.1 Biodistribution of MDA-MB-231 tumour bearing mice

Biodistribution studies were carried out using remaining tumour bearing mice from each group [group #1 and #2]. These animals were studied at 15 minutes pi. From group #1, one animal was also studied post PET/CT imaging to afford a 74 minute pi data point. These results were briefly described earlier when overlaying with PET data, but a fuller discussion is given in this section.

6.2.1.0 Results - study #1 / group #1

([^{18}F]44) was delivered in 10% n.d.c. e.o.s. yield from [^{18}F]fluoride in 180 minutes at 61.0 MBq/mL as a phosphate buffer /ethanol solution (9:1; v/v), with specific activity 0.98 GBq/µmol. 100 µL was injected *via* the tail vein to each MDA-MB-231 tumour bearing mouse (n = 3). The animals were sacrificed at 15 minutes pi and tissues dissected for analysis. This preparation of **([^{18}F]44)** is the same as used in study #2, group #1 PET imaging, where the 74 minute pi time point was afforded post-imaging.

Time p.i. [min]	15 (n=3)	15 (n=3)	74	74
	Mean % ID ± SD	Mean % ID/g ± SD	% ID	% ID/g
Bone	2.0 ± 0.2	2.1 ± 0.3	4.1	4.3
Muscle	26.1 ± 1.0	3.3 ±0.3	34.9	4.3
Blood	5.4 ± 0.6	3.8 ±0.6	6.0	4.1
Kidneys	1.6 ± 0.2	6.2 ± 0.9	1.7	6.4
Bladder/urine	0.8 ± 0.2	-	1.6	-
Lung	1.8 ± 0.0	12.9 ± 0.9	0.9	5.7
Liver	22.8 ± 1.9	25.5 ± 0.3	7.9	8.5
Heart	0.4 ± 0.1	4.7 ± 0.5	0.6	5.6
Brain	1.9 ± 0.2	4.9 ± 0.6	2.4	6.1
Skin	12.9 ± 0.3	4.7 ± 0.3	16.9	5.9
Tumour	0.2 ± 0.1	4.7 ± 1.5	0.4	4.2

Table 6.5: Biodistribution data of MDA-MB-231 tumour bearing mice at 15 minutes (n=3) and 74 minutes (n=1; post PET/CT scan) pi [group #1].

The 15 minute biodistribution of the MDA-MB-231 tumour bearing mice showed similar uptake in the tumour and heart (heart 4.7 ± 0.5% ID/g *vs* tumour 4.7 ± 1.5% ID/g; 15 minutes), however binding to the cardiac tissue appeared to be preferred (as the SD error is smaller). Uptake in the brain was approximately comparable (4.9 ± 0.6% ID/g; 15 minutes). **([^{18}F]44)** was also present in the lung in high level (12.9 ± 0.9% ID/g; 15 minutes) and a large part of the radioactivity was found in the liver (25.5± 0.3% ID/g; 15 minutes). Interestingly, uptake in the skin (4.7 ± 0.3% ID/g; 15 minutes) was higher than seen previously (4.07 ± 0.32% ID/g; näive biodistribution) and bone uptake remained the lowest (2.1 ± 0.3% ID/g; 15 minutes), comparable to levels seen previously (1.88 ± 0.15% ID/g; näive biodistribution). Blood uptake was used as background (3.8 ± 0.6% ID/g). These data showed for this study, only muscle and bone exhibited below background concentration of radiotracer.

At 74 minutes post-imaging, radiotracer concentration in the brain (6.1% ID/g), muscle (4.3% ID/g) and heart (5.6% ID/g) showed higher uptake than seen at 15 minutes. Whilst uptake in the liver (8.5% ID/g), lung (5.7% ID/g) and tumour (4.2% ID/g) had all decreased. No standard error was calculated for these results (n=1 only). (Please

note: these data from the 74 minute pi was afforded from an animal not included at 15 minutes pi.)

6.2.1.1 Discussion

Overall this study showed uptake in the tumour and heart above blood background (15 minutes pi). Unfortunately as with the PET data, these results showed that **([^{18}F]44)** does not bind to the neo-natal sodium channel in high concentration. Moreover this compound is better at interacting with the adult cardiac sodium channel.

Clearance of the tracer was seen from the liver, but most tissues exhibited little or no clearance showing binding is not reversible.

6.2.1.2 Results - study #2 / group #2

In the next study, **([^{18}F]44)** was delivered in 3.7% n.d.c. e.o.s. yield in 150 minutes from [^{18}F]fluoride, at 57.0 MBq/mL as a phosphate buffer /ethanol solution (9:1 v/v), with specific activity 4.0 GBq/µmol (same radiotracer as used for imaging study #3 / group #2). 100 µL was injected *via* the tail vein to each MDA-MB-231 tumour bearing mouse (average weight: 54 ± 38 mg) (n = 3).

Time p.i. [min]	**15 (n=3)**	**15 (n=3)**
	Mean % ID ± SD	Mean % ID/g ± SD
Bone	1.8 ± 0.3	1.8 ± 0.4
Muscle	26.8 ± 2.6	3.2 ± 0.4
Blood	6.8 ± 0.3	4.5 ± 0.3
Kidneys	1.9 ± 0.1	6.5 ± 0.2
Bladder/urine	0.9 ± 0.1	-
Lung	1.5 ± 0.3	9.4 ± 0.8
Liver	21.5 ± 1.9	23.0 ± 1.9
Heart	0.6 ± 0.1	5.0 ± 0.3
Brain	1.9 ± 0.1	5.1 ± 0.2
Skin	11.7 ± 0.3	4.0 ± 0.2
Tumour	0.2 ± 0.1	4.3 ± 1.6
Fat	6.8 ± 2.3	5.0 ± 1.8

Table 6.6: Biodistribution data of MDA-MB-231 tumour bearing mice at 15 minutes (n=3 / group #2)

These biodistribution data showed uptake in the tumour (4.3 ± 1.6% ID/g) to be approximately comparable to uptake in the heart (5.0 ± 0.3% ID/g). Uptake in the brain was similar (5.1 ± 0.2% ID/g), whilst the radiotracer was concentrated mostly in the liver and lung (23.0 0 ± 1.9% and 9.4 ± 0.8% ID/g), respectively. Blood levels were used as background (4.5 ± 0.3% ID/g) which indicated that uptake in the skin, bone and muscle were below background.

Time p.i. [min]	**15 (n=3)**
Ratio	Mean ± SD
Tumour : Muscle	1.29 ± 0.42
Tumour : Skin	1.03 ± 0.35
Tumour : Fat	0.85 ± 0.21

Table 6.7: Table of tissue ratios at 15 minutes pi

To gain a better understanding of the significance of radiotracer concentration in the tumour, uptake was compared with muscle, skin and fat tissue (Table 6.7). The level of radiotracer concentration in the muscle and skin was shown to be lower than the tumour, but fat had a higher concentration and with the lowest standard deviation, likely to be consistent with non-specific binding.

6.2.1.3 Discussion

This biodistribution study afforded radiotracer concentration values at 15 minutes only (n=3). A 74 minute time point was not achieved (as was in study #1), as only three animals remained for this study.

These data gave good agreement with the previous biodistribution study (study #1). Uptake in the tumour was similar (4.7 ± 1.5% *vs*. 4.3 ± 1.6% ID/g; study #1 *vs* study #2) while uptake in Study #1 was above blood background (3.8 ± 0.6% ID/g), this study showed uptake to be comparable to blood background (4.5 ± 0.3% ID/g). Uptake in the tumour (4.3 ± 1.6% ID/g) was higher than levels in the skin (4.0 ± 0.2% ID/g) and muscle (3.2 ± 0.4% ID/g), indicating some targeted binding, (as Na_v 1.5 is not expressed in skin nor muscle tissue). The increased uptake in the fat was likely to be consistent with non-specific binding of **([^{18}F]44)** as it is a particularly lipophilic radiotracer. Uptake in the brain (5.1 ± 0.2% ID/g) was higher than the tumour (4.3 ± 1.6% ID/g) but comparable to the heart (5.0 ± 0.3% ID/g). High uptake was seen in the liver (23.0 ± 1.9% ID/g) and lung (9.4 ± 0.8% ID/g) as seen previously at 15 minutes pi. All of these

results appear to be common across all the studies, supporting the conclusion that **([^{18}F]44)** does not appear to be a good PET tracer for targeting neo-natal Na_v 1.5.

6.2.2 Tumour growth and PET imaging of non-metastatic breast tumours

MCF-7 cells 1 x 10^6 cells (100 µl) in PBS were inoculated into the inner right thigh of six female nude mice. Shortly after, a 60-day slow release estradiol pellet was co-administered into the nape of the neck (as tumour growth in this model is estradiol dependent).[196] Tumours were allowed to grow for up to six weeks and a maximum size of 10 mm. In fact, four tumours grew ranging from 9.0 by 8.1 mm - 5.8 by 3.5 mm. The largest tumour was chosen for imaging.

6.2.2.0 Results

([^{18}F]44) was delivered in 3.7% n.d.c. e.o.s. yield from [^{18}F]fluoride in 150 minutes at 57.0 MBq/mL as a phosphate buffer /ethanol solution (9:1 v/v), with specific activity 2.4 GBq/µmol. 100 µL was injected *via* the tail vein to a MCF-7 tumour bearing nude mouse.

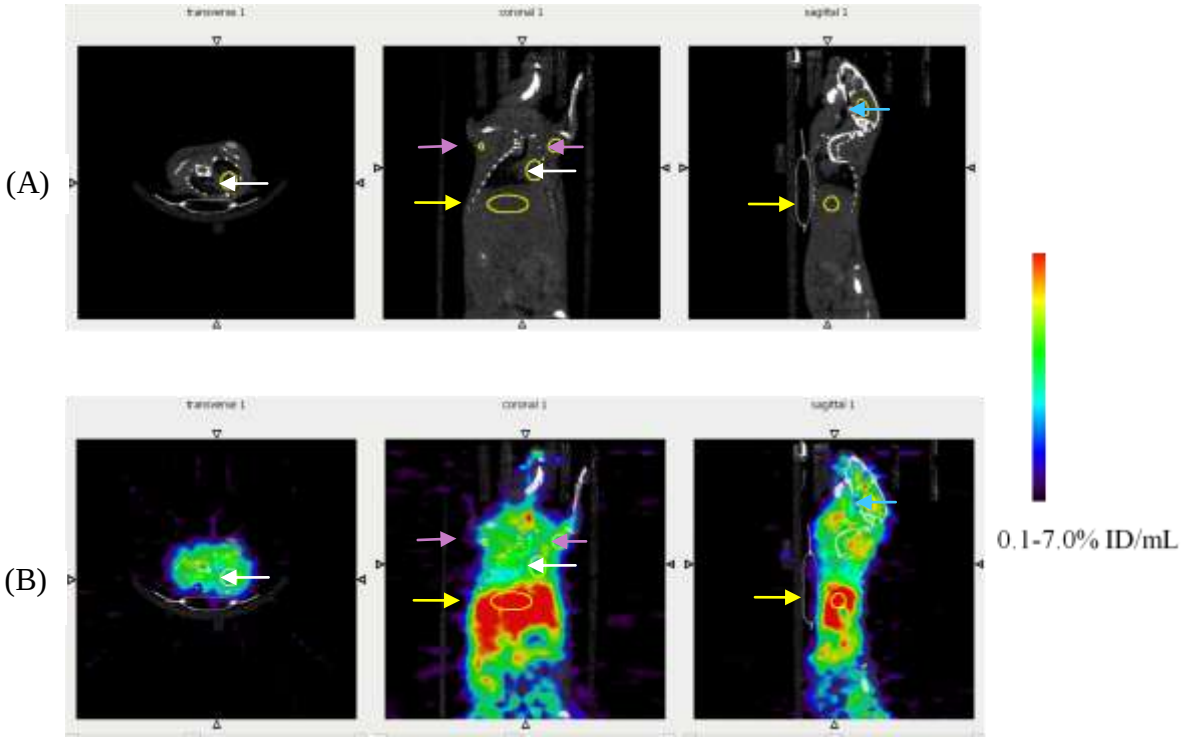

Figure 6.14: Dynamic PET image 6-7 minutes pi: ROIs for heart (transverse, coronal and sagittal view, white arrow), muscle left and right (coronal view, purple arrow), brain (sagittal view, blue arrow) and liver (coronal and sagittal views, yellow arrow). (A) CT image (B) PET/CT image. PET colour indicating 0.1-7% ID/g

Upon analysis of the PET images, it was seen that the field of view of the PET camera was not wide enough to image the thigh (tumour location) and whole body. So the tumour image was not captured. It was not possible to see image captures during the scanning, so this was not apparent until data analysis. The images of the näive tissues are included here for comparison with data from the MDA-MB-231 tumour bearing mice.

At 6-7 minutes pi (Figure 6.14), uptake of **([^{18}F]44)** was seen in the brain with high uptake in the liver. Little uptake is apparent in the heart and muscle. The radiotracer appears to have been distributed evenly among most tissues.

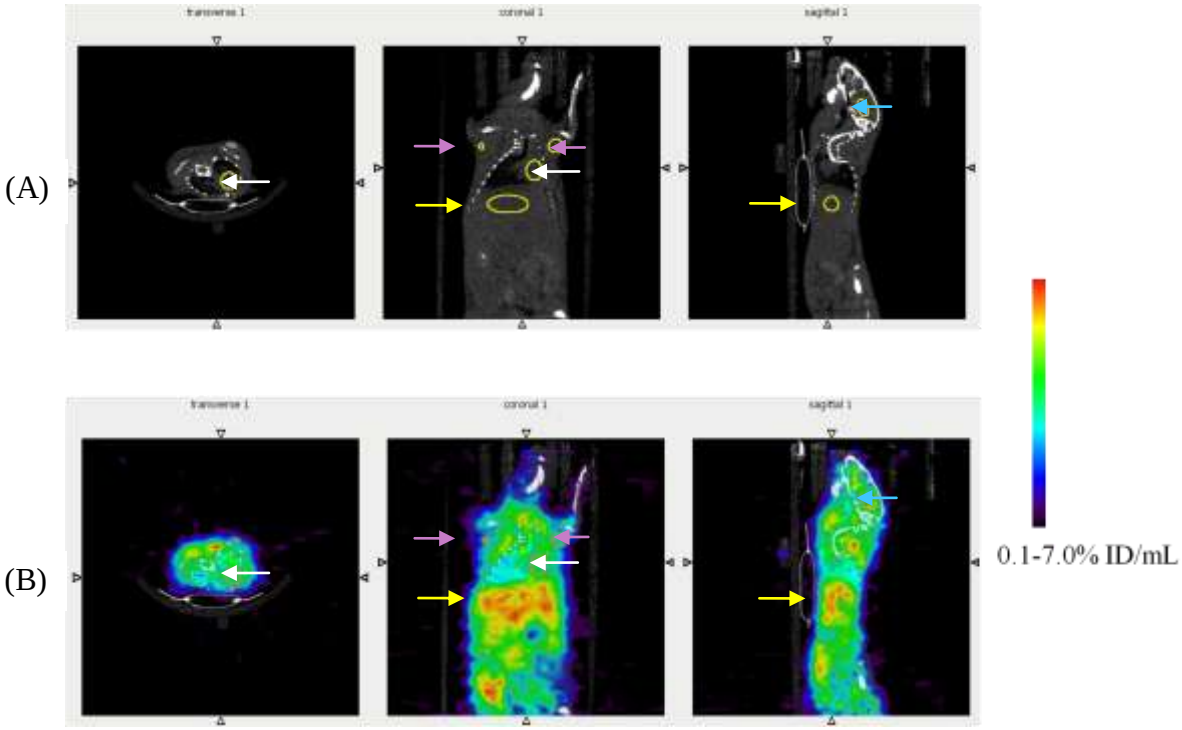

Figure 6.15: Dynamic PET image 16-17 minutes pi: ROIs for heart (transverse and coronal view, white arrow), muscle left and right (coronal view, purple arrow), brain (sagittal view, blue arrow) and liver (coronal and sagittal views, yellow arrow). (A) CT image (B) PET/CT image. PET colour indicating 0.1-7% ID/g

At 16-17 minutes pi (Figure 6.15), the images appeared similar to those seen at 6-7 minutes pi. Radiotracer concentration is no-longer present above background in the brain, and uptake in the heart remains low. Some clearance from the liver is seen with uptake of radioactivity in the bladder appearing (ROI not indicated).

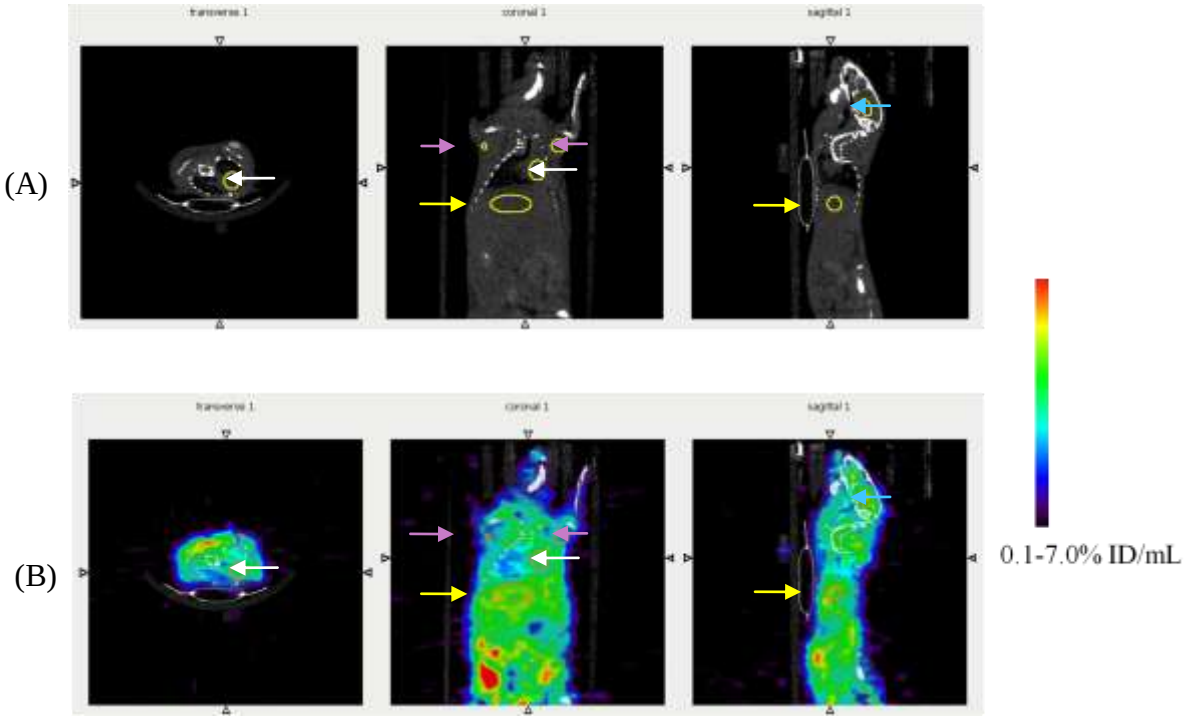

Figure 6.16: Dynamic PET image 65-66 minutes pi: ROIs for heart (transverse and coronal view, white arrow), muscle left and right (coronal view, purple arrow), and liver (coronal and sagittal views, yellow arrow). (A) CT image (B) PET/CT image. PET colour indicating 0.1-7% ID/g

At 65 minutes pi (Figure 6.16), the radiotracer had cleared to the intestines and bladder. No activity was seen above background in other tissues.

An imaging time course (Figure 6.17) was plotted and overlaid with points from a later biodistribution study (15 minutes, n=3, Section 6.2.3).

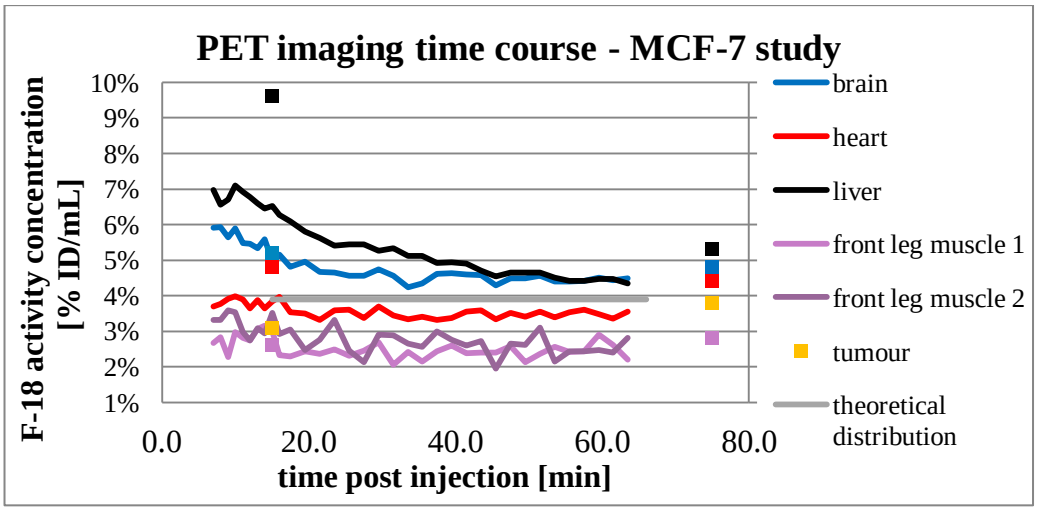

Figure 6.17: PET imaging time course (6-66 minutes, pi) in key tissues (lines) and biodistribution data (75 minutes pi; points) of MCF-7 tumour bearing mice.

Overall the PET time curve showed clearance from the liver and brain over the 60 minute imaging, whilst the heart and muscle showed little clearance, indicating little reversible uptake. Moreover, the 2 muscle ROIs highlighted, generally showed minimal uptake (<3% ID/mL) across all time points. The tumour (3.1% ID/g, 15 minute pi) also showed low uptake. Heart uptake (3.9%, 15 minutes pi) was higher than tumour level, at the same time point.

The time course highlighted some similarity with the biodistribution data. For instance, the imaging showed uptake in the brain to be higher than in the heart, which corroborated well with the biodistribution data. In terms of accuracy of ROIs with respect to biodistribution values, the muscle and brain is aligned almost perfectly, while the liver and heart level (in the biodistribution) was markedly higher than obtained from PET data.

6.2.2.1 Discussion

The MCF-7 PET images allowed for comparison of radiotracer uptake with the MDA-MB-231 images (tumour not included). Overall, the images showed a similar profile to that seen in the previous imaging study. **([^{18}F]44)** was concentrated in the brain and some heart uptake at early time points, while high uptake is evident in the liver throughout the time course. Radiotracer uptake in the liver and brain reverses throughout the time course of the imaging, while uptake in the heart and muscle appears not to reverse.

Due to the small field of view of the PET camera which did not allow for imaging of the tumour, no further animals were studied *via* PET/CT imaging.

The PET time course allowed clearance from tissues to be visualised. Little clearance of radiotracer was seen by the heart and muscle, whilst clearance was apparent in the brain and liver. Overlay of PET and biodistribution results allowed for comparison of data, which showed good corroboration across most tissues.

6.2.3 Biodistribution of MCF-7 tumour bearing mice

6.2.3.0 Results

([^{18}F]43) was delivered in 3.7% n.d.c. e.o.s. yield from [^{18}F]fluoride in 150 minutes at 57.0 MBq/mL as a phosphate buffer /ethanol solution (9:1 v/v), with specific activity 2.4 GBq/µmol. 100 µL was injected iv *via* the tail vein to each MCF-7 tumour bearing mouse. The animals were sacrificed at 15 minutes pi and tissues dissected for analysis as described in section 2.5.0. An animal was also sacrificed post PET imaging to afford a 75 minute time point.

Tissue	15 mins pi	15 mins pi	75 mins pi	75 mins pi
	Mean % ID ± SD	Mean % ID/g ± SD	% ID	% ID/g
Bone	1.90 ± 0.37	1.46 ± 0.27	3.86	3.00
Muscle	29.15 ± 1.64	2.61 ± 0.18	31.38	2.83
Blood	7.08 ± 0.44	3.49 ± 0.18	6.91	3.44
Kidneys	2.21 ± 0.13	6.70 ± 0.33	2.02	5.24
Bladder/Urine	0.78 ± 0.08	-	0.63	-
Lung	1.12 ± 0.04	6.09 ± 0.33	0.76	4.07
Liver	13.05 ± 1.68	9.55 ± 1.50	7.28	5.3
Heart	0.60 ± 0.01	4.79 ± 0.26	0.51	4.4
Brain	2.23 ± 0.38	5.17 ± 0.65	2.13	4.8
Skin	16.29 ± 0.31	4.18 ± 0.03	18.62	4.82
Tumour	0.35 ± 0.27	3.07 ± 0.48	1.74	3.8

Table 6.8: Biodistribution of MCF-7 tumour bearing mice at 15 minutes (n=3) and 75 minutes (n=1; post PET/CT scan)

This study highlighted radiotracer uptake in both the heart and tumour, with the tumour showing significantly lower uptake (tumour 3.07 ± 0.48% ID/g *vs* heart 4.79 ± 0.26% ID/g). Interestingly, the animal studied at 75 minutes highlighted an increase in radiotracer concentration in the tumour by 0.74% ID/g, whereas some clearance from the heart was reported 0.39% ID/g (although there is no standard error reported; n=1). The brain had high uptake (5.17 ± 0.65% ID/g) at 15 minutes, which reversed somewhat (4.8% ID/g; 75 minutes). Using blood level as background (3.49 ± 0.18% ID/g), radiotracer concentration in the muscle and tumour fell below. Interestingly, initial uptake in the liver (9.55 ± 1.5% ID/g) was lower than seen in the previous disease

model (MDA-MB-231 tumours) which also decreased at the 75 minute time point (7.28% ID/g).

6.2.3.1 Discussion

The low uptake in the tumour with respect to the heart is an encouraging indication. Previously, the MDA-MB-231 tumours showed similar or in some data, lower uptake compared to the heart, suggesting little difference in binding to the adult and neo-natal splice variant. It appears the radiotracer is equally able to bind to both splice variants. It was thought that these MCF-7 tumours would show a marked decrease in radiotracer uptake compared to the MDA-MB-231 tumours due to low/no expression of the target channel (MCF-7 tumour 3.07 ± 0.48% ID/g *vs* MDA-MB-231 tumour 4.3 ± 1.6% ID/g), as was found. The lower uptake in the MCF-7 tumours suggests lower expression of the neo-natal Na_v 1.5 channel as reported in the literature. Whereas the concentration of radiotracer in the heart decreased from 15 to 75 minutes (4.79 ± 0.26% ID/g to 4.4% ID/g; in the tumour, a slight increase was reported (3.07 ± 0.48% ID/g to 3.8% ID/g). Unusual patterns were also seen during the biodistribution of the MDA-MB-231 tumours, again it is difficult to tell if these are true increases or whether these values would be within error if the study were repeated at this time point.

6.3 Conclusions of Chapter 6

In summary, this preliminary study into **([^{18}F]44)** as a PET tracer for imaging sodium ion channel activity in metastatic breast cancer, has delivered some interesting, but mixed results. Firstly, the cell binding assay indicated some higher binding to the MDA-MB-231 cells than the MCF-7 cells, as was expected. The specific binding results were not encouraging; these data showed there was high non-specific binding. This could imply that the concentration of **(44)** was not high enough, or high binding to cell debris was inhibiting blocking. Developing assays is a time consuming process and requires a prolonged radiation dose to be received during development, therefore, assay validation was not continued and was put forward for future considerations.

Alongside *in vitro* work, i*n vivo* inoculations allowed for growth of the two tumour types. Initially, this study was for model validation of sodium ion channel expression in

IHC experiments, but later developed into an imaging and biodistribution study to quantify *in vivo* uptake in a disease model. Again some mixed but hopeful results were produced here. Some tracer uptake was seen in the MDA-MB-231 tumours during imaging, however, it was difficult to note uptake above background. Moreover, the combined biodistribution studies allowed for quantified uptake in the tumour to be recorded. Using blood as background, some uptake in the tumour was noteworthy but mainly uptake was below background.

In comparison with the MCF-7 tumours, the biodistribution here, showed lower uptake in the tumours, potentially suggesting a lower expression of target. It would have been beneficial to have the tumour images of these animals alongside the MDA-MB-231 tumour bearing mice, but due to equipment limitations (small camera field of view), it was not possible. Encouragingly though, the biodistribution allowed for a positive quantitative comparison of the two tumour models.

Overall, these studies into PET imaging of VGSCs in breast cancer highlighted some interesting results. Although **([^{18}F]44)** was not able to image the MDA-MB-231 tumours, it was able to highlight the heart, in most images. This suggested that this radiotracer is able to bind to the inactivated-state of Na_v 1.5 *in vivo*. Recent studies into the sodium currents produced by neo-natal Na_v 1.5 in MDA-MB-231 cells, have sought to determine which type of sodium current is expressed by these cells. Since undertaking this work, Yang *et. al.*, have reported that it is the persistent component of the sodium current likely to be predominant in these cells.[56] The persistent sodium current corresponds to the delayed inactivation of Na_v 1.5.[197] VGSCs typically inactivate within a few milliseconds of opening following depolarisation, and remain inactivated until the membrane repolarises.[198] Several subtypes, including Na_v 1.5, do not inactivate completely, they continue to carry a small steady-state persistent sodium current at depolarised potentials.[199] Furthermore, it has been shown that cancer cells typically have a more depolarised membrane potential than normal epithelial cells or neurones.[200] Also, the persistent sodium current is more prevalent in hypoxic cells.[201] Thus, it has been proposed that the persistent component of the sodium current is likely to be predominant in MDA-MB-231 cells.

When the findings from this report are considered, it now seems likely that **([^{18}F]44)** was not able to bind to neo-natal Na_v 1.5, due to the channel remaining activated. It was demonstrated that **(44)** binds preferentially to the inactivated state of the channel,

therefore this literature report corroborates our results, that an inactivated state-dependent VGSC ligand, is not a good ligand for neo-natal Na_v 1.5. Importantly, this report has highlighted that a fluorine-18 labelled VGSC ligand binding to the activated state, would likely be a better VGSC PET tracer. Further work is required to support this hypothesis and also determine whether the channels ever inactivate. If it is supported that the channels cannot inactivate, then **(44)** and the 3-(4-R-phenoxy)phenyl pyrazoles in general, cannot be used to highlight neo-natal Na_v 1.5 in metastatic breast cancer.

7. Thesis conclusion

Overall, this thesis has described some interesting and novel work. This project set out to develop a VGSC PET tracer which could highlight sodium channels in metastatic cancer. In order to achieve this, the 3-(4-R-phenoxy)phenyl pyrazoles were initially studied. Numerous radiolabelling strategies were studied and implemented, but unfortunately, these studies could not produce a PET tracer. The main problem was identified to be the ether bridge linking the two phenyl rings causing inactivation of the ring toward any S_NAr substitution for fluorine-18. To overcome this, an ether bridge was changed to a thioether bridge. The thioether bridge was oxidised to a sulphone and sulphoxide prior to radiolabelling. This change to the structure showed vastly different reaction kinetics under radiolabelling conditions. Many products were found but unfortunately, no desired product could be identified and the unwanted products could not be determined either. Although the 3-(4-((4-R-phenyl)thio)phenyl)-pyrazoles had been reported to be potent VGSC ligands, our subsequent electrophysiology studies on **(25)** showed apparent no affinity for VGSCs. Moreover, **(9)** was shown to be highly potent for Na_v 1.4 and 1.5, as reported, so analogues of these compounds were prepared consequently to these data.

Thereafter, **([^{18}F]41)** was afforded by replacing the terminal carboxamide with a fluoroethyl chain produced *via* [^{18}F]fluoroethyl tosylate. I*n vitro* electrophysiology showed **(41)** to be a potent state-dependent VGSC ligand. The radiochemistry followed a reproducible 2-step procedure where the synthesis of [^{18}F]fluoroethyl tosylate was afforded using a FX-N Tracerlab™. Following *in vivo* assessment however, this PET tracer was shown to clear within 15 minutes from nearly all tissues. This tracer was not studied further following these results. Although *in vivo* work was not promising, it may be interesting to develop this tracer in the future, with a view to improve *in vivo* stability.

Finally, **([^{18}F]44)** was produced also in a two-step reproducible procedure. Click chemistry was employed to produce high yields and the synthesis of [^{18}F]fluoroethyl azide was carried out *via* a GE Healthcare FASTlab™. *In vitro* assessment of **(44)** identified this compound to be a potent state-dependent VGSC ligand, binding specifically to Na_v 1.4 and 1.5, with equal potency. *In vivo* assessment of this compound looked promising, high uptake was seen in the heart with good retention and some clearance within 2 hours. Little uptake was monitored in the skeletal muscle highlighting this compound to more selective for Na_v 1.5 (cardiac sodium channel), than was expressed by *in vitro* data. Thereafter, a metabolism study was carried out which

showed this PET tracer to have some stability up to 60 minutes with high parent uptake apparent in the heart. These näive data were used as a basis for further investigations in a disease model.

The metastatic and non-metastatic cell lines for B Ca were studied. A cell binding assay was performed alongside *in vivo* inoculation of cells into small animals. The cell binding assay highlighted a positive difference between binding to the MDA-MB-231 cells (positive control; express Na_v 1.5) and MCF-7 (negative control; little/no expression of Na_v 1.5). The tumour bearing mice were both PET/CT imaged and underwent a biodistribution study to assess uptake in the tumours. In both studies, these data did not look promising. Little uptake was seen in the positive control tumours and more importantly uptake was not seen above background. The negative control tumours did show lower uptake, but the difference was so small it was difficult to infer it as significant. During these studies, a report was published to indicate that sodium channels in tumour cells exhibit a persistent current causing slow or no inactivation of the channels as a result. Our negative results could be explained by this report as our compound binds nearly exclusively in the inactivated state. However, further work is required to identify these results in more detail and indicate whether there is still some inactivation of the channels.

In summary, this project bordered on a series of different research areas. Chemistry and radiochemistry research lead to the generation of two novel potential VGSC PET tracers. A series of electrophysiological studies were implemented to identify the potency and selectivity of these compounds prior to *in vivo* assessment. **([^{18}F]44)** appeared the more promising and this PET tracer allowed the project to diversify into many areas of *in vivo* biology. Näive data looked interesting and it was hoped that results in our B Ca model would appear the same, but little uptake was reported. Nevertheless, this thesis describes the first study into developing a PET tracer for imaging sodium ion channels in cancer. VGSCs in cancer although recognised, is still at a discovery phase. The kinetic behaviour of these VGSCs for example, is only just being established. It now appears that they exhibit a characteristic current which slows inactivation. Therefore the key in designing subsequent VGSC PET tracers could be to target the persistent current using an activated state-dependent VGSC ligand.

8. Future Work

This project carried out a number of preliminary studies which require further investigations. **(44)** will need to undergo manual patch clamp studies at much lower concentrations than those already tested in order to gain confidence in the IC_{50} values afforded. For completeness and for comparison, the remaining compounds **(9)** and **(41)** will need to be added to this study. Moreover, the binding studies which we were unable to commission will need to be carried out to determine the B_{max} and K_d, therefore confirming whether the binding potentials for each of the three compounds are indeed ≥10. This would complete the näive characterisation of these compounds.

Current reports suggest neo-natal Na_v 1.5 exhibits prolonged activation. A study into the kinetics of this channel will be required to confirm what state the channel predominantly resides in. If that study shows there is no inactivation, then our compounds will not be able to bind and a study into activation-dependent ligands will be required. If inactivation is present, then completion of **([^{18}F]44)** studies will be necessary.

In order to complete work in the disease model; the cell binding assay of **([^{18}F]44)** with MDA-MB-231 and MCF-7 cells will need to be repeated with modified conditions, to give a reproducible assay with high cell viability count. If these results look interesting, then a tumour growth study will need to be commissioned to produce both tumour types in good size and over a reasonable time-frame. These tumours will need to undergo IHC studies with the neo-natal Na_v 1.5 antibody before any further studies could proceed, to determine relative expression level of the channel. Previously, an academic collaboration was sought, but was not successful in obtaining the anti-body. Therefore, the growth of the anti-body would need to be generated in-house. Once the antibody is available and the relative expression of neo-natal Na_v 1.5 known, PET imaging studies could be repeated. For comparison, these animals would need to undergo an [^{18}F]FDG screen as a control scan to check the tumours could be highlighted.

In summary, there is still work needed to investigate this area further and moreover, determine fully whether **([^{18}F]44)** is able to highlight metastatic breast cancer.

9. References

1. Chanda, B.; Bezanilla, F., *J Gen Physiol* **2002,** *120* (5), 629-645.
2. Brackenbury, W. J.; Djamgoz, M. B. A., *The Journal of Physiology* **2006,** *573* (2), 343-356.
3. Brackenbury, W. J.; Djamgoz, M. B.; Isom, L. L., *Neuroscientist* **2008,** *14* (6), 571-83.
4. Bennett, E.; Smith, B.; Harper, J., *Pflügers Archiv European Journal of Physiology* **2004,** *447* (6), 908-914.
5. Grimes, J. A.; Fraser, S. P.; Stephens, G. J.; Downing, J. E. G.; Laniado, M. E.; Foster, C. S.; Abel, P. D.; Djamgoz, M. B. A., *FEBS Letters* **1995,** *369* (2-3), 290-294.
6. Roger, S.; Besson, P.; Le Guennec, J. Y., *Biochim Biophys Acta* **2003,** *1616* (2), 107-11.
7. Yang, J.; Gharagozloo, P.; Yao, J. C.; Ilyin, V. I.; Carter, R. B.; Nguyen, P.; Robledo, S.; Woodward, R. M.; Hogenkamp, D. J., *J Med Chem* **2004,** *47* (6), 1547-1552.
8. Iversen, L. L., *Br J Pharmacol* **1971,** *41* (4), 571-91.
9. Ames, A.; Pollen, D. A., *Journal of Neurophysiology* **1969,** *32* (3), 424-42.
10. Thomas, E. A.; Bornstein, J. C., *Neuroscience* **2003,** *120* (2), 333-351.
11. Williamson, B. http://www.brianwilliamson.id.au/cit/level1/substance-K/images/Neurotransmission.gif.
12. Macdonald, P. E.; Rorsman, P., *PLoS Biol* **2006,** *4* (2), e49.
13. Barnett, M. W.; Larkman, P. M., *Practical Neurology* **2007,** *7* (3), 192-197.
14. Hodgkin, A. L.; Huxley, A. F., *J Physiol* **1952,** *117* (4), 500-44.
15. Mccormick, D. A.; Shu, Y.; Yu, Y., *Nature* **2007,** *445* (7123), E1-E2.
16. Osorio, N.; Delmas, P., *Nat. Protocols* **2011,** *6* (1), 15-27.
17. Kyle, D. J.; Ilyin, V. I., *Journal of Medicinal Chemistry* **2007,** *50* (11), 2583-2588.
18. Catterall, W. A., *Neuron* **2000,** *26* (1), 13-25.
19. Goldin, A. L., *Annual Review of Physiology* **2001,** *63*, 871-894.
20. Westenbroek, R. E.; Merrick, D. K.; Catterall, W. A., *Neuron* **1989,** *3* (6), 695-704.
21. Westenbroek, R. E.; Noebels, J. L.; Catterall, W. A., *Journal of Neuroscience* **1992,** *12* (6), 2259-2267.

22. Caldwell, J. H.; Schaller, K. L.; Lasher, R. S.; Peles, E.; Levinson, S. R., *Proceedings of the National Academy of Sciences of the United States of America* **2000,** *97* (10), 5616-5620.
23. Khaliq, Z. M.; Raman, I. M., *J Neurosci* **2006,** *26* (7), 1935-1944.
24. Gordon, D.; Merrick, D.; Auld, V.; Dunn, R.; Goldin, A. L.; Davidson, N.; Catterall, W. A., *Proc Natl Acad Sci U S A* **1987,** *84* (23), 8682-6.
25. Sasaki, R.; Takano, H.; Kamakura, K.; Kaida, K.; Hirata, A.; Saito, M.; Tanaka, H.; Kuzuhara, S.; Tsuji, S., *Arch Neurol* **1999,** *56* (6), 692-696.
26. Mohler, P. J.; Rivolta, I.; Napolitano, C.; Lemaillet, G.; Lambert, S.; Priori, S. G.; Bennett, V., *Proceedings of the National Academy of Sciences of the United States of America* **2004,** *101* (50), 17533-17538.
27. Cohen, S. A., *Circulation* **1996,** *94* (12), 3083-6.
28. Scriven, D. R.; Dan, P.; Moore, E. D., *Biophysical Journal* **2000,** *79* (5), 2682-91.
29. Nassar, M. A.; Stirling, L. C.; Forlani, G.; Baker, M. D.; Matthews, E. A.; Dickenson, A. H.; Wood, J. N., *Proceedings of the National Academy of Sciences of the United States of America* **2004,** *101* (34), 12706-12711.
30. Laird, J. M.; Souslova, V.; Wood, J. N.; Cervero, F., *Journal of Neuroscience* **2002,** *22* (19), 8352-6.
31. Beneng, K.; Renton, T.; Yilmaz, Z.; Yiangou, Y.; Anand, P., *BMC Neuroscience* **2010,** *11* (1), 71.
32. Bubien, J. K.; Keeton, D. A.; Fuller, C. M.; Gillespie, G. Y.; Reddy, A. T.; Mapstone, T. B.; Benos, D. J., *Am J Physiol Cell Physiol* **1999,** *276* (6), C1405-1410.
33. Sloane, B. F.; Mohamed, M. M., *Nat. Rev. Cancer* **2006,** *6* (10), 764-775.
34. Bennett, E. S.; Smith, B. A.; Harper, J. M., *Pflugers Arch* **2004,** *447* (6), 908-14.
35. Grimes, J. A.; Fraser, S. P.; Stephens, G. J.; Downing, J. E. G.; Laniado, M. E.; Foster, C. S.; Abel, P. D.; Djamgoz, M. B. A., *FEBS Letters* **1995,** *369* (2-3), 290-294.
36. Monk, M.; Holding, C., *Oncogene* **2001,** *20* (56), 8085-91.
37. Boyerinas, B.; Park, S. M.; Shomron, N.; Hedegaard, M. M.; Vinther, J.; Andersen, J. S.; Feig, C.; Xu, J.; Burge, C. B.; Peter, M. E., *Cancer Res* **2008,** *68* (8), 2587-91.
38. Onkal, R.; Mattis, J. H.; Fraser, S. P.; Diss, J. K. J.; Shao, D.; Okuse, K.; Djamgoz, M. B. A., *Journal of Cellular Physiology* **2008,** *216* (3), 716-726.

39. Sheets, M. F.; Hanck, D. A., *Biophys J* **2002,** *82* (6), 3048-55.
40. Henrikson, C. A.; Xue, T.; Dong, P.; Sang, D.; Marban, E.; Li, R. A., *J Biol Chem* **2003,** *278* (16), 13647-54.
41. Chen, T.; Inoue, M.; Sheets, M. F., *Am J Physiol Heart Circ Physiol* **2005,** *288* (6), H2666-76.
42. Parkin, D. M.; Pisani, P.; Ferlay, J., *Int J Cancer* **1999,** *80* (6), 827-41.
43. Wingo, P. A.; Ries, L. A.; Rosenberg, H. M.; Miller, D. S.; Edwards, B. K., *Cancer* **1998,** *82* (6), 1197-207.
44. Fraser, S. P.; Ding, Y.; Liu, A.; Foster, C. S.; Djamgoz, M. B., *Cell Tissue Res* **1999,** *295* (3), 505-12.
45. Fraser, S. P.; Salvador, V.; Manning, E. A.; Mizal, J.; Altun, S.; Raza, M.; Berridge, R. J.; Djamgoz, M. B., *J Cell Physiol* **2003,** *195* (3), 479-87.
46. Djamgoz, M. B. A.; Mycielska, M.; Madeja, Z.; Fraser, S. P.; Korohoda, W., *J Cell Sci* **2001,** *114* (Pt 14), 2697-705.
47. Smith, P.; Rhodes, N. P.; Shortland, A. P.; Fraser, S. P.; Djamgoz, M. B. A.; Ke, Y. Q.; Foster, C. S., *FEBS Letters* **1998,** *423* (1), 19-24.
48. Fraser, S. P.; Salvador, V.; Manning, E. A.; Mizal, J.; Altun, S.; Raza, M.; Berridge, R. J.; Djamgoz, M. B. A., *Journal of Cellular Physiology* **2003,** *195* (3), 479-487.
49. Djamgoz, M. B. A.; Krasowska, M.; Grzywna, Z. J.; Mycielska, M. E., *Eur Biophys J Biophy* **2004,** *33* (6), 535-542.
50. Gao, R.; Wang, J.; Shen, Y.; Lei, M.; Wang, Z., *J Huazhong Univ Sci Technolog Med Sci* **2009,** *29* (1), 64-7.
51. Djamgoz, M. B. A., *Febs J* **2006,** *273*, 9-9.
52. Roger, S.; Potier, M.; Vandier, C.; Besson, P.; Le Guennec, J. Y., *Curr Pharm Des* **2006,** *12* (28), 3681-95.
53. Roger, S.; Rollin, J.; Barascu, A.; Besson, P.; Raynal, P. I.; Iochmann, S.; Lei, M.; Bougnoux, P.; Gruel, Y.; Le Guennec, J. Y., *Int J Biochem Cell Biol* **2007,** *39* (4), 774-86.
54. Roger, S.; Brisson, L.; Gillet, L.; Calaghan, S.; Besson, P.; Le Guennec, J. Y.; Gore, J., *Oncogene* **2011,** *30* (17), 2070-2076.
55. Fraser, S. P.; Pardo, L. A., *Embo Rep* **2008,** *9* (6), 512-515.
56. Yang, M.; Kozminski, D. J.; Wold, L. A.; Modak, R.; Calhoun, J. D.; Isom, L. L.; Brackenbury, W. J., *Breast Cancer Res Treat* **2012,** *134* (2), 603-15.

57. Chioni, A. M.; Brackenbury, W. J.; Calhoun, J. D.; Isom, L. L.; Djamgoz, M. B., *Int J Biochem Cell Biol* **2009,** *41* (5), 1216-27.
58. Diss, J. K.; Fraser, S. P.; Djamgoz, M. B., *Eur Biophys J* **2004,** *33* (3), 180-93.
59. Gillet, L.; Roger, S.; Besson, P.; Lecaille, F.; Gore, J.; Bougnoux, P.; Lalmanach, G.; Le Guennec, J. Y., *J Biol Chem* **2009,** *284* (13), 8680-91.
60. Jemal, A.; Siegel, R.; Ward, E.; Murray, T.; Xu, J.; Smigal, C.; Thun, M. J., *CA: A Cancer Journal for Clinicians* **2006,** *56* (2), 106-130.
61. Laniado, M. E.; Lalani, E. N.; Fraser, S. P.; Grimes, J. A.; Bhangal, G.; Djamgoz, M. B.; Abel, P. D., *Am J Pathol* **1997,** *150* (4), 1213-21.
62. Fraser, S. P.; Diss, J. K. J.; Chioni, A.-M.; Mycielska, M. E.; Pan, H.; Yamaci, R. F.; Pani, F.; Siwy, Z.; Krasowska, M.; Grzywna, Z.; Brackenbury, W. J.; Theodorou, D.; Koyutürk, M.; Kaya, H.; Battaloglu, E.; De Bella, M. T.; Slade, M. J.; Tolhurst, R.; Palmieri, C.; Jiang, J.; Latchman, D. S.; Coombes, R. C.; Djamgoz, M. B. A., *Clinical Cancer Research* **2005,** *11* (15), 5381-5389.
63. Diss, J. K.; Archer, S. N.; Hirano, J.; Fraser, S. P.; Djamgoz, M. B., *Prostate* **2001,** *48* (3), 165-78.
64. Diss, J. K.; Stewart, D.; Fraser, S. P.; Black, J. A.; Dib-Hajj, S.; Waxman, S. G.; Archer, S. N.; Djamgoz, M. B., *FEBS Lett* **1998,** *427* (1), 5-10.
65. Diss, J. K. J.; Archer, S. N.; Hirano, J.; Fraser, S. P.; Djamgoz, M. B. A., *Prostate* **2001,** *48* (3), 165-178.
66. Anderson, J. D.; Hansen, T. P.; Lenkowski, P. W.; Walls, A. M.; Choudhury, I. M.; Schenck, H. A.; Friehling, M.; Höll, G. M.; Patel, M. K.; Sikes, R. A.; Brown, M. L., *Molecular Cancer Therapeutics* **2003,** *2* (11), 1149-1154.
67. Fidler, I. J., *Nature Reviews Cancer* **2003,** *3* (6), 453-458.
68. Brackenbury, W. J.; Djamgoz, M. B., *J Cell Physiol* **2007,** *210* (3), 602-8.
69. Russell, P. J.; Bennett, S.; Stricker, P., *Clin Chem* **1998,** *44* (4), 705-23.
70. Gann, P. H.; Klein, K. G.; Chatterton, R. T.; Ellman, A. E.; Grayhack, J. T.; Nadler, R. B.; Lee, C., *Prostate* **1999,** *40* (4), 248-55.
71. Uysal-Onganer, P.; Djamgoz, M. B., *Mol Cancer* **2007,** *6*, 76.
72. Ding, Y.; Brackenbury, W. J.; Onganer, P. U.; Montano, X.; Porter, L. M.; Bates, L. F.; Djamgoz, M. B., *J Cell Physiol* **2008,** *215* (1), 77-81.
73. Montano, X.; Djamgoz, M. B., *FEBS Lett* **2004,** *571* (1-3), 1-8.
74. Ferlay, J.; Shin, H. R.; Bray, F.; Forman, D.; Mathers, C.; Parkin, D. M., *Int J Cancer* **2010,** *127* (12), 2893-917.
75. Roden, R.; Wu, T. C., *Nat Rev Cancer* **2006,** *6* (10), 753-63.

76. Hernandez-Plata, E.; Ortiz, C. S.; Marquina-Castillo, B.; Medina-Martinez, I.; Alfaro, A.; Berumen, J.; Rivera, M.; Gomora, J. C., *Int J Cancer* **2012,** *130* (9), 2013-23.
77. Diss, J. K.; Fraser, S. P.; Walker, M. M.; Patel, A.; Latchman, D. S.; Djamgoz, M. B., *Prostate Cancer Prostatic Dis* **2008,** *11* (4), 325-33.
78. Lin, X. A.; Ren, J. L.; Huo, J. F.; Zhang, J. B.; Wang, X. B., *Nucl Med Biol* **2010,** *37* (6), 702-702.
79. Lin, Y.; Yang, W. J.; Zhang, X. Z.; Zhang, J. B.; Tang, Z. G., *Nucl Med Biol* **2010,** *37* (6), 701-702.
80. Fowler, J., *J Nucl Med* **2002,** *43* (1), 20N-+.
81. Fowler, J. E.; Bigler, S. A.; Farabaugh, P. B., *Cancer* **2002,** *94* (6), 1661-1667.
82. Fowler, J. S.; Ido, T., *Semin Nucl Med* **2002,** *32* (1), 6-12.
83. Fowler, J. S.; Volkow, N. D.; Wang, G. J.; Logan, J., *Abstr Pap Am Chem S* **2002,** *223*, B151-B151.
84. Hao, G. Y.; Singh, A. N.; Liu, W.; Sun, X. K., *Curr Top Med Chem* **2010,** *10* (11), 1096-1112.
85. Love, C.; Din, A. S.; Tomas, M. B.; Kalapparambath, T. P.; Palestro, C. J., *Radiographics* **2003,** *23* (2), 341-58.
86. Schnall, M.; Rosen, M., *J Clin Oncol* **2006,** *24* (20), 3225-33.
87. Hayes, D. F., *Ann Oncol* **1993,** *4* (10), 807-19.
88. Barentsz, J.; Takahashi, S.; Oyen, W.; Mus, R.; De Mulder, P.; Reznek, R.; Oudkerk, M.; Mali, W., *J Clin Oncol* **2006,** *24* (20), 3234-44.
89. Von Schulthess, G. K.; Steinert, H. C.; Hany, T. F., *Radiology* **2006,** *238* (2), 405-22.
90. Rohren, E. M.; Turkington, T. G.; Coleman, R. E., *Radiology* **2004,** *231* (2), 305-32.
91. Mariani, G.; Bruselli, L.; Kuwert, T.; Kim, E.; Flotats, A.; Israel, O.; Dondi, M.; Watanabe, N., *Eur J Nucl Med Mol I* **2010,** *37* (10), 1959-1985.
92. Rosenthal, M. S.; Cullom, J.; Hawkins, W.; Moore, S. C.; Tsui, B. M. W.; Yester, M., *J Nucl Med* **1995,** *36* (8), 1489-1513.
93. Smith, S. V., *Journal of Inorganic Biochemistry* **2004,** *98* (11), 1874-1901.
94. Wolf, A. P., *Clinical Neuropharmacology* **1984,** *7*, S284.
95. Snm What is PET. http://interactive.snm.org/index.cfm?PageID=972.

96. Young, H.; Baum, R.; Cremerius, U.; Herholz, K.; Hoekstra, O.; Lammertsma, A. A.; Pruim, J.; Price, P., *European Journal of Cancer* **1999,** *35* (13), 1773-1782.

97. Young, H.; Baum, R.; Cremerius, U.; Herholz, K.; Hoekstra, O.; Lammertsma, A. A.; Pruim, J.; Price, P., *Eur J Cancer* **1999,** *35* (13), 1773-82.

98. Liu, X. D.; Laforest, R., *Nucl Med Biol* **2009,** *36* (5), 551-559.

99. Ido, T.; Wan, C. N.; Fowler, J. S.; Wolf, A. P., *J Org Chem* **1977,** *42* (13), 2341-2342.

100. Medscape PET case cavalcade, Case X. http://www.medscape.com/viewarticle/477469&usg=__p-irQ_NwoCS0djY6CR7LAtifQko=&h=579&w=400&sz=31&hl=en&start=19&zoom=1&tbnid=NYDMXJU233iykM:&tbnh=134&tbnw=93&prev=/images%3Fq%3DFDG%2BPET%2Bimage%26hl%3Den%26sa%3DX%26rls%3Dcom.microsoft:en-gb:IE-SearchBox%26rlz%3D1I7GZAZ_en%26biw%3D1259%26bih%3D599%26tbs%3Disch:10%2C485&itbs=1&iact=hc&vpx=332&vpy=234&dur=1938&hovh=270&hovw=187&tx=107&ty=293&ei=pending&oei=s7_0TKyVHIGGhQeJ5rXCBQ&esq=2&page=2&ndsp=19&ved=1t:429,r:14,s:19&biw=1259&bih=599.

101. Mosconi, L.; Berti, V.; Glodzik, L.; Pupi, A.; De Santi, S.; De Leon, M. J., *Journal of Alzheimer's Disease* **2010,** *20* (3), 843-854.

102. Foster, N. L.; Heidebrink, J. L.; Clark, C. M.; Jagust, W. J.; Arnold, S. E.; Barbas, N. R.; Decarli, C. S.; Scott Turner, R.; Koeppe, R. A.; Higdon, R.; Minoshima, S., *Brain* **2007,** *130* (10), 2616-2635.

103. Johnson, K. A.; Dickerson, B. C., *Neurology* **2011,** *77* (23), 2008-2009.

104. Herholz, K.; Westwood, S.; Haense, C.; Dunn, G., *J Nucl Med* **2011,** *52* (8), 1218-1226.

105. Zhou, J.; Greicius, M. D.; Gennatas, E. D.; Growdon, M. E.; Jang, J. Y.; Rabinovici, G. D.; Kramer, J. H.; Weiner, M.; Miller, B. L.; Seeley, W. W., *Brain* **2010,** *133* (5), 1352-1367.

106. Lin, K. J.; Hsu, W. C.; Hsiao, I. T.; Wey, S. P.; Jin, L. W.; Skovronsky, D.; Wai, Y. Y.; Chang, H. P.; Lo, C. W.; Yao, C. H.; Yen, T. C.; Kung, M. P., *Nucl Med Biol* **2010,** *37* (4), 497-508.

107. Lilly, E. FDA Approves Amyvid™ (Florbetapir F 18 Injection) for Use in Patients Being Evaluated for Alzheimer's Disease and Other Causes of Cognitive Decline. http://www.prnewswire.com/news-releases/fda-approves-amyvid-

florbetapir-f-18-injection-for-use-in-patients-being-evaluated-for-alzheimers-disease-and-other-causes-of-cognitive-decline-146497155.html?utm_source=twitterfeed&utm_medium=twitter.

108. Ametamey, S. M.; Samnick, S.; Leenders, K. L.; Vontobel, P.; Quack, G.; Parsons, C. G.; Schubiger, P. A., *J Recept Signal Tr R* **1999,** *19* (1-4), 129-141.
109. Robins, E. G.; Zhao, Y.; Khan, I.; Wilson, A.; Luthra, S. K.; Arstad, E., *Bioorg Med Chem Lett* **2010,** *20* (5), 1749-1751.
110. Labas, R.; Gilbert, G.; Nicole, O.; Dhilly, M.; Abbas, A.; Tirel, O.; Buisson, A.; Henry, J.; Barre, L.; Debruyne, D.; Sobrio, F., *Eur J Med Chem* **2011,** *46* (6), 2295-309.
111. Hille, B., *J Gen Physiol* **1977,** *69* (4), 497-515.
112. Lagan, G.; Mclure, H. A., *Current Anaesthesia & Critical Care* **2004,** *15* (4-5), 247-254.
113. Ruetsch, Y. a. B. T. B. A., *Curr Top Med Chem* **2001,** *1*, 175-182.
114. Lima, M. S. D.; Soares, B. G. D. O.; Reisser, A. a. P.; Farrell, M., *Addiction* **2002,** *97* (8), 931-949.
115. Tayama, M.; Solomon, S. B.; Glantz, S. A., *Am J Physiol* **1998,** *274* (6 Pt 2), H2100-9.
116. Langenfeld, H.; Weirich, J.; Kohler, C.; Kochsiek, K., *J Cardiovasc Pharmacol* **1990,** *15* (2), 338-45.
117. Fiske, J. L.; Fomin, V. P.; Brown, M. L.; Duncan, R. L.; Sikes, R. A., *Cancer and Metastasis Reviews* **2006,** *25* (3), 493-500.
118. Hwang, D.; Noguchi, T., Tetrodotoxin Poisoning. In *Advances in Food and Nutrition Research*, Steve, L. T., Ed. Academic Press: 2007; Vol. Volume 52, pp 141-236.
119. Kishi, Y.; Aratani, M.; Fukuyama, T.; Nakatsubo, F.; Goto, T.; Inoue, S.; Tanino, H.; Sugiura, S.; Kakoi, H., *J Am Chem Soc* **1972,** *94* (26), 9217-9219.
120. Jover, E.; Massacrier, A.; Cau, P.; Martin, M. F.; Couraud, F., *J Biol Chem* **1988,** *263* (3), 1542-8.
121. Lombet, A.; Bidard, J.-N.; Lazdunski, M., *FEBS Letters* **1987,** *219* (2), 355-359.
122. Lipkind, G. M.; Fozzard, H. A., *Biophys J* **1994,** *66* (1), 1-13.
123. Qu, Y.; Rogers, J.; Tanada, T.; Scheuer, T.; Catterall, W. A., *P Natl Acad Sci USA* **1995,** *92* (25), 11839-11843.
124. Vianna-Jorge, R.; Oliveira, C. F.; Ponte, C. G.; Suarez-Kurtz, G., *Eur J Pharmacol* **2001,** *428* (1), 45-49.

125. Wanner, S. G.; Glossmann, H.; Knaus, H.-G.; Baker, R.; Parsons, W.; Rupprecht, K. M.; Brochu, R.; Cohen, C. J.; Schmalhofer, W.; Smith, M.; Warren, V.; Garcia, M. L.; Kaczorowski, G. J., *Biochemistry-Us* **1999,** *38* (34), 11137-11146.

126. Palmer, R. A.; Potter, B. S.; Leach, M. J.; Jenkins, T. C.; Chowdhry, B. Z., *MedChemComm* **2010,** *1* (1), 45-49.

127. Shao, B.; Victory, S.; Ilyin, V. I.; Goehring, R. R.; Sun, Q.; Hogenkamp, D.; Hodges, D. D.; Islam, K.; Sha, D.; Zhang, C. W.; Nguyen, P.; Robledo, S.; Sakellaropoulos, G.; Carter, R. B., *J Med Chem* **2004,** *47* (17), 4277-4285.

128. Ramu, K.; Lam, G. N.; Hughes, H., *Drug Metab Dispos* **2000,** *28* (10), 1153-1161.

129. Patel, S.; Gibson, R., *Nucl Med Biol* **2008,** *35* (8), 805-15.

130. Laruelle, M.; Slifstein, M.; Huang, Y., *Mol Imaging Biol* **2003,** *5* (6), 363-75.

131. Dimmock, J. R.; Puthucode, R. N.; Smith, J. M.; Hetherington, M.; Quail, J. W.; Pugazhenthi, U.; Lechler, T.; Stables, J. P., *J Med Chem* **1996,** *39* (20), 3984-97.

132. Akiko, O.; Katsuya, M.; Hideaki, O.; Noriyuki, Y., *Synthetic Communications: An International Journal for Rapid Communication of Synthetic Organic Chemistry* **2007,** *37* (16), 2701 - 2715.

133. Thomas, L.; Johannes, E.; Heinz, H. C., *Nucl Med Biol* **2002,** *29* (2), 255-262.

134. Stang, P. J., *Angewandte Chemie International Edition in English* **1992,** *31* (3), 274-285.

135. Kamierczak, P.; Skulski, L., *Synthesis* **1995,** *1995* (08), 1027,1032.

136. Sperotto, E.; De Vries, J. G.; Van Klink, G. P. M.; Van Koten, G., *Tetrahedron Letters* **2007,** *48* (41), 7366-7370.

137. Glaser, M.; Årstad, E., *Bioconjugate Chemistry* **2007,** *18* (3), 989-993.

138. Constanti, A.; Bagetta, G.; Libri, V., *Neuroscience* **1993,** *56* (4), 887-904.

139. Bergman, J.; Solin, O., *Nucl Med Biol* **1997,** *24* (7), 677-683.

140. Toorongian, S. A.; Mulholland, G. K.; Jewett, D. M.; Bachelor, M. A.; Kilbourn, M. R., *International Journal of Radiation Applications and Instrumentation. Part B. Nuclear Medicine and Biology* **1990,** *17* (3), 273-279.

141. Arstad, E. L., Gb), 2009.

142. Chirakal, R., *Nucl Med Biol* **1996,** *23*, 41-45.

143. Nahmias, R. C. G. C. G. F. G. J. S. C., *Nucl Med Biol* **1996,** *23*, 41-45.

144. Coenen, H. H.; Elsinga, P. H.; Iwata, R.; Kilbourn, M. R.; Pillai, M. R. A.; Rajan, M. G. R.; Wagner, H. N.; Zaknun, J. J., *Nucl Med Biol* **2010,** *37* (7), 727-740.

145. Blom, E.; Karimi, F.; Långström, B., *Journal of Labelled Compounds and Radiopharmaceuticals* **2009,** *52* (12), 504-511.

146. El Kazzouli, S.; Koubachi, J.; Berteina-Raboin, S.; Mouaddib, A.; Guillaumet, G., *Tetrahedron Letters* **2006,** *47* (48), 8575-8577.

147. Merritt, E. A.; Carneiro, V. M.; Silva, L. F., Jr.; Olofsson, B., *J Org Chem* **2010,** *75* (21), 7416-9.

148. Papoutsi, I.; Spyroudis*, S.; Varvoglis*, A.; Raptopoulou, C. P., *Tetrahedron* **1997,** *53* (17), 6097-6112.

149. Ludwig, T.; Ermert, J.; Coenen, H. H., *Nucl Med Biol* **2002,** *29* (2), 255-262.

150. *Journal of Labelled Compounds and Radiopharmaceuticals* **1997,** *40* (1), 1-72.

151. Pews, R. G.; Tsuno, Y.; Taft, R. W., *J Am Chem Soc* **1967,** *89* (10), 2391-2396.

152. Ermert, J.; Hocke, C.; Ludwig, T.; Gail, R.; Coenen, H. H., *J Labelled Compd Rad* **2004,** *47* (7), 429-441.

153. Berridge, M.; Crouzel, C.; Comar, D., *J Labelled Compd Rad* **1982,** *19* (11-1), 1639-1640.

154. Lemaire, C.; Guillaume, M.; Christiaens, L.; Palmer, A. J.; Cantineau, R., *Appl Radiat Isotopes* **1987,** *38* (12), 1033-1038.

155. Karramkam, M.; Hinnen, F.; Bramoulle, Y.; Jubeau, S.; Dolle, F., *J Labelled Compd Rad* **2002,** *45* (13), 1103-1113.

156. *Journal of Labelled Compounds and Radiopharmaceuticals* **1995,** *37* (6), 510-612.

157. Maeda, M.; Fukumura, T.; Kojima, M., *Appl Radiat Isotopes* **1987,** *38* (4), 307-310.

158. Martin-Santamaria, S.; Carroll, M. A.; Carroll, C. M.; Carter, C. D.; Pike, V. W.; Rzepa, H. S.; Widdowson, D. A., *Chemical Communications* **2000,** (8), 649-650.

159. Shah, A.; W. Pike, V.; A. Widdowson, D., *Journal of the Chemical Society, Perkin Transactions 1* **1998,** (13), 2043-2046.

160. Ermert, J.; Hocke, C.; Ludwig, T.; Gail, R.; Coenen, H. H., *Journal of Labelled Compounds and Radiopharmaceuticals* **2004,** *47* (7), 429-441.

161. W. Pike, V.; Butt, F.; Shah, A.; A. Widdowson, D., *Journal of the Chemical Society, Perkin Transactions 1* **1999,** (3), 245-248.

162. Barriga, S., *Synlett* **2001,** (4), 563-563.

163. Hogenkamp, D., 6414011B1, 2002.

164. Liu G., S. H. L., Szczepankiewicz B. G., Xin A., Zhao H., Serby M. D., Liu B., Liu, M., 2006.

165. Elmaleh D. R., F. a. J., Shoup T. M.,, 2008.

166. Royeck, M.; Horstmann, M.-T.; Remy, S.; Reitze, M.; Yaari, Y.; Beck, H., *Journal of Neurophysiology* **2008,** *100* (4), 2361-2380.

167. Whalley, B. J.; Wilkinson, J. D.; Williamson, E. M.; Constanti, A., *Neuroscience Letters* **2004,** *365* (1), 58-63.

168. Schwabe, K.; Ebert, U.; Löscher, W., *Neuroscience* **2004,** *126* (3), 727-741.

169. Sheldon, R. S.; Duff, H. J.; Thakore, E.; Hill, R. J., *J Pharmacol Exp Ther* **1994,** *268* (1), 187-94.

170. Arstad, E., 2008/152109, 2008.

171. Elsinga, P. H.; Kawamura, K.; Kobayashi, T.; Tsukada, H.; Senda, M.; Vaalburg, W.; Ishiwata, K., *Synapse* **2002,** *43* (4), 259-267.

172. Lu, S.-Y.; Chin, F. T.; Mccarron, J. A.; Pike, V. W., *Journal of Labelled Compounds and Radiopharmaceuticals* **2004,** *47* (5), 289-297.

173. Hara, T.; Kosaka, N.; Kishi, H., *J Nucl Med* **2002,** *43* (2), 187-199.

174. Bauman, A.; Piel, M.; Schirrmacher, R.; Rösch, F., *Tetrahedron Lett* **2003,** *44* (51), 9165-9167.

175. Schmitz, A.; Shiue, C. Y.; Feng, Q.; Shiue, G. G.; Deng, S.; Pourdehnad, M. T.; Schirrmacher, R.; Vatamaniuk, M.; Doliba, N.; Matschinsky, F.; Wolf, B.; Rösch, F.; Naji, A.; Alavi, A. A., *Nucl Med Biol* **2004,** *31* (4), 483-491.

176. Hogenkamp, D. J., Upasani, C. A, Nguyen P.,, 2000.

177. Block, D.; Coenen, H. H.; Stöcklin, G., *Journal of Labelled Compounds and Radiopharmaceuticals* **1987,** *24* (9), 1029-1042.

178. Hoigebazar, L.; Jeong, J. M.; Hong, M. K.; Kim, Y. J.; Lee, J. Y.; Shetty, D.; Lee, Y.-S.; Lee, D. S.; Chung, J.-K.; Lee, M. C., *Bioorgan Med Chem* **2011,** *19* (7), 2176-2181.

179. Huang, Y.; Hwang, D. R.; Narendran, R.; Sudo, Y.; Chatterjee, R.; Bae, S. A.; Mawlawi, O.; Kegeles, L. S.; Wilson, A. A.; Kung, H. F.; Laruelle, M., *J Cereb Blood Flow Metab* **2002,** *22* (11), 1377-98.

180. Samnick, S.; Ametamey, S.; Leenders, K. L.; Vontobel, P.; Quack, G.; Parsons, C. G.; Neu, H.; Schubiger, P. A., *Nucl Med Biol* **1998,** *25* (4), 323-30.

181. Peterson, L. B.; Blagg, B. S., *Bioorg Med Chem Lett* **2010,** *20* (13), 3957-60.

182. Evans, R. A., *Australian Journal of Chemistry* **2007,** *60* (6), 384-395.

183. Kolb, H. C.; Finn, M. G.; Sharpless, K. B., *Angewandte Chemie International Edition* **2001,** *40* (11), 2004-2021.

184. Hein, C. D.; Liu, X. M.; Wang, D., *Pharm Res* **2008,** *25* (10), 2216-30.

185. Kolb, H. C.; Finn, M. G.; Sharpless, K. B., *Angew Chem Int Ed Engl* **2001,** *40* (11), 2004-2021.

186. Katz, E.; Willner, I., *Angew Chem Int Ed Engl* **2004,** *43* (45), 6042-108.

187. Straub, B. F., *Chem Commun (Camb)* **2007,** (37), 3868-70.

188. Iddon, L.; Leyton, J.; Indrevoll, B.; Glaser, M.; Robins, E. G.; George, A. J. T.; Cuthbertson, A.; Luthra, S. K.; Aboagye, E. O., *Bioorganic & Medicinal Chemistry Letters* **2011,** *21* (10), 3122-3127.

189. Djamgoz, M. B. A., *Iubmb Life* **2009,** *61* (3), 298-298.

190. Djamgoz, M. B. A.; Brackenbury, W. J.; Chioni, A. M.; Diss, J. K. J., *Breast Cancer Res Tr* **2007,** *101* (2), 149-160.

191. Grönroos, T.; Eskola, O.; Lehtiö, K.; Minn, H.; Marjamäki, P.; Bergman, J.; Haaparanta, M.; Forsback, S.; Solin, O., *J Nucl Med* **2001,** *42* (9), 1397-1404.

192. Brunner, M.; Langer, O.; Dobrozemsky, G.; Müller, U.; Zeitlinger, M.; Mitterhauser, M.; Wadsak, W.; Dudczak, R.; Kletter, K.; Müller, M., *Antimicrobial Agents and Chemotherapy* **2004,** *48* (10), 3850-3857.

193. Tang, G.; Wang, M.; Tang, X.; Luo, L.; Gan, M., *Appl Radiat Isotopes* **2003,** *58* (2), 219-225.

194. Fraser, S. P.; Diss, J. K.; Chioni, A. M.; Mycielska, M. E.; Pan, H.; Yamaci, R. F.; Pani, F.; Siwy, Z.; Krasowska, M.; Grzywna, Z.; Brackenbury, W. J.; Theodorou, D.; Koyuturk, M.; Kaya, H.; Battaloglu, E.; De Bella, M. T.; Slade, M. J.; Tolhurst, R.; Palmieri, C.; Jiang, J.; Latchman, D. S.; Coombes, R. C.; Djamgoz, M. B., *Clin Cancer Res* **2005,** *11* (15), 5381-9.

195. In Vivo Biology Team, S. U., Hoppmann, S., Ed. 2012.

196. Gottardis, M. M.; Robinson, S. P.; Jordan, V. C., *Journal of Steroid Biochemistry* **1988,** *30* (1–6), 311-314.

197. Letienne, R.; Bel, L.; Bessac, A. M.; Vacher, B.; Le Grand, B., *Eur J Pharmacol* **2009,** *624* (1-3), 16-22.

198. Crill, W. E., *Annu Rev Physiol* **1996,** *58*, 349-62.

199. Ju, Y. K.; Saint, D. A.; Gage, P. W., *J Physiol* **1996,** *497 (Pt 2)*, 337-47.

200. Kunzelmann, K., *J Membr Biol* **2005,** *205* (3), 159-73.

201. Hammarström, A.; Gage, P., *European Biophysics Journal* **2002,** *31* (5), 323-330.